Extending Quantum Dot Arrays Into Three Dimensions

Hanifa Tidjani

EXTENDING QUANTUM DOT ARRAYS INTO THREE DIMENSIONS

EXTENDING QUANTUM DOT ARRAYS INTO THREE DIMENSIONS

Dissertation

Dissertation for the purpose of obtaining the degree of doctor
at Delft University of Technology
by the authority of the Rector Magnificus Prof.dr.ir.H.Bijl,
chair of the Board for Doctorates
to be defended publicly on Friday 6th March 2026 at 10 o'clock

by

Hanifa TIDJANI

This dissertation has been approved by the promotors

Composition of the doctoral committee:

Rector Magnificus	Chairperson
Prof. dr. ir. M. Veldhorst	Delft University of Technology, promotor
Dr. G. Scappucci	Delft University of Technology, promotor
Independent members:	
Prof. dr. ir. L. M. K. Vandersypen	Delft University of Technology
Prof. dr. ir. F. A. Zwanenburg	University of Twente
Prof. dr. A. Hofmann	University of Basel, Switzerland
Dr. S. Bosco	Delft University of Technology
Reserve member:	
Prof. dr. Leonardo DiCarlo	Delft University of Technology


Keywords: Ge/SiGe, quantum dots, spin qubits, quantum computing, hole spin qubits, vertical double quantum dots, bilayers

Printed by: ProefschriftMaken

ISBN 978-94-6384-921-0

An electronic version of this dissertation is available at
http://repository.tudelft.nl/

Security is largely a superstition; it does not exist in nature... Life is either a grand adventure or nothing.

— Helen Keller

For the girls who are told their place is in the home.

CONTENTS

1

INTRODUCTION

The next frontier: quantum computation

1

THE landscape in which fundamental particles exist is within an elegant interplay of the four fundamental forces; gravity, electromagnetic, weak and strong. These forces play an essential role in defining the potential energy landscapes that underpin quantum systems [1, 2]. Physicists have long sought to understand the landscape in which particles exist, with the ultimate goal of mastering them well enough to control and utilize them, and validate or refute theories [3, 4]. When a system exhibits quantum mechanical features, this means that its properties such as *Energy, Position, Momentum, and Spin* are not well defined quantities, but exist in uncertainty relations, with all the summary of this quantum information contained within the *wavefunction*.

The quantum mechanical interaction between particles may give rise to collective phenomena such as superconductivity[5, 6]. Technologies which exploit quantum phenomena are already present in modern life, such as in magnetic resonance imaging, or lasers. In quantum computing we wish to have a higher level of control over quantum matter, for instance to engineer interactions to realise new materials and predict new medicines, or as quantum bits as building blocks for computational technology.

What exactly is the building block of a quantum computer? A qubit is a quantum mechanical two-level system and is mathematically described by two complex numbers. A qubit does not have to exist in a definite state, but rather can be in a superposition of states. The the basic picture of a qubit is expanded upon in chapter2. Quantum mechanical interactions between multiple qubits can lead to entanglement, where information is encoded in their joint states. Exploitation of this property has led to the development of quantum algorithms (e.g. Shor's algorithm[7]) that may offer an exponential advantage compared to classical computers, far surpassing the binary capacity of classical systems which exist in well-defined ones and zeroes. These quantum states could be further exploited to facilitate advances, such as entanglement-based information transfer and quantum teleportation [8].

Maintaining perfect quantum states would be possible by decoupling them from whichever noise sources cause decoherence, whether from the hyperfine interaction, charge noise, or phonons. However, isolating quantum systems from unwanted interactions often implies they are also decoupled from desired interactions, thus challenging the control. It is commonly expected that the performance of individual qubits will not be sufficient for practical applications. Instead, quantum error correction schemes must be employed to make quantum bits which are both protected from decoherence, but can still be manipulated [9].

One of the key promises of quantum computing is its potential to accelerate computation, enabling us to solve problems that have been out of reach due to the hardware limitations of supercomputers. This promise has largely been predicated on the slowdown of transistor scaling observed in recent years. Yet, the emergence of high performance graphical processing units (GPUs), such as those developed by NVIDIA, suggests that classical computing chips will become more efficient at computational tasks [10], including those which quantum computing is intended for. Thus, we minimally expect that quantum computers will interface with classical computers, only employing them when the advantage is significant. A summary of problems which are suited for quantum applications are listed in table 1.1[1].

[1] The citation in the problems panel applies to the whole row.

Problem	Quantum Time Complexity	Classical Time Complexity	Speedup	Fundamental Quantum Operation
Factorization [11] (e.g., RSA encryption)	Polynomial $O(n^3)$	Sub-exponential $O(e^{n^{1/3}(\log n)^{2/3}})$	Exponential	Quantum Fourier Transform
Unstructured Search [12] (e.g., Searching in a database)	Quadratic $O(\sqrt{N})$	Linear $O(N)$	Quadratic	Amplitude Amplification
Quantum Simulation [13] (e.g., Simulating chemical reactions)	Polynomial $O(\log N)$	Exponential $O(N^k)$	Exponential	Hamiltonian Evolution
Quantum Chemistry [14] (e.g., Predicting molecular ground states)	Polynomial $O(\log N)$	Exponential $O(N^k)$	Exponential	Variational Principles
Solving Linear Systems [15] (e.g., Sparse matrix inversion)	Polynomial $O(\log N)$	Exponential $O(N^k)$	Exponential	Quantum Phase Estimation
Sampling Problems [16] (e.g., Boson Sampling)	Polynomial or sublinear	Exponential	Exponential	Quantum Interference
Graph Problems [17] (e.g., Finding shortest paths)	Polynomial or sublinear	Exponential (in some cases)	Potential exponential	Quantum Walks
Quantum Key Distribution [18] (e.g., BB84 Protocol)	Instantaneous $O(1)$	Not secure classically	Fundamental advantage	Quantum Entanglement

Table 1.1: Comparison of Quantum and Classical Time Complexities of certain problems, and the quantum operation which provides the speed-up.

.

One field which is often considered to be an area where quantum systems may excel is analogue quantum simulations [19, 20, 21]. This use case is inherently suited to quantum computers and will continue to be a compelling area of application. Interactions in nature are rarely confined to simple, one- or two-dimensional interactions. As a result, simulating effective systems in one, two, or three dimensions, is a highly computationally intensive task. In particular, the transition between different dimensions can lead to highly intriguing and complex behavior. For quantum computers designed for quantum simulations, it is therefore crucial to be able to replicate the three-dimensional interactions found in nature.

There has been an extraordinary scale of investment into quantum technologies in the past 30 years. There are a myriad of platforms determined to become the quantum computer of the future. However, the properties of different platforms varies, with some better suited to some applications than others. For instance, quantum dot based quantum computers have a highly tunable tunnel coupling and detuning energies, making them well suited for simulating Fermi-hubbard hamiltonians[22], while cold atoms with their long-and short range interactions are better suited to encoding pure spin models such as the Ising model. The research in this thesis focuses on the development of semiconductor based spin qubit quantum computers. Specifically, we use Germanium/Silicon Germanium heterostructures to isolate single holes, and form qubits using the underlying spin states. The interest in forming quantum computers using semiconductors stems from a few ideas:

- **CMOS compatibility:** They can leverage the mature existing semiconductor manufacturing techniques, to produce at scale.
- **Footprint:** Quantum dots which host semiconducting spin qubits can be as small as ~100nm, and when compared to other platforms this is extremely small. Many

can fit in a smaller area, **important for scaling to millions of physical qubits**. However, this argument can be nuanced depending on the exact qubit encodings, error correction overheads and the ability to industrially fabricate electrical interconnects which can control the quantum dots.

However they face some challenges:

- **Cooling power:** They need to be cooled to near to 100m K ($-272.9^{\circ}C$) to be operated, and this costs a lot of energy. Highertemperature operation with high fidelity has been achieved above 1 K, however it is an open question whether this will yield high fidelity control of large systems[23].
- **Variability:** The electrons and holes formed in semiconductors often vary in their properties, due to slight changes in their local environments. This leads to many variations in the exact properties of spins held in the quantum dots with many implications on voltage tuning, gate fidelity and more.
- **Fabrication:** Precisely fabricating many layers of metallic gates has limitations from semiconducting manufacturing, limiting array sizes.
- **High power operation:** The signals used to control the qubits often need to be high in power and in frequency, and range from MHz-GHz.

These are just a few of the challenges that need to be overcome in the lowest layers of a future full-stack fault-tolerant quantum computer in semiconducting heterostrucutres. The research presented in this thesis, explores various themes and challenges within the spin qubit quantum computing field. In particular, there is an emphasis on using multilayered heterostrucutres to scale quantum dots out of the plane.

WHY GERMANIUM?

Combining metallic gating and ohmic contacts to Germanium/Silicon Germanium heterostructures, we confine single holes where we use the spin degree of freedom to encode quantum information. Semiconductor quantum dot platforms can be realized in different manners with the other leading platforms being holes/electrons in SiMOS and electrons in Si/SiGe. Summarised below are the properties that make Ge/SiGe special in the context of gate defined semiconductor-based quantum computing:

- **Buried quantum wells** can be grown to reduce sensitivity to charge noise from dielectrics in layers on top, whilst also compatible with existing CMOS semiconductor manufacturing.
- **Fermi level pinning near the valence band:** Many metals can make an ohmic contat to germanium, thus alleviating the need for dopants to make electric contacts. When ohmic contact is made to Ge, holes can be directly conducted because as the Fermi level is pinned close to the valence band. In materials such as Si/SiGe, the Fermi level is not pinned near the conduction or valence band, and doping is used to artificially shift it. Doping can increase disorder and adds extra steps in fabrication. This property makes it much easier to fabricate in-house devices.

- **Small effective mass (m^*) of holes:** The effective mass of an electron ($m^* \approx m_e$) is much larger than that for holes, where ($m^* \approx 0.055 m_e$)[24, 25]. The small effective mass of holes allows the fabrication of larger quantum dots than with electrons, as $L \propto 1/\sqrt{m^*}$, where L is the effective dot size set by the electrostatic confinement. When considering limitations of fabrication, this is an important factor.
- **Absence of valley states:** In Ge/SiGe quantum dots, orbital energies are of the of order several meV (enabled by the low effective mass and the absence of valley states), while valleys in the Si/SiGe electron band structure often appear with small splittings[26, 27, 28] and increase system preparation and measurement (SPAM)-related errors.
- **Spin–orbit coupling and g-tensor variation:** Sometimes seen as an advantage and disadvantage, holes in Ge exhibit strong spin–orbit coupling and g-tensor variation. Spin–orbit coupling can allow for electrical spin manipulation of single spins, and baseband operation. On the other hand it can increase SPAM errors, due to the spin orbit anticrossing.

Expanding device connectivity: Bilayers

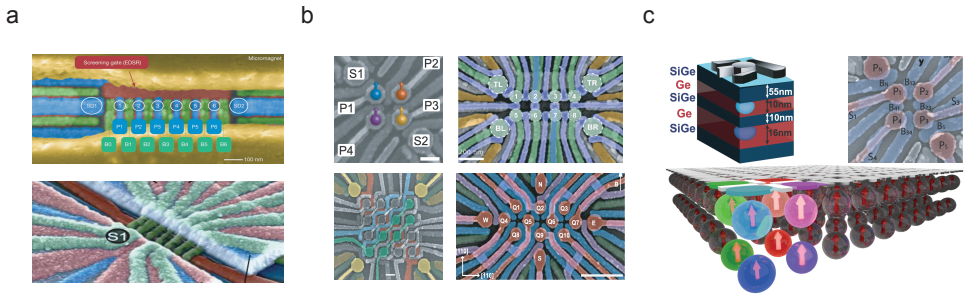

Figure 1.1: **Quantum dot arrays in Silicon and Germanium. a** Silicon spin qubits often need artificial spin orbit coupling using a micromagnet, limiting the scaling to linear or bilinear. silicon[29, 30]. **b** Arrays in germanium have scaled from 2x2 to larger arrays. [31, 32, 33, 34](citations from top left anticlockwise). **c** Expanding the heterostructure from a single well to a double well in germanium enables array scaling into the out of plane axis [35]

In quantum computing architectures, the connectivity of the qubits is an important aspect, as this determines which qubits can be brought into contact with others. The intrinsic connectivity is determined by the nearest neighbors within the device geometry. Higher connectivity can be achieved by moving qubits, or swapping their quantum states. Higher connectivity reduces gate overhead for algorithm implementation—most notably for error-correcting codes such as the surface code—and enables more efficient entanglement generation.

In gate-defined semiconductor quantum dot systems, achieving high connectivity is non-trivial because qubits are typically confined to planar heterostructures, which limits the available coupling geometry. To circumvent this, shuttling links and coupling via superconducting resonators, or SWAP operations are proposed to increase connectivity.

Quantum dot arrays in Si/SiGe have traditionally been linear, driven by the need for micromagnet-induced field gradients, as shown in Fig. 1.1a. For exchange-only qubit implementations, micromagnets are not required, allowing scaling beyond one dimension. In Ge/SiGe, intrinsic spin–orbit coupling removes the need for micromagnet gradients altogether, making two-dimensional scaling substantially more straightforward (Fig. 1.1b). Introducing an additional quantum well further enables scaling out of the plane, as illustrated in Fig. 1.1c.

One of the main questions in this thesis is whether Ge/SiGe heterostructures can have higher instrinsic connectivity by scaling the heterostructures out of the plane[36, 37]. The capability to build quantum dots in three-dimensional structures also has important implications for quantum simulations, where accurately mimicking interactions in nature often requires three dimensional couplings.

THESIS OVERVIEW

The remaining sections of this thesis will have the following structure:
In **Chapter 2**, an introduction is made on the materials, devices and basics of quantum computation in the context of Ge/SiGe gate defined quantum dot spin qubits. In **Chapter 3**, information is provided on the specifics of operating bilayer devices. In **Chapter 4**, we begin by operating on a planar 2×2 spin qubit array, We calibrate the exchange interaction of the nearest neighbor spins in the array. We then turn them on diabatically to the equal exchange points and demonstrate a resonating valence bond. In **Chapter 5**, on the same 2×2 device we establish high fidelity baseband control technique of single spin qubit and two qubit gates, benchmarked using both interleaved randomized benchmarking (IRB) and gate set tomography (GST). We realize fast gates with low magnetic fields, naturally extending coherence times. In **Chapter 6** the bilayer heterostructure is experimentally introduced, and form a vertical double quantum dot in a Ge/SiGe double quantum well heterostructure. In **Chapter 7** we expand on this concept and form a 2×2 aligned in the xz- plane, by forming two vertical double quantum dots. In **Chapter 8**, we iterate on the bilayer heterostructure design and demonstrate the formation of a minimally three-dimensional quantum dot array. We show how this can be used for qubit operation, using the hopping spin control technique.

BIBLIOGRAPHY

[1] M. A. Nielsen and I. L. Chuang. *Quantum Computation and Quantum Information*. Cambridge University Press, June 2012. ISBN: 9781107002173.

[2] D. J. Griffiths and D. F. Schroeter. *Introduction to Quantum Mechanics*. Cambridge University Press, Aug. 2018. ISBN: 9781316995433.

[3] S. Weinberg and D. Park. "Dreams of a Final Theory". In: *American Journal of Physics* 62 (1 Jan. 1994), pp. 94–95. ISSN: 0002-9505.

[4] R. P. Feynman. "Simulating physics with computers". In: *International Journal of Theoretical Physics* 21 (6-7 June 1982), pp. 467–488. ISSN: 0020-7748.

[5] J. F. Annett. *Superconductivity, superfluids, and condensates*. Oxford University Press, 2004, p. 186. ISBN: 9780198507567.

[6] B. T. Matthias, T. H. Gkballk, and V. B. Compton. "Modern Superconductivity". In: *Reviews of Modern Physics* 37.35 (1963), pp. 1–22.

[7] P. Shor. "Algorithms for quantum computation: discrete logarithms and factoring". In: *Proceedings 35th Annual Symposium on Foundations of Computer Science*. IEEE Comput. Soc. Press, pp. 124–134. ISBN: 0-8186-6580-7.

[8] C. H. Bennett, G. Brassard, C. Crépeau, R. Jozsa, A. Peres, and W. K. Wootters. "Teleporting an unknown quantum state via dual classical and Einstein-Podolsky-Rosen channels". In: *Physical Review Letters* 70 (13 Mar. 1993), pp. 1895–1899. ISSN: 0031-9007.

[9] A. G. Fowler, M. Mariantoni, J. M. Martinis, and A. N. Cleland. "Surface codes: Towards practical large-scale quantum computation". In: *Physical Review A* 86 (3 Sept. 2012), p. 032324. ISSN: 1050-2947.

[10] J. Faj, I. Peng, J. Wahlgren, and S. Markidis. "Quantum Computer Simulations at Warp Speed: Assessing the Impact of GPU Acceleration: A Case Study with IBM Qiskit Aer, Nvidia Thrust amp; cuQuantum". In: IEEE, Oct. 2023, pp. 1–10. ISBN: 979-8-3503-2223-1.

[11] P. W. Shor. "Polynomial-Time Algorithms for Prime Factorization and Discrete Logarithms on a Quantum Computer". In: *SIAM Journal on Computing* 26 (5 Oct. 1997), pp. 1484–1509. ISSN: 0097-5397.

[12] L. K. Grover. "A fast quantum mechanical algorithm for database search". In: ACM Press, 1996, pp. 212–219. ISBN: 0897917855.

[13] M. Suzuki. "General theory of fractal path integrals with applications to many-body theories and statistical physics". In: *Journal of Mathematical Physics* 32 (2 Feb. 1991), pp. 400–407. ISSN: 0022-2488.

[14] A. Peruzzo, J. McClean, P. Shadbolt, M.-H. Yung, X.-Q. Zhou, P. J. Love, A. Aspuru-Guzik, and J. L. O'Brien. "A variational eigenvalue solver on a photonic quantum processor". In: *Nature Communications* 5 (1 July 2014), p. 4213. ISSN: 2041-1723.

[15] A. W. Harrow, A. Hassidim, and S. Lloyd. "Quantum Algorithm for Linear Systems of Equations". In: *Physical Review Letters* 103 (15 Oct. 2009), p. 150502. ISSN: 0031-9007.

[16] S. Aaronson and A. Arkhipov. "The Computational Complexity of Linear Optics". In: *Theory of Computing* 9 (1 2013), pp. 143–252. ISSN: 1557-2862.

[17] A. M. Childs. "Universal Computation by Quantum Walk". In: *Physical Review Letters* 102 (18 May 2009), p. 180501. ISSN: 0031-9007.

[18] C. H. Bennett and G. Brassard. "Quantum cryptography: Public key distribution and coin tossing". In: (Mar. 2020).

[19] J. I. Cirac and P. Zoller. "Quantum Computations with Cold Trapped Ions". In: *Physical Review Letters* 74 (20 May 1995), pp. 4091–4094. ISSN: 0031-9007.

[20] P. Atkins and R. Friedman. *Molecular Quantum Mechanics*. Oxford University Press, Nov. 2010. ISBN: 9780199541423.

[21] A. Aspuru-Guzik, A. D. Dutoi, P. J. Love, and M. Head-Gordon. "Simulated Quantum Computation of Molecular Energies". In: *Science* 309 (5741 Sept. 2005), pp. 1704–1707. ISSN: 0036-8075.

[22] T. Hensgens, T. Fujita, L. Janssen, X. Li, C. J. van Diepen, C. Reichl, W. Wegscheider, S. Das Sarma, and L. M. K. Vandersypen. "Quantum simulation of a Fermi-Hubbard model using a semiconductor quantum dot array". In: *Nature* 548 (2017), pp. 70–73.

[23] L. Petit, M. Russ, H. G. J. Eenink, W. I. L. Lawrie, J. S. Clarke, L. M. K. Vandersypen, and M. Veldhorst. "Design and integration of single-qubit rotations and two-qubit gates in silicon above one Kelvin". In: *Communications Materials* 3 (2022), p. 82.

[24] L. A. Terrazos, A. L. Saraiva, X. Hu, M. Friesen, S. N. Coppersmith, B. Koiller, and R. B. Capaz. "Light-mass hole-spin qubits formed in a Ge quantum well". In: (2018), pp. 1–7.

[25] M. Lodari, A. Tosato, D. Sabbagh, M. A. Schubert, G. Capellini, A. Sammak, M. Veldhorst, and G. Scappucci. "Light effective hole mass in undoped Ge/SiGe quantum wells". In: *Physical Review B* 100 (4 July 2019). ISSN: 24699969.

[26] M. Friesen, S. Chutia, C. Tahan, and S. N. Coppersmith. "Valley splitting theory of Si Ge Si Si Ge quantum wells". In: *Physical Review B* 75.11 (Mar. 2007), p. 115318. ISSN: 1098-0121.

[27] C. H. Yang, A. Rossi, R. Ruskov, N. S. Lai, F. A. Mohiyaddin, S. Lee, C. Tahan, G. Klimeck, A. Morello, and A. S. Dzurak. "Spin-valley lifetimes in a silicon quantum dot with tunable valley splitting". In: *Nature Communications* 4.1 (Dec. 2013), p. 2069. ISSN: 2041-1723.

[28] M. Friesen and S. N. Coppersmith. "Theory of valley-orbit coupling in a Si/SiGe quantum dot". In: *Physical Review B - Condensed Matter and Materials Physics* 81.11 (2010), pp. 1–17. ISSN: 10980121.

[29] S. G. J. Philips, M. T. Mądzik, S. V. Amitonov, S. L. de Snoo, M. Russ, N. Kalhor, C. Volk, W. I. L. Lawrie, D. Brousse, L. Tryputen, B. P. Wuetz, A. Sammak, M. Veldhorst, G. Scappucci, and L. M. K. Vandersypen. "Universal control of a six-qubit quantum processor in silicon". In: *Nature* 609 (7929 Sept. 2022), pp. 919–924. ISSN: 0028-0836.

[30] A. R. Mills, C. R. Guinn, M. J. Gullans, A. J. Sigillito, M. M. Feldman, E. Nielsen, and J. R. Petta. "Two-qubit silicon quantum processor with operation fidelity exceeding 99%". In: *Science Advances* 8 (2022), eabn5130.

[31] N. W. Hendrickx, W. I. L. Lawrie, M. Russ, F. van Riggelen, S. L. de Snoo, R. N. Schouten, A. Sammak, G. Scappucci, and M. Veldhorst. "A four-qubit germanium quantum processor". In: *Nature* 591 (2021), pp. 580–585.

[32] F. Borsoi, N. W. Hendrickx, V. John, M. Meyer, S. Motz, F. van Riggelen, A. Sammak, S. L. de Snoo, G. Scappucci, and M. Veldhorst. "Shared control of a 16 semiconductor quantum dot crossbar array". In: *Nature Nanotechnology* (Aug. 2023). ISSN: 1748-3387.

[33] C.-A. Wang, V. John, H. Tidjani, C. X. Yu, A. S. Ivlev, C. Déprez, F. van Riggelen-Doelman, B. D. Woods, N. W. Hendrickx, W. I. L. Lawrie, L. E. A. Stehouwer, S. D. Oosterhout, A. Sammak, M. Friesen, G. Scappucci, S. L. de Snoo, M. Rimbach-Russ, F. Borsoi, and M. Veldhorst. "Operating semiconductor quantum processors with hopping spins". In: *Science* 385 (6707 July 2024), pp. 447–452. ISSN: 0036-8075.

[34] P. C. Fariña, D. Jirovec, X. Zhang, E. Morozova, S. D. Oosterhout, S. Reale, T.-K. Hsiao, G. Scappucci, M. Veldhorst, and L. M. Vandersypen. "Site-resolved magnon and triplon dynamics on a programmable quantum dot spin ladder". In: *arXiv preprint arXiv:2506.08663* (2025).

[35] H. Tidjani, D. Denora, M. Chan, J. H. Ungerer, B. van Straaten, S. D. Oosterhout, L. Stehouwer, G. Scappucci, and M. Veldhorst. "A Three-Dimensional Array of Quantum Dots". In: *arXiv:2512.01634* (Dec. 2025).

[36] H. Tidjani, A. Tosato, A. Ivlev, C. Déprez, S. Oosterhout, L. Stehouwer, A. Sammak, G. Scappucci, and M. Veldhorst. "Vertical gate-defined double quantum dot in a strained germanium double quantum well". In: *Phys. Rev. Appl.* 20 (5 Nov. 2023), p. 054035.

[37] A. Ivlev, H. Tidjani, S. D. Oosterhout, L. Stehouwer, A. Sammak, G. Scappucci, and M. Veldhorst. "Coupled vertical double quantum dots at single-hole occupancy". In: *Applied Physical Letters* (July 2024).

2

HOLE SPIN QUBITS

This chapter will provide a theoretical basis for understanding the context of the quantum dots and hole spin qubits in order to interpret the experiments conducted in this thesis.

2.1. QUBITS AND SPINS

A qubit can be understood as the controlled use of a two-level quantum system. In semiconductors the natural choice is the spin-$\frac{1}{2}$ of a confined charge carrier, with the basis states defined as $|\uparrow\rangle$ and $|\downarrow\rangle$ along the quantization axis of an applied magnetic field. The relevant Hamiltonian is the Zeeman interaction,

$$H_Z = \tfrac{1}{2} g \mu_B \mathbf{B} \cdot \boldsymbol{\sigma}, \tag{2.1}$$

where g is the effective Landé g-factor, μ_B the Bohr magneton, and $\boldsymbol{\sigma}$ the Pauli matrices. This defines two eigenstates, $|\uparrow\rangle$ and $|\downarrow\rangle$, separated in energy by

$$\Delta E = g \mu_B |\mathbf{B}|, \tag{2.2}$$

which sets the qubit frequency and provides the handle for both initialization and control.

A general qubit state is a coherent superposition

$$|\psi\rangle = \alpha|\uparrow\rangle + \beta|\downarrow\rangle, \quad |\alpha|^2 + |\beta|^2 = 1, \tag{2.3}$$

and can be represented as a point on the Bloch sphere.

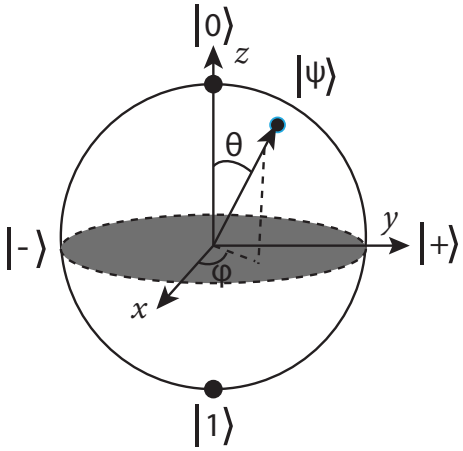

Figure 2.1: **The Bloch sphere representation of quantum states.** A pure state of a quantum two-level system can be written as $|\psi\rangle = \cos\left(\frac{\theta}{2}\right)|0\rangle + e^{i\phi}\sin\left(\frac{\theta}{2}\right)|1\rangle$. Each such state corresponds to a point on the surface of the unit sphere (blue dot), with the north pole representing $|0\rangle$ and the south pole representing $|1\rangle$. The equatorial states $|+\rangle = \frac{|0\rangle+|1\rangle}{\sqrt{2}}$ and $|-\rangle = \frac{|0\rangle-|1\rangle}{\sqrt{2}}$ lie on the y-axis of the Bloch sphere.

In the case of single spin qubits, the $|0\rangle = |\uparrow\rangle$ and $|1\rangle = |\downarrow\rangle$.

HOLES IN GERMANIUM

The effective Hamiltonian of a Ge quantum dot can be written as[1, 2]

$$H = H_{\mathrm{LK}} + H_{\mathrm{BP}} + H_Z + H_E + V, \tag{2.4}$$

where H_{LK} is the Luttinger–Kohn Hamiltonian, H_{BP} the Bir–Pikus strain Hamiltonian[3], H_Z the Zeeman term, H_E the coupling to external electric fields, and V the gate-defined confinement potential.

The following sections will explain the individual components of the Hamiltonian in further detail.

LUTTINGER KOHN HAMILTONIAN, FERMI LEVEL PINNING AND BAND STRUCTURE

When bound to a material, the interaction of the discrete energy levels on which electrons exist, and the pauli exclusion principle with other electrons result in the formation of discrete energy bands within the solid, on which the electrons can exist. This forms the band structure. When there is a separation between the energy bands, and there are no available states to occupy, there is a band gap. We call the first band above the band gap the conduction band, which can be occupied with electrons, and the first band below the band gap the valence band, which can be occupied with holes.

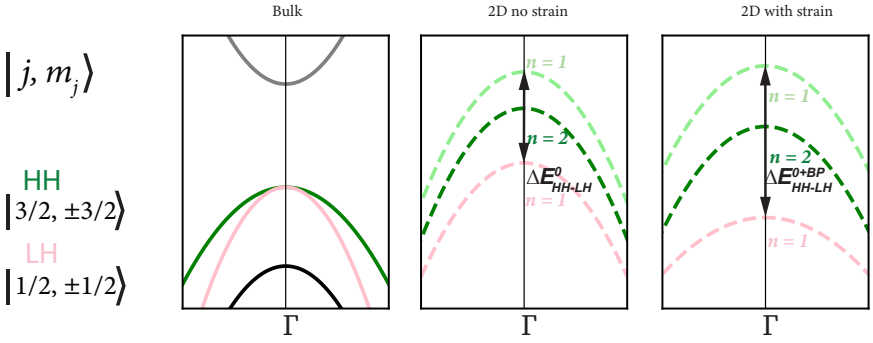

Figure 2.2: **Schematic cartoons of the dispersion of bulk semiconductor conduction and valence bands in Ge**. The dashed lines indicate the splitting of the $J = 3/2$ valence bands (heavy hole and light hole) due to confinement, as occurs in a two-dimensional hole gas. The heavy-hole band is shown in green and the light-hole band in red. The split-off band lies much lower in energy. The conduction band, shown in blue, hosts spin-1/2 electrons.

Whether a semiconductor can accumulate holes or electrons at all depends on how the *fermi level* is pinned. If we cross the fermi level we can expect to conduct charges. As electrons (holes) are negatively (positively) charged, positive (negative) electric potentials are required to make accumulation channels to conduct them. In germanium, the fermi level is pinned near the valence band. In consequence, we can make direct ohmic contact to the quantum well, and by applying negative potentials accumulate holes. The holes in planar germanium are characterized by$p$-type orbital states. The p-type orbital character of holes naturally suppresses hyperfine-induced decoherence.

LUTTINGER–KOHN HAMILTONIAN.

The Luttinger-Kohn[4] hamiltonian describes the valence band structure near the Γ-point of the HH and LH bands:

$$H_{\mathrm{LK}} = \left(\gamma_1 + \tfrac{5\gamma_s}{2}\right)\frac{p^2}{2m} - \frac{\gamma_s}{m}(\mathbf{p}\cdot\mathbf{J})^2, \tag{2.5}$$

where $\mathbf{p} = -i\hbar\nabla$ is the canonical momentum, $\mathbf{J} = (J_x, J_y, J_z)$ the spin-3/2 matrices, and γ_1, γ_s are Luttinger parameters with values $\gamma_1 \approx 13.35$ and $\gamma_s \equiv (\gamma_2 + \gamma_3)/2 \approx 4.96$. The eigenstates of J_z are $|\pm 3/2\rangle_{\mathrm{HH}}$ and $|\pm 1/2\rangle_{\mathrm{LH}}$. The corresponding effective masses are

$$m_{HH} = \frac{m_0}{\gamma_1 - 2\gamma_s} \approx 0.33 m_0, \qquad m_{LH} = \frac{m_0}{\gamma_1 + 2\gamma_s} \approx 0.04 m_0, \tag{2.6}$$

showing an order-of-magnitude difference between HH and LH masses[5].

The interactions of the heavy hole and light hole bands are captured in this 4×4 matrix, incorporating spin-orbit coupling.

$$H_{\mathrm{LK}} = \begin{pmatrix} P+Q & L & M & 0 \\ L^* & P-Q & 0 & M \\ M^* & 0 & P-Q & -L \\ 0 & M^* & -L^* & P+Q \end{pmatrix}$$

where

$$P = \frac{\hbar^2}{2m_0}\gamma_1\left(k_x^2 + k_y^2 + k_z^2\right), \quad Q = \frac{\hbar^2}{2m_0}\gamma_2\left(k_x^2 + k_y^2 - 2k_z^2\right)$$

$$M = \frac{\hbar^2}{2m_0}\sqrt{3}\gamma_3\left(k_x - i\,k_y\right)^2, \quad L = \frac{\hbar^2}{2m_0}2\sqrt{3}\gamma_3 k_z\left(k_x - i\,k_y\right)$$

and at *k=0*, the LH and HH states are degenerate. The Hamiltonian is written in the basis $|j, m_j\rangle = |\frac{3}{2}, \frac{3}{2}\rangle, |\frac{3}{2}, -\frac{3}{2}\rangle, |\frac{3}{2}, \frac{1}{2},\rangle, |\frac{3}{2}, -\frac{1}{2}\rangle$

At the Γ point, where the moment $k = 0$, the heavy-hole (HH) and light-hole (LH) bands are degenerate, until they are split by strain. The split off band is energetically very far away from the other two bands, and is generally approximated not to interact with the other two. The LH-HH degeneracy is lifted due to strain.

STRAIN EFFECTS

In semiconductor heterostructures[1], confinement in the z-direction is typically achieved by layering materials with different bandgaps on top of each other. The difference in band gaps of the layered materials results in a potential well in both the conduction and valence bands. Electrons (or holes) in the narrow-bandgap material experience a potential barrier at the interfaces with the wider-bandgap material, leading to spatial confinement in the z-direction. If the well is sufficiently thin (up to ~ 25 nanometers), quantum effects dominate, and the Schrödinger equation for the system yields discrete energy levels, similar to those in an atomic system.

Since germanium (Ge) has a larger lattice constant than silicon (Si), a Ge quantum well grown on a SiGe substrate experiences compressive strain as it conforms to the smaller lattice constant of Si. The strain from lattice mismatch creates a strong confinement field in the z-direction, splitting the heavy and light hole bands from each other by

[1] this discussion is restricted to Si/Ge and III/IV materials

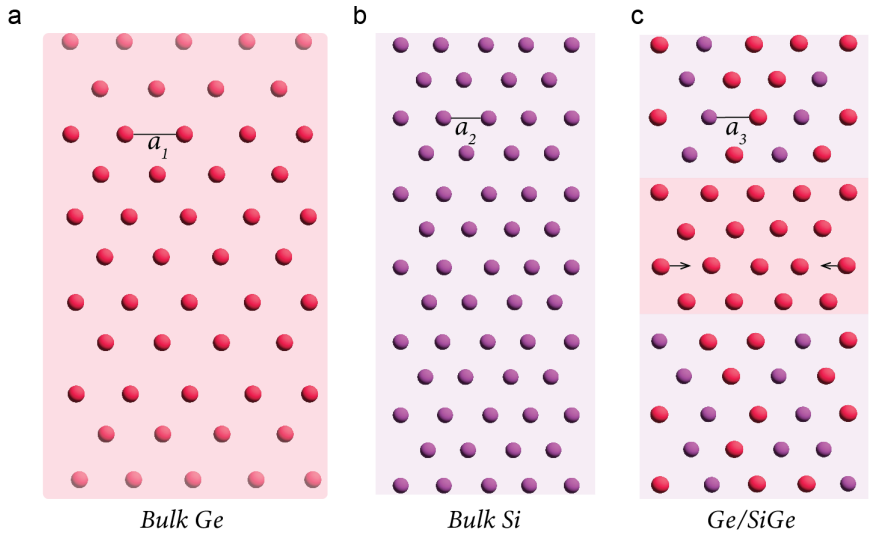

Figure 2.3: As **Ge** (panel a) has a larger lattice constant than **Si** (panel b), a **SiGe** alloy has a lattice constant smaller than bulk Ge. When a pure Ge quantum well is grown on a relaxed SiGe buffer (panel c), it is forced to match the smaller in-plane lattice constant, placing it under *compressive strain*. This strain lifts the heavy-hole–light-hole degeneracy and creates strong quantum confinement in the z-direction, allowing a two-dimensional hole gas to form when carriers are accumulated.

tens of mV, with the heavy hole band remaining as the lowest energy state. In the case of germanium core-shell nanowires which have compressive stress instead of strain, the lowest energy is the light-hole band. The band structure of strained germanium is visualised in Fig.2.2.

Strain induced by lattice mismatch visualised in Fig.2.3 is described by the Bir–Pikus Hamiltonian

$$H_{\mathrm{BP}} = |b|\epsilon_s J_z^2, \tag{2.7}$$

where b is the deformation potential and $\epsilon_s = \epsilon_\perp - \epsilon_{yy}$ is the relevant strain component. In Ge/SiGe heterostructures, $|b|\epsilon_s < 0$ leads to HH ground states oriented perpendicular to the substrate [2]. In contrast, in Si/Ge core–shell nanowires with $|b|\epsilon_s > 0$, LH ground states are favored. The strain, tunable via the Si concentration in the SiGe, lifts the fourfold degeneracy at $k = 0$ and generates strong vertical confinement, forming a two-dimensional hole gas.

After lifting the LH-HH degeneracy, the next to lift is the fourfold degeneracy of the spin $\frac{3}{2}$ heavy hole band, which has four potential spin states: $\pm\frac{1}{2}$ and $\pm\frac{3}{2}$. The $\pm\frac{1}{2}$ and $\pm\frac{3}{2}$ are split using gate defined confining potentials in the xy plane, defining the quantum dots. The final degeneracy $\frac{1}{2}$ and $-\frac{1}{2}$ is lifted using an external magnetic field, due to the Zeeman energy.

EXTERNAL FIELDS

The Zeeman Hamiltonian describes spin coupling to an external magnetic field **B**,

$$H_Z = 2\kappa\mu_{\mathrm{B_j}}\, B_j + 2qB_j^3 \tag{2.8}$$

which lifts the twofold spin degeneracy of the HH states. The electric field **E** contribution, where κ is a material dependent parameter (for Ge $\kappa = 3.41$), μ_B is the magnetic dipole moment, and q is the electron charge.

$$H_E = -e\mathbf{E}\cdot\mathbf{r}, \tag{2.9}$$

arises from external gate voltages, where **r** is the width of the confinement potential. This field breaks inversion symmetry, by causing a spin splitting in the energy bands, leading to Rashba spin–orbit coupling.

When the quantum dot hosts an unpaired hole, it can be operated as a spin qubit. The strong intrinsic spin–orbit coupling provides a mechanism for electrical control of hole spins[6].

SPIN–ORBIT ANISOTROPY

Spin–orbit coupling in Ge is highly anisotropic. As a result, the effective g-factor varies across directions and between different dots. This variability poses challenges for uniform qubit control but also enables frequency-selective qubit addressability. The anisotropy originates from cubic spin–orbit terms arising from HH–LH mixing, in addition to the direct Rashba spin–orbit interaction (DRSOI). In 2DHG nanowires, confinement suppresses HH–LH mixing so that only the direct Rashba contribution remains, producing a strong and nearly homogeneous g-factor. Bosco *et al.* [7] proposed that strong planar confinement in quantum dots enhances this direct Rashba coupling while reducing the cubic terms, thereby improving coherence and tunability.

Further to this, the g-tensor of the qubits also varies from site to site. When a magnetic field is varied in the xyz- directions, a 3D peanut shape represents the g-tensor[8]. This strong anisotropy means the magnetic field orientation is an important tool for defining the properties of hole spin qubits in Germanium.

2.2. MATERIALS AND DEVICES

In semiconducting spin qubits, the foundation of the device is the heterostructure. A heterostructure (Fig. 2.4) is a stack of different semiconductor layers, engineered to host quantum wells. This thesis focuses on group IV materials, germanium and silicon. Silicon, being highly abundant, is typically used as the substrate for both $Si/Si_{1-x}Ge_x$ and Ge/Si_yGe_{1-y} heterostructures, with the prefix indicating the main composition of the quantum well. The growth is performed by chemical vapor deposition (CVD).

MATERIAL GROWTH:

In a process known as reverse grading, pure germanium is first grown on a silicon substrate to a thickness of several microns. The silicon content is then gradually increased until a relaxed $Si_{0.2}Ge_{0.8}$ layer is obtained, forming a so-called virtual substrate. Next, a 16 nm quantum well of pure germanium is grown, followed by a 55 nm $Si_{0.2}Ge_{0.8}$ barrier. Finally, a thin silicon cap layer of a few nanometers is deposited. The silicon capping

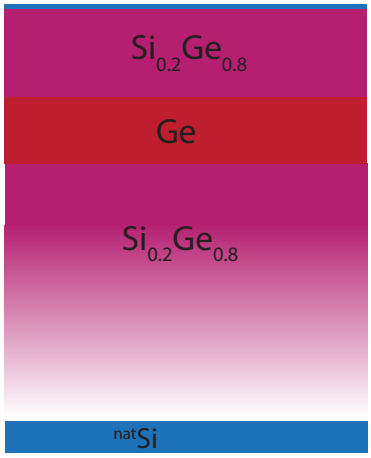

Figure 2.4: **Ge/$Si_{0.2}Ge_{0.8}$ heterostructure.** The blue region indicates the natural silicon substrate, above which the reverse-graded germanium is grown. Holes can be accumulated and confined in the germanium quantum well.

layer is important, as both germanium and its oxide are chemically reactive and can degrade upon exposure to water, producing a rough surface that introduces charge traps.

The thin quantum well is highly strained in the z-direction due to the lattice mismatch between Ge and SiGe. Since Ge has a larger lattice constant than SiGe, the Ge quantum well experiences compressive strain. This strain creates a strong confinement field along z, restricting the motion of charge carriers to the xy plane (Fig. 2.3). Such systems are referred to as two-dimensional electron or hole gases (2DEG/2DHG).

Electrons are the most familiar charge carriers, while holes can be understood as the absence of an electron in the valence band. More precisely, holes emerge when an electron is excited from the valence band to the conduction band, leaving behind a mobile positive charge. At low temperatures, charges in semiconductors freeze out, so carriers must be deliberately accumulated. This is achieved using electric potentials from metallic gates, which attract charges into the quantum well and shape the confinement landscape to form quantum dots — quantized puddles of charge.

QUANTUM DOTS

A quantum dot can be thought of as a tiny artificial atom, where electrons or holes are confined in all three spatial dimensions x, y, and z.

Confinement in the x- and y-directions is implemented using electrostatic gates positioned on top of the heterostructure. These gates create an in-plane potential well, whose depth and shape determine the lateral confinement. The strength of this confinement depends on material properties and the effective mass of the trapped particle. A lower effective mass (a fraction of the free electron mass) results in a larger quantum confinement length, since the characteristic width of the wavefunction is inversely proportional to the square root of the effective mass.

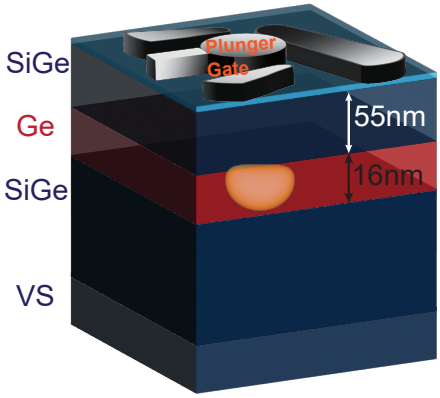

Figure 2.5: The plunger gate controls the accumulation of charges in the quantum well, defining the localized potential of a quantum dot.

For the system to behave as a quantum dot, the confinement must be strong enough that the energy levels are quantized, meaning that only discrete energy states are available to the trapped particle. The boundaries of the quantum dot provides quantum confinement, resulting in discrete energy levels. Quantum dots can be approximated as circular disks, such that the energy separation between levels scales as $\propto 1/mL^2$, where m the effective mass, is and L is the in-plane confinement length

In addition to quantization energy, another important energy scale is the charging energy, which arises from Coulomb repulsion. The energy required to add an extra electron to the quantum dot is given by:

$$E_C = \frac{e^2}{2C}$$

where e is the elementary charge and C is the capacitance of the quantum dot. This charging energy plays a crucial role in phenomena such as Coulomb blockade, where electron transport through the quantum dot is suppressed unless an external bias provides sufficient energy to overcome E_C.

DOUBLE QUANTUM DOT

We consider the lowest spin states in a double quantum dot that is tunnel coupled. In the basis: $S(0,2), |\uparrow,\uparrow\rangle, |\uparrow,\downarrow\rangle, |\downarrow,\uparrow\rangle, |\downarrow,\downarrow\rangle$, the low lying energy states can be described by the following matrix[9, 10]:

$$H(\varepsilon) = \begin{bmatrix} U-\varepsilon & 0 & t_0 & -t_0 & 0 \\ 0 & \tilde{E}_Z & 0 & 0 & 0 \\ t_0 & 0 & \Delta E_Z/2 & 0 & 0 \\ -t_0 & 0 & 0 & -\Delta E_Z/2 & 0 \\ 0 & 0 & 0 & 0 & -\tilde{E}_Z \end{bmatrix}$$

Where $\bar{E}_Z = \frac{1}{2}(g_1 + g_2)\mu_B B$ is the average Zeeman energy of the two quantum dots, and $\Delta E_Z = (g_1 - g_2)\mu_B B$ the Zeeman energy difference. U is the charging energy. ϵ is the energy detuning between the two dots. The detuning axis corresponds to the energy difference between the two quantum dots. t_0 is the interdot tunnel coupling which we assume here to be real. By crossing the interdot transition line via the detuning axis a charge can coherently move between two quantum dots. We will commonly work in the energy landscape of total dot energy, $U = \frac{vP_1 + vP_2}{2}$ and detuning, $\epsilon = \frac{vP_1 - vP_2}{2}$.

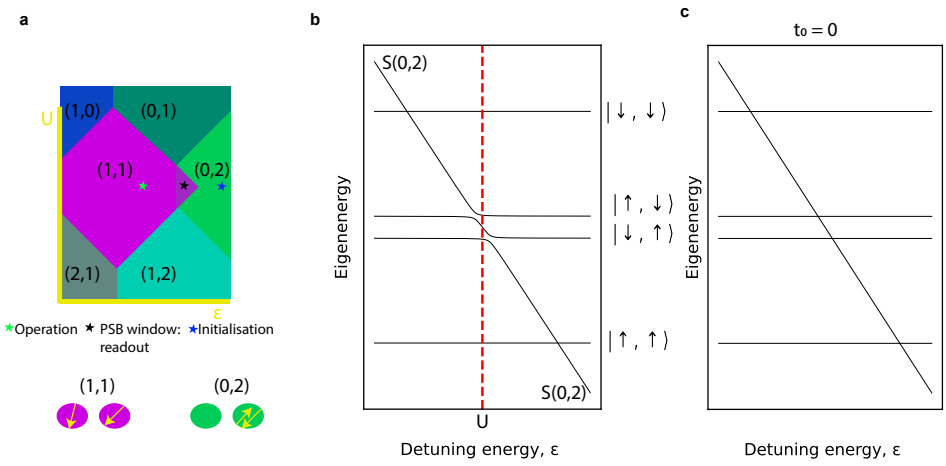

Figure 2.6: **Energy level diagram of a spin qubit defined in a double quantum dot.** **a** The charge stability diagram of a double quantum dot, shown in the detuning ϵ vs combined chemical potential U of two quantum dots. The labels in the regions define the charge occupation of the quantum dots. **b** The eigenenergies of the 5 lowest energy states from matrix 2.2 are plotted. Qubits can be initialised by pulsing across the (0,2)-(1,1) transition. The adiabticity and magnetic field will determine the exact state which is intialised. **c** The eigenenergies when the interdot tunnel coupling $t_0 = 0$ and there can be no spin conserved tunneling between the quantum dots, and the anticrossings from b turn into crossings.

We determine the charge state of the quantum dots through charge sensing, using a sensing dot. A sensing dot is a large quantum dot with many holes occupying it. When a hole is added to the sensing dot, there is a peak in the signal corresponding to the addition of a charge. We set the sensing dot on one of these coulomb peaks, and the due to the capacitance to the quantum dots in the array, when a charge is added or taken away, the coulomb peak of the sensing dot moves in response. This signal is transformed using a reflectometry circuit into a visible diagram, such as in Fig.2.6.

SPIN STATE INITIALISATION AND READOUT

Qubits can be initialized by waiting in the $(0,2)$ charge state, where two spins naturally relax into the singlet. By pulsing adiabatically from $(0,2)$ to $(1,1)$, we cross the spin–orbit anticrossing between the two states, which can flip one of the spins and thereby initialize a triplet state.

Readout proceeds in a similar way. We pulse back from $(1,1)$ to $(0,2)$ but pause near the anticrossing. Here, the tunneling dynamics depend on the spin configuration: the

$|\uparrow,\uparrow\rangle$ state tunnels at a different rate than the $|\uparrow,\downarrow\rangle$ state. This requires the interdot tunnel coupling to be tuned such that tunneling is fast on the charge timescale but slow compared to the spin relaxation processes.

Due to the Pauli exclusion principle which prevents fermions of the same state existing on the same energy level, a triplet$|\uparrow,\uparrow\rangle$ must first relax into a singlet $|\uparrow,\downarrow\rangle$ before it can occupy the $(0,2)$ $|\uparrow\downarrow\rangle$ state, while a singlet can tunnel directly. If the sensor integration time is chosen to match this timescale, the resulting charge motion can be distinguished. The coulomb peak of the sensor moves in response to a charge moving in case of a singlet tunneling, and doesn't move when a triplet is in the metastable state. This process is known as spin to charge conversion, enabling spin readout. We note that in germanium, there can be additional anticrossings between the various spin states. As a result, there can be various types of spin read out, depending on which levels are blocked and which levels are not.

2.3. DEVICE CHARACTERIZATION

Devices are glued onto home built printed circuit boards (PCB), and bonded using a semi-automatic Bontec bonder. Before loading into a fridge, devices are usually tested first at 4K in liquid helium, to determine if the device works. One chip produces 8 chiplets with a devices on each chiplet. Device failure modes can be due to broken metal, shorts between gates, and shorts to the ohmic contacts. At room temperature, it can be established if the gates are shorted by measuring their resistance using a *beeper box*, which sends a small current and measures the resistance. For the gates, anything less than $1G\Omega$ resistance can indicate that there is a short or leakage between the lines. For the ohmic contacts, we expect a very low resistance as the substrate is conductive at room temperature.

Once the device is lowered into the liquid helium, the substrate freezes out and is no longer conductive and the device screening can commence. We run a current across the sensors first as they have direct ohmic contacts, and determine at what voltage the gates hit the threshold voltage needed to make a conductive channel, ie a 2DHG. In a single quantum well device, if there is a single conductive channel there should be a single turn on. In a double quantum well device, there should be two turn-ons, as there is a conductive channel through each layer. After the sensors are tested we then make a conductive channel across the device, and test that all the gates have a lever arm on the conductance, establishing that they are connected. If leakage currents are found, we pinch off the gates until we determine which gates are leaking. For barrier gates, it can often be afforded that they leak beyond -500mV, as they should never accumulate below them. However for plunger gates, this can be detrimental to the functioning of the device. Other factors can also be determined at 4K testing, such as at what point the device becomes hysteretic in voltage. This is important for device stability and drift over time. Devices that pass all these tests then have inductors bonded to the ohmic contacts for RF reflectometry and can be loaded into a dilution fridge.

BIBLIOGRAPHY

[1] J. M. Luttinger and W. Kohn. "Motion of Electrons and Holes in Perturbed Periodic Fields". In: *Phys. Rev.* 97 (1955), pp. 869–883.

[2] C. Adelsberger, M. Benito, and S. B. et al. "Hole Spin Qubits in Ge Nanowire Quantum Dots: Interplay of Orbital Magnetic Field, Strain, and Growth Direction". In: *preprint: https://arxiv.org/pdf/2110.15039.pdf* ((2021)).

[3] G. L. Bir and G. E. Pikus. *Symmetry and strain-induced effects in semiconductors*. Vol. 484. Wiley New York, 1974.

[4] J. M. Luttinger and W. Kohn. "Motion of Electrons and Holes in Perturbed Periodic Fields". In: *Physical Review* 97 (4 Feb. 1955), pp. 869–883. ISSN: 0031-899X.

[5] M. Lodari, A. Tosato, D. Sabbagh, M. A. Schubert, G. Capellini, A. Sammak, M. Veldhorst, and G. Scappucci. "Light Effective Hole Mass in Undoped Ge/SiGe Quantum Wells". In: *Physical Review B* 100.4 (2019), p. 041304.

[6] J. C. Abadillo-Uriel, E. A. Rodríguez-Mena, B. Martinez, and Y.-M. Niquet. "Hole-Spin Driving by Strain-Induced Spin-Orbit Interactions". In: *Physical Review Letters* 131 (9 Sept. 2023), p. 097002. ISSN: 0031-9007.

[7] S. B. *et al.* "Squeezed hole spin qubits in Ge quantum dots with ultrafast gates at low power". In: *Phys. Rev. B 104, 115425* ((2021)).

[8] N. W. Hendrickx, L. Massai, M. Mergenthaler, F. J. Schupp, S. Paredes, S. W. Bedell, G. Salis, and A. Fuhrer. "Sweet-spot operation of a germanium hole spin qubit with highly anisotropic noise sensitivity". In: *Nature Materials* (May 2024). ISSN: 1476-4660.

[9] M. Veldhorst, C. H. Yang, J. C. C. Hwang, W. Huang, J. P. Dehollain, J. T. Muhonen, S. Simmons, A. Laucht, F. E. Hudson, K. M. Itoh, A. Morello, and A. S. Dzurak. "A two-qubit logic gate in silicon". In: *Nature* 526 (7573 Oct. 2015), pp. 410–414. ISSN: 0028-0836.

[10] B. Hetényi, C. Kloeffel, and D. Loss. "Exchange interaction of hole-spin qubits in double quantum dots in highly anisotropic semiconductors". In: *Phys. Rev. Res.* 2 (3 July 2020), p. 033036.

3

BILAYER DEVICES

There are many potential gains to be had from high connectivity quantum computing architectures. While most experiments with quantum dots for spin qubits have largely been in one or two dimensional arrays, we explore the possibility of scaling them in the out of plane direction. This chapter introduces the fundamentals bilayer device operation and characterisation.

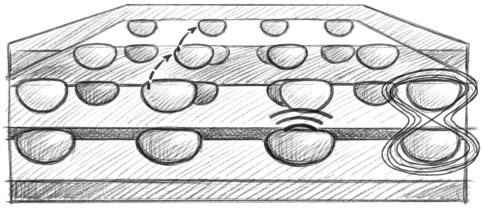

3.1. BILAYER HETEROSTRUCTURES

THe bilayer Ge/SiGe heterostructure is formed by growing an additional Ge quantum well in the CVD process. In these experiments, the upper quantum well is placed at the same depth (55 nm) as in single-layer devices to minimise charge noise, but made thinner (10 nm). Below it, a thin (4-10 nm) SiGe spacer separates a thicker lower quantum well (16 nm). In Fig.3.1, both single (a) and double (b) quantum well heterostructures are visualized. In panels c and d are TEMs of a double quantum well heterostructure. The thickness of the spacer between the quantum wells can be used as a tuning knob to control the tunnel coupling and capacitance between the quantum wells.

In planar gate structures such as hall-bar shaped field effect transistors, bilayers are well studied, and the occupation of the two quantum wells is identified by measuring two overlapping fan diagrams[1, 2] (see chapter 6). The first fan diagram represents the landau levels of the bottom quantum well being occupied. As the top quantum well crosses the fermi level, it also begins to conduct and thus a second fan diagram emerges. In the context of 2D structures, it is important that the quantum wells have slightly different z-confinement potentials. This is achieved by making the lower quantum well thicker (and thus less confined), ensuring that its states cross the fermi level first. If the upper quantum well conducts first, then it will screen the lower quantum well and there will only be one fan diagram.

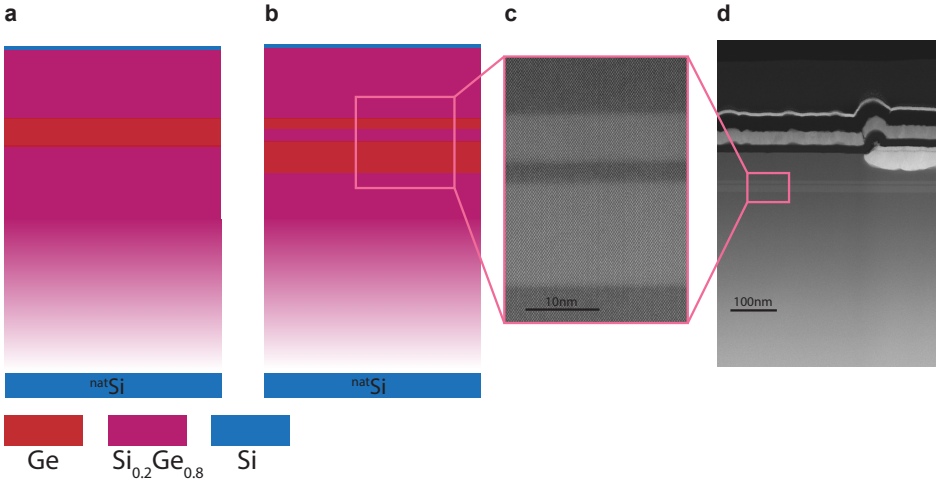

Figure 3.1: **Single and Double quantum well heterostructures. a,** Single quantum well Ge/SiGe heterostructure, where the 16 nm Ge quantum well is buried 55 nm below the surface. **b,** Double quantum well heterostructure, which features two quantum wells separated by a $Si_{0.2}Ge_{0.8}$ spacer. **c,** TEM of a double quantum well heterostructure, zoomed in on the double quantum well area from [3]. **d** Zoomed out TEM of the same heterostructure, also showing the gate and ohmic layers.

While this is a key characterization tool in 2D structures, in quantum dots we instead use turn-on measurements. By changing the bias voltage of the top gates, both quantum wells can be turned on. At high source–drain bias this appears as a double turn-on: the

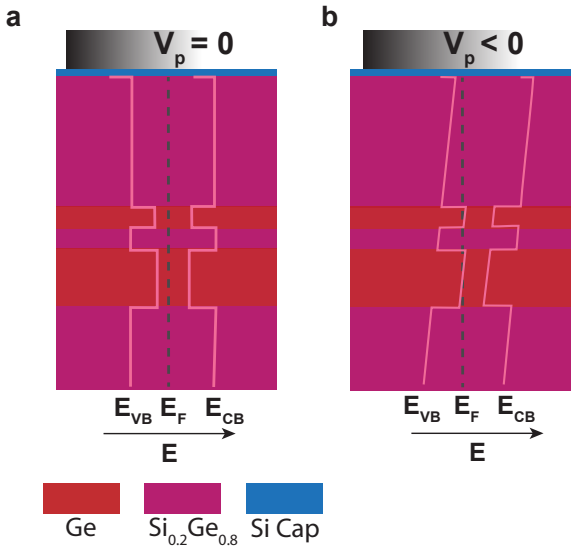

Figure 3.2: **Animation depicting the band structure of a double quantum well Ge/SiGe heterostructure a,** When no voltage is applied to the top gate V_P, there are no states crossing the fermi level, which is pinned near the valence band E_{VB} and the quantum wells are depleted. **b** As a negative voltage is applied to the top gate, the band structure begins to bend in response, and the heavy hole states in the valence band cross the fermi level, and the quantum wells can accumulate charges.

first, at lower current, corresponds to the onset of conduction in the lower quantum well, while the second marks the increased conductance through the upper quantum well as it crosses the fermi level. In the few-hole regime at low bias, a vertical double quantum dot can be identified through charge sensing, where two charge-transition lines, strongly coupled to the same plunger gate, emerge with high mutual capacitance. A detailed characterization of a multiwell device is given in Chapter 6. In Fig.3.2 a visualisation of the band structure of the double quantum well is presented, both with no top gate voltage and with a top gate voltage applied.

3.2. INTERPRETING AND TUNING VERTICAL DOUBLE QUANTUM DOT CHARGE STABILITY DIAGRAMS

When tuning bilayer devices, the system often first settles in the single-layer regime. To reach the bilayer regime, we relax the confinement by lowering the voltages on the gates surrounding the plungers, making it favourable for a hole to occupy the lower dot before the upper. Before discussing this transition in detail, we first outline how to interpret the charge stability diagrams of vertical double quantum dots. Figure 3.4a shows such a diagram, identifiable by two charge-transition lines strongly coupled to the same plunger gate and separated by a broad interdot line due to the large mutual capacitance between the dots. In panel (a), measured under gate P_3 (virtual gate O3), new transition lines are labelled as they appear with added charge. The first dot forms in the upper quan-

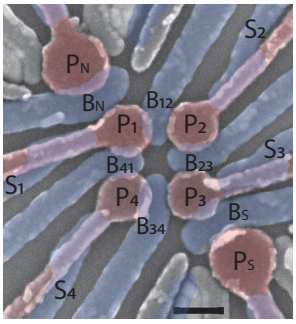

Figure 3.3: **False coloured SEM of a typical device, used in the experiments in chapter8, for both single layer and multi layer devices.** The scale bar indicates 100nm. Coloured in red are the plunger gates, and in blue are the barrier gates. This device was fabricated on top of a bilayer heterostructure, leading to a maximum of eight quantum dots in the device[4].

tum well, as indicated by the slope of the transition lines most strongly coupled to the plunger. In this representation, O3 and O4 are virtualised with respect to the upper dot, leaving the lower dot only partially compensated. A nearby gate can therefore be used to tune the lower dot while maintaining virtualisation of the upper dot.

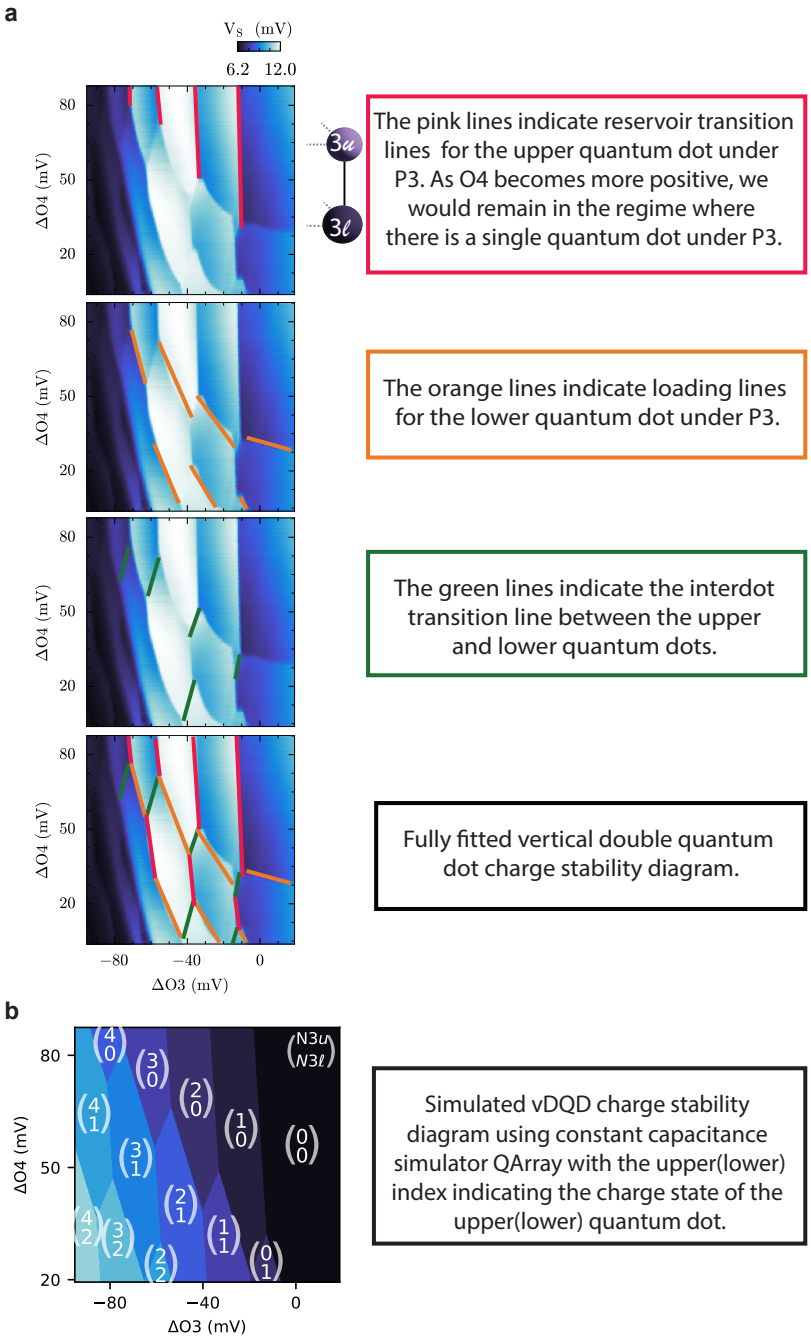

Figure 3.4: **Interpreting a vertical double quantum dot charge stability diagram. a,** Progressively labeled charge transition lines. **b,** Simulated vertical double quantum dot charge stability diagram, showing the charge occupations for the upper and lower quantum dots under P3. The gates O3 and O4 represent virutal gates where all surrounding gates are virtualised with respect to the charge transition lines of the upper quantum dots under P3 and P4 respectively. The quantum dot under P4 is not yet accumulated.

We can also recreate this in simulation using the constant capacitance simulator Qarray[5], as shown in Fig.3.4b.

As we go more negative in the plunger gate value of O4, we will eventually accumulate under P4 as well, and the charge stability diagram of a triple quantum dot will emerge in one plot, as shown in Fig.3.5.

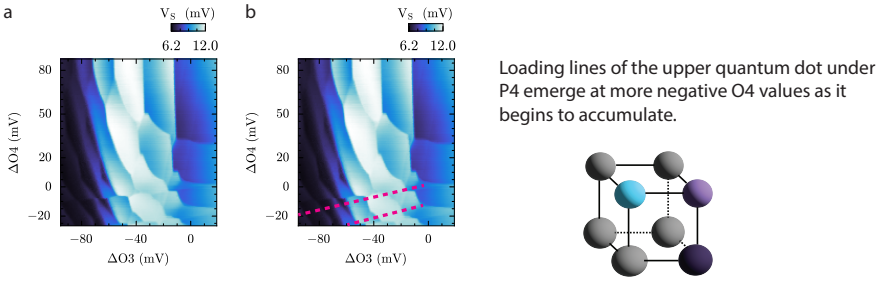

Figure 3.5: **The charge stability diagram for a triple quantum dot. a,** Triple quantum dot charge stability diagram, in **b,** the upper quantum dot under P4 begins to accumulate as indicated by the dashed pink lines.

Being able to label these charge transition lines with confidence is important when we go on to triangulate the position of the quantum dots by measuring the relative lever arm of the surrounding gates.

VIRTUAL CONTROL: TUNING BETWEEN THE SINGLE LAYER AND THE BILAYER REGIME

Schrödinger-poisson simulations of the relative lever arms of the plunger and barrier gates in chapter6[2]revealed that the barrier gates can have a larger relative lever arm on lower quantum dot than the upper quantum dot. This is attributed to the difference in the size of the wavefunctions of the upper and lower quantum dots. As the lower quantum dot is less confined, it is slightly larger and the wavefunction is less confined to the plunger gate, and creeps under the barrier gates. Therefore, as we vary the voltage of the barrier gate, we tune the energy levels in the lower quantum dots. The effect of the barrier and plunger gates is visualised in a simple quantum well diagram in Fig.3.6. We note that we use a nested virtualization scheme which allows us to form as arbitrary virtual gates, rather than defining everything in one matrix as is typically done[6]. This has further applications such as having different cross capacitance's in different operating regimes.

As there are fewer plunger gates than there are potential quantum dots in the bilayer system, we exploit all the existing gates in the system to gain control over all the quantum dots. In order to tune from having a single quantum dot in the upper layer, to also having a quantum dot in the lower layer, we need to make it favourable for a hole to occupy the lower quantum dot. To get to this regime, we can use the surrounding barrier gates which have a larger relative lever arm on the lower quantum dot than the upper quantum dot, as expanded in chapter6. Therefore by biasing the surrounding barrier gates more negatively we begin to accumulate charges in the lower quantum well. To

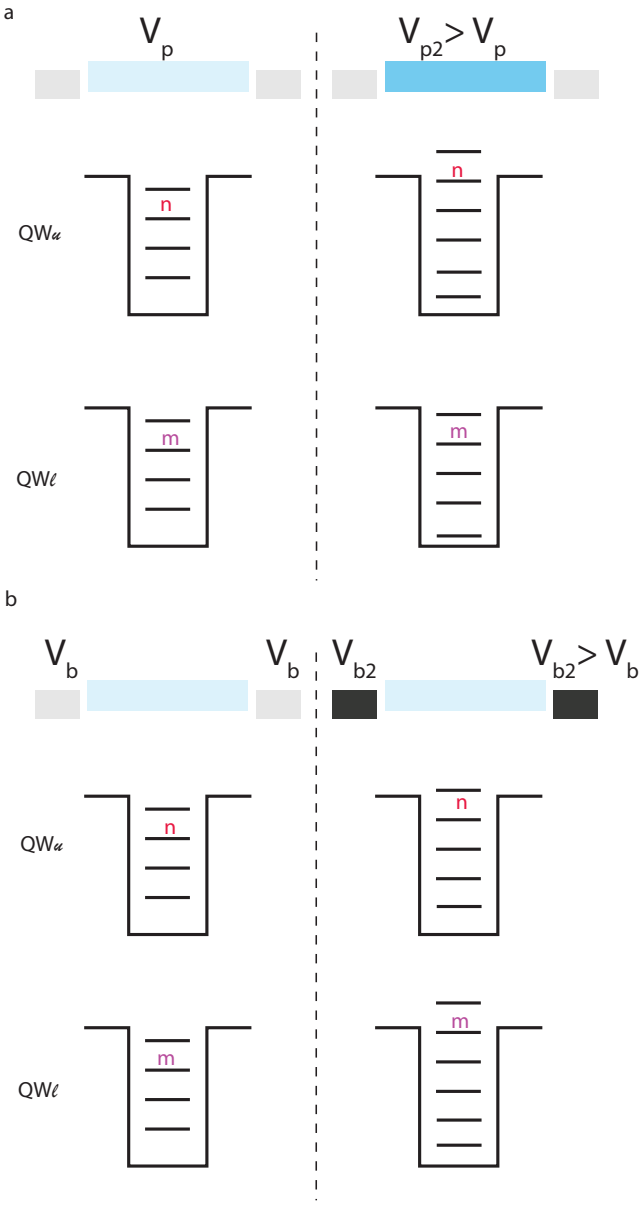

Figure 3.6: **Schematic indicating the different effect of the plunger and barrier gates on quantum dots on the upper and lower quantum wells. a** The plunger gates move the energy levels of the upper and lower quantum dots, however it has a stronger effect on the upper quantum dot as it is closer. **b** The barrier gates also have an effect on both the upper and lower quantum dots however as the wavefunction of the lower quantum dot has a larger component under the barrier gates, it has a larger effect on the lower quantum dots. Furthermore, the effect of the barrier can be virtualised such that it has no effect on the upper quantum dot, thus only tuning the energy levels of the lower quantum dot.

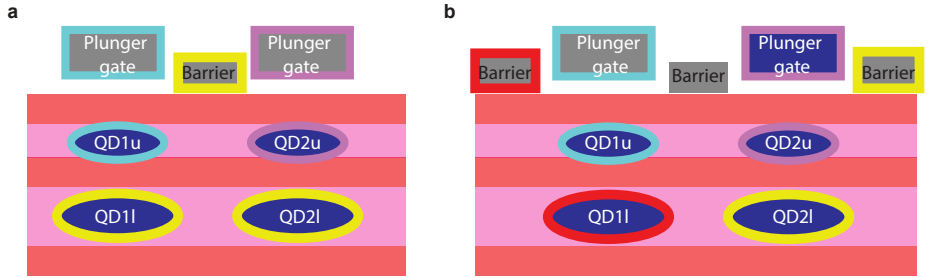

Figure 3.7: **Virtualisation can be used to ensure individual addressability of vertically scaled quantum dots.** **a** Barrier gates between plunger gates can be tuned to tune quantum dots in the lower layer near their accumulation voltage by becoming more negative. When they are between two vertical double quantum dots, both lower quantum dots can be simultaneously tuned. **b** The lower quantum dots can be individually addressed using side gates which are adjacent to only one vertical double quantum dot.

tune two lower quantum dots in and out of the bilayer regime together, we can use the barrier gate between the two quantum dots(Fig.3.7a). To tune a quantum dot independently, we can use the barrier or screening gate that is adjacent to only that quantum dot(Fig.3.7b). Care must be taken to prevent accumulation under the barrier gate itself, however with the small size of the gate it is usually easily avoided. Furthermore, the barrier gates can also be used as virtual plunger gates for the lower quantum dots, with very high virtual gate matrix coefficients to amplify the effect of the barrier gate. The relative tuning of the plunger and barrier gates is visualised in Fig.3.6, and the virtualisation scheme which exploits this difference in lever arm is visualised in Fig.3.7 .

In chapter 6 we learn that the wavefunction of the lower quantum dot is less localised under the plunger gate than the upper quantum dot. As a direct consequence, the barrier gates have a larger relative lever arm on the lower quantum dot than the upper quantum dot. Therefore, using this difference we can virtualise such that the upper quantum dot is controlled by the plunger gate, and the lower quantum dot is controlled by the barrier gate.

In Fig.3.8 we tune the device completely to the bilayer regime, containing 4 quantum dots in total; 2 dots in the upper and lower layers beneath gate P_3 and P_4, from the single layer regime, containing just only the two quantum dots in the upper layer. This is achieved by a positive voltage pulse on xB_{34}, the barrier between the two relevant plungers, to increase the confinement of the quantum dots. This tunes the chemical potential of the lower quantum dots away with respect to the upper quantum dots. In the leftmost plot of Fig.3.8 we have reached the planar regime for the first hole fillings, as is evident from the two charge loading lines at the first filling. We do note that charge loading lines of the lower quantum dots appear at higher occupation at more negative O3 and O4 gate values. Conversely, when pulsing more negatively on xB_{34} (going left-right), we tune the lower quantum dots to be more energetically favorable to occupy. This is seen as moving the loading lines of the lower quantum dots towards more positive O3 and O4 gate voltages, towards the first loading. After this point, pulsing more negatively on the barrier increases the charge regions containing any holes in the lower layer. This

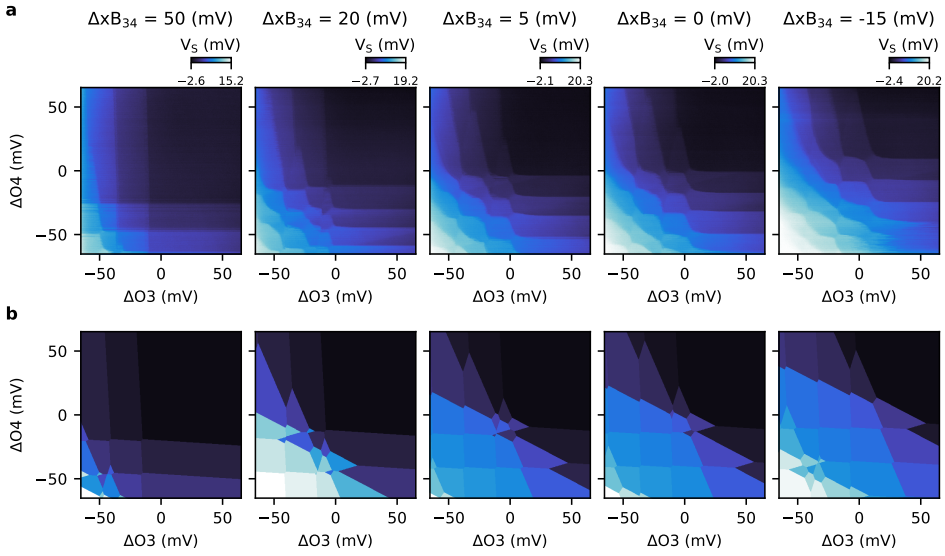

Figure 3.8: **Tuning between the planar regime and the bilayer regime.** **a** We can actively tune between the single layer regime, seen in the left most panel, to the bilayer regime (right most panel). We observe four charge transition lines, with two dots strongly coupled to O3, and two dots strongly coupled to O4, indicating the presence of two vertical double quantum dots. The gate xB_{34} represents the virtual gate where B_{34} is virtualised against the upper quantum dots. **b** We qualitatively replicate this effect using quantum capacitance simulator Qarray[5]. Deviations between experiment in **a** and simulation **b** is attributed to change in the quantum dot shape, and thereby lever arms, as function of the barrier gate which is not captured in the constant capacitance model[4]/

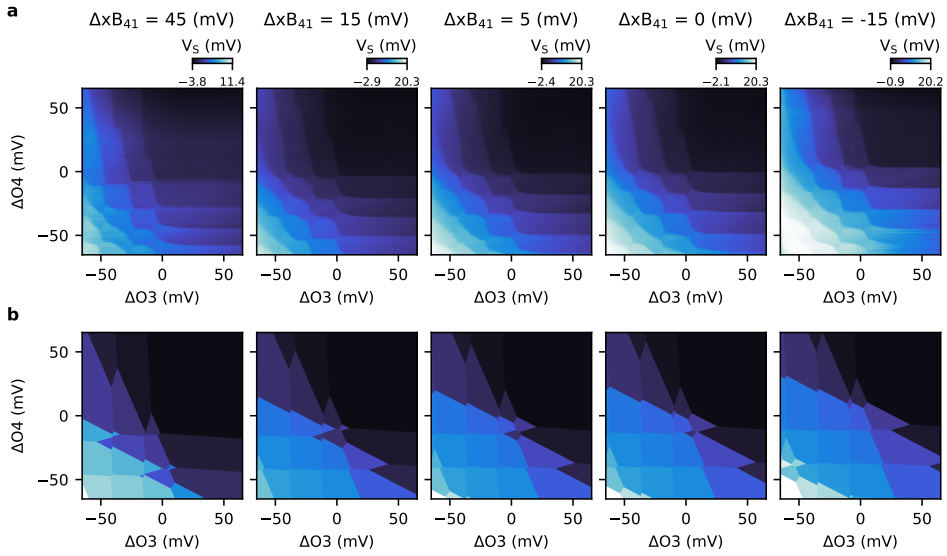

Figure 3.9: **Tuning between single and bilayer regime for a single vertical double quantum dot. a** The gate xB_{41} represents the virtual gate where B_{41} is virtualised against the upper quantum dots. By pulsing on xB_{41}, we are able to tune from a vertical double quantum dot underneath P_4 (left most plot) to just a single quantum dot in the upper layer (right most plot). The vertical double quantum dot underneath P_3 is only slightly affected. **b** Qarray simulations using the same capacitance parameters as in Fig. 3.9b. Qualitative features and behavior is replicated in the simulation.

is observed for example in the right most plot, where in the first hole filling the charge region in which the hole is in either QD3ℓ or QD4ℓ has enlarged. The experimental data are qualitatively replicated using Qarray, as depicted in Fig. 3.8b.

Alternatively, we can also pulse on xB_{41} as shown in Fig.3.9. Barrier gate B_{41} is located closer to plunger P_4 and further away from P_3. As such, we expect a larger leverarm of this barrier gate to QD4ℓ compared to QD3ℓ. This is indeed seen in Fig.3.9, where we actively tune from a vertical double quantum dot (right most panel) to just a single quantum dot (left most panel) in the upper layer, underneath P_4. Again, we note that the first loading of QD4ℓ in the left most panel is still observed, albeit at more negative O4 gate value. In contrast, the vertical double quantum dot underneath P_3 is barely affected by the pulsing on xB_{41}. It indicates that we are able to detune the energy level of QD4ℓ more effective than QD3ℓ using B_{41}. This demonstrate the ability to control the occupation of quantum dots in the upper and lower layer independently. Using the same capacitance input for the Qarray simulation in Fig.3.8, we are able to reproduce this behaviour in the simulations shown in Fig.3.9b.

3.3. LOCATING QUANTUM DOTS IN A BILAYER

As the approach for multi quantum well heterostructures for quantum dots is novel, we make a point in all the work to physically locate the position of all the quantum dots in

the system. To do this, we triangulate the position of the quantum dots by sweeping the plunger gates against the surrounding gates.

From these charge stability diagrams, we can manually fit the charge transition lines, which are sorted into categories based on their features such as gradient, and latching. Once a honeycomb is identified, fitting the rest of the charge transition lines follows. The GUI created to manually fit the charge stability diagrams is shown below. We then find the lever arms of the surround gates relative to the plunger gates. From this we ascertain where the quantum dots are located in the device.

An extensive description of the triangulation process can be found in the chapters 6 7, 8.

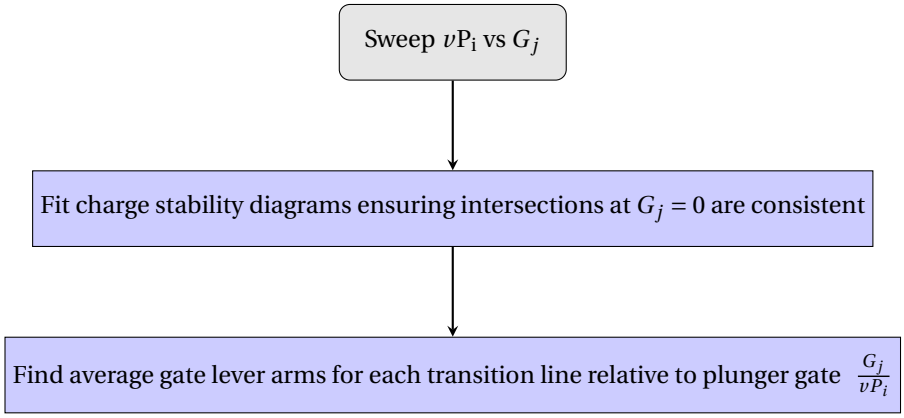

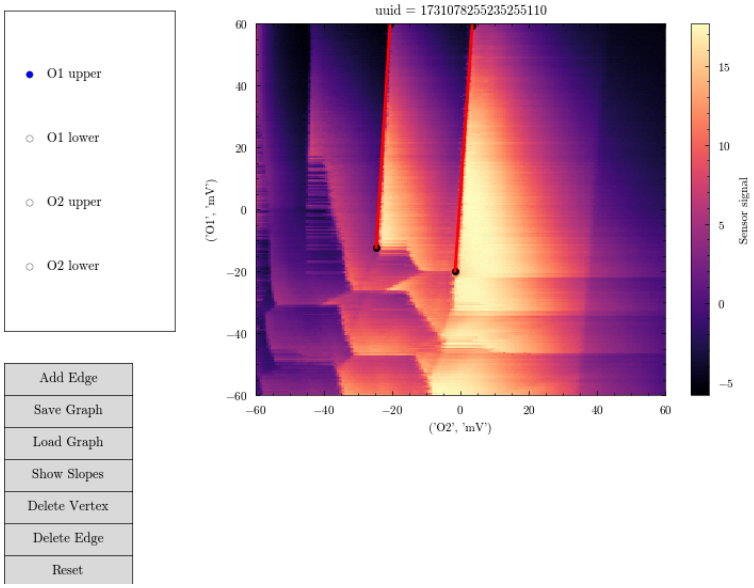

Figure 3.10: **The GUI created to label charge transitions lines.** The data is processed for all surrounding gates, and converted into a heatmap of cross capacitance strengths.

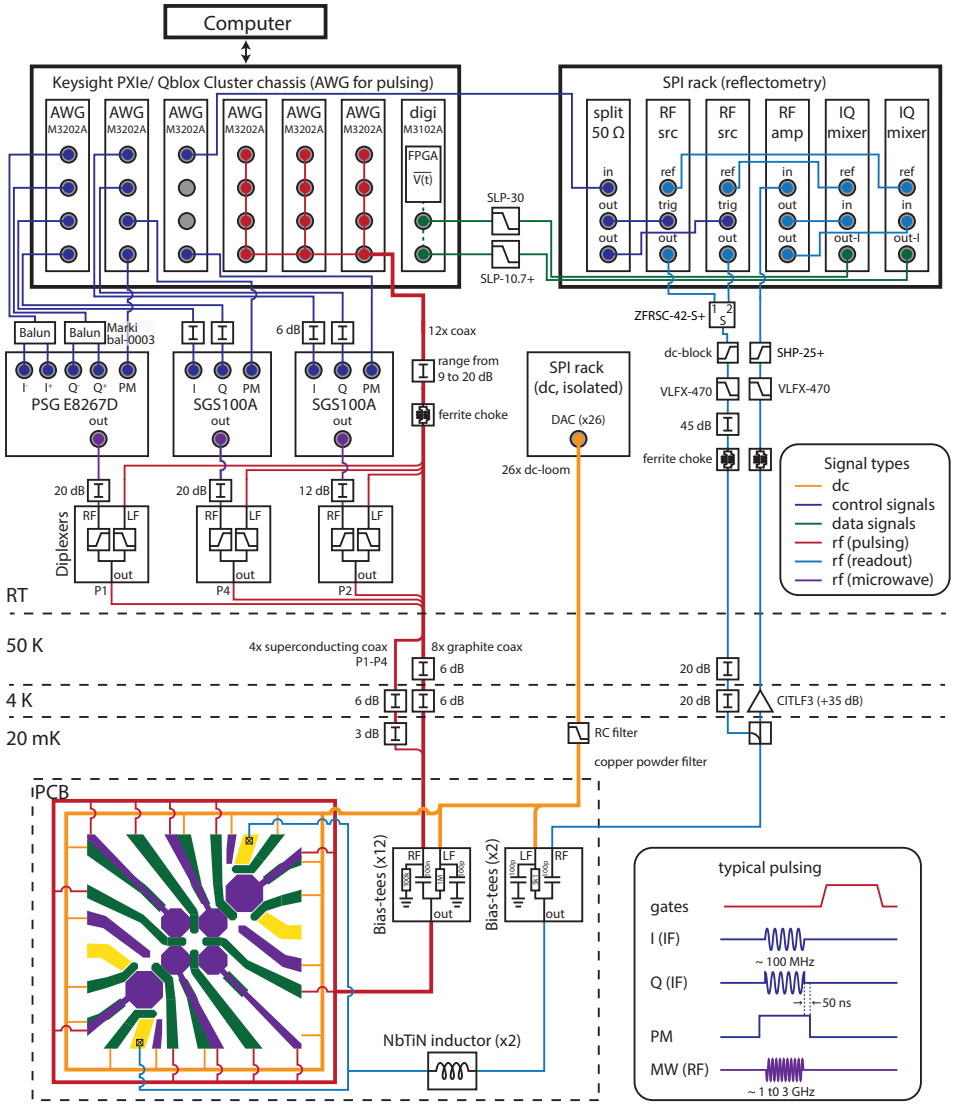

Figure 3.11: Experimental setup. Both Keysight and Qblox chassis were used in the following experiments. (adapted from [7])

BIBLIOGRAPHY

[1] A. Tosato, B. Ferrari, A. Sammak, A. R. Hamilton, M. Veldhorst, M. Virgilio, and G. Scappucci. “A High-Mobility Hole Bilayer in a Germanium Double Quantum Well”. In: *Advanced Quantum Technologies* 5 (5 May 2022), p. 2100167. ISSN: 2511-9044.

[2] H. Tidjani, A. Tosato, A. Ivlev, C. Déprez, S. Oosterhout, L. Stehouwer, A. Sammak, G. Scappucci, and M. Veldhorst. “Vertical gate-defined double quantum dot in a strained germanium double quantum well”. In: *Phys. Rev. Appl.* 20 (5 Nov. 2023), p. 054035.

[3] A. Tosato, B. Ferrari, A. Sammak, A. R. Hamilton, M. Veldhorst, M. Virgilio, and G. Scappucci. “A High-Mobility Hole Bilayer in a Germanium Double Quantum Well”. In: *Advanced Quantum Technologies* 5.5 (2022), p. 2100167. ISSN: 2511-9044.

[4] H. Tidjani, D. Denora, M. Chan, J. H. Ungerer, B. van Straaten, S. D. Oosterhout, L. Stehouwer, G. Scappucci, and M. Veldhorst. “A Three-Dimensional Array of Quantum Dots”. In: *arXiv:2512.01634* (Dec. 2025).

[5] B. van Straaten, J. Hickie, L. Schorling, J. Schuff, F. Fedele, and N. Ares. “QArray: A GPU-accelerated constant capacitance model simulator for large quantum dot arrays”. In: *SciPost Physics Codebases* (Oct. 2024), p. 35. ISSN: 2949-804X.

[6] A. S. Rao, D. Buterakos, B. van Straaten, V. John, C. X. Yu, S. D. Oosterhout, L. Stehouwer, G. Scappucci, M. Veldhorst, F. Borsoi, and J. P. Zwolak. “Modular Autonomous Virtualization System for Two-Dimensional Semiconductor Quantum Dot Arrays”. In: *Physical Review X* 15 (2 Apr. 2025), p. 021034. ISSN: 2160-3308.

[7] N. W. Hendrickx, W. I. L. Lawrie, M. Russ, F. van Riggelen, S. L. de Snoo, R. N. Schouten, A. Sammak, G. Scappucci, and M. Veldhorst. “A four-qubit germanium quantum processor”. In: *Nature* 591 (2021), pp. 580–585.

4

PROBING RESONATING VALENCE BONDS ON A PROGRAMMABLE GERMANIUM QUANTUM SIMULATOR

Simulations using highly tunable quantum systems may enable investigations of condensed matter systems beyond the capabilities of classical computers. Quantum dots and donors in semiconductor technology define a natural approach to implement quantum simulation. Several material platforms have been used to study interacting charge states, while gallium arsenide has also been used to investigate spin evolution. However, decoherence remains a key challenge in simulating coherent quantum dynamics. Here, we introduce quantum simulation using hole spins in germanium quantum dots. We demonstrate extensive and coherent control enabling the tuning of multi-spin states in isolated, paired, and fully coupled quantum dots. We then focus on the simulation of resonating valence bonds and measure the evolution between singlet product states which remains coherent over many periods. Finally, we realize four-spin states with s-wave and d-wave symmetry. These results provide means to perform non-trivial and coherent simulations of correlated electron systems.

Parts of this chapter have been published in C.-A. Wang, C. Déprez, H. Tidjani, W.I.L. Lawrie, N.W. Hendrickx, A. Sammak, G. Scappucci, and M. Veldhorst, Probing resonating valence bonds on a programmable germanium quantum simulator, *npj Quantum Information* **9**, 58 (2023).

4.1. INTRODUCTION

Quantum computers have the potential of simulating physics beyond the capacity of classical computers [1, 2, 3, 4]. Gate-defined quantum dots are extensively studied for quantum computation [5, 6], but are also a natural platform for implementing quantum simulations [7, 8, 9, 10, 11]. The control over the electrical charge degree of freedom has facilitated the exploration of novel configurations such as effective attractive electron-electron interactions [12], collective Coulomb blockade [13], and topological states [14]. Coherent systems may be simulated when using the spin states of electrons in quantum dots, though experiments thus far have relied on gallium arsenide heterostructures [15, 16, 17], where the hyperfine interaction limits the spin coherence and therefore the complexity of simulations that can be performed. This bottleneck can be tackled by using group IV materials with nuclear spin-free isotopes. A natural candidate would be silicon, but this material comes with additional challenges due to the presence of valley states and a large effective electron mass [18].

Hole quantum dots in planar Ge/SiGe heterostructures exhibit many favorable properties found in different quantum dot platforms [19]. Natural germanium has a high abundance of nuclear spin-free isotopes and can be isotopically purified [20]. Holes in germanium benefit from a low effective mass [21, 22], absence of valley degeneracies, ohmic contacts to metals [23], and strong spin-orbit coupling for all-electrical control [24, 25]. Recent advances in heterostructure growth have resulted in stable, low-noise germanium devices [26]. This has sparked rapid progress, with demonstrations of hole quantum dots [23], single hole qubits [25], singlet-triplet (ST) qubits [27], two-qubit logic [28], and a four qubit quantum processor [29].

Here, we explore the prospects of hole quantum dots in Ge/SiGe for quantum simulation. We focus on the simulation of resonating valence bond (RVB) states, which are of fundamental relevance in chemistry [30] and solid state physics [31, 32, 33, 34] and have been used in other platforms as a feasibility test for quantum simulation [35, 36, 37, 38]. In our simulation, we probe RVB states in a square 2×2 configuration. First, we realize Singlet-Triplet (ST) qubits for all nearest-neighbour configurations. We then study the coherent evolution of four-spin states and demonstrate exchange control spanning an order of magnitude. Furthermore, we tune the system to probe valence bond resonances whose observed characteristics comply with predictions derived from the Heisenberg model. We finally demonstrate the preparation of s-wave and d-wave RVB states from spin-singlet states via adiabatic initialization and tailored pulse sequences.

The experiments are based on a quantum dot array defined in a high-quality Ge/SiGe quantum well, as shown in Fig. 4.1a [39, 29]. The array comprises four quantum dots and we obtain good control over the system, enabling to confine zero, one, or two holes in each quantum dot as required for the quantum simulation. The dynamics of resonating valence bonds is governed by Heisenberg interactions. The spin states in germanium quantum dots, however, also experience Zeeman, spin-orbit and hyperfine interactions (see Section 4.9). We therefore operate in small magnetic fields and acquire a detailed understanding of the system dynamics to apply tailored pulses. In the regime where Heisenberg interactions are dominating, the total spin is conserved. We can therefore study the subspaces of different total spin separately. The relevant subspace for the RVB physics is the zero total spin space spanned by the basis formed by the four-spin states

$|S_x\rangle = |S_{12}S_{34}\rangle$ and $\frac{1}{\sqrt{3}}(|T^+_{12}T^-_{34}\rangle + |T^-_{12}T^+_{34}\rangle - |T^0_{12}T^0_{34}\rangle)$, where $|S_{ij}\rangle = \frac{1}{\sqrt{2}}(|\uparrow_i\downarrow_j\rangle - |\downarrow_i\uparrow_j\rangle)$ and $|T^0_{ij}\rangle = \frac{1}{\sqrt{2}}(|\uparrow_i\downarrow_j\rangle + |\downarrow_i\uparrow_j\rangle)$, $|T^+_{ij}\rangle = |\uparrow_i\uparrow_j\rangle$, $|T^-_{ij}\rangle = |\downarrow_i\downarrow_j\rangle$ denote the singlet and triplet states formed by the spins in the quantum dots i and j. In this basis, the Heisenberg Hamiltonian H_J reads:

$$H_J(S_{\text{tot}} = 0) \equiv H_S = \begin{pmatrix} -J_x - \frac{J_y}{4} & \frac{\sqrt{3}}{4}J_y \\ \frac{\sqrt{3}}{4}J_y & -\frac{3}{4}J_y \end{pmatrix}, \tag{4.1}$$

where $J_x = J_{12} + J_{34}$ and $J_y = J_{14} + J_{23}$. Figures 4.1.b-c show the eigen energies and eigenstates of H_S for different regimes of exchange interaction. When the exchange interaction is turned on in only one direction, $J_x \gg J_y$ or $J_x \ll J_y$, the system is equivalent to two uncoupled double quantum dots. The ground state is then a product of singlet states $|S_x\rangle$ or $|S_y\rangle = |S_{14}S_{23}\rangle$. However, when all exchanges are on and in particular when they are equal, $J_x = J_y$, the eigenstates are coherent superpositions of $|S_x\rangle$ and $|S_y\rangle$, which simulate the RVB state. In this regime, the ground state is the s-wave superposition state $|s\rangle = \frac{1}{\sqrt{3}}(|S_x\rangle - |S_y\rangle)$ and the excited state is the d-wave superposition state $|d\rangle = |S_x\rangle + |S_y\rangle$.

Fig. 4.1.b shows that RVB states can be generated from uncoupled spin singlets by adiabatically equalizing the exchange couplings. Alternatively, if the exchange couplings are pulsed diabatically to equal values, valence bond resonances between $|S_x\rangle$ or $|S_y\rangle$ states occur.

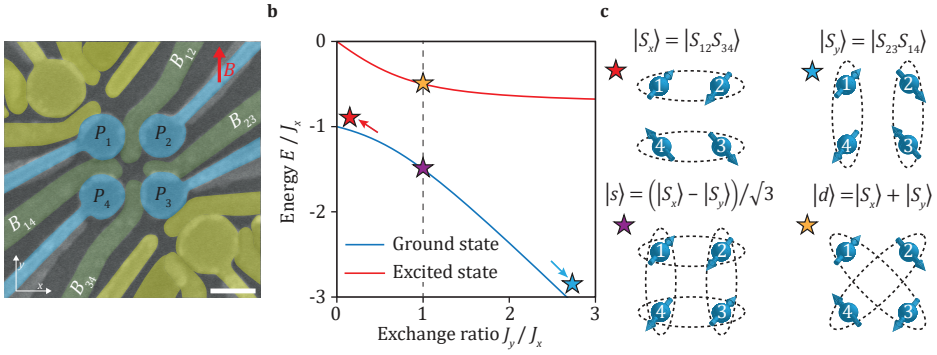

Figure 4.1: **RVB states in a 2×2 quantum dot array. a**, False-coloured scanning electron micrograph of the Ge quantum dot array. Plunger and barrier gates are coloured in blue and green respectively, and the corresponding gate voltages applied on them are labelled. To achieve independent control of the quantum dot potentials and tunnel couplings, virtual plunger and barrier gate voltages are defined (see Supplementary Note 1 [40]). Single hole transistors used as charge sensors are coloured in yellow. The scale bar corresponds to 100 nm. **b**, Energy diagram corresponding to the Hamiltonian H_S. The stars denote the corresponding eigenstates depicted in **c**. When the exchange interaction is dominated by horizontal (vertical) pairs, the ground state is $|S_x\rangle$ ($|S_y\rangle$), and in our experiments we use this configuration for initialization. Resonating valence bond states appear when $J_y = J_x$, the eigenstates are the ground state with s-wave symmetry and excited state with d-wave symmetry.

4.2. SINGLET-TRIPLET OSCILLATIONS IN THE FOUR DOUBLE QUANTUM DOTS

Probing the RVB physics relies on measuring the singlet probabilities in the (1,1) charge state [36, 17]. We thus investigate singlet-triplet (ST) oscillations within all nearest-neighbour pairs.

To generate ST oscillations, we operate in a virtual gate landscape and apply pulses on the virtual plunger gates vP_i of each quantum dot pair according to the pulse sequence depicted in Fig. 4.2.a [41, 42, 43, 27, 44]. The double quantum dot system is initialized in a singlet (0,2) state. Then, the detuning between the quantum dots is varied by changing the virtual plunger gate voltages. The system is diabatically brought to a manipulation point in the (1,1) sector creating a coherent superposition of $|S\rangle$, $|T^-\rangle$ and $|T^0\rangle$ [41, 42, 43, 27, 44]. After a dwell time t_D, the system is diabatically pulsed back to the (0,2) sector where the ST probabilities are determined via single-shot readout using (latched) Pauli-spin-blockade [45, 46, 47].

Results of such experiments performed at B = 3 mT with Q_3Q_4 pair are presented in Fig. 4.2.c. Clear oscillations between the $|S\rangle$ and $|T^-\rangle$ state are observed over a large range of gate voltage. Importantly, using this method we find the S-T^- anticrossing, which is the position where the frequency has a minimum. The observation of such oscillations, predominating over oscillations between $|S\rangle$ and $|T^0\rangle$ states, agrees with recent investigations suggesting that S-T^- oscillations dominate in germanium ST qubits placed in an in-plane B field [44].

Fig. 4.2.c also suggests that a (1,1)-singlet can be initialized from a (0,2)-singlet, by changing the energy detuning between the quantum dots while avoiding to pass the S-T^- anticrossing. We achieve this by shifting the anticrossing towards the center of the (1,1) charge sector by decreasing the magnetic field to B = 1 mT and increasing the tunnel couplings (Fig. 4.6). Fig. 4.2.d demonstrates clear S-T^- oscillations observed in this regime for all nearest-neighbour configurations (see also Fig. 4.7). Importantly, these oscillations also enable to determine the singlet/triplet states on two parallel quantum dot pairs by using sequential readout [48].

4.3. TUNING OF INDIVIDUAL EXCHANGES USING COHERENT OSCILLATIONS

The overlap of the H_S eigenstates with $|S_x\rangle$ and $|S_y\rangle$ depends on J_x and J_y (see Section 4.7). A quantitative comparison between experiments and theoretical expectations thus requires fine control over the exchange couplings.

In this purpose, we focus on the evolution of coherent four-spin ST oscillations. These oscillations are induced using the experimental sequence depicted in Fig. 4.3.a (see also Supplementary Figure 3 [40]). We turn off two parallel exchange couplings and initialize a $|S_x\rangle$ or a $|S_y\rangle$ state in parallel double quantum dots. We then rotate one of the singlet pairs to a triplet $|T^-\rangle$ state through coherent time evolution after pulsing to the S-T^- anticrossing, creating a four-spin singlet-triplet product state (e.g. $|T^-_{34}S_{12}\rangle$ or $|T^-_{23}S_{14}\rangle$). All barrier gate voltages are then diabatically pulsed to turn on all the exchange couplings leading to coherent evolution of the four-spin system. After a dwell time t_D, two pairs are

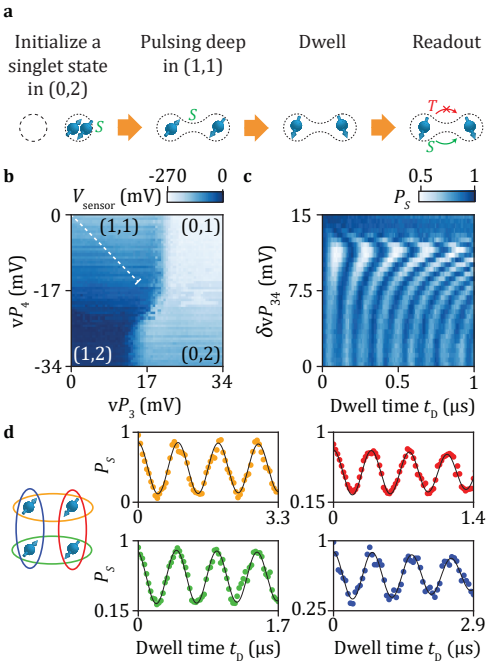

Figure 4.2: **Singlet-triplet qubits on all nearest-neighbour configurations.** **a**, Schematics of the pulse sequence used to generate singlet-triplet oscillations in double quantum dots. **b**, Charge stability diagram of a double quantum dot (Q_3Q_4) in the few-hole regime. **c**, S-T^- oscillations as a function of time and detuning $\delta vP_{34} = 0.5(vP_3 - vP_4)$ varied along the dashed line in **b**. At larger magnetic fields, here $B = 3$ mT, and limited tunnel couplings, we observe a minimum oscillation frequency due to the S-T^- anticrossing. We tune the system in a regime with smaller magnetic fields ($B = 1$ mT) and larger tunnel couplings, to operate away from this point. **d**, S-T^- oscillations observed in this regime for all possible permutations of nearest-neighbour quantum dot pairs. Black lines are fits of the data (see Section 4.6).

isolated (not necessarily the initial ones) and their spin-states are readout sequentially, which allows to deduce spin-correlations of opposite pairs, as was realized in linear arrays in GaAs [17].

The observation of resonating valence bond requires equal couplings between all four quantum dots. In navigating to this point, we carefully develop a virtual landscape, keep control over all the individual exchange interactions. First, we separately equalize the horizontal ($J_{12} = J_{34}$) and vertical ($J_{14} = J_{23}$) exchange couplings. Then, we tune the vertical and horizontal exchanges to the same coupling strength. The Chevron patterns displayed in Fig. 4.3.c-d are consistent with a Heisenberg Hamiltonian (see see Fig. 4.8 to Fig. 4.10) and the minima in the oscillation frequency mark the location of equal exchange couplings for horizontal ($J_{12} \simeq J_{34} \simeq J_x/2$ for Fig. 4.3.c) or vertical pairs ($J_{14} \simeq J_{23} \simeq J_y/2$ for Fig. 4.3.d). Through an iterative process, we can find ranges of virtual gate voltages where $J_{12} \simeq J_{34}$ and $J_{23} \simeq J_{14}$.

We can now control the spin pairs simultaneously, while maintaining the exchange couplings in both the horizontal and vertical directions equal (see Section 4.8), with *a priori* $J_x \neq J_y$. Through the readout of both pairs, we can obtain the frequency of four-

spin ST oscillations observed in this regime (Fig. 4.3.e), which is given by $f_{ST} = J_y/2h$ or $J_x/2h$ depending on the initial state, and with that determine the exchange interaction. As highlighted in Fig. 4.3.f., the virtual control enables to tune J_x from 15 MHz to 109 MHz with J_y remaining between 46 and 56 MHz. Clearly, the exchange interaction can be controlled and measured over a significant range and tuned to a regime where all couplings are equal (we obtain a precision of ≈ 3 MHz, as discussed in Section 4.8, mostly determined by drifts between experiments).

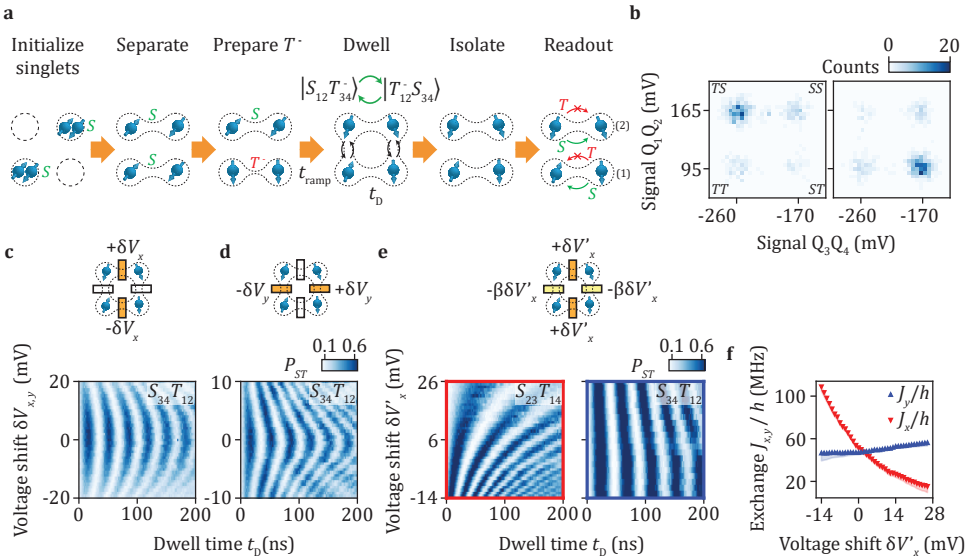

Figure 4.3: **Four-spin coherent singlet-triplet oscillations and exchange characterization.** **a**, Schematics of the pulse sequence used to measure four-spin ST oscillations from an initial $|T^-_{34}S_{12}\rangle$ state. **b**, The 2D histograms of the sensor signals formed by sequential 500 single-shot readouts of Q_3Q_4 and Q_1Q_2 ST states. The left panel shows the initial state $|T^-_{34}S_{12}\rangle$ at $t_D = 0$ ns. The right panel shows the state at $t_D = 19$ ns corresponding to half an oscillation period. (Data corresponds to **c** for $\delta V_x = 0$.) **c**, Oscillations in ST probability $P_{S_{34}T_{12}}$ as a function of gate voltage variation δV_x. The amplitude of exchange pulses applied on the virtual barrier gates during the free evolution step are varied between measurements around a predetermined set of barrier gate voltages where $J_x < J_y$. The amplitude of voltage pulses on $vB_{12,34}$ are varied anti-symmetrically while the amplitudes of the pulses on $vB_{23,14}$ are kept constant, as shown in the top illustration. The initial state is $|T^-_{34}S_{12}\rangle$. **d**, Similar experiment where oscillations in $P_{S_{34}T_{12}}$ are studied as a function of the gate voltage variation δV_y. δV_y is the shift in the amplitudes of the exchange pulses applied anti-symmetrically on $vB_{23,14}$ (see top illustration). The initial state is $|T^-_{34}S_{12}\rangle$. **e**, Oscillations in $P_{S_{23}T_{14}}$ (left) and $P_{S_{34}T_{12}}$ (right) as functions of t_D and $\delta V'_x$. The amplitude of exchange pulses are varied symmetrically around the operation point ($\delta V'_x = 0$ mV where $J_x \simeq J_y$) according to the top illustration ensuring that $J_{12} \simeq J_{34}$ and $J_{14} \simeq J_{23}$ along the full voltage range. The initial states are respectively a $|T^-_{23}S_{14}\rangle$ (left) and a $|T^-_{34}S_{12}\rangle$ state (right). **f**, Exchange couplings $J_{x,y}$ extracted by fitting the oscillations in **e** with $A\cos(2\pi f_{ST} t_D + \phi)\exp(-(t_D/T_\varphi)^2) + A_0$ as a function of gate voltage variation $\delta V'_x$. The oscillation frequencies of $P_{S_{23}T_{14}}$ ($P_{S_{34}T_{12}}$) corresponds to $J_x/2h$ ($J_y/2h$). The shaded areas correspond to the estimated uncertainty on the exchange couplings derived based on assumptions discussed in Section 4.8.

4.4. VALENCE BOND RESONANCES

Valence band resonances can occur when all J_{ij} are equal. To experimentally assess this, we prepare $|S_x\rangle$ or $|S_y\rangle$, which are superposition states of H_S. We then pulse the exchanges such that $J_x \approx J_y$. Fig. 4.4.a shows the result of the time evolution in this regime of equal exchange couplings. Since we start from a superposition state of H_S, the time evolution leads to coherent oscillations between $|S_x\rangle$ or $|S_y\rangle$, which results in periodic swaps between the singlet states as depicted in Fig. 4.4.b. In addition, we readout both in the horizontal and vertical configuration, and observe an anti-correlated signal, consistent with signatures of valence bond resonances [32, 36]. The observation of more than ten oscillations shows the relatively high level of coherence achieved during these experiments further confirmed by the characteristic dephasing time $T_\varphi \approx 150$ ns.

Fig. 4.4.c-d show a more detailed measurement, which we can fit using $\frac{\mathcal{V}_{x,y}}{2}\cos(2\pi f_{SS} t_D + \phi)\exp(-(t_D/T_\varphi)^2) + A_0$ to extract the evolution of the frequencies f_{SS} and of the visibilities $\mathcal{V}_{x,y}$, plotted on Fig. 4.4.e and Fig. 4.4.f. We find a quantitative agreement between the measured frequencies and the theoretical expectation $f_{SS} = \sqrt{J_x^2 + J_y^2 - J_x J_y}/h$ despite deviations for the lowest values of $\delta V_x'$ that could result from the uncertainties in the exchange couplings. We also find a qualitative agreement for the visibilities though the measured $\mathcal{V}_{x,y}$ remain lower, in particular when the exchange is larger. Fermi-Hubbard simulations and further analysis (see Supplementary Notes 7 and 8 [40]) reveal that part of the visibility loss can be attributed to leakage and to the insufficient diabaticity of the voltages pulses. We speculate that the rest of the visibility loss is mainly due to the decoherence induced by the voltage pulses at the manipulation stage, or by pulse distortion arising from the non-ideal electrical response of the wiring. The underlying mechanism affects similarly the results of the measurements in the both readout directions over most of the voltage range spanned (see Supplementary Note 8 [40]). Consequently, a more quantitative agreement is reached when comparing the ratio $\mathcal{V}_y/(\mathcal{V}_x+\mathcal{V}_y)$ (Fig. 4.4.g) of the visibilities measured over the visibilities predicted, similarly as is done in ref. [36]. Overall, the good agreement observed confirms that the dynamics is governed by H_S.

PREPARATION OF RESONATING VALENCE BOND EIGENSTATES

Having observed valence bond resonances, we now focus on the preparation of eigenstates of H_S which are the $|s\rangle$ and $|d\rangle$ RVB states. $|s\rangle$ is the ground state of H_S when $J_x = J_y$, whereas $|S_x\rangle$ and $|S_y\rangle$ are the ground states when $J_x \gg J_y$ and $J_x \ll J_y$. Experimentally we therefore prepare $|s\rangle$ from $|S_x\rangle$ or $|S_y\rangle$ by adiabatically tuning the exchange interactions to equal values. Fig. 4.5.a shows experiments where we control the ramp time t_{ramp} to tune to this regime and we observe a progressive vanishing of phase oscillations. For large $t_{\text{ramp}} \gtrsim 140$ ns, the oscillations nearly disappear and the measured probability saturates to $P_{S_{12}S_{34}} \simeq 0.78$. Performing similar experiments starting from a $|S_y\rangle$ state or measuring $P_{S_{23}S_{14}}$ leads to identical features with singlet-singlet probabilities saturating between 0.66 and 0.72 (see Supplementary Figure 22 [40]). These values are close to the probabilities $|\langle S_{x,y}|s\rangle|^2 = 3/4$ expected when the s-wave state is prepared.

We can now also prepare the ground state H_S for arbitrary exchange values, by care-

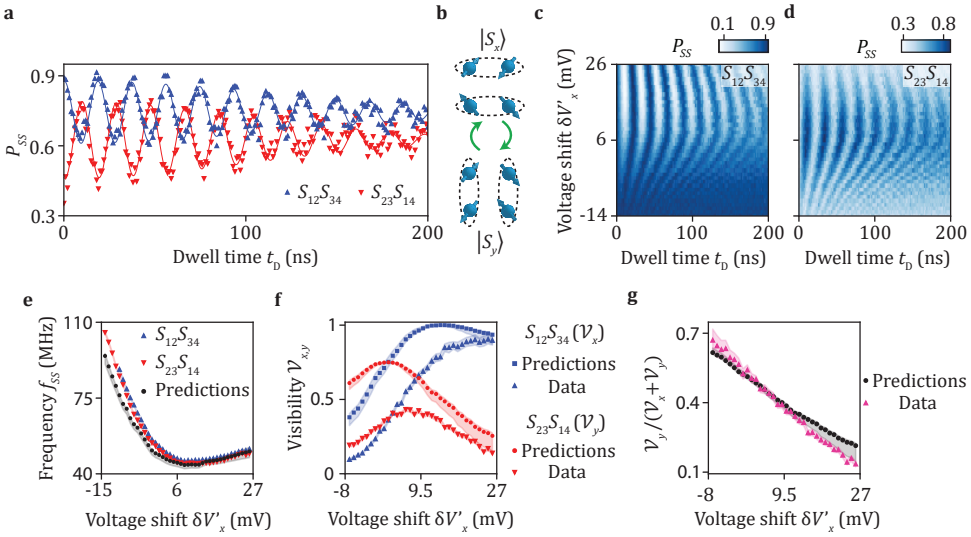

Figure 4.4: **Valence bond resonances.** **a**, Probabilities of having horizontal singlet pairs $P_{S_{12}S_{34}}$ and vertical singlet pairs $P_{S_{23}S_{14}}$ as a function of dwell time t_D. All the exchange couplings are tuned toward an identical value of $J_{ij}/h \simeq 25$ MHz. Lines are fits to the data with $P_{SS} = 1/2\,\mathcal{V}\cos(2\pi f_{SS} t_D + \phi)\exp(-(t_D/T_\varphi)^2) + A_0$ giving respectively $T_\varphi = 167$ ns and 143 ns for data corresponding to $P_{S_{12}S_{34}}$ and $P_{S_{23}S_{14}}$. The state is initialized as $|S_x\rangle$. **b**, Illustration showing valence bond resonances characterized by oscillations between the singlet product states $|S_x\rangle$ and $|S_y\rangle$. **c**, $P_{S_{12}S_{34}}$ and, **d**, $P_{S_{23}S_{14}}$ as a function of t_D and virtual barrier gate voltage variation $\delta V'_x$. The state is initialized as $|S_x\rangle$. **e**, The oscillation frequency as a function of $\delta V'_x$. The blue (red) points are extracted from **c** (**d**). The black points are the theoretical predictions $f_{SS} = \sqrt{J_x^2 + J_y^2 - J_x J_y}/h$ computed using the exchanges J_x and J_y measured in Fig. 4.3.e. **f**, Visibility $\mathcal{V}_{x,y}$ as a function of gate voltage variation $\delta V'_x$. The triangles in blue (red) are extracted from **c** (**d**). The expected values are derived from equations (4.4) and (4.6) of Section 4.7 using the measured exchanges. The shaded areas correspond to one standard deviation from the best fit for the experimental data, and for the theoretical data they correspond to the uncertainties on the amplitude and the frequency computed using the uncertainties on the exchange couplings values. **g**, Ratio of the visibilities $\mathcal{V}_y/(\mathcal{V}_x + \mathcal{V}_y)$ as a function of the gate voltage variation $\delta V'_x$.

fully tuning the ramp time ($t_{\text{ramp}} = 160$ ns in our experiments). Fig. 4.5.b shows the evolution of $P_{S_{12}S_{34}}$ for different $\delta V'_x$. Since we prepare the ground state, coherent phase evolution results in a $P_{S_{12}S_{34}}$ that is virtually constant for any $\delta V'_x$ and only faint oscillations are observed. $P_{S_{12}S_{34}}$, however, is strongly dependent on $\delta V'_x$, as increasing J_x changes the ground state to $|S_x\rangle$.

The measured $P_{S_{12}S_{34}}$ values can be compared with predictions using $J_{x,y}$ values extracted from four-spin singlet-triplet oscillations (see Section 4.7). Fig. 4.5.c shows that a good agreement exists between the theory and the experiments. The raw experimental probabilities $P_{S_{12}S_{34}}$ remains smaller than the theoretical predictions due to systematic errors during the experiments, which are most likely state initialization and readout errors (see Supplementary Note 8 [40]). Measuring $P_{S_{23}S_{14}}$ leads to a similar agreement, although the imperfections have a larger impact in this experiment. Rescaling the data by constant factors, that compensate for systematic errors, allows to reach a quantitative

agreement, as shown in Fig. 4.5.c. From this we conclude that the ground state of H_S is adiabatically initialized in these experiments.

We prepare the d-wave state by including an additional operation where we exchange two neighbouring spins [36]. This results in a transformation of neighbouring spin-spin correlations to diagonal correlations. We experimentally implement this step by adding, before the free evolution step, an exchange pulse of duration t_J during which only one exchange coupling is turned on (see Fig. 4.5.d).

Fig. 4.5.e-f shows $P_{S_{12}S_{34}}$ and $P_{S_{23}S_{14}}$ measured as functions of t_D and t_J in experiments where the system is initialized in $|S_x\rangle$ and the exchange J_{23} is pulsed. As a function of the exchange pulse duration, we observe a periodic vanishing of RVB oscillations (linecuts provided in Fig. 4.5.g-h, imperfections in exchange control cause residual oscillations). Due to the exchange pulse, a periodic swapping of neighbouring spins occurs, and thus a periodic evolution between neighbouring spin-spin correlations and diagonal correlations. Thus the regime where the d-wave eigenstate is prepared is marked by the vanishing of RVB states. The mean of the probabilities, $P_{S_{23}S_{14}} \simeq 0.21$ and $P_{S_{12}S_{34}} \simeq 0.13$, measured for $t_J = 25$ ns are in the direction of theoretical expectations $|\langle S_{x,y}|d\rangle|^2 = 1/4$.

4.5. DISCUSSION

In this work we demonstrated a coherent quantum simulation using germanium quantum dots. Clear evolution of resonating valence bond states appeared after tuning to a regime where all nearest neigbours have equal exchange coupling. We furthermore established the preparation of the s-wave and d-wave eigenstates. In addition, we have shown that we can control the exchange interaction over a significant range in a multi-spin setting.

The low-disorder and quantum coherence make germanium a compelling candidate for more advanced quantum simulations. Improving the initialization and readout fidelities will enable to observe a stronger correspondence between ideal predictions and experimental results. Additionally, advanced voltage pulsing may facilitate to reduce errors occurring when controlling the spin states. Furthermore, a significant improvement in the quantum coherence may be obtained by exploring sweet spots [49] and by using purified germanium.

Controlling multi-spin states is also highly relevant in the context of quantum computation. The realization of exchange-coupled singlet-triplet qubits enables to implement fast two-qubit gates [50, 51, 52, 53]. Leakage may then be reduced by exploiting the large out-of-plane g-factor for holes in germanium [27, 44]. Also, operation with four-spin manifolds provides means for decoherence-free subspaces [54].

Extensions of this work leveraging the full tunability of germanium quantum dots could provide new insights for extensive studies of strongly-correlated magnetic phases and associated quantum phase transitions. In particular, the implementation of similar simulations in triangular lattices offer new possibilities to investigate the emergence of non-trivial phases arising from frustration [33, 34]. Likewise, the preparation of RVB states and the investigation of their dynamics in larger devices may help to probe their properties experimentally and explore how they relate to superconductivity in doped cuprates [31].

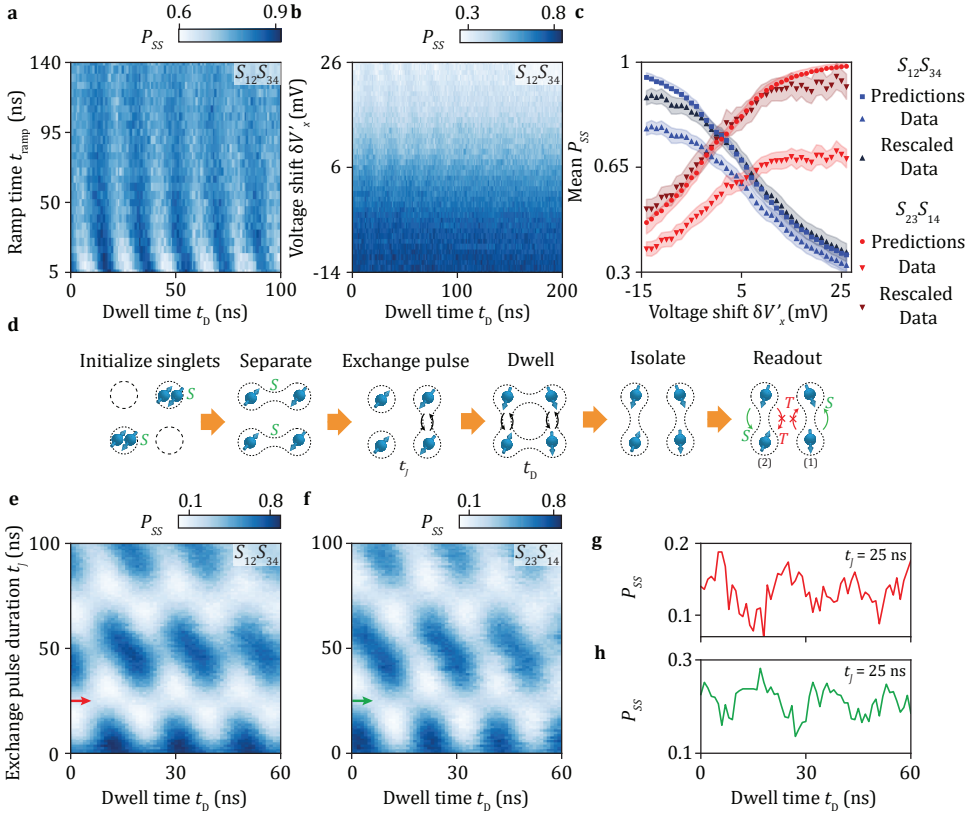

Figure 4.5: **Initialization of RVB eigenstates. a**, Evolution of RVB oscillations as a function of the time to set all exchanges equal ($J_{ij} \simeq 25$ MHz) (see Fig. 4.3.a). For $t_{\text{ramp}} \gtrsim 140$ ns, the ground state with s-wave symmetry is adiabatically prepared. **b**, Evolution of the singlet-singlet probability $P_{S_{12}S_{34}}$ with $\delta V'_x$ after adiabatic initialization of the ground state. **c**, Evolution of the mean singlet-singlet probability measured after adiabatic initialization of the ground state with $\delta V'_x$ for both readout directions. The experiments are compared to theoretical expectations using exchange coupling values extracted from four-spin singlet-triplet oscillations (Section 4.7 and 4.8). The shaded areas correspond to one standard deviation from the best fit for the experimental data, and for the theoretical data they correspond to the uncertainties on the amplitude and the frequency computed using the uncertainties on the exchange couplings values. Rescaled data (dark red and blue triangles) are obtained by multiplying each raw dataset (red and blue triangles) by a constant factor corresponding to the mean ratio of the predicted probabilities over the measured probabilities. **d**, Experimental sequence used to investigate the formation of the d-wave state. Before the free evolution step, one exchange pulse on vB_{23} is applied for a time t_J. **e, f**, Evolution of singlet-singlet oscillations measured for different exchange pulse durations t_J. The vanishing of oscillations at $t_J \simeq 25$ ns marks the formation of a d-wave state. **g, h**, Linecuts of **e** and **f** for $t_J = 25$ ns.

4.6. EXTENDED DATA OF TWO-SPIN S-T^- OSCILLATIONS

In a double dot, the (1,1) singlet energy reads as $E_S \simeq \frac{\varepsilon}{2} - \sqrt{\frac{\varepsilon^2}{4} + 2t_c^2}$, with t_c the tunnel coupling between the quantum dots and ε the detuning between the quantum dots (taken as zero at the (2,0)-(1,1) charge transition) [27]. The energy of the triplet states

are $E_{T^0} \simeq 0$ and $E_{T^\pm} \simeq \pm\frac{\Sigma g}{2}\mu_B B$ with Σg the g-factor sum. The corresponding energy diagram is sketched in Fig. 4.6.

In the (1,1) charge sector, the ground state is the singlet $|S\rangle$. Above a given value of detuning ε_{SO}, the $|T^-\rangle$ state becomes the ground state. Consequently there is an anti-crossing between the $|S\rangle$ and $|T^-\rangle$ due to the spin-orbit interaction. In order to maintain the singlet ground state in the (1,1) charge sector, one can decrease the magnetic field B or increase the tunnel coupling t_c.

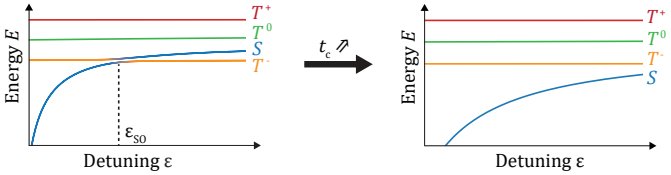

Figure 4.6: **Energy diagrams of a double quantum dot system at low fields.** At low tunnel couplings t_c, the singlet S and the triplet T^- energy states anti-cross due to the spin-orbit interaction. Increasing t_c, the energy of singlet state is lowered. At sufficiently large t_c, the singlet state remains the ground state in the (1,1) charge state for any value of the detuning ε.

At $B = 1$ mT, the ground state is the singlet state for Q_1Q_2 and Q_1Q_4 pairs in the whole (1,1) charge sector. It gives more freedom for the singlet-(1,1) initialization with these two quantum dot pairs. For the Q_2Q_3 and Q_3Q_4, there is still a S-T^- anticrossing that appears at finite detuning but sufficiently far from the charge transition line. It reduces charge noise effects detrimental for four-spin experiments.

To observe high visibility ST oscillations, pulses on the virtual barrier voltages are applied to reduce t_c while going from the initialization to the manipulation point. This configuration offers more flexibility to initialize $|S_x\rangle$ or $|S_y\rangle$ states.

Fig. 4.7 presents the ST oscillations of Fig. 4.2.d over larger ranges of dwell time t_D. By fitting the data, we extract the characteristic dephasing times T_φ and the frequency of the oscillations f for each pair (4.1). We note that there are large variations of both T_φ and f. The variation of f can be explained by differences in the strengths of the tunnel couplings t_c, the differences in the g-factor and in the amplitudes of the barrier voltage pulses. They lead to variations of the energy splitting between the $|T^-\rangle$ and $|S\rangle$ states. The variations of T_φ can result from different effects like residual exchange interactions with the other quantum dots or leakage to the $|T^0\rangle$ states. The lower coherence of Q_2Q_3 and Q_1Q_4 pairs compared to that of Q_1Q_2 and Q_3Q_4 could also result from the field orientation. Additionally, the spin life time is reduced when the spin-orbit field is oriented perpendicular to the external magnetic field [55, 29].

4.7. FOUR-SPIN COHERENT OSCILLATIONS IN THE GLOBAL SINGLET SUBSPACE

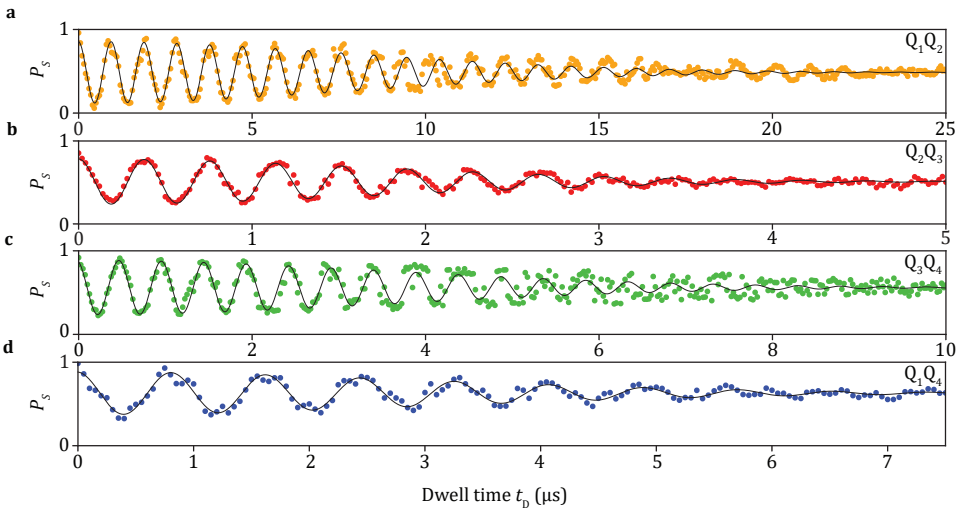

Figure 4.7: **Singlet-Triplet oscillations observed with each double quantum dot.** Same measurements than ones showed in Fig. 4.2.d. Data (points) are fitted with $A\cos(2\pi f t_D + \phi)\exp(-(t/T_\varphi)^2) + A_0$ to extract T_φ and f.

Dot Pair	Frequency (MHz)	T_φ (μs)
Q_1Q_2	1.056 ± 0.001	11.2 ± 0.4
Q_2Q_3	2.636 ± 0.005	2.5 ± 0.1
Q_3Q_4	2.043 ± 0.004	5.1 ± 0.3
Q_1Q_4	1.223 ± 0.004	4.2 ± 0.2

Table 4.1: **Characteristics of singlet-triplet oscillations of individual dot pairs.** The uncertainties correspond to one standard deviation from the best fits.

THEORETICAL MODEL

The Heisenberg Hamiltonian H_S in the global singlet subspace can be written, up to an overall energy shift, as:

$$H_S = (-\frac{1}{2}J_x + \frac{1}{4}J_y)\sigma_z + \frac{\sqrt{3}}{4}J_y\sigma_x = h_0\cos\theta\sigma_z + h_0\sin\theta\sigma_x, \tag{4.2}$$

where $\cos\theta = \frac{-2J_x+J_y}{2\sqrt{J_x^2-J_xJ_y+J_y^2}}$, $\sin\theta = \frac{\sqrt{3}J_y}{2\sqrt{J_x^2-J_xJ_y+J_y^2}}$, $h_0 = \frac{1}{2}\sqrt{J_x^2 - J_xJ_y + J_y^2}$, and $\sigma_{x,z}$ are the Pauli matrices. Here we denote the basis states $\{|0\rangle, |1\rangle\} \equiv \{|S_{12}S_{34}\rangle, \frac{1}{\sqrt{3}}(|T_{12}^+T_{34}^-\rangle + |T_{12}^-T_{34}^+\rangle - |T_{12}^0T_{34}^0\rangle)\} \equiv \{\begin{pmatrix}1\\0\end{pmatrix}, \begin{pmatrix}0\\1\end{pmatrix}\}$.

The eigen energies are $E_g = -h_0$ and $E_e = h_0$. The eigenstates are:

$$\begin{cases} |g\rangle = \begin{pmatrix} -\sin\frac{\theta}{2} \\ \cos\frac{\theta}{2} \end{pmatrix} \\ |e\rangle = \begin{pmatrix} \cos\frac{\theta}{2} \\ \sin\frac{\theta}{2} \end{pmatrix} \end{cases} . \tag{4.3}$$

In the singlet-singlet oscillation experiments, the state is initialized in a singlet-singlet state $|S_{12}S_{34}\rangle = \begin{pmatrix} 1 \\ 0 \end{pmatrix}$ which can be written as $-\sin\frac{\theta}{2}|g\rangle + \cos\frac{\theta}{2}|e\rangle$. After the free evolution this state becomes, up to a phase factor:

$$|\psi(t)\rangle = -\sin\tfrac{\theta}{2}|g\rangle + \cos\tfrac{\theta}{2}e^{-i\omega_{eg}t}|e\rangle = \begin{pmatrix} \sin^2(\frac{\theta}{2}) + \cos^2(\frac{\theta}{2})e^{-i\omega_{eg}t} \\ \sin(\frac{\theta}{2})\cos(\frac{\theta}{2})(-1+e^{-i\omega_{eg}t}) \end{pmatrix} = e^{-i\omega_{eg}t/2}\begin{pmatrix} \cos\left(\frac{\omega_{eg}t}{2}\right) - i\cos\theta\sin\left(\frac{\omega_{eg}t}{2}\right) \\ -i\sin\theta\sin\left(\frac{\omega_{eg}t}{2}\right) \end{pmatrix},$$

where $\omega_{eg} \equiv \omega_e - \omega_g = \frac{1}{\hbar}\sqrt{J_x^2 - J_xJ_y + J_y^2}$ is the frequency of the singlet oscillations.

The probability of being in the state $|0\rangle$ is $P_{S_{34}S_{12}}(t) = |\langle S_{12}S_{34}|\psi(t)\rangle|^2 = \frac{1}{2}\left(1+\cos^2\theta+\sin^2\theta\cos(\omega_{eg}t)\right)$. The visibility of the oscillations is then:

$$\mathcal{V}_x = P^{\max}_{S_{34}S_{12}} - P^{\min}_{S_{34}S_{12}} = \sin^2\theta = \frac{3J_y^2}{4(J_x^2 - J_xJ_y + J_y^2)}. \tag{4.4}$$

To describe the readout in the y direction, we use the basis $\{|0_y\rangle, |1_y\rangle\} = \{|S_{14}S_{23}\rangle, \frac{1}{\sqrt{3}}(|T_{14}^+T_{23}^-\rangle + |T_{14}^-T_{23}^+\rangle - |T_{14}^0T_{23}^0\rangle)\}$. The original basis can be re-written in terms of the new basis as:

$$\begin{cases} |0\rangle = -\frac{1}{2}|0_y\rangle - \frac{\sqrt{3}}{2}|1_y\rangle \\ |1\rangle = \frac{\sqrt{3}}{2}|0_y\rangle - \frac{1}{2}|1_y\rangle \end{cases} . \tag{4.5}$$

Therefore, $P_{S_{23}S_{14}}(t) = |\langle 0_y|\psi(t)\rangle|^2 = \frac{1}{4}(1+(\sin^2\theta - \sqrt{3}\sin\theta\cos\theta)\left(1-\cos(\omega_{eg}t)\right)$. The visibility is then:

$$\mathcal{V}_y = \frac{1}{2}(\sin^2\theta - \sqrt{3}\sin\theta\cos\theta) = \frac{3J_xJ_y}{4(J_x^2 - J_xJ_y + J_y^2)}. \tag{4.6}$$

We note that $\sin^2\theta - \sqrt{3}\sin\theta\cos\theta = \frac{6J_yJ_x}{4(J_x^2-J_xJ_y+J_y^2)} > 0$ and thus $P_{S_{34}S_{12}}(t)$ and $P_{S_{23}S_{14}}(t)$ oscillate in phase opposition. There are periodic swaps between $|S_x\rangle$ and $|S_y\rangle$ which are the resonating valence bond oscillations as shown in Fig. 4.4.

SINGLET PROBABILITIES OF S-WAVE AND D-WAVE STATES

To prepare the s-wave and d-wave states, the exchanges are set to be equal. It corresponds to the Hamiltonian of equation (4.2) with $\theta = 120°$. The s-wave state is the ground state and reads $|s\rangle = |g\rangle = (-\frac{\sqrt{3}}{2}, \frac{1}{2})$. The singlet-singlet probability in both x and y directions for this state are $P_{S_{34}S_{12}} = P_{S_{23}S_{14}} = \frac{3}{4}$. The d-wave state is the excited state and reads $|d\rangle = |e\rangle = (\frac{1}{2}, \frac{\sqrt{3}}{2})$. The singlet-singlet probabilities for this state are $P_{S_{34}S_{12}} = P_{S_{23}S_{14}} = \frac{1}{4}$.

When the exchanges are different, the equation (4.3) gives the ground state singlet-singlet readout probability $P_{S_{34}S_{12}} = \sin^2\frac{\theta}{2} = \frac{1-\cos\theta}{2} = \frac{1}{2} - \frac{-2J_x+J_y}{4\sqrt{J_x^2-J_xJ_y+J_y^2}}$ and $P_{S_{23}S_{14}} = (\frac{1}{2}\sin\frac{\theta}{2} + \frac{\sqrt{3}}{2}\cos\frac{\theta}{2})^2 = \frac{1}{2} + \frac{1}{4}\cos\theta + \frac{\sqrt{3}}{4}\sin\theta = \frac{1}{2} + \frac{-J_x+2J_y}{4\sqrt{J_x^2-J_xJ_y+J_y^2}}$. These formula are used in Fig. 4.5.c.

4.8. FOUR-SPIN COHERENT OSCILLATIONS IN THE GLOBAL TRIPLET SUBSPACE

THEORETICAL MODEL

Here we derive the theoretical results used to infer the exchange coupling $J_{x,y}$ from the four-spin singlet-triplet oscillations. In our experiments, we operated in the $m_S = -1$ global triplet subspace spanned by a natural basis $\{|S_{12}T_{34}^-\rangle, |T_{12}^-S_{34}\rangle, \frac{1}{\sqrt{2}}(|T_{12}^0T_{34}^-\rangle - |T_{12}^-T_{34}^0\rangle)\}$. Considering only Heisenberg exchange interactions, the Hamiltonian can be written as:

$$H_T = \begin{pmatrix} -J_{12} - \frac{J_{23}+J_{14}}{4} & -\frac{J_{23}+J_{14}}{4} & -\frac{J_{23}-J_{14}}{2\sqrt{2}} \\ -\frac{J_{23}+J_{14}}{4} & -J_{34} - \frac{J_{23}+J_{14}}{4} & -\frac{J_{23}-J_{14}}{2\sqrt{2}} \\ -\frac{J_{23}-J_{14}}{2\sqrt{2}} & -\frac{J_{23}-J_{14}}{2\sqrt{2}} & -\frac{J_{23}+J_{14}}{2} \end{pmatrix} = \begin{pmatrix} -\frac{J_x+\delta_x}{2} - \frac{J_y}{4} & -\frac{J_y}{4} & -\frac{\delta_y}{2\sqrt{2}} \\ -\frac{J_y}{4} & -\frac{J_x-\delta_x}{2} - \frac{J_y}{4} & -\frac{\delta_y}{2\sqrt{2}} \\ -\frac{\delta_y}{2\sqrt{2}} & -\frac{\delta_y}{2\sqrt{2}} & -\frac{J_y}{2} \end{pmatrix}. \tag{4.7}$$

We focus on the situation where $\delta_{x,y} \ll J_{x,y}$. First, we notice that in this limit $\frac{1}{\sqrt{2}}(|T_{12}^0T_{34}^-\rangle - |T_{12}^-T_{34}^0\rangle)$ is decoupled from the other states. Thus, when the system is diabatically initialized to $|S_{12}T_{34}^-\rangle$, it evolves to $|T_{12}^-S_{34}\rangle$ and back to $|S_{12}T_{34}^-\rangle$ at a frequency f_{ST}. To calculate f_{ST}, we perform a basis change to $\{|0\rangle, |1\rangle, |2\rangle\} \equiv \{\frac{1}{\sqrt{2}}(|S_{12}T_{34}^-\rangle - |T_{12}^-S_{34}\rangle), \frac{1}{\sqrt{2}}(|S_{12}T_{34}^-\rangle + |T_{12}^-S_{34}\rangle), \frac{1}{\sqrt{2}}(|T_{12}^0T_{34}^-\rangle - |T_{12}^-T_{34}^0\rangle)\}$ and separate the Hamiltonian into two terms:

$$H_T' = \begin{pmatrix} -\frac{J_x}{2} & -\frac{\delta_x}{2} & 0 \\ -\frac{\delta_x}{2} & -\frac{J_x+J_y}{2} & -\frac{\delta_y}{2} \\ 0 & -\frac{\delta_y}{2} & -\frac{J_y}{2} \end{pmatrix} = \begin{pmatrix} -\frac{J_x}{2} & 0 & 0 \\ 0 & -\frac{J_x+J_y}{2} & 0 \\ 0 & 0 & -\frac{J_y}{2} \end{pmatrix} + \begin{pmatrix} 0 & -\frac{\delta_x}{2} & 0 \\ -\frac{\delta_x}{2} & 0 & -\frac{\delta_y}{2} \\ 0 & -\frac{\delta_y}{2} & 0 \end{pmatrix} = H_0 + V, \tag{4.8}$$

where H_0 only contains diagonal elements $J_{x,y}$ and V only contains off-diagonal elements $\delta_{x,y}$. In the non-degenerate case $\delta_{x,y} \lesssim |J_x - J_y|$, we apply the second order perturbation theory to the term V. The eigen energies become:

$$E_0 = E_0^{(0)} + E_0^{(1)} + E_0^{(2)} = \langle 0|H_0|0\rangle + \langle 0|V|0\rangle + \sum_{i=\{1,2\}} \frac{|\langle i|V|0\rangle|^2}{E_0^{(0)} - E_i} = -\frac{J_x}{2} + \frac{\delta_x^2}{2J_y}, \tag{4.9}$$

$$E_1 = E_1^{(0)} + E_1^{(1)} + E_1^{(2)} = \langle 1|H_0|1\rangle + \langle 1|V|1\rangle + \sum_{i=\{0,2\}} \frac{|\langle i|V|1\rangle|^2}{E_1^{(0)} - E_i} = -\frac{J_x+J_y}{2} - \frac{\delta_x^2}{2J_y} - \frac{\delta_y^2}{2J_x}, \tag{4.10}$$

$$E_2 = E_2^{(0)} + E_2^{(1)} + E_2^{(2)} = \langle 2| H_0 |2\rangle + \langle 2| V |2\rangle + \sum_{i=\{0,1\}} \frac{|\langle i| V |2\rangle|^2}{E_2^{(0)} - E_i} = -\frac{J_y}{2} + \frac{\delta_y^2}{2J_x}. \tag{4.11}$$

$|S_{12}T_{34}^-\rangle = \frac{1}{\sqrt{2}}(|0\rangle + |1\rangle)$ and $|T_{12}^- S_{34}\rangle = \frac{1}{\sqrt{2}}(|1\rangle - |0\rangle)$. Thus, we infer that f_{ST} corresponds to the energy difference:

$$f_{ST} = \frac{E_0 - E_1}{h} = \frac{J_y}{2h} + \frac{\delta_x^2}{J_y h} + \frac{\delta_y^2}{2J_x h}. \tag{4.12}$$

Equation (4.12) shows that the S-T^- oscillation frequency minimum allows to extract the exchange value J_y.

According to these calculations, when the barrier gate voltages are varied by δV_x and δV_y at fixed evolution time t, the constant ST probability lines should draw ellipses centered at the voltages where $J_{12} = J_{34}$ and $J_{14} = J_{23}$. One can use this property to equalize the exchange couplings.

The Hamiltonian H_T' can also be diagonalized in the degenerate case $J_x = J_y = J$. The eigen energies read as:

$$\begin{cases} E_g = \frac{-3J - \sqrt{J^2 + 4\delta_x^2 + 4\delta_y^2}}{4} \approx -J - \frac{\delta_x^2 + \delta_y^2}{2J} \\ E_{e_1} = -\frac{J}{2} \\ E_{e_2} = \frac{-3J + \sqrt{J^2 + 4\delta_x^2 + 4\delta_y^2}}{4} \approx -\frac{J}{2} + \frac{\delta_x^2 + \delta_y^2}{2J} \end{cases} \tag{4.13}$$

$$\begin{cases} |g\rangle = \frac{2\delta_x|0\rangle + (J + \sqrt{J^2 + 4\delta_x^2 + 4\delta_y^2})|1\rangle + 2\delta_y|2\rangle}{N_g} \approx |1\rangle \\ |e_1\rangle = \frac{-\delta_y|0\rangle + \delta_x|2\rangle}{N_{e_1}} \approx \frac{\delta_y}{\sqrt{\delta_x^2 + \delta_y^2}}|0\rangle + \frac{\delta_x}{\sqrt{\delta_x^2 + \delta_y^2}}|2\rangle \\ |e_2\rangle = \frac{2\delta_x|0\rangle + (J - \sqrt{J^2 + 4\delta_x^2 + 4\delta_y^2})|1\rangle + 2\delta_y|2\rangle}{N_{e_2}} \approx -\frac{\delta_x}{\sqrt{\delta_x^2 + \delta_y^2}}|0\rangle + \frac{\delta_y}{\sqrt{\delta_x^2 + \delta_y^2}}|2\rangle \end{cases} \tag{4.14}$$

The initialized $|S_{12}T_{34}^-\rangle$ state can be decomposed as:

$$|S_{12}T_{34}^-\rangle = \frac{1}{\sqrt{2}}|g\rangle + \frac{1}{\sqrt{2}}\left(\frac{\delta_y}{\sqrt{\delta_x^2 + \delta_y^2}}|e_1\rangle - \frac{\delta_x}{\sqrt{\delta_x^2 + \delta_y^2}}|e_2\rangle\right). \tag{4.15}$$

As the system evolves, the measured singlet-triplet probability is:

$$P_{ST}(t) = |\langle S_{12}T_{34}^{-}|\, e^{-iH_T' t/\hbar}\, |S_{12}T_{34}^{-}\rangle|^2 = |\frac{1}{2}e^{-i\omega_g t} + \frac{1}{2}\frac{\delta_y^2}{\delta_x^2+\delta_y^2}e^{-i\omega_{e_1} t} + \frac{1}{2}\frac{\delta_x^2}{\delta_x^2+\delta_y^2}e^{-i\omega_{e_2} t}|^2$$
$$= \frac{\delta_x^4+\delta_x^2\delta_y^2+\delta_y^4}{2(\delta_x^2+\delta_y^2)^2} + \frac{\delta_x^2}{2(\delta_x^2+\delta_y^2)}\cos\big((\omega_{e_2}-\omega_g)t\big) + \frac{\delta_y^2}{2(\delta_x^2+\delta_y^2)}\cos\big((\omega_{e_1}-\omega_g)t\big) + \frac{\delta_x^2\delta_y^2}{2(\delta_x^2+\delta_y^2)^2}\cos\big((\omega_{e_2}-\omega_{e_1})t\big)$$
$$= \frac{\delta_x^4+\delta_x^2\delta_y^2+\delta_y^4}{2(\delta_x^2+\delta_y^2)^2} + \frac{1}{2}\cos\big(\frac{\omega_{e_1}+\omega_{e_2}-2\omega_g}{2}t\big)\cos\big(\frac{\omega_{e_1}-\omega_{e_2}}{2}t\big) + \frac{\delta_x^2-\delta_y^2}{2(\delta_x^2+\delta_y^2)}\sin\big(\frac{\omega_{e_1}+\omega_{e_2}-2\omega_g}{2}t\big)\sin\big(\frac{\omega_{e_1}-\omega_{e_2}}{2}t\big)$$
$$+ \frac{\delta_x^2\delta_y^2}{2(\delta_x^2+\delta_y^2)^2}\cos\big((\omega_{e_2}-\omega_{e_1})t\big). \tag{4.16}$$

According to equation (4.16), in two special cases (1) when $\delta_x = 0$, f_{ST} equals to $\frac{J}{2h} + \frac{\delta_y^2}{2Jh}$ and (2) when $\delta_y = 0$, f_{ST} equals to $\frac{J}{2h} + \frac{\delta_x^2}{Jh}$. In the general case $\delta_{x,y} \neq 0$, P_{ST} oscillates with three frequencies where two of them are close to each other resulting in a beating. More specifically, P_{ST} oscillates with a fast frequency $\frac{\omega_{e_1}+\omega_{e_2}-2\omega_g}{2} = \frac{J}{2\hbar} + \frac{3}{4}\frac{\delta_x^2}{J\hbar}$ while the amplitude is modulated at a lower frequency $\frac{\omega_{e_1}-\omega_{e_2}}{2} = \frac{\delta_x^2+\delta_y^2}{4J\hbar}$. Therefore, as long as $\delta_{x,y}$ remains sufficiently small, such that $\frac{\delta_x^2+\delta_y^2}{2J\hbar}t \lesssim \pi$, a frequency minimum still appears when $\delta_{x,y} = 0$ which allows us to extract $J_{x,y}$.

COMPARISON WITH EXPERIMENTS

We perform experiment where we study how four-spin singlet-triplet oscillations evolve when δV_x, δV_y and the dwell time t_D are varied. Fig. 4.8-4.10 show the results of these experiments for different operation points that we compare with numerical simulations of time evolution using the Hamiltonian H_T.

To perform the simulations, the exchange couplings away from $\delta V_{x,y} = 0$ are modelled using exponential models $J_{34/12} = \frac{J_x}{2}\exp(\pm\kappa\delta V_x)$ and $J_{14/23} = \frac{J_y}{2}\exp\big(\pm\kappa\delta V_y\big)$ [16]. The factor $\kappa = 0.059$ mV^{-1} is extracted from the frequency of isolated two-spin S-T^- oscillations whereas the $J_{x,y}$ values are taken from the frequency minimum in the corresponding sub-figures c-f. The exchange values here are within 10 % of deviation compared to the exchanges displayed in Fig. 4.3.f.

Fig. 4.8, 4.9, and 4.10 show three sets of data/simulations corresponding to experiments where the barrier gate voltages are varied by $\delta V_{x,y}$ around the points $\{vB_{12}^0 + \delta V_x', vB_{23}^0 - \beta\delta V_x', vB_{34}^0 + \delta V_x', vB_{14}^0 - \beta\delta V_x'\}$ with $\delta V_x'$ =20, 0, -20 mV and $vB_0 = \{vB_{12}^0, vB_{34}^0, vB_{23}^0, vB_{14}^0\} = \{16, -10.5, 0, 9.5\}$ mV (vB_0 is the predetermined set of voltages where exchange couplings are approximately equals mentioned in the main text). These $\delta V_x'$ values correspond approximately to the center and the limits of the range spanned in Fig. 4.3.e. In the three cases, the data and the simulations show an overall remarkably good agreement.

Fig. 4.8.a-b, 4.9.a-b and 4.10.a-b show the results of these measurements consisting in varying δV_x, δV_y at fixed t_D and the corresponding simulations. We observe that constant probability lines form a network of stripes drawing ellipses centered around $\delta V_{x,y} \simeq 0$ mV in agreement with the above discussion.

Fig. 4.8.c-f, 4.9.c-f and 4.10.c-f display the time evolution of four-spin singlet-triplet probabilities measured while varying either δV_x or δV_y around the centers of these el-

lipses. It confirms that the frequency minimum is reached when $\delta V_{x,y} \simeq 0$ mV i.e. at the center of the ellipse.

In these three configurations, we clearly have $J_{12} \simeq J_{34}$ and $J_{14} \simeq J_{23}$ for $\delta V_{x,y} \simeq 0$ mV. Similarly for $\delta V'_x = 26$ mV, singlet-triplet probabilities also draw an ellipse centered on $\delta V_{x,y} \simeq 0$ mV (Fig. 4.11). Extrapolating these results, we assume that these equalities remain valid over the full range of voltage -20 mV $\leqslant \delta V'_x \leqslant 26$ mV spanned in Fig. 4.3.e and thus that the frequency of four-spin ST oscillations f_{ST} directly gives $J_{x,y}/2$.

We note that the ellipses are tilted and even distorted especially when J_x is large. It could indicate a cross-talk between vertical and horizontal virtual barrier gates but also a deviation from the equations derived above which are valid only for small variations of exchange couplings.

In Fig. 4.9.b (initialization/readout in y direction), we also remark that both the measurements and the simulation show a complex pattern when voltages are varied away from the origin. This pattern appears less clearly in the measurement data of Fig. 4.9.a (initialization/readout in x direction).

Likewise, we notice beating patterns in Fig. 4.8.e and 4.10.d. They result from the third level, $\frac{1}{\sqrt{2}}(|T^0_{12}\, T^-_{34}\rangle - |T^-_{12}\, T^0_{34}\rangle)$, that is not completely decoupled and has an overlap with the initial state.

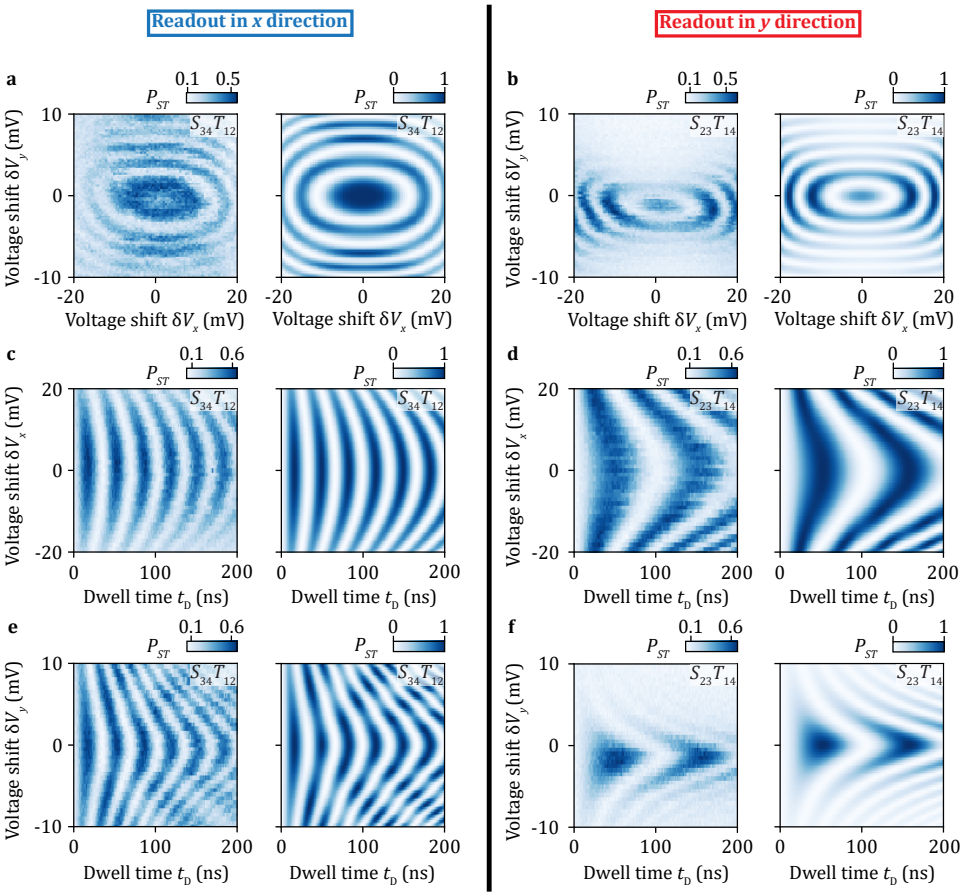

Figure 4.8: **Additional measurement data and numerical simulations of four-spin coherent singlet-triplet oscillations at low J_x.** **a**, **b**, Probabilities $P_{S_{34}T_{12}}$ and $P_{S_{23}T_{14}}$ as functions of barrier gate voltage variations $\delta V_{x,y}$ at fixed evolution time $t_D = 180$ ns. **c**, **d**, Oscillations in $P_{S_{34}T_{12}}$ and $P_{S_{23}T_{14}}$ as functions of gate voltage variation δV_x. **e**, **f**, Oscillations in $P_{S_{34}T_{12}}$ and $P_{S_{23}T_{14}}$ as functions of virtual gate voltage variation δV_y. The right panels are numerical simulations based on the Hamiltonian H_T. The virtual barrier voltages are varied around the operation point $\{36, -14.1, 20, 5.9\}$ mV which corresponds to the point $\delta V_x' = 20$ mV in Fig. 4.3.e.

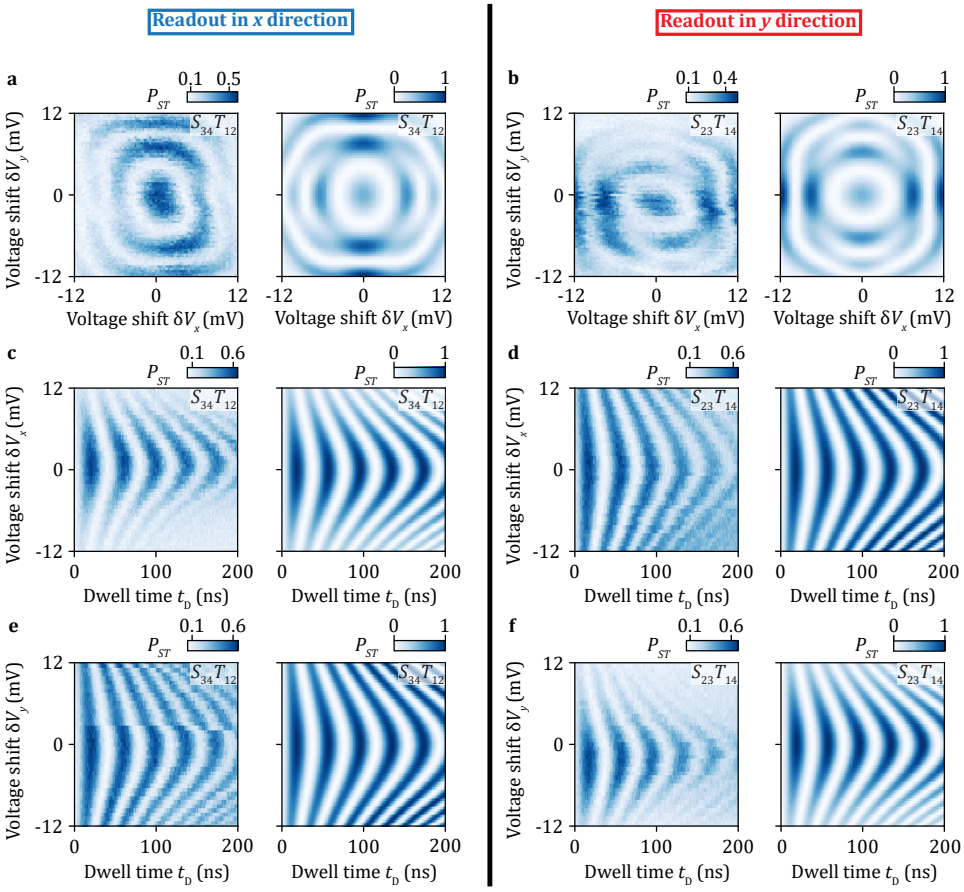

Figure 4.9: **Additional measurement data and numerical simulations of four-spin coherent singlet-triplet oscillations at medium J_x. a**, **b**, Probabilities $P_{S_{34}T_{12}}$ and $P_{S_{23}T_{14}}$ as functions of virtual barrier voltage variations $\delta V_{x,y}$ with a fixed evolution time $t_D = 105$ ns. **c**, **d**, Oscillations in $P_{S_{34}T_{12}}$ and $P_{S_{23}T_{14}}$ as functions of gate voltage variation δV_x. **e**, **f**, Oscillations in $P_{S_{34}T_{12}}$ and $P_{S_{23}T_{14}}$ as functions of gate voltage variations δV_y. The right panels are numerical simulations based on the Hamiltonian H_T. The virtual barrier voltages are varied around $vB_0 = \{16, -10.5, 0, 9.5\}$ mV which corresponds to the point $\delta V_x' = 0$ mV in Fig. 4.3.e.

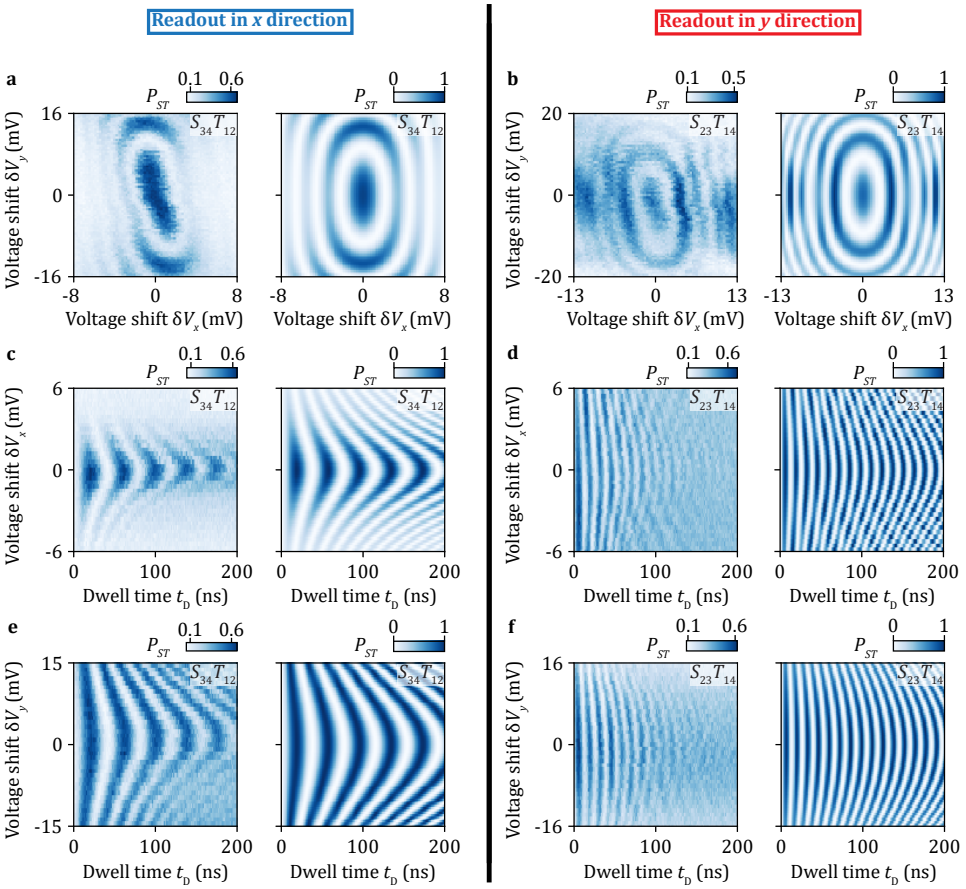

Figure 4.10: **Additional measurement data and numerical simulations of four-spin coherent singlet-triplet oscillations at large J_x. a**, **b**, Probabilities $P_{S_{34}T_{12}}$ and $P_{S_{23}T_{14}}$ as functions of virtual barrier voltage variations $\delta V_{x,y}$ with a fixed evolution time $t_D = 60$ ns. **c**, **d**, Oscillations in $P_{S_{34}T_{12}}$ and $P_{S_{23}T_{14}}$ probabilities as functions of gate voltage variation δV_x. **e, f**, Oscillations in $P_{S_{34}T_{12}}$ and $P_{S_{23}T_{14}}$ as functions of gate voltage variation δV_y. The panels on the right are numerical simulation based on the Hamiltonian H_T. The virtual barrier voltages are varied around $\{-4, -6.9, -20, 13.1\}$ mV, which corresponds to the point $\delta V_x' = -20$ mV (outside the range spanned in Fig. 4.3.e).

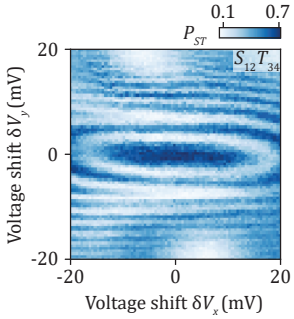

Figure 4.11: **Signature of equal exchange couplings.** Probability $P_{S_{12}T_{34}}$ as a function of the voltage variation $\delta V_{x,y}$ at fixed t_D = 113 ns. The barrier gate voltages are varied around $\{42,-15.18,26,4.82\}$ mV which corresponds to the extreme point δV_x^I = 26 mV in Fig. 4.3.e. The ellipse drawn by constant probability lines is centered around $\delta V_{x,y} \simeq 0$ indicating that at this point $J_{12} \simeq J_{34}$ and $J_{23} \simeq J_{14}$.

UNCERTAINTY ON THE EXCHANGE COUPLING VALUES

Our method to determine the barrier gate voltages required to have $J_{12} = J_{34}$ and $J_{23} = J_{14}$ leads to some uncertainties on the values of the exchange couplings. They originate from the uncertainty on the determination of the center of ellipse drawn by the oscillations when varying $\delta V_{x,y}$ at fixed t_D (see Fig. 4.8 to 4.11). We estimate that the center's position can be determined with a ±2 mV precision. Small drifts between experiments also typically lead to such uncertainties. Using the exponential models described above, we can then translate this uncertainty into an uncertainty on the exchange values at a given set of barrier gate voltages.

To express it, we assume that at $\delta V_{x,y} = 0$, the parallel exchange couplings are actually imbalance ($J_{12} \neq J_{34}$ and $J_{14} \neq J_{23}$). We note $\delta V_{x,y}^0$ the voltage shifts required to reach the balance $J_{12} = J_{34} = J_x^0/2$ and $J_{14} = J_{23} = J_y^0/2$. Then, as $\kappa|\delta V_{x,y} - \delta V_{x,y}^0| \lesssim 0.1$, we can write the differences of exchange couplings as:

$$\begin{cases} \delta_x = J_{12} - J_{34} = \frac{J_x^0}{2}\exp\left(-\kappa(\delta V_x - \delta V_x^0)\right) - \frac{J_x^0}{2}\exp\left(\kappa(\delta V_x - \delta V_x^0)\right) \simeq J_x^0\kappa(\delta V_x^0 - \delta V_x) \\ \delta_y = J_{23} - J_{14} = \frac{J_y^0}{2}\exp\left(-\kappa(\delta V_y - \delta V_y^0)\right) - \frac{J_y^0}{2}\exp\left(\kappa(\delta V_y - \delta V_y^0)\right) \simeq J_y^0\kappa(\delta V_y^0 - \delta V_y) \end{cases} . \tag{4.17}$$

Likewise, the sums of the exchange couplings are given by:

$$\begin{cases} J_x = J_{12} + J_{34} \simeq J_x^0(1 + \frac{\kappa^2(\delta V_x - \delta V_x^0)^2}{2}) \\ J_y = J_{14} + J_{24} \simeq J_y^0(1 + \frac{\kappa^2(\delta V_y - \delta V_y^0)^2}{2}) \end{cases} . \tag{4.18}$$

Using equation (4.12), the errors on the exchange couplings extracted are then given by:

$$\begin{cases} \sigma_{J_y} = 2f_{ST} - J_y/h = 2\frac{(J_x^0)^2}{J_y^0 h}\kappa^2(\delta V_x - \delta V_x^0)^2 + \frac{(J_y^0)^2}{J_x^0 h}\kappa^2(\delta V_y - \delta V_y^0)^2 \\ \sigma_{J_x} = 2\frac{(J_y^0)^2}{J_x^0 h}\kappa^2(\delta V_y - \delta V_y^0)^2 + \frac{(J_x^0)^2}{J_y^0 h}\kappa^2(\delta V_x - \delta V_x^0)^2 \end{cases} . \tag{4.19}$$

Notably, the uncertainty on the position of the center of the ellipse can only lead to an overestimation of the exchange values. The latter is about 3 MHz in average for the data displayed in Fig. 4.3.f. Additionally, fitting the four-spin singlet-triplet oscillations also leads to uncertainty on the value of f_{ST} from which the exchanges are inferred. We thus assume that the precision on the determination of the exchange couplings is set by the maximum of the two above uncertainties and we use it to draw the error bars in Fig. 4.3.f. Typically the former uncertainty is much larger than the uncertainty on the frequency fit.

The errors bars on the predicted singlet-singlet oscillation frequency f_{SS} (Fig. 4.4.e), visibilities $\mathcal{V}_{x,y}$ (Fig. 4.4.f) and on the singlet-singlet probabilities in the RVB ground state (Fig. 4.5.c) are then drawn by computing the minimum and maximum values of these quantities in the exchange coupling ranges fixed by the uncertainties on $J_{x,y}$.

4.9. LIMITS OF THE THEORETICAL DESCRIPTIONS

Up to now, we assumed that the system dynamics is only governed by the Heisenberg Hamiltonian. Yet, the effective Hamiltonian H_{tot} of the system contains other terms. When each quantum dot contains one hole, H_{tot} can be written as:

$$H_{\text{tot}} = H_J + H_Z + H_{SO} + H_{hp}, \tag{4.20}$$

where $H_J = \sum_{<i,j>} J_{ij}(\vec{S}_i \cdot \vec{S}_j - \frac{1}{4})$, $H_Z = \sum_i g_i \mu_B B$, H_{SO} and H_{hp} are respectively the Heisenberg, Zeeman, spin-orbit and hyperfine terms. The physics of RVB states is solely determined by the Heisenberg term H_J that conserves the total spin and the spin projection whereas the other terms couple states of different spin subspaces. To prevent these couplings, we operate the device with few milli-Teslas in-plane magnetic fields ensuring that the exchange couplings are the largest energy scales. In that case, one can assume that $H_{\text{tot}} \simeq H_J$ and derive analytical formulas describing the system dynamics. Here we justify further this approximation by quantifying the magnitude of the other terms.

HYPERFINE INTERACTION

We first focus on the effects of hyperfine interaction. It results in a Zeeman-like term that randomly varies in time and couple different total spin subspaces. In ref. [27], the authors evaluated the Zeeman energy noise in germanium ST qubits placed in a 1 mT perpendicular magnetic field, supposedly the most unfavorable direction regarding hyperfine interaction [56, 57]. They found $\delta E_Z < 2$ neV or $\delta E_Z/h < 0.48$ MHz [44]. This suggests that the hyperfine coupling can be safely discarded in the theoretical description.

ZEEMAN GRADIENTS

To express the Zeeman term H_Z, we need a full basis of the 16×16 Hilbert space. A convenient choice of basis for our theoretical description consists in using the basis $\psi_{1111} = \{0_S, 1_S, 0_{T^-}, 1_{T^-}, 2_{T^-}, 0_{T^0}, 1_{T^0}, 2_{T^0}, 0_{T^+}, 1_{T^+}, 2_{T^+}, Q^-, Q^0, Q^+, Q^{--}, Q^{++}\}$ that decomposes the Hilbert space into the different total spin S subspaces and that also decomposes these subspaces into smaller subspaces with different spin projections m_S [17]. The different states that compose the ψ_{1111} basis are expressed in Table 4.2. Note that the states

$\{0_S, 1_S\}$ and $\{0_{T^-}, 1_{T^-}, 2_{T^-}\}$ correspond to the basis-states of the global singlet and $m_S = -1$ triplet subspaces used above.

(S, m_S)	States
(0,0)	$\{0_S, 1_S\} = \{\|S_{12}S_{34}\rangle, \frac{1}{\sqrt{3}}(\|T_{12}^+ T_{34}^-\rangle + \|T_{12}^- T_{34}^+\rangle - \|T_{12}^0 T_{34}^0\rangle)\}$
(-1,1)	$\{0_{T^-}, 1_{T^-}, 2_{T^-}\} = \{\|S_{12}T_{34}^-\rangle, \|T_{12}^- S_{34}\rangle, \frac{1}{\sqrt{2}}(\|T_{12}^0 T_{34}^-\rangle - \|T_{12}^- T_{34}^0\rangle)\}$
(0,1)	$\{0_{T^0}, 1_{T^0}, 2_{T^0}\} = \{\|S_{12}T_{34}^0\rangle, \|T_{12}^0 S_{34}\rangle, \frac{1}{\sqrt{2}}(\|T_{12}^+ T_{34}^-\rangle - \|T_{12}^- T_{34}^+\rangle)\}$
(1,1)	$\{0_{T^+}, 1_{T^+}, 2_{T^+}\} = \{\|S_{12}T_{34}^+\rangle, \|T_{12}^+ S_{34}\rangle, \frac{1}{\sqrt{2}}(\|T_{12}^0 T_{34}^+\rangle - \|T_{12}^+ T_{34}^0\rangle)\}$
(-1,2)	$\{Q^-\} = \frac{1}{\sqrt{2}}(\|T_{12}^0 T_{34}^-\rangle + \|T_{12}^- T_{34}^0\rangle)$
(0,2)	$\{Q^0\} = \frac{1}{\sqrt{6}}(\|T_{12}^+ T_{34}^-\rangle + \|T_{12}^- T_{34}^+\rangle + 2\|T_{12}^0 T_{34}^0\rangle)$
(1,2)	$\{Q^+\} = \frac{1}{\sqrt{2}}(\|T_{12}^0 T_{34}^+\rangle + \|T_{12}^+ T_{34}^0\rangle)$
(-2,2)	$\{Q^{--}\} = \|T_{12}^- T_{34}^-\rangle$
(2,2)	$\{Q^{++}\} = \|T_{12}^+ T_{34}^+\rangle$

Table 4.2: **16 basis-states used to describe the effect of Zeeman gradients.** Each line corresponds to a subspace with given total spin S and a given spin projection m_S. The states that form the basis of each subspace are expressed in terms of two-spin singlet and triplet states. The Heisenberg Hamiltonian does not couple the different subspaces.

In this basis, the Zeeman Hamiltonian can be expressed as:

$$H_{\text{Zeeman}} = \mu_B B \left(\begin{array}{cccccccccccccccc}
0 & 0 & 0 & 0 & 0 & \frac{g_{34}^-}{2} & \frac{g_{12}^-}{2} & 0 & 0 & 0 & 0 & 0 & 0 & 0 & 0 & 0 \\
0 & 0 & 0 & 0 & 0 & \frac{-g_{12}^-}{2\sqrt{3}} & \frac{-g_{34}^-}{2\sqrt{3}} & \frac{g^-}{\sqrt{6}} & 0 & 0 & 0 & 0 & 0 & 0 & 0 & 0 \\
\hline
0 & 0 & \frac{-g_{34}^+}{2} & 0 & \frac{g_{12}^-}{2\sqrt{2}} & 0 & 0 & 0 & 0 & 0 & 0 & \frac{g_{12}^-}{2\sqrt{2}} & 0 & 0 & 0 & 0 \\
0 & 0 & 0 & \frac{-g_{12}^+}{2} & \frac{-g_{34}^-}{2\sqrt{2}} & 0 & 0 & 0 & 0 & 0 & 0 & \frac{g_{34}^-}{2\sqrt{2}} & 0 & 0 & 0 & 0 \\
0 & 0 & \frac{g_{12}^-}{2\sqrt{2}} & \frac{-g_{34}^-}{2\sqrt{2}} & \frac{-g^+}{4} & 0 & 0 & 0 & 0 & 0 & 0 & \frac{g^-}{4} & 0 & 0 & 0 & 0 \\
\hline
\frac{g_{34}^-}{2} & \frac{-g_{12}^-}{2\sqrt{3}} & 0 & 0 & 0 & 0 & 0 & 0 & 0 & 0 & 0 & 0 & \frac{g_{12}^-}{\sqrt{6}} & 0 & 0 & 0 \\
\frac{g_{12}^-}{2} & \frac{-g_{34}^-}{2\sqrt{3}} & 0 & 0 & 0 & 0 & 0 & 0 & 0 & 0 & 0 & 0 & \frac{g_{34}^-}{\sqrt{6}} & 0 & 0 & 0 \\
0 & \frac{g^-}{\sqrt{6}} & 0 & 0 & 0 & 0 & 0 & 0 & 0 & 0 & 0 & 0 & \frac{g^-}{2\sqrt{3}} & 0 & 0 & 0 \\
\hline
0 & 0 & 0 & 0 & 0 & 0 & 0 & 0 & \frac{g_{34}^+}{2} & 0 & \frac{g_{12}^-}{2\sqrt{2}} & 0 & 0 & \frac{g_{12}^-}{2\sqrt{2}} & 0 & 0 \\
0 & 0 & 0 & 0 & 0 & 0 & 0 & 0 & 0 & \frac{g_{12}^+}{2} & \frac{-g_{34}^-}{2\sqrt{2}} & 0 & 0 & \frac{g_{34}^-}{2\sqrt{2}} & 0 & 0 \\
0 & 0 & 0 & 0 & 0 & 0 & 0 & 0 & \frac{g_{12}^-}{2\sqrt{2}} & \frac{-g_{34}^-}{2\sqrt{2}} & \frac{g^+}{4} & 0 & 0 & \frac{-g^-}{4} & 0 & 0 \\
\hline
0 & 0 & \frac{g_{12}^-}{2\sqrt{2}} & \frac{g_{34}^-}{2\sqrt{2}} & \frac{g^-}{4} & 0 & 0 & 0 & 0 & 0 & 0 & \frac{-g^+}{4} & 0 & 0 & 0 & 0 \\
0 & 0 & 0 & 0 & 0 & \frac{g_{12}^-}{\sqrt{6}} & \frac{g_{34}^-}{\sqrt{6}} & \frac{g^-}{2\sqrt{3}} & 0 & 0 & 0 & 0 & 0 & 0 & 0 & 0 \\
0 & 0 & 0 & 0 & 0 & 0 & 0 & 0 & \frac{g_{12}^-}{2\sqrt{2}} & \frac{g_{34}^-}{2\sqrt{2}} & \frac{-g^-}{4} & 0 & 0 & \frac{g^+}{4} & 0 & 0 \\
0 & 0 & 0 & 0 & 0 & 0 & 0 & 0 & 0 & 0 & 0 & 0 & 0 & 0 & \frac{-g^+}{2} & 0 \\
0 & 0 & 0 & 0 & 0 & 0 & 0 & 0 & 0 & 0 & 0 & 0 & 0 & 0 & 0 & \frac{g^+}{2}
\end{array}\right), \tag{4.21}$$

where $g_{ij}^- = g_i - g_j$, $g^\pm = g_1 + g_2 \pm g_3 \pm g_4$. We observe that the Zeeman terms lead to leakage outside from the global singlet subspace $\{0_S, 1_S\}$ and from $m_S = -1$ triplet subspace $\{0_{T^-}, 1_{T^-}, 2_{T^-}\}$ which are relevant for our experiments. It can lead to discrepancies between experimental results and theoretical expectations derived only from the Heisenberg Hamiltonian. In our system, we have $0.15 < g_i < 0.3$. Therefore the magnitudes of the couplings induced by the Zeeman fields remain typically of the order of a

few MHz at 1 mT and thus are small compared to the exchange couplings J_{ij}. That is why we can neglect them in our theoretical description.

As a side note, we mention that this expression assumes that the spin quantization axis of all the quantum dots are the same. In practise, for an in-plane magnetic field, the spin quantization axis in the laboratory frame can be different for the different quantum dots due to the variations in the local electrostatic potentials. Yet, we can always redefine with a local spin basis ensuring that all quantization axis are aligned providing a renormalization of the spin-conserving and spin-non-conserving tunnel couplings.

SPIN-ORBIT TERMS

In absence of spin-orbit interaction, a double quantum dot system can be described by the following Hamiltonian [58]:

$$H_{\mathrm{DQD}} = \epsilon\,|S_{20}\rangle\langle S_{20}| + \sqrt{2}t_{\mathrm{c}}\,(|S_{20}\rangle\langle S_{11}| + |S_{11}\rangle\langle S_{20}|) + H_{\mathrm{Z}}. \tag{4.22}$$

In this expression, H_{Z} is the Zeeman term, ϵ the energy detuning (taken as zero at (0,2) - (1,1) charge transition), t_{c} the spin-conserving tunnel coupling whereas $|S_{20}\rangle$ and $|S_{11}\rangle$ are respectively the singlet (2,0) and (1,1) states.

To take into account the spin-orbit effects, one can allow for spin-non-conserving tunneling processes to occur [58]. This can be model by adding another term H_{SO} to the previous Hamiltonian. It writes as :

$$H_{\mathrm{SO}} = \mathrm{i}\sqrt{2}t_z\,|T^0\rangle\langle S_{20}| - \sum_{\pm}(t_y \pm \mathrm{i}t_x)\,|T^{\pm}\rangle\langle S_{20}| + \mathrm{h.c.}, \tag{4.23}$$

where $t_{\mathrm{SO}} = (t_x, t_y, t_z)$ is the spin-non-conserving tunneling term due to spin-orbit coupling and $|T^0\rangle$,$|T^-\rangle$ and $|T^+\rangle$ are the different triplet (1,1) states. The main effect of the spin-orbit interaction is thus to couple the singlet states to the triplet states. Similarly to the Zeeman gradients, the spin-orbit coupling leads to leakage outside the total singlet and $m_S = -1$ triplet subspaces.

In our experiments we operate in the regime $t_{\mathrm{c}} < 10$ GHz and $\epsilon \sim 300$ GHz, which allows us to treat the effect of the higher excited charge state $|S_{20}\rangle$ using the second order quasi-degenerate perturbation theory [59]. The resulting energy change of the state $|S_{11}\rangle$ due to the spin-conserving coupling to the $|S_{20}\rangle$ is $-\frac{2t_{\mathrm{c}}^2}{\epsilon}$. This change of energy corresponds to the exchange coupling J. Alternatively, the effective couplings between the $|S_{11}\rangle$ state and triplet states mediated by the virtual state $|S_{20}\rangle$ are $-\frac{2\mathrm{i}t_{\mathrm{c}}t_z}{\epsilon}$ for the coupling between the $|T^0\rangle$ and $|S_{11}\rangle$ states, and $-\frac{\sqrt{2}t_{\mathrm{c}}(t_y \pm \mathrm{i}t_x)}{\epsilon}$ for the coupling between the $|T^{\pm}\rangle$ and$|S_{11}\rangle$ states. Therefore, the relative amplitude of the spin-orbit couplings over the exchange couplings is given by $t_{\mathrm{SO}}/t_{\mathrm{c}}$. In ref. [44], a ratio $t_{\mathrm{SO}}/t_{\mathrm{c}}$ of 0.034 was found in germanium double quantum dots. Although the exact values of t_{SO} and t_{c} depend on the details of the electrostatics, we still expect the ratio $t_{\mathrm{SO}}/t_{\mathrm{c}}$ to remain small in our system and thus we also expect that the spin-orbit terms have a limited impact on the dynamics of the system. This is in agreement with the measured leakage features and Fermi-Hubbard model simulations presented in Supplementary Note 7 [40]. We observe that the probability of leakage fluctuates slower than the four-spin singlet-singlet oscillations or singlet-triplet oscillations, and the magnitude is in general below 0.2 if it is away

from the point $J_x \approx J_y$ (Supplementary Figure 9, Supplementary Figure 10 and Supplementary Figure 12 to Supplementary Figure 15 [40]).

DIAGONAL EXCHANGE COUPLINGS

We have also neglected the impact of diagonal exchange couplings J_{13} and J_{24} in our system. This assumption is based on different arguments. First, from the square geometry of our device, we expect that the spin-conserving tunnel couplings t_c between Q_1 and Q_3 and between Q_2 and Q_4 are much smaller than the couplings between adjacent quantum dots due the larger distance between quantum dots. Considering that for, a double quantum dot, the exchange coupling is given by $J = \sqrt{\epsilon^2/4 + 2t_c^2} - \epsilon/2 \simeq \frac{2t_c^2}{\epsilon}$ (limit $\frac{t_c}{\epsilon} \ll 1$), one can expect a significant reduction of the exchange couplings along the diagonals. Further, for four-spin experiments, the operation point O is chosen far from the center of the (1,1,1,1) charge region, as shown in Supplementary Figure 3 [40]. It ensures that the double well potentials of Q_1Q_2, Q_2Q_3, Q_3Q_4 and Q_4Q_1 pairs are all asymmetric and it allows to induce a finite exchange couplings between spins in adjacent quantum dots. At this point, the quantum dots' energy levels corresponding to different charge configurations are positioned with respect to each other as depicted in Fig. 4.12. In this configuration, it is likely that $\epsilon_{13}, \epsilon_{24} > \epsilon_{12}, \epsilon_{23}, \epsilon_{34}, \epsilon_{41}$ suggesting again that the diagonal exchange couplings are reduced compared to the vertical and horizontal ones.

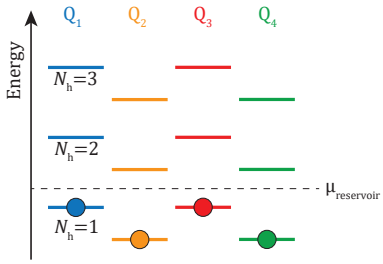

Figure 4.12: **Sketch of the quantum dot energy levels at the operation point O.** The chemical potentials of the quantum dots are tuned by controlling the plunger gate voltages to ensure charge occupations N_h of one hole per quantum dot while keeping a sufficiently large asymmetry of the double well potentials for adjacent quantum dots. The asymmetries of the potentials for Q_2Q_4 and Q_1Q_3 are comparatively smaller.

To get more understanding of the effects of diagonal exchange couplings on the measurements, we can compare theoretical predictions with and without diagonal exchange couplings.

Adding the diagonal exchange couplings, the Heisenberg Hamiltonian becomes:

$$H_J^* = \sum_{<i,j>} J_{ij}(\vec{S}_i \cdot \vec{S}_j - \frac{1}{4}) + J_{13}(\vec{S}_1 \cdot \vec{S}_3 - \frac{1}{4}) + J_{24}(\vec{S}_2 \cdot \vec{S}_4 - \frac{1}{4}), \tag{4.24}$$

and in the singlet subspace, with the $\{|0\rangle, |1\rangle\} = \{|S_{12}S_{34}\rangle, \frac{1}{\sqrt{3}}(|T_{12}^+ T_{34}^-\rangle + |T_{12}^- T_{34}^+\rangle - |T_{12}^0 T_{34}^0\rangle)\}$ basis, it can be written as:

$$H_S^* = \begin{pmatrix} -J_x - \frac{J_y+J_D}{4} & \frac{\sqrt{3}}{4}(J_y - J_D) \\ \frac{\sqrt{3}}{4}(J_y - J_D) & -\frac{3}{4}(J_y + J_D) \end{pmatrix}, \tag{4.25}$$

where $J_D = J_{13} + J_{24}$.

When $J_x = J_y = J$, the Hamiltonian becomes:

$$H_S^* = \begin{pmatrix} -\frac{5}{4}J - \frac{1}{4}J_D & \frac{\sqrt{3}}{4}(J - J_D) \\ \frac{\sqrt{3}}{4}(J - J_D) & -\frac{3}{4}(J + J_D) \end{pmatrix}. \tag{4.26}$$

This Hamiltonian can be diagonalized easily and the eigen energies are $E_1 = -\frac{3}{2}J$ and $E_2 = -\frac{1}{2}J - J_D$ (see also ref. [60, 61], note that there is a difference in the conventions for the overall energy offset). The associated eigenvectors are actually still the s-wave RVB state $|s\rangle = \frac{1}{\sqrt{3}}(|S_x\rangle - |S_y\rangle)$ and the d-wave RVB state $|d\rangle = |S_x\rangle + |S_y\rangle$ independently of the values of J and J_D (providing $J_D \neq J$). $|s\rangle$ is the ground state for $J > J_D$ which corresponds the regime investigated in our experiments according to the data displayed in Fig. 4.5.a-c. On the other hand, $|d\rangle$ is the ground state for $J < J_D$. In both cases, we expect to see resonating valence bond oscillations having a frequency given by $f_{SS}^* = \frac{1}{h}|E_1 - E_2| = \frac{1}{h}|J - J_D|$. More generally, f_{SS}^* is given by:

$$f_{SS}^* = \sqrt{J_x^2 + J_y^2 - J_x J_y + J_D^2 - J_D(J_x + J_y)} = \sqrt{(J_x - J_D)^2 + (J_y - J_D)^2 - (J_x - J_D)(J_y - J_D)}. \tag{4.27}$$

Therefore, in the limit where $J_{x,y} > J_D$, the presence of diagonal exchange leads to an effective reduction of the exchange couplings that drives the oscillations between singlet product states.

In the $m_S = -1$ global triplet subspace spanned by $\{|S_{12}T_{34}^-\rangle, |T_{12}^- S_{34}\rangle, \frac{1}{\sqrt{2}}(|T_{12}^0 T_{34}^-\rangle - |T_{12}^- T_{34}^0\rangle)\}$, the Hamiltonian can be written as:

$$\begin{aligned} H_T &= \begin{pmatrix} -J_{12} - \frac{J_{23}+J_{14}+J_{13}+J_{24}}{4} & \frac{-J_{23}-J_{14}+J_{13}+J_{24}}{4} & \frac{J_{23}-J_{14}-J_{13}+J_{24}}{2\sqrt{2}} \\ \frac{-J_{34}-J_{14}+J_{13}+J_{24}}{4} & -J_{34} - \frac{J_{23}+J_{14}+J_{13}+J_{24}}{4} & \frac{J_{23}-J_{14}-J_{13}+J_{24}}{2\sqrt{2}} \\ \frac{J_{23}-J_{14}-J_{13}+J_{24}}{2\sqrt{2}} & \frac{J_{23}-J_{14}-J_{13}+J_{24}}{2\sqrt{2}} & -\frac{J_{23}+J_{14}+J_{13}+J_{24}}{2} \end{pmatrix} \\ &= \begin{pmatrix} -\frac{J_x+\delta_x}{2} - \frac{J_y+J_D}{4} & -\frac{J_y-J_D}{4} & \frac{\delta_y+\delta_D}{2\sqrt{2}} \\ -\frac{J_y-J_D}{4} & -\frac{J_x-\delta_x}{2} - \frac{J_y+J_D}{4} & \frac{\delta_y+\delta_D}{2\sqrt{2}} \\ \frac{\delta_y+\delta_D}{2\sqrt{2}} & \frac{\delta_y+\delta_D}{2\sqrt{2}} & -\frac{J_y+J_D}{2} \end{pmatrix}, \end{aligned} \tag{4.28}$$

where $\delta_D = -J_{13} + J_{24}$.

Repeating the calculation of four-spin singlet-triplet oscillations in Section 4.8, we derive that for the initial state $|S_{12}T_{34}^-\rangle$, the minimum singlet-triplet oscillation frequency occurs when $\delta_x = \delta_y + \delta_D = 0$. Similarly, for the initial state $|S_{14}T_{23}^-\rangle$, the minimum frequency occurs when $\delta_x + \delta_D = \delta_y = 0$. The corresponding minimum oscillation frequencies are $f_{ST,\min}^{x(y)} = \frac{1}{2}(J_{y(x)} - J_D)$. Thus diagonal exchange may be one of the contributions to the small shift of frequency minimum $\delta V_{x,\min} - \delta V_{y,\min}$ observed in the experiments

shown in Fig. 4.8 to 4.10. We notice that the voltage shift between x and y direction readout $|\delta V_{x,\min} - \delta V_{y,\min}| < 2$ mV are small. Therefore we can assume that the measured frequency of four-spin singlet-triplet oscillations at every voltage shift $\delta V_x'$ in Fig. 4.3.e-f is approximately equal to the corresponding frequency minimum, $f_{ST}^{x(y)} \simeq f_{ST,\min}^{x(y)} = \frac{1}{2h}(J_{y(x)} - J_D)$, with an estimated frequency uncertainty described in Section 4.8. The singlet-singlet oscillation frequency derived from the Hamiltonian (4.25) can then be expressed as $f_{SS}^* = 2\sqrt{(f_{ST,\min}^y)^2 + (f_{ST,\min}^x)^2 - f_{ST,\min}^y f_{ST,\min}^x}$. Therefore, the method used to equalize parallel exchange couplings and tune them does not allow us to determine the magnitude of the diagonal exchange couplings.

To summarize, we expect that diagonal exchange couplings to have a very limited effects in the four-spin oscillation experiments but our measurements do not allow to estimated their values.

BIBLIOGRAPHY

[1] R. P. Feynman. “Simulating physics with computers”. In: *International Journal of Theoretical Physics* 21 (6-7 June 1982), pp. 467–488. ISSN: 0020-7748.

[2] S. Lloyd. “Universal Quantum Simulators”. In: *Science* 273 (1996), pp. 1073–1078.

[3] D. S. Abrams and S. Lloyd. “Simulation of Many-Body Fermi Systems on a Universal Quantum Computer”. In: *Phys. Rev. Lett.* 79 (13 1997), pp. 2586–2589.

[4] A. Aspuru-Guzik, A. D. Dutoi, P. J. Love, and M. Head-Gordon. “Simulated Quantum Computation of Molecular Energies”. In: *Science* 309.5741 (2005), pp. 1704–1707.

[5] D. Loss and D. P. DiVincenzo. “Quantum computation with quantum dots”. In: *Phys. Rev. A* 57 (1 1998), pp. 120–126.

[6] L. M. K. Vandersypen, H. Bluhm, J. S. Clarke, A. S. Dzurak, R. Ishihara, A. Morello, D. J. Reilly, L. R. Schreiber, and M. Veldhorst. “Interfacing spin qubits in quantum dots and donors—hot, dense, and coherent”. In: *npj Quantum Inf.* 3 (2017), p. 34.

[7] E. Manousakis. “A Quantum-Dot Array as Model for Copper-Oxide Superconductors: A Dedicated Quantum Simulator for the Many-Fermion Problem”. In: *J. Low Temp. Phys.* 126 (2002), pp. 1501–1513.

[8] A. Y. Smirnov, S. Savel’ev, L. G. Mourokh, and F. Nori. “Modelling chemical reactions using semiconductor quantum dots”. In: *EPL* 80 (2007), p. 67008.

[9] T. Byrnes, N. Y. Kim, K. Kusudo, and Y. Yamamoto. “Quantum simulation of Fermi-Hubbard models in semiconductor quantum-dot arrays”. In: *Phys. Rev. B* 78 (7 2008), p. 075320.

[10] P. Barthelemy and L. M. K. Vandersypen. “Quantum Dot Systems: a versatile platform for quantum simulations”. In: *Annalen der Physik* 525 (2013), pp. 808–826.

[11] J. Gray, A. Bayat, R. K. Puddy, C. G. Smith, and S. Bose. “Unravelling quantum dot array simulators via singlet-triplet measurements”. In: *Phys. Rev. B* 94 (19 2016), p. 195136.

[12] A. Hamo, A. Benyamini, I. Shapir, I. Khivrich, J. Waissman, K. Kaasbjerg, Y. Oreg, F. von Oppen, and S. Ilani. “Electron attraction mediated by Coulomb repulsion”. In: *Nature* 535 (7612 July 2016), pp. 395–400. ISSN: 0028-0836.

[13] T. Hensgens, T. Fujita, L. Janssen, X. Li, C. J. van Diepen, C. Reichl, W. Wegscheider, S. Das Sarma, and L. M. K. Vandersypen. “Quantum simulation of a Fermi-Hubbard model using a semiconductor quantum dot array”. In: *Nature* 548 (2017), pp. 70–73.

[14] M. Kiczynski, S. K. Gorman, H. Geng, M. B. Donnelly, Y. Chung, Y. He, J. G. Keizer, and M. Y. Simmons. “Engineering topological states in atom-based semiconductor quantum dots”. In: *Nature* 606 (2022), pp. 694–699.

[15] J. P. Dehollain, U. Mukhopadhyay, V. P. Michal, Y. Wang, B. Wunsch, C. Reichl, W. Wegscheider, M. S. Rudner, E. Demler, and L. M. K. Vandersypen. “Nagaoka ferromagnetism observed in a quantum dot plaquette”. In: *Nature* 579 (2020), pp. 528–533.

[16] H. Qiao, Y. P. Kandel, K. Deng, S. Fallahi, G. C. Gardner, M. J. Manfra, E. Barnes, and J. M. Nichol. “Coherent Multispin Exchange Coupling in a Quantum-Dot Spin Chain”. In: *Phys. Rev. X* 10 (3 2020), p. 031006.

[17] C. J. van Diepen, T.-K. Hsiao, U. Mukhopadhyay, C. Reichl, W. Wegscheider, and L. M. K. Vandersypen. “Quantum Simulation of Antiferromagnetic Heisenberg Chain with Gate-Defined Quantum Dots”. In: *Phys. Rev. X* 11 (4 2021), p. 041025.

[18] F. A. Zwanenburg, A. S. Dzurak, A. Morello, M. Y. Simmons, L. C. L. Hollenberg, G. Klimeck, S. Rogge, S. N. Coppersmith, and M. A. Eriksson. “Silicon quantum electronics”. In: *Rev. Mod. Phys.* 85 (3 2013), pp. 961–1019.

[19] G. Scappucci, C. Kloeffel, F. A. Zwanenburg, D. Loss, M. Myronov, J.-J. Zhang, S. De Franceschi, G. Katsaros, and M. Veldhorst. “The germanium quantum information route”. In: *Nature Reviews Materials* 6 (2021), pp. 926–943.

[20] A. J. Sigillito, R. M. Jock, A. M. Tyryshkin, J. W. Beeman, E. E. Haller, K. M. Itoh, and S. A. Lyon. “Electron Spin Coherence of Shallow Donors in Natural and Isotopically Enriched Germanium”. In: *Phys. Rev. Lett.* 115 (24 2015), p. 247601.

[21] A. Sammak, D. Sabbagh, N. W. Hendrickx, M. Lodari, B. P. Wuetz, A. Tosato, L. Yeoh, M. Bollani, M. Virgilio, M. A. Schubert, P. Zaumseil, G. Capellini, M. Veldhorst, and G. Scappucci. “Shallow and Undoped Germanium Quantum Wells: A Playground for Spin and Hybrid Quantum Technology”. In: *Advanced Functional Materials* 29 (14 Apr. 2019), p. 1807613. ISSN: 1616-301X.

[22] M. Lodari, A. Tosato, D. Sabbagh, M. A. Schubert, G. Capellini, A. Sammak, M. Veldhorst, and G. Scappucci. “Light effective hole mass in undoped Ge/SiGe quantum wells”. In: *Physical Review B* 100 (4 July 2019). ISSN: 24699969.

[23] N. W. Hendrickx, D. P. Franke, A. Sammak, M. Kouwenhoven, D. Sabbagh, L. Yeoh, R. Li, M. L. V. Tagliaferri, M. Virgilio, G. Capellini, G. Scappucci, and M. Veldhorst. “Gate-controlled quantum dots and superconductivity in planar germanium”. In: *Nat. Commun.* 9 (2018), p. 2835.

[24] H. Watzinger, J. Kukucka, L. Vukusic, F. Gao, T. Wang, F. Schäffler, J.-J. Zhang, and G. Katsaros. “A germanium hole spin qubit”. In: *Nat. Commun.* 9 (2018), p. 3902.

[25] N. W. Hendrickx, W. I. L. Lawrie, L. Petit, A. Sammak, G. Scappucci, and M. Veldhorst. “A single-hole spin qubit”. In: *Nat. Commun.* 11 (2020), p. 3478.

[26] M. Lodari, N. W. Hendrickx, W. I. L. Lawrie, T.-K. Hsiao, L. Vandersypen, A. Sammak, M. Veldhorst, and G. Scappucci. “Low percolation density and charge noise with holes in germanium”. In: *Mater. Quantum. Technol.* 1 (2021), p. 011002.

[27] D. Jirovec, A. Hofmann, A. Ballabio, P. M. Mutter, G. Tavani, M. Botifoll, A. Crippa, J. Kukucka, O. Sagi, F. Martins, J. Saez-Mollejo, I. Prieto, M. Borovkov, J. Arbiol, D. Chrastina, G. Isella, and G. Katsaros. "A singlet-triplet hole spin qubit in planar Ge". In: *Nature Materials* 20 (2021), pp. 1106–1112.

[28] N. W. Hendrickx, D. P. Franke, A. Sammak, G. Scappucci, and M. Veldhorst. "Fast two-qubit logic with holes in germanium". In: *Nature* 577 (2020), pp. 487–491.

[29] N. W. Hendrickx, W. I. L. Lawrie, M. Russ, F. van Riggelen, S. L. de Snoo, R. N. Schouten, A. Sammak, G. Scappucci, and M. Veldhorst. "A four-qubit germanium quantum processor". In: *Nature* 591 (7851 Mar. 2021), pp. 580–585. ISSN: 0028-0836.

[30] L. Pauling. "The nature of chemical bonds. Application of results obtained from quantum mechanics and from a theory of paramagnetic susceptibility to the structures of molecules". In: *J. Am. Chem. Soc.* 53 (4 1931), pp. 1367–1400.

[31] P. W. Anderson. "The Resonating Valence Bond State in La_2CuO_4 and Superconductivity". In: *Science* 235 (1987), pp. 1196–1198.

[32] S. A. Kivelson, D. S. Rokhsar, and J. P. Sethna. "Topology of the resonating valence-bond state: Solitons and high-T_c superconductivity". In: *Phys. Rev. B* 35 (16 1987), pp. 8865–8868.

[33] H. T. Diep. "Frustrated Spin Systems, 2nd Edition". In: *World Scientific Publishing* (2013).

[34] Y. Zhou, K. Kanoda, and T.-K. Ng. "Quantum spin liquid states". In: *Rev. Mod. Phys.* 89 (2 2017), p. 025003.

[35] S. Trebst, U. Schollwöck, M. Troyer, and P. Zoller. "d-Wave Resonating Valence Bond States of Fermionic Atoms in Optical Lattices". In: *Phys. Rev. Lett.* 96 (25 2006), p. 250402.

[36] S. Nascimbène, Y.-A. Chen, M. Atala, M. Aidelsburger, S. Trotzky, B. Paredes, and I. Bloch. "Experimental Realization of Plaquette Resonating Valence-Bond States with Ultracold Atoms in Optical Superlattices". In: *Phys. Rev. Lett.* 108 (20 2012), p. 205301.

[37] X.-S. Ma, B. Dakic, W. Naylor, A. Zeilinger, and W. Walther. "Quantum simulation of the wavefunction to probe frustrated Heisenberg spin systems". In: *Nature Physics* 7 (2011), pp. 399–405.

[38] K. Yang, S.-H. Phark, Y. Bae, T. Esat, P. Willke, A. Ardavan, A. J. Heinrich, and C. P. Lutz. "Probing resonating valence bond states in artificial quantum magnets". In: *Nat. Commun.* 12 (2021), p. 993.

[39] F. van Riggelen, N. W. Hendrickx, W. I. L. Lawrie, M. Russ, A. Sammak, G. Scappucci, and M. Veldhorst. "A two-dimensional array of single-hole quantum dots". In: *Appl. Phys. Lett.* 118.4 (2021), p. 044002.

[40] "See Supplementary Information of npj Quantum Information 9, 58 (2023)." In: ().

[41] J. R. Petta, A. C. Johnson, J. M. Taylor, E. A. Laird, A. Yacoby, M. D. Lukin, C. M. Marcus, M. P. Hanson, and A. C. Gossard. "Coherent Manipulation of Coupled Electron Spins in Semiconductor Quantum Dots". In: *Science* 309 (2005), pp. 2180–2184.

[42] J. R. Petta, H. Lu, and A. C. Gossard. “A Coherent Beam Splitter for Electronic Spin States”. In: *Science* 327 (2010), pp. 669–672.

[43] X. Wu, D. R. Ward, J. R. Prance, D. Kim, J. K. Gamble, R. T. Mohr, Z. Shi, D. E. Savage, M. G. Lagally, M. Friesen, S. N. Coppersmith, and M. A. Eriksson. “Two-axis control of a singlet-triplet qubit with an integrated micromagnet”. In: *PNAS* 111.33 (2014), pp. 11938–11942.

[44] D. Jirovec, P. M. Mutter, A. Hofmann, A. Crippa, M. Rychetsky, D. L. Craig, J. Kukucka, F. Martins, A. Ballabio, N. Ares, D. Chrastina, G. Isella, G. Burkard, and G. Katsaros. “Dynamics of hole Singlet-Triplet qubits with large g-factor differences”. In: *Phys. Rev. Lett.* 128 (2022), p. 126803.

[45] K. Ono, D. G. Austing, Y. Tokura, and S. Tarucha. “Current Rectification by Pauli Exclusion in a Weakly Coupled Double Quantum Dot System”. In: *Science* 297 (2002), pp. 1313–1317.

[46] S. A. Studenikin, J. Thorgrimson, G. C. Aers, A. Kam, P. Zawadzki, Z. R. Wasilewski, A. Bogan, and A. S. Sachrajda. “Enhanced charge detection of spin qubit readout via an intermediate state”. In: *Appl. Phys. Lett.* 101.23 (2012), p. 233101.

[47] P. Harvey-Collard, B. D’Anjou, M. Rudolph, N. T. Jacobson, J. Dominguez, G. A. Ten Eyck, J. R. Wendt, T. Pluym, M. P. Lilly, W. A. Coish, M. Pioro-Ladrière, and M. S. Carroll. “High-Fidelity Single-Shot Readout for a Spin Qubit via an Enhanced Latching Mechanism”. In: *Phys. Rev. X* 8 (2 2018), p. 021046.

[48] M. D. Shulman, O. E. Dial, S. P. Harvey, H. Bluhm, V. Umansky, and A. Yacoby. “Demonstration of Entanglement of Electrostatically Coupled Singlet-Triplet Qubits”. In: *Science* 336 (2012), pp. 202–205.

[49] N. Piot, B. Brun, V. Schmitt, S. Zihlmann, V. P. Michal, A. Apra, J. C. Abadillo-Uriel, X. Jehl, B. Bertrand, H. Niebojewski, L. Hutin, M. Vinet, M. Urdampilleta, T. Meunier, Y.-M. Niquet, R. Maurand, and S. De Franceschi. “A single hole spin with enhanced coherence in natural silicon”. In: *Nat. Nanotechnol.* 17 (2022), pp. 1072–1077.

[50] J. Levy. “Universal Quantum Computation with Spin-1/2 Pairs and Heisenberg Exchange”. In: *Phys. Rev. Lett.* 89 (2002), p. 147902.

[51] R. Li, X. Hu, and J. Q. You. “Controllable exchange coupling between two singlet-triplet qubits”. In: *Phys. Rev. B* 86 (2012), p. 205306.

[52] J. Klinovaja, D. Stepanenko, B. I. Halperin, and D. Loss. “Exchange-based CNOT gates for singlet-triplet qubits with spin-orbit interaction”. In: *Phys. Rev. B* 86 (2012), p. 085423.

[53] M. P. Wardrop and A. C. Doherty. “Exchange-based two-qubit gate for singlet-triplet qubits”. In: *Phys. Rev. B* 90 (2014), p. 045418.

[54] D. A. Lidar, I. L. Chuang, and K. B. Whaley. “Decoherence-Free Subspaces for Quantum Computation”. In: *Phys. Rev. Lett.* 81 (1998), pp. 2594–2597.

[55] J. Danon and Y. V. Nazarov. “Pauli spin blockade in the presence of strong spin-orbit coupling”. In: *Phys. Rev. B* 80 (4 2009), p. 041301.

[56] J. Fischer, W. A. Coish, D. V. Bulaev, and D. Loss. “Spin decoherence of a heavy hole coupled to nuclear spins in a quantum dot”. In: *Phys. Rev. B* 78 (2008), p. 155329.

[57] C. Testelin, F. Bernardot, B. Eble, and M. Chamarro. “Hole–spin dephasing time associated with hyperfine interaction in quantum dots”. In: *Phys. Rev. B* 79 (2009), p. 195440.

[58] P. M. Mutter and G. Burkard. “All-electrical control of hole singlet-triplet spin qubits at low-leakage points”. In: *Phys. Rev. B* 104 (19 2021), p. 195421.

[59] R. G. Winkler. “Spin-orbit Coupling Effects in Two-Dimensional Electron and Hole Systems”. In: *Springer* (2003).

[60] R. R. P. Singh, Z. Weihong, C. J. Hamer, and J. Oitmaa. “Dimer order with striped correlations in the $J_1 - J_2$ Heisenberg model”. In: *Phys. Rev. B* 60 (1999), pp. 7278–7283.

[61] R. L. Doretto. “Plaquette valence-bond solid in the square-lattice J_1-J_2 antiferromagnet Heisenberg model: A bond operator approach”. In: *Phys. Rev. B* 89 (10 2014), p. 104415.

5

OPERATING SEMICONDUCTOR QUANTUM PROCESSORS WITH HOPPING SPINS

Qubits that can be efficiently controlled are essential for the development of scalable quantum hardware. Although resonant control is used to execute high-fidelity quantum gates, the scalability is challenged by the integration of high-frequency oscillating signals, qubit crosstalk and heating. Here, we show that by engineering the hopping of spins between quantum dots with a site-dependent spin quantization axis, quantum control can be established with discrete signals. We demonstrate hopping-based quantum logic and obtain single-qubit gate fidelities of 99.97%, coherent shuttling fidelities of 99.992% per hop, and a two-qubit gate fidelity of 99.3%, corresponding to error rates that have been predicted to allow for quantum error correction. We also show that hopping spins constitute a tuning method by statistically mapping the coherence of a 10-quantum dot system. Our results show that dense quantum dot arrays with sparse occupation could be developed for efficient and high-connectivity qubit registers.

Parts of this chapter have been published in C.-A. Wang, V. John, H. Tidjani, C.X. Yu, A.S. Ivlev, C. Déprez, F. van Riggelen-Doelman, B.D. Woods, N.W. Hendrickx, W.I.L. Lawrie, L.E.A. Stehouwer, S.D. Oosterhout, A. Sammak, M. Friesen, G. Scappucci, S.L. de Snoo, M. Rimbach-Russ, F. Borsoi, M. Veldhorst, Operating semiconductor quantum processors with hopping spins, *Science* **385**, 447-452 (2024).

5.1. INTRODUCTION

Loss and DiVincenzo proposed hopping of electrons between two quantum dots as an efficient method for coherent spin control [1]. By applying discrete pulses to the quantum dot gates, a single spin can be transferred between qubit sites with differently oriented spin quantization axes, thereby enabling two-axis control of the qubit. Universal quantum logic is then achieved through a tunable exchange interaction between spins residing in different quantum dots. That work initiated the field of semiconductor spin qubits and inspired more than two decades of extensive research, but a successful implementation of Loss and DiVincenzo's initial proposal has remained elusive because of experimental challenges [2].

Alternative methods for coherent single-spin control have emerged, including electron spin resonance [3, 4] and electric dipole spin resonance using either micromagnets [5, 6] or spin-orbit interaction [7, 8, 9, 10] to enable a coupling between the electric field and the spin degree of freedom. However, all of these methods rely on resonant Rabi driving and require high-power, high-frequency analog control signals that already limit qubit performance in small quantum processors [11, 12, 13]. The development of local, efficient, low-power control mechanisms of semiconductor spins is now a key driver [14, 15, 16]. To this end, qubits encoded in multiple spins and in multiple quantum dots, such as singlet-triplet, hybrid, and exchange-only qubits, have been investigated as possible platforms [2]. Although these qubit encodings have enabled digital single-qubit control, they also come with new challenges in coherence, control, and creation of quantum links. For example, the exchange-only qubits are susceptible to leakage outside of their computational subspace and require four exchange pulses to execute an arbitrary single-qubit gate and ≥ 12 exchange pulses for a single two-qubit gate [17, 18, 19].

Here, we demonstrate that single-spin qubits can be operated using baseband control signals, as envisaged in the original proposal for quantum computation with quantum dots [1]. We used hole spins in germanium quantum dots, in which the strong spin-orbit interaction gives rise to an anisotropic g-tensor that is strongly dependent on the electrostatic and strain environment [20]. We harnessed the resulting differences in the spin quantization axis between quantum dots [21, 22] to achieve high-fidelity single-qubit control using discrete pulses by shuttling the spin between quantum dot sites. A key advantage in such a hopping-based operation is that the spin rotation frequency is given by the Larmor precession. The latter remains sizeable even at small magnetic fields where quantum coherence is substantially improved [23, 24]. This enabled us to perform universal quantum control with error rates exceeding the thresholds predicted for practical quantum error correction[25] while also operating with low-frequency baseband signals. We then exploited the differences in quantization axes to map the spin dephasing times and g-factor distributions of an extended 10-quantum dot array, thereby efficiently gathering statistics on relevant metrics in large spin qubit systems.

5.2. HIGH-FIDELITY SINGLE-QUBIT OPERATIONS AND LONG QUBIT COHERENCE TIMES AT LOW MAGNETIC FIELD

A large difference in the orientation of the spin quantization axes between quantum dots is essential for hopping-based qubit operations. Holes in planar germanium heterostructures manifest a pronounced anisotropic g-tensor, with an out-of-plane g-factor $g_\perp$ that can be two orders of magnitude larger than the in-plane component, $g_\parallel$ [20, 26, 27, 24]. Consequently, a small tilt of the applied magnetic field from the in-plane g-tensor will lead to a strong reorientation of the spin quantization axis in the out-of-plane direction. Subsequently, when an in-plane magnetic field is applied, the orientation of the spin quantization axis is highly sensitive to the local g-tensor, and thus to confinement, strain, and electric fields, thus becoming a site-dependent property [24, 28, 21, 29]. Here, we exploited this aspect to establish hopping-based quantum operations in two different devices: a four-quantum dot array [30] arranged in a 2×2 configuration and a 10-quantum dot system arranged in a 3-4-3 configuration.

We populated the four-quantum dot array with quantum dots Dm with $m \in [[1, 4]]$ with two hole spins Q_A and Q_B which can be shuttled between quantum dots by electrical pulses on the gate electrodes (Fig. 5.1A). A magnetic field up to 40 mT was applied to split the spin states and positioned in-plane up to sample-alignment accuracy (see Section 5.5). The relatively small magnetic fields ensured that the maximum qubit frequency (140 MHz) and its corresponding precession period (7 ns) were within the bandwidth of the arbitrary waveform generators used. In combination with engineered voltage pulses with sub-nanosecond resolution [21] (Section 5.13), we were able to shuttle a spin qubit to an empty quantum dot and thereby accurately change the qubit precession direction several times within one precession period. Altogether, this enables efficient single-qubit control through discrete voltage pulses (Fig. 5.1B).

The net effect of a multiple-shuttle protocol is a rotation $R(\hat{n},\theta)$ of the spin state around an axis $\hat{n}$ and with an angle θ. To implement a specific rotation such as the quantum gate $X_{\pi/2}$, the number of required shuttling steps depends on the angle between the two quantization axes. Because of the large angle between the axes of D1 and D4, $\theta_{14} > 90°/4 = 22.5°$, a pulse consisting of four shuttling steps is sufficient to realize a precise quantum gate $X_{\pi/2,A}$ (Section 5.8 and the supplementary materials [31], Section 3). As outlined on the top right panel of Fig. 5.1C, such a four-shuttle pulse moves the spin between D1 and D4 four times with waiting periods t_1 and t_4, respectively. By measuring the spin-flip probability of Q_A, $P_{A\uparrow}$, after two consecutive rotations $R(\hat{n},\theta)^2$, we could determine the values of t_1 and t_4 where $P_{A\uparrow}$ is maximal, which occurs when $R(\hat{n},\theta) = X_{\pi/2,A}$.

Although this method allows calibration of the pulse timing to compose an $X_{\pi/2,A}$ gate, it is not necessarily the optimal trajectory. Different choices of (t_1, t_4) are possible (Fig. 5.1C), including a composition of four-shuttle pulses with different waiting times in D4. The latter implementation allows for the construction of gates with a rotation angle θ less sensitive to Larmor frequency fluctuations in D4. We constructed such a gate by fitting the data in Fig. 5.1C to an effective model and determined the quantization axes angle θ_{14} between the quantum dots D1 and D4, the individual Larmor frequencies, and the effective precession time during the ramp. Through simulation of the qubit dynam-

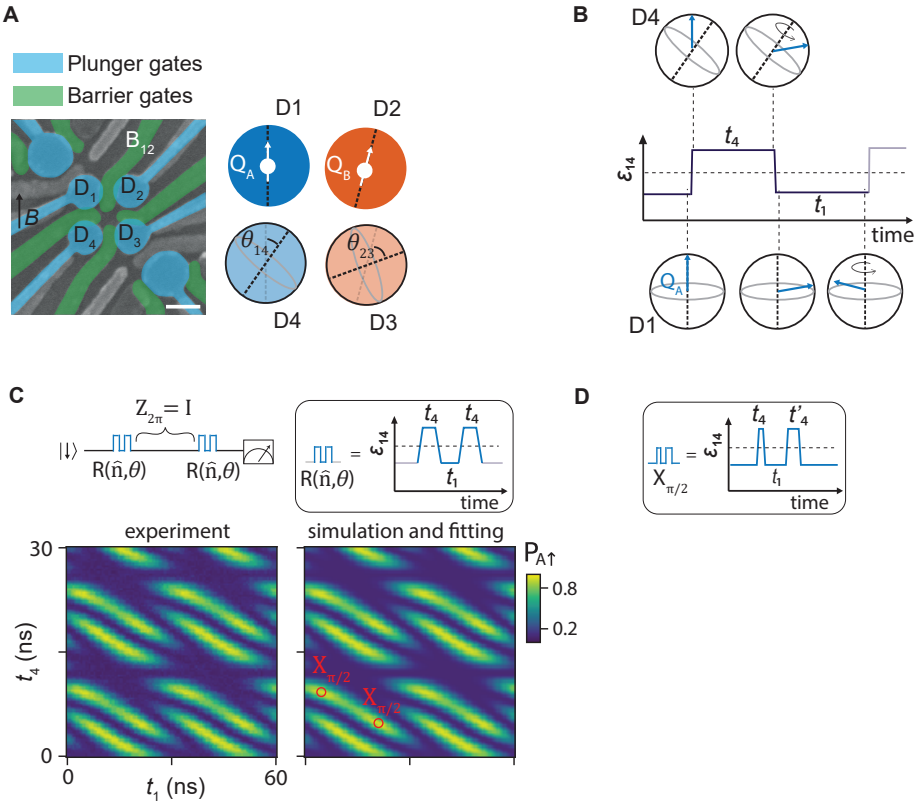

Figure 5.1: **Hopping-based single-qubit operations - schematics and tune-up.** **(A)** Left: scanning electron microscopy image of the 2×2 quantum dot array device [30], including gate-defined charge sensors at two corners. Scale bar, 100 nm. Right: schematic of the two spin qubits, Q_A and Q_B. The black dashed lines mark the relative quantization axis direction in the quantum dot pair D1-D4 (D2-D3), with the angle θ_{14} (θ_{23}). **(B)** Example of a baseband pulse $\epsilon_{14}(t)$ used to manipulate qubit Q_A, by shuttling the spin back and forth between quantum dots D1 and D4 and allowing the spin to precess in the individual quantum dots for the time t_4 and t_1. **(C)** Tune-up procedure of a four-shuttle pulse for the $X_{\pi/2}$ gate of Q_A at 20 mT. Top: pulse sequence of the experiment. Bottom left: measured spin-up probability $P_{A\uparrow}(t_1, t_4)$. Bottom right: simulation results. The red markers identify the timings for implementing an $X_{\pi/2,A}$ gate and corresponds to the maximal spin-up probability. The markers are periodic in t_1 and t_4, but for clarity we only plot a few of them. **(D)** Calibrated pulse for $X_{\pi/2,A}$ gate with unequal wait time t_4 and t_4'.

ics, we designed a more noise-resilient $X_{\pi/2,A}$ gate based on four shuttling steps with unequal wait times t_4 and t_4' in D4 (Fig. 5.1D). Following the same approach, we design an $X_{\pi/2,B}$ gate for Q_B that only requires a two-shuttle protocol because the angle of the difference in quantization axes of D2 and D3, θ_{23}, is very close to 45° (supplementary materials [31], Section 3).

We further calibrated the pulse timing using repetition sequences, as shown in Fig. 5.2C, and in AllXY sequences [32] (see the supplementary materials [31], Section 3). The $Y_{\pi/2}$

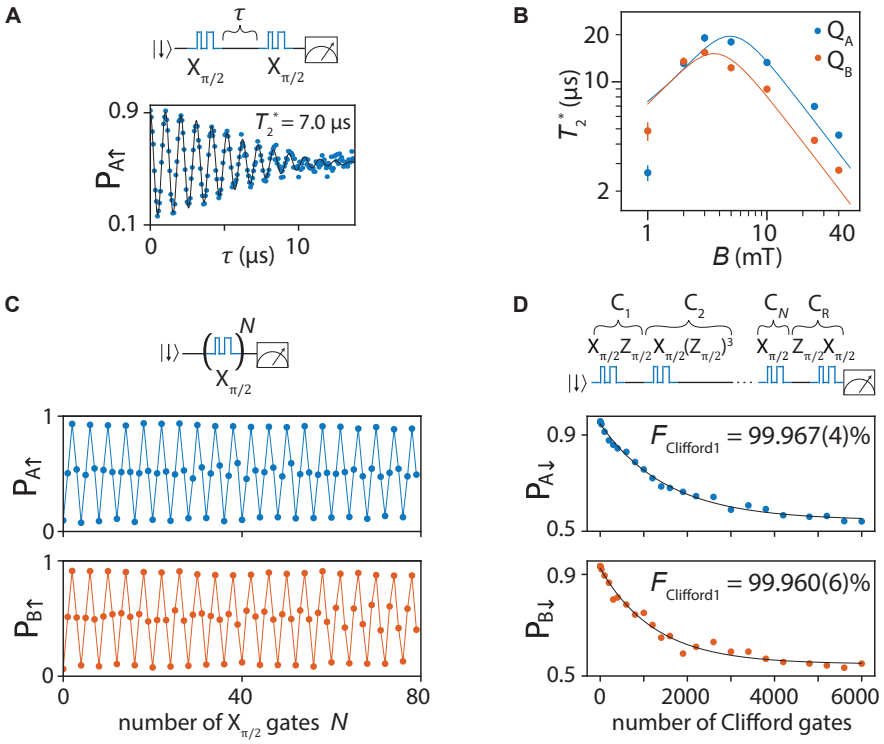

Figure 5.2: **Hopping-based single-qubit operations - gate fidelity and coherence times at low magnetic field.** **(A)** Free induction decay obtained from Ramsey experiments at 25 mT. **(B)** T_2^* as a function of magnetic field. The data points are fitted with an effective model including electric noise and nuclear noise (Section 5.13). **(C)** Spin-up probability after applying a varying number of $X_{\pi/2}$ gates on each qubit. **(D)** Example of a pulse sequence in Q_A single-qubit randomized benchmarking and the measurement results of both qubits. The uncertainties are obtained from bootstrapping with 95% confidence intervals.

gate in the AllXY sequences was realized by $Y_{\pi/2} = Z_{\pi/2}X_{\pi/2}Z_{3\pi/2}$ and the $Z_{\pi/2}$ gate was implemented by idling the qubit for the time defined by its precession in the lab frame. The calibrated $X_{\pi/2}$ gates had a total gate time of 98 (35) ns for $Q_A(Q_B)$, corresponding to effective qubit rotation frequencies of 2.6 (7.1) MHz, considerable compared with the Larmor frequencies $f_{A(B)} = 42.6$ (89.5) MHz at the in-plane magnetic field of 25m̃T.

The high ratio between qubit rotation and Larmor frequency results in low power dissipation, which is a critical aspect for scaling up quantum processors [33]. To compare the power consumption of the hopping-based single-qubit control with the electric dipole spin resonance technique, we defined the required number of voltage oscillations to flip a qubit, N_{cycles}, and the derived energy efficiency, $\eta = 1/N_{\text{cycles}}$, which we found largely determines the power dissipation under the assumption that dielectric losses are dominant over other dissipation mechanisms (Section 5.6). For our system, we estimate an efficiency of $\eta = 25(50)\%$ for $Q_A(Q_B)$. By comparison, previous demonstrations of high-fidelity universal qubit logic in silicon exhibited η in the range of 0.04 to 0.07% [12, 15, 11]. Moreover, despite applying sizeable amplitudes to move the spins

between localized orbitals of adjacent quantum dots, we still obtained a factor of 20 reduction in power dissipation with respect to the electric dipole spin resonance technique (Section 5.6). Engineering lower required pulse amplitudes and increasing the orthogonality of the spin quantization axes will enable a further reduction of the dissipated power. Furthermore, the hopping-based approach can simplify the signal delivery and required control electronics and thus alleviate the detrimental heating effects.

Having established universal single-qubit control, we used the set of gates $\{X_{\pi/2}, Y_{\pi/2}\}$ to investigate the qubit coherence times at low magnetic fields. By using a Ramsey sequence (Fig. 5.2A), we obtained a dephasing time T_2^* of 7.0 (4.5) μs at 25 mT for $Q_A(Q_B)$, an order of magnitude larger than that measured at 1 T in the same sample [30, 23]. We were able to further extend the coherence times using Hahn and Carr-Purcell-Meiboom-Gill (CMPG) techniques, obtaining $T_2^{\mathrm{H}} = 32(24)\mu s$ and $T_2^{\mathrm{CPMG-512}} = 1.9(1.7)$ ms, respectively. The dependence of the dephasing times as a function of magnetic field (Fig. 5.2B) indicates that charge noise remains the main cause for decoherence for magnetic fields as low as 5 mT (Section 5.13).

We characterize the single-qubit gate fidelity using randomized benchmarking (RB) and gate set tomography (GST) [34, 35, 36] (Section 5.7 and Section 5.7). The results of RB with average Clifford fidelity (Fig. 5.2D) set the lower bounds of the $X_{\pi/2}$ average gate fidelity at $F_{X_{\pi/2},A} \geq 99.967(4)\%$ and $F_{X_{\pi/2},B} \geq 99.960(6)\%$, consistent with the error modeling (Section 5.10). Using GST we benchmarked the $X_{\pi/2}$ and $Y_{\pi/2}$ gates, obtaining an average gate fidelity $\gtrsim 99.9\%$. From the GST analysis, we infer that dephasing is the dominant contribution to the average gate infidelity. Taking into account the multiple shuttling steps to execute a single gate, we estimate a coherent shuttling fidelity per hop as high as $F_{\mathrm{shuttle}} = 99.992\%$ (Section 5.7).

5.3. HIGH-FIDELITY TWO-QUBIT EXCHANGE GATE

We now focus on assessing the single-qubit and two-qubit gate performance in the two-qubit space. We implemented a two-qubit state preparation and measurement (SPAM) protocol (Figs. 5.3A,B). For the state preparation, we adiabatically converted the two-spin singlet in D2 to the triplet $|Q_AQ_B\rangle = |\downarrow\downarrow\rangle$. For the state measurement, we performed sequential Pauli spin blockade (PSB) readouts on Q_A and Q_B by loading ancillary spins from the reservoir and adiabatic conversion to the state $|\downarrow\downarrow\rangle$ in quantum dots D3 and D4. The difference in the effective g-factor between the quantum dots D1 and D2 allows for the construction of a controlled-Z (CZ) gate even at low magnetic fields. We did so by pulsing the virtual barrier gate voltage vB_{12}, which controls the exchange coupling J between Q_A and Q_B from 10 kHz to 40 MHz (Fig. 5.4C) (Section 5.13 and Section 5.8). Because the maximum exchange coupling strength is non-negligible compared with the Zeeman energy difference ΔE_Z and the qubit frequency f_A, pulse shaping is essential to mitigate coherent errors [12, 37]. We implemented exchange pulses with a Hamming window and performed the CZ gate calibration (Fig. 5.4D) (Section 5.13).

We now advance to benchmarking a two-qubit gate in germanium, by executing two-qubit randomized benchmarking (Section 5.7 for further details, and Section 5.7 for two-qubit GST). Individual Clifford gates were implemented by sequentially applying one or more of the gates CZ, $X_{\pi/2}^{A(B)}$, $Z_{\pi/2}^{A(B)}$, and I. From the fit of the decay constants of the reference and interleaved sequence in Fig. 5.4E, we determined the average Clifford gate

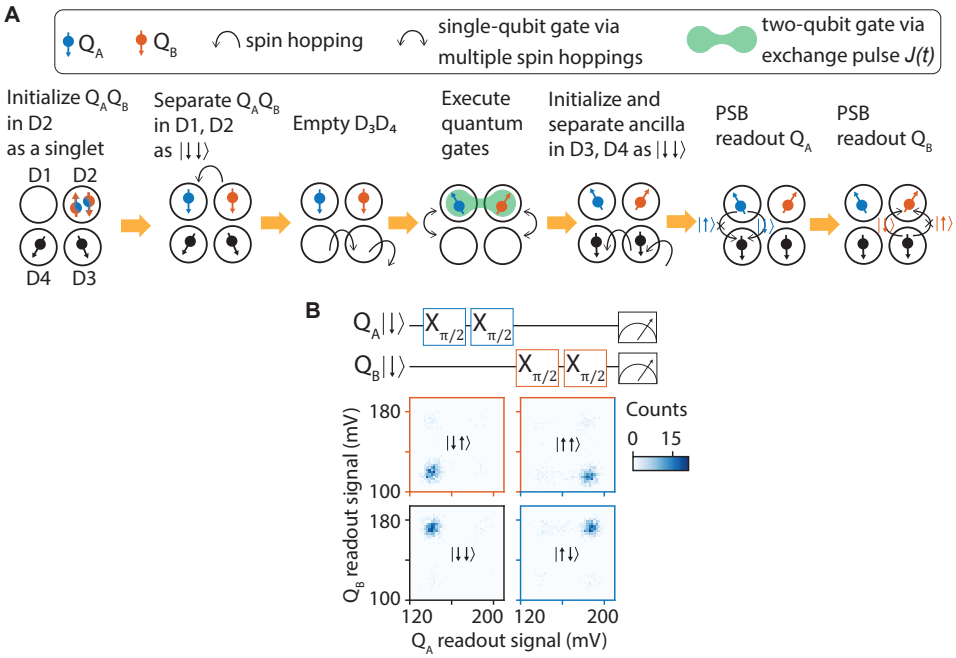

Figure 5.3: **High-fidelity two-qubit gate in germanium - schematics.** **(A)** Schematics of two-qubit initialization, manipulation and individual readout. $|Q_AQ_B\rangle$ was initialized by relaxing to the singlet ground state in D2 and then adiabatically moving one spin to D1. Quantum circuits consisting of single-qubit gates (spin hoppings) and two-qubit gates (exchange pulse $J(t)$) were performed. The final quantum state was read out by preparing ancillary spins and then performing two PSB readouts. In each readout, the chemical potentials of the quantum dots were pulsed such that the spin can either move to the neighboring dot (indicated by arrows) or stay in the original dot (indicated by arrows with × markers) with probabilities depending on the spin state $|Q_{A(B)}\rangle$. **(B)** Two dimensional histograms of the sensor signals formed by 500 single-shot measurements for four different two-qubit states, which are prepared by applying $X_{\pi/2,A(B)}$ gates.

fidelity as $F_{\text{Clifford2}} = 98.60(6)\%$ and the average CZ gate fidelity as $F_{\text{CZ}} = 99.33(10)\%$, consistent with the result of error modeling (Section 5.10). For the single-qubit gate performance in the two-qubit space, we estimate the lower bound of fidelity, averaged between both qubits, as $\frac{1}{2}(F_{X_{\pi/2},A} + F_{X_{\pi/2},B}) \geq 99.90(5)\%$. We believe that these high fidelities to result from the high driving efficiency and relatively long $T_2^\star$ at low magnetic field.

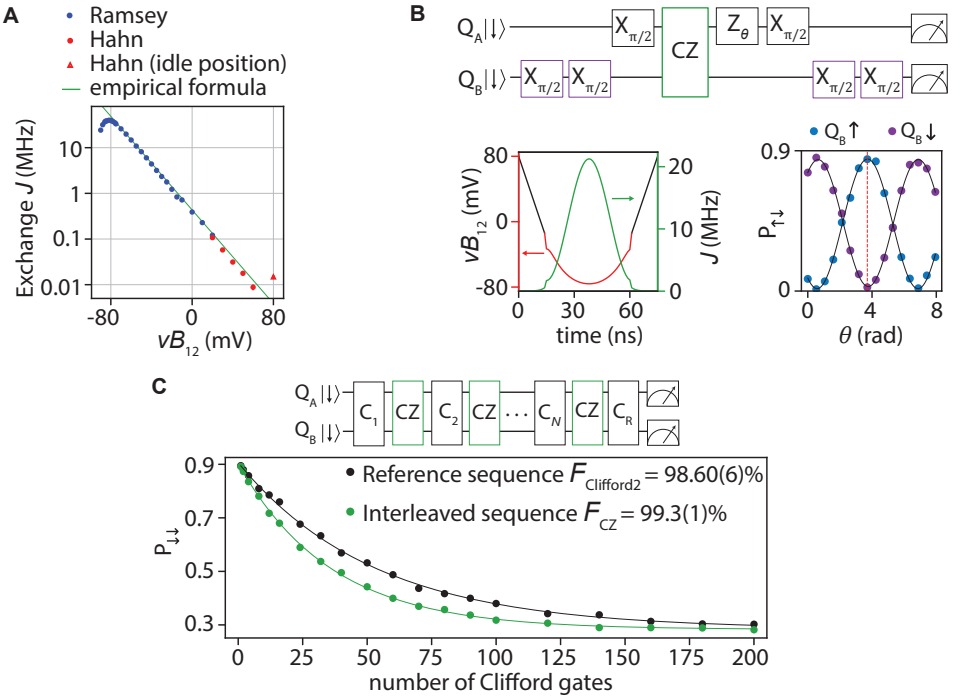

Figure 5.4: **High-fidelity two-qubit gate in germanium - measurement results.** **(A)** Exchange coupling as a function of virtual barrier gate vB_{12}, measured by Ramsey (Hahn echo) experiments in the large (small) coupling regime. The idle position corresponds to the barrier voltage where single qubit gates were performed, but at slightly different plunger gate voltage. The empirical formula for mapping vB_{12} and J is detailed in Section 5.13. The bending on the left side of the plot results from the energy level anti-crossing when $J \sim f_A$. **(B)** The voltage pulse of the CZ gate was shaped to have exchange $J(t)$ in the form of a Hamming window, as illustrated on the bottom left. The CZ gate calibration circuit for single-qubit phases is on the top, with the measurement outcome plotted on the bottom right. The target qubit (Q_A) phase depends on the control qubit Q_B being in the state $|\downarrow\rangle$ in blue ($|\uparrow\rangle$ in purple). The red dashed line marks the required single-qubit phase of Q_A for the CZ gate. **(C)** Gate sequence and measurement result of two-qubit interleaved RB.

HOPPING SPINS TO BENCHMARK LARGE AND HIGH-CONNECTIVITY QUANTUM DOT ARCHITECTURES

The presented sparse occupation of a quantum dot array allows the construction of high-fidelity hopping-based quantum logic, but it may also facilitate the implementation of quantum circuits with high-connectivity. Although two-dimensional quantum circuits with nearest neighbor connectivity can already tolerate high error rates [38, 25, 39], an increased connectivity may substantially lower the physical qubit overhead and lower the logical qubit error rate [40]. We therefore envision a qubit architecture with sparse occupation (Fig. 5.5A) to be a potential platform. Here, qubits may be shuttled to remote sites for distant two-qubit logic, and single-qubit logic can be executed during this trajectory.

As a first step toward such architectures, we developed and characterized an extended system comprising 10 quantum dots. The system (Fig. 5.5B) consists of a multilayer gate architecture with quantum dots, Dn with $n \in [[1,10]]$, and peripheral charge sensors, which may be integrated within the array through development of vertical interconnects such as in [41]. By exploiting dedicated (virtual) barrier and plunger gate voltages, we prepared the quantum dots D1 and D4 in the single-hole regime, leaving the others empty (see Section 14 of the supplementary material [31], and Section 5.13). The hopping-based qubit gates were used to rapidly characterize the different quantum dot g-factors and coherence times. After initializing the associated qubit pair Q1,Q4 into its $|\uparrow\downarrow\rangle$ eigenstate, we diabatically shuttled the Q4 spin to another quantum dot site, Dn. We let it precess for a time $t_{\mathrm{D}n}$, after which the spin was shuttled back and read out. The misalignment between the spin quantization axes gives rise to spin rotations with the Larmor frequency $f_{\mathrm{D}n}$ [21]. The resulting oscillations are shown as a function of waiting time in D6, t_{D6}, and magnetic field (Fig. 5.5D). From the linear scaling of the D6 Larmor frequency with the magnetic field, we extracted an effective g-factor of 0.062 (Fig. 5.5E) and from the decay of the oscillations a dephasing time of $T_2^* = 1.12\,\mu$s (Fig. 5.5F). Repeating this protocol to reach all the quantum dots, we extracted the Larmor frequency and dephasing time at each site, as displayed in Figs. 5.5G, H. For the case of Q1 (Q4), we shuttled the spin to D5 (D8) back and forth twice, interleaved by a varying precession time in D1, t_{Q1} (in D4, t_{Q4}), which we explain in detail in Section 16 of the supplementary material [31]. Our experiments showed an average T_2^* of $1.3 \pm 0.4\,\mu$s at a magnetic field of 41.4 mT (Section 5.13), and we attribute the fast dephasing of D9 (T_2^* = 290 ns) to charge noise originating from a fluctuator nearby. Furthermore, we obtained an average g-factor of 0.04 ± 0.03. The observed variability in this distribution is likely a result of multiple factors: the heterogeneity inherent in the shapes of the quantum dots (dot-to-dot variability), the presence of strain gradients in the quantum well arising from the gates above or the SiGe strained relaxed buffer below, and the impact of interface charges. The average g-factor that we obtained was considerably lower than what has been observed in the literature [10, 30, 26, 24]. We suggest that this reduction is primarily due to two phenomena: a precise in-plane magnetic field configuration and an appreciable renormalization of the gyromagnetic ratio from the pure heavy-hole value of ~ 0.18 [42, 28, 27]. Such renormalization is driven by substantial inter-band mixing between the heavy-hole and the light-hole band, which we attribute to asymmetries in the strain, as simulated in Section 18 of the supplementary material [31]. Furthermore,

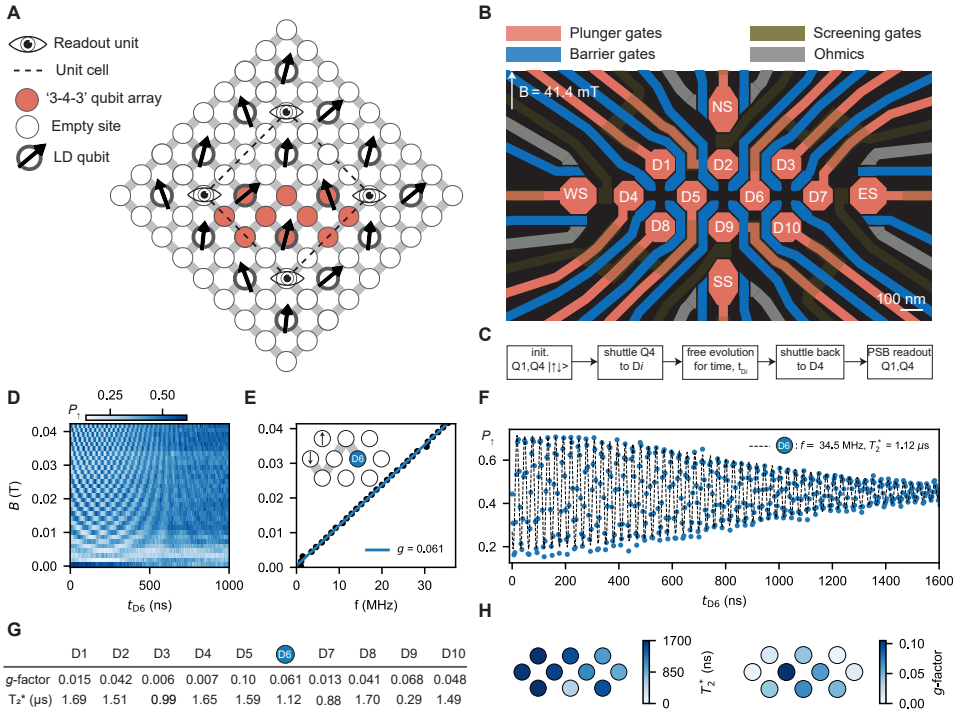

	D1	D2	D3	D4	D5	D6	D7	D8	D9	D10
g-factor	0.015	0.042	0.006	0.007	0.10	0.061	0.013	0.041	0.068	0.048
T_2^* (μs)	1.69	1.51	0.99	1.65	1.59	1.12	0.88	1.70	0.29	1.49

Figure 5.5: **Hopping spins to benchmark large and high-connectivity quantum dot architectures. (A)** Our vision of a semiconductor quantum computing architecture comprising hopping Loss-DiVincenzo (LD) spin qubits (black arrows), readout units (eyes), and empty quantum dot sites for shuttling operations. **(B)** Layout of the 10 quantum dot array, with gate-defined charge sensors labelled in analogy to the four cardinal points (NS, ES, WS, and SS). **(C)** Control sequence used to characterize the array. A spin originally in D4 was shuttled across the whole array, allowed to evolve at a certain quantum dot, and read out. **(D)** Qubit rotations induced by the difference in quantization axes as a function of idling time in quantum dot D6 and magnetic field. **(E)** D6 Larmor frequency, extracted from the Fourier analysis of (D) versus magnetic field. Linear fit yields an estimated g-factor of 0.062. Inset shows the shuttling trajectory of the spin qubit from D4 to D6. **(F)** Extended time evolution in D6 at B = 41.4 mT, yielding a qubit frequency of 34.51 MHz and a dephasing time of $T_2^* = 1.12\ \mu s$. The experimental trace was fitted (dashed lines) as described in Section 5.13. **(G and H)** Table and visualization of the extracted parameters: g-factors and T_2^*, respectively.

these simulations indicate that such a low average effective g-factor only occurs when the misalignment of the magnetic field is smaller than 0.1° with respect to the plane of the g-tensors, emphasizing the importance of accurately controlling the magnetic field orientation when operating with germanium qubits.

5.4. CONCLUSION

We have shown that hopping spin qubits between quantum dots with site-dependent g-tensors allows for coherent shuttling with fidelities up to 99.992%, single-qubit gate fidelities up to 99.97%, and two-qubit gate fidelities up to 99.3%. This method allows for efficient control with baseband pulses only and fast execution of quantum gates even at low magnetic fields where the coherence is high. Using this approach for the control of dense quantum dot arrays with sparse qubit occupation can alleviate challenges in crosstalk and heating, while providing high connectivity. Recent theoretical developments predict that increased connectivity can substantially improve logical qubit performance and reduce the required overhead on physical qubits [40]. Sparse spin qubit arrays could be particularly suited for error correction schemes requiring either a larger number of nearest neighbors or coupling beyond nearest neighbors. A substantial challenge remains in addressing the qubit-to-qubit variation. This was already highlighted in the original work by Loss and DiVincenzo [1]. We envision that the characterization of larger qubit arrays and statistical analysis will become pivotal, with the presented 10-quantum dot array already providing a first indication that design considerations can determine relevant qubit parameters. Site-dependent quantization axes can be realized by g-tensor engineering such as in elongated quantum dots [43], by using nanomagnets, or by applying currents through nanowires above the qubit plane [44]. The developed control methods for high timing accuracy can also advance exchange-only qubits that are operated using baseband pulses [19] and affect platforms such as superconducting qubits [45]. We envision establishing high-fidelity quantum operation through low-power control in uniform and large-scale systems to be a critical step in realizing fault-tolerant quantum computing.

5.5. MATERIAL AND METHODS

The two devices are fabricated on a Ge/SiGe heterostructure with a 16 nm germanium quantum well buried 55 nm below the semiconductor/oxide interface [46, 47]. The devices gate stack is realised using a multilayer of Pd gates and Al_2O_3 gate oxide, grown by atomic layer deposition. Ohmic contacts are made by a thermally-diffused Al and Pt contact layer for the 2×2 and 10 quantum dot devices, respectively. Details on the fabrication of the first device can be found in ref. [30]. The second device is based on a similar approach, but has an additional layer of gates and gate oxide. The experiments are performed in two Bluefors dilution refrigerators with an electron temperature lower than 140 mK [48]. We estimate a possible misalignment angle between the device plane and the magnetic field axis of ±2°. We also note that due to an offset in the height position of the 10 quantum dots chip on the cold finger of the cryostat with respect to the center of the field, the effective magnetic field is 69% of the applied field. We have determined this factor using the Ge-73 gyromagnetic ratio, measured via

CPMG sequences on a different device mounted in the same position in a different cool-down. This factor also agrees well to what estimated using simulations of the coil field. In each of the two setups, we utilize an in-house built battery-powered SPI rack `https://qtwork.tudelft.nl/~mtiggelman/spi-rack/chassis.html` to set direct-current (DC) voltages, while we use a Keysight M3202A arbitrary waveform generator (AWG) to apply alternating-current (AC) pulses via coaxial lines. The DC and AC voltage signals are combined on the printed circuit board (PCB) with bias-tees and applied to the gates. In the individual bias-tee, the DC signal undergoes a resistor of 1 MΩ, and the high-frequency signal undergoes a capacitor of 100 nF. Each charge sensor is galvanically connected to a NbTiN inductor with an inductance of a few μH forming a resonant tank circuit with resonance frequencies of ~ 100 MHz. The reflectometry circuit also consists of a directional coupler (ZEDC-15-2B) mounted on the mixing chamber stage. The readout signals are amplified by a cryogenic SiGe amplifier mounted on the 4 K stage (a CITLF3 with gain of 33 dB), by a room-temperature amplifier (a M2j module of the SPI Rack with a gain of 70 dB) and demodulated with a Keysight M3102A digitizer module with a sampling rate of 500 MSa/s.

5

5.6. POWER DISSIPATION AND SCALING ADVANTAGES OF SHUTTLING-BASED CONTROL

To execute the shuttling operations, trapezoidal voltage pulses are applied on the gates. To achieve high-fidelity single qubit control a handful of such shuttling pulses are required, each with ramp times of a few nanoseconds between two discrete voltage levels. This stands in stark contrast with state-of-the-art electron dipole spin resonance (EDSR) control where typically high frequency, sinusoidal pulses are applied, and many oscillations of the driving signal are needed to achieve the desired gate fidelity [12, 11]. This gives an advantage to a shuttling-based architecture considering energy dissipation, crosstalk and complexity of the required control electronics.

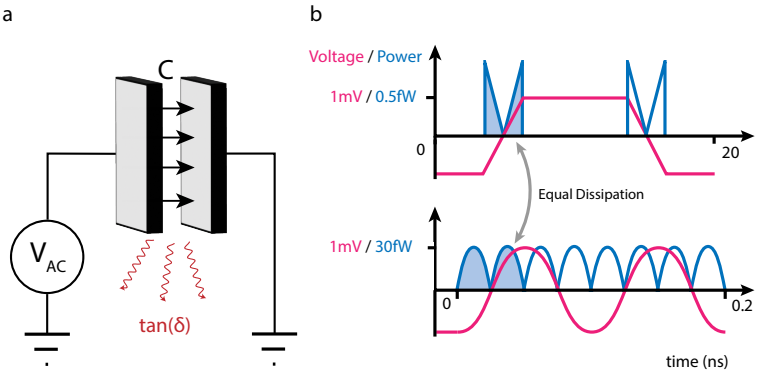

Figure 5.6: **Heat dissipation. a,** Schematic of the model of the heat dissipation, due to some capacitor C with loss tangent $\tan(\delta)$. **b,** For equal pulse amplitude and DC-offset, the heat dissipated per cycle is the same independent of the pulse shape. $C \cdot \tan(\delta) = 10^{-}18F$ was assumed in this example.

Already at the current system sizes, EDSR-based devices experience a drift in qubit frequency that is linked to heat dissipation of the signal [16]. When resistive losses are limited, this heat-dissipation is believed to result from a dielectric loss of energy is stored in the electric field around the signal-line. Effectively the system is a capacitor with some loss tangent $\tan(\delta)$, defined as $\tan(\delta) = \epsilon''/\epsilon'$ in a non-conductive system, with ϵ'' and ϵ' the imaginary and real part of the electric permittivity [49]. During each charging cycle, a fraction proportional to $\tan(\delta)$ of the stored electric energy is lost as depicted in Fig. 5.6. With a DC bias around zero the total capacitive energy stored and discharged by the signal line is proportional to CV_{AC}^2, where C is the capacitance and V_{AC} the EDSR amplitude, with which the capacitor is charged. The total energy lost is proportional to $E_{\mathrm{Loss}} = N_{\mathrm{cycles}} \tan(\delta) C V_{\mathrm{AC}}^2$, where N_{cycles} gives the number of oscillations required to perform a qubit operation. In a simplified model, we can take the electric permittivity and with it the loss tangent of silicon and germanium to be largely independent of frequency in the relevant frequency range [50, 51]. In this model, for an identical geometry and driving amplitude, the energy dissipation is assumed to solely depends on the number of cycles of the operation and not on the pulse-shape, as indicated in Fig. 5.6. Hence $1/N_{\mathrm{cycles}}$ is a measure of the efficiency of the operation.

For an EDSR-based X_π-gate the number of cycles is given by $N_{\mathrm{cycles,EDSR}} = \frac{f_{\mathrm{Larmor}}}{2f_{\mathrm{Rabi}}}$, which is exactly the inverse of the efficiency η as defined in the main text. The driving efficiency is inherently limited by the relatively small Rabi frequency $f_{\mathrm{Rabi}} \ll f_{\mathrm{Larmor}}$ when operating in the weak-driving (adiabatic) regime, in which the rotating-wave approximation holds. We note that while faster driving is possible, it requires complex amplitude and phase modulation for high-fidelity implementations [52, 37] which also dissipate additional heat. An experimental demonstration of high-fidelity qubit logic is given by Xue et al. operated with Rabi (Larmor) frequencies of $f_{\mathrm{Rabi}} = 2\tilde{\mathrm{M}}\mathrm{H}$ ($f_{\mathrm{Larmor}} = 12\tilde{\mathrm{G}}\mathrm{Hz}$) [12, 15]. This corresponds to an efficiency of $\eta = 2f_{\mathrm{Rabi}}/f_{\mathrm{Larmor}} \approx 1/3000$. Similarly Noiri et al. demonstrated $\eta \approx 1/1500$ [11]. For the prior device, an EDSR amplitude of $V_{\mathrm{AC}} \approx 5\tilde{\mathrm{m}}\mathrm{V}$ is reported at the bond pads of the chip [15]. This corresponds to an energy dissipation of $E_{\mathrm{Loss}} \approx 0.075 \tan(\delta) C\, V^2$ per X_π-gate for high-fidelity EDSR control.

Shuttling based gates do not face a similar inherit efficiency limitation, instead being limited by the relative tilt in quantization axis. In the main part of the paper we demonstrate that to perform an X_π-gate using shuttling, the hole is shuttled two to four times back and forth depending on the angle between the quantization axes of the quantum dot pairs. With periodic pulse timings and negligible ramp times this corresponds to $N_{\mathrm{cycles}} = 1/\eta$. This is done with a typical amplitude $V_{\mathrm{AC}} = 20\mathrm{mV}$. Using the $N_{\mathrm{cycles}} = 4$, this corresponds to a heat-dissipation corresponding to $E_{\mathrm{Loss}} = 2 \cdot 0.0016 \tan(\delta) C\, V^2 = 0.0032 \tan(\delta) C\, V^2$, where the additional factor of two accounts for the two plunger gates on which the voltage is applied.

Crosstalk, like heat dissipation, is a problem observed in the current spin-qubit devices and is expected to become more significant as the number and density of qubits increase [13]. This crosstalk can originate from close spacing of signal lines, both on and off the qubit chip. As the density of the quantum dots increases, the capacitance between the gates is expected to grow accordingly, increasing the crosstalk further. Since the admittance between signal lines is directly proportional to the signal frequency, the capacitive crosstalk will be less for low-frequency shuttling-based pulses, compared to

high-frequency EDSR experiments which face challenges similar to conventional high-frequency integrated circuits [53]. In integrated circuits design, a rule of thumb is to keep the distance between traces to three times the trace width [53]. This might pose a significant limitation for qubit routing, especially for larger 2D arrays. An architecture based on the demonstrated high-fidelity shuttling gates is thus expected to be less sensitive to crosstalk, which will be advantageous in scaling to large qubit counts.

In large spin systems consisting of many hundreds or thousands of qubits, the scalability of control electronics is a major consideration. The electronic hardware required to generate the IQ modulated sinusoidal EDSR pulses need high analog voltage resolution, which is significantly more involved than the shuttling pulses consisting of two voltage levels. The lower required voltage accuracy and precision of the shuttling based control allows scaling the qubit count while limiting the electronic overhead, cost and energy consumption. The required timing resolution of shuttling based control should be below 90p̃s for a 40M̃Hz Larmor frequency (Section 5.13), higher than the sampling resolution of the IQ modulated EDSR driving. However, EDSR signals need to control the qubit phase with a similar precision as the shuttling pulses, thus requiring a similarly high resolution.

5.7. FIDELITY BENCHMARKING

RANDOMIZED BENCHMARKING

Experiment implementation In the single-qubit randomized benchmarking (RB), the sequence lengths are varied from { 1, 3, 10, 30, ..., 6000 }, in total 25 different lengths. We execute sequences of different lengths once in a random order. After going over all the 25 sequences, we repeat a random execution again with different random order. In total we repeat this execution 32 times. For every sequence we perform 400 single-shot readout. The final spin-down probability $P_{\mathrm{A(B)},\downarrow}$ of the RB sequences on qubit A(B) with the idled qubit B(A) is obtained by averaging over 400 single-shot readout and tracing out the qubit B(A) from the two-qubit state probability $\mathrm{P}_{\sigma\sigma'}$. An experiment takes 4.5 hours to complete, with no re-calibration within the individual experiment.

In the two-qubit interleaved randomized benchmarking (IRB), the sequence lengths are { 1, 2, 4, 8, ..., 200 }, in total 20 different lengths. The order of sequence execution is similar to the single-qubit RB. We execute a reference sequence and right afterward an interleaved sequence with the same length, and then continue on the sequences with different lengths in a random order. After going over all the 20 sequences, we repeat a random execution again with different random order. In total we repeat 128 times. For every sequence we perform 200 single-shot readout. An experiment takes 7.5 hours to complete, with no re-calibration during the individual experiment.

In both single- and two-qubit RB, we observe the 2D histograms of the charge sensor signal are well-separate even at the maximal sequence lengths, while they have an overall shift which gradually increases for the longer sequence. We speculate that the intensive pulsing locally heats up the two-level fluctuators and the high-kinetic inductors, shifting chemical potential of the single-hole charge sensor and the impedance of the LC circuits, respectively [16]. For the single-qubit RB and the first two-qubit RB (IRB_1), we apply adaptive thresholding on the histograms to obtain the two-qubit state probability $\mathrm{P}_{\sigma\sigma'}$.

For the other two-qubit RB experiments ($IRB_{2,3}$), we add an extra wait time of 300μs before reloading the ancilla qubits for readout. This amount of wait time is sufficient to reduce the sensor signal shift and we are able to use pre-defined constant thresholds to obtain the two-qubit state probability $P_{\sigma\sigma'}$.

Fidelity extraction In single-qubit RB, the single-qubit Cliffords consist of the gates $X_{\pi/2}$, $Z_{\pi/2}$, and the idle gate I. We measure the final state probability of the sequences containing m Clifford gates and a recovery Clifford gate which is the inverse of the corresponding m-Clifford sequence. The spin-down probability averaged over 32 random sequences is fitted to $P_{\downarrow}(m) = Ap^m + B$, where p is the decay rate of the sequence, m is the number of Cliffords, A and B are the parameters absorbing SPAM errors. The average Clifford fidelity is related to the decay rate by $F_{\text{Clifford1}} = 1 - \frac{1}{2}(1-p)$. The measurements in Fig. 5.2D shows the average Clifford fidelity $F_{\text{Clifford1,A}} = 99.967(4)\%$ and $F_{\text{Clifford1,B}} = 99.960(6)\%$. The uncertainties are obtained from bootstrapping re-sampling with 95% confidence intervals. The average number of gates for single-qubit Clifford is 1.0 $X_{\pi/2}$, 2.42 $Z_{\pi/2}$ and 0.04 I. Defining the infidelity of gate i as $r_i = 1 - F_i$ and assuming the Clifford gate infidelity equals to the sum of the primitive gate infidelity weighted by the average composition, $r_{\text{Clifford}} = r_{X_{\pi/2}} + 2.42 r_{Z_{\pi/2}} + 0.04 r_{\text{I}}$, the average Clifford fidelity sets the lower bounds of the $X_{\pi/2}$ average gate fidelity $F_{X_{\pi/2},\text{A}} \geq F_{\text{Clifford1,A}}$ and $F_{X_{\pi/2},\text{B}} \geq F_{\text{Clifford1,B}}$.

In two-qubit RB, the two-qubit Cliffords consist of the gates CZ, $X_{\pi/2}^{\text{A(B)}}$, $Z_{\pi/2}^{\text{A(B)}}$, and I. Similar to the single-qubit RB, we measure the final state probability of the sequences containing m Clifford gates and a recovery Clifford gate. The return probability of the reference sequence (interleaved sequence) is fitted to $P_{\downarrow\downarrow,\text{ref(int)}}(m) = Ap_{\text{ref(int)}}^m + B$, where $p_{\text{ref(int)}}$ is the decay rate of the sequence, m is the number of Cliffords, while A and B are the parameters absorbing the SPAM errors. From the reference sequence decay curve in Fig. 5.4E, we determine the average Clifford gate fidelity $F_{\text{Clifford2}} \equiv F_{\text{ref}} = 1 - \frac{3}{4}(1 - p_{\text{ref}}) = 98.60(6)\%$. The uncertainties are obtained from bootstrapping re-sampling with 95% confidence intervals. The average number of gates for two-qubit Clifford is 1.63 CZ, 1.60 $X_{\pi/2}^{\text{A(B)}}$, 2.68 $Z_{\pi/2}^{\text{A(B)}}$, and 0.00009 I. This implies the relation between gate errors, $r_{\text{Clifford2}} \equiv r_{\text{ref}} = 1.63 r_{\text{CZ}} + \Sigma_{i=\text{A,B}} 1.60 r_{X_{\pi/2},\text{i}} + 2.68 r_{Z_{\pi/2},\text{i}}$. From this relation we find the average Clifford gate fidelity sets the lower bound of CZ gate fidelity $F_{\text{CZ}} = 1 - r_{\text{CZ}} \geq 1 - \frac{r_{\text{ref}}}{1.63} = 99.14(4)\%$, which is consistent with the IRB result $F_{\text{CZ}} = 1 - \frac{3}{4}(1 - p_{\text{int}}/p_{\text{ref}}) = 99.33(10)\%$. We estimate the lower bound of single qubit gate fidelity in the two-qubit subspace, average between both qubits, as $\frac{1}{2}(F_{X_{\pi/2},\text{A}} + F_{X_{\pi/2},\text{B}}) = 1 - \frac{1}{2}(r_{X_{\pi/2},\text{A}} + r_{X_{\pi/2},\text{B}}) \geq 1 - \frac{1}{2}\frac{r_{\text{ref}} - 1.63 r_{\text{CZ}}}{1.60} = 99.90(5)\%$.

We perform additional check for the potential echoing effect in two-qubit RB/IRB experiments, by fitting the data with super-exponential formula. As shown in Table 5.1, the exponents are in the range of 0.86 - 1.05, showing small deviations from a pure exponential decay.

GATE SET TOMOGRAPHY AND COMPARISON WITH TWO-QUBIT RANDOMIZED BENCHMARKING

Gate set tomography implementation We carried out gate set tomography (GST) experiments using the python package pyGSTi [34]. For single-qubit GST, we use the default gateset {I, X, Y}, where I is the idle gate of $\frac{5}{f_{\text{A}}} \approx 118$ ns ($\frac{9}{f_{\text{B}}} \approx 102$ ns), X(Y) stands for

Fitting formula	Results	IRB_1	IRB_2	IRB_3
Fit with super-exponent model $P(m) = Ap^{(m^\alpha)} + B$	α_{ref}	0.862 ± 0.046	1.050 ± 0.058	0.988 ± 0.057
	α_{int}	0.867 ± 0.041	0.946 ± 0.047	0.954 ± 0.047
	r_{ref} (%)	2.55 ± 0.40	1.17 ± 0.25	1.55 ± 0.31
	r_{CZ} (%)	1.20 ± 0.68	1.36 ± 0.49	1.21 ± 0.56
Fit with single-exponent model $P(m) = Ap^m + B$	r_{ref} (%)	1.56 ± 0.07	1.40 ± 0.06	1.48 ± 0.06
	r_{CZ} (%)	0.79 ± 0.11	0.67 ± 0.10	0.86 ± 0.11

Table 5.1: **Two-qubit interleaved randomized benchmarking results for three individual runs.** The parameter settings are identical to two-qubit GST experiments, where magnetic field B = 25 mT and the CZ gate has maximum exchange coupling $J \approx 21$ MHz. The infidelity of the two-qubit Clifford r_{ref} is related to the decay rate of the reference RB sequence by $r_{\text{ref}} = 1 - F_{\text{ref}} = \frac{3}{4}(1 - p_{\text{ref}})$. The infidelity of the interleaved CZ gate r_{CZ} is related to the decay rates of the reference sequence and interleaved sequence by $r_{\text{CZ}} = 1 - F_{\text{CZ}} = \frac{3}{4}(1 - p_{\text{int}}/p_{\text{ref}})$. The uncertainty represents the 95% confidence interval.

of $X(Y)_{\pi/2}$. The six fiducials for state preparation and measurements are { null, X, Y, XX, XXX, YYY }, where null is the gate with zero idle time. The five germs are {I, X, Y, XY, XXY }. The circuit length are power of two from 1 up to 128, resulting in total 1120 sequences, which takes 17 minutes to complete in the experiment. In every sequence, the spin-up probability $P_{\text{A(B)},\uparrow}$ of qubit A(B) with the idled qubit B(A) are obtained by averaging over 500 single-shot readout and tracing out the qubit B(A) state from the two-qubit state probability $P_{\sigma\sigma'}$.

For two-qubit GST, we use the default gateset {I, X_A, X_B, Y_A, Y_B, CZ}. Here the idle gate takes 100 ns. The 11 measurement fiducials are {null, X_B, Y_B, X_BX_B, X_A, Y_A, X_AX_A, X_AX_B, X_AY_B, Y_AX_B, Y_AY_B }. The 16 preparation fiducials are measurement fiducials plus the gates {$X_AX_BX_B$, $Y_AX_BX_B$, $X_AX_AX_B$, $X_AX_AY_B$, $X_AX_AX_BX_B$ }. The 16 germs are { I, X_A, Y_A, X_B, Y_B, CZ, X_AY_A, X_BY_B, $X_AX_AY_A$, $X_BX_BY_B$, X_BY_BCZ, $CZX_AX_AX_A$, $X_AX_BY_BX_AY_BY_A$, $X_AY_BX_BY_AX_BX_A$, $CZX_BY_ACZY_BX_A$, $Y_AX_AY_BX_AX_BX_AY_AY_B$ }. The circuit length are {1,2,4,8}, resulting in total 1702 sequences, which takes 18 minutes to complete in the experiment. In every sequence the two-qubit state probability $P_{\sigma\sigma'}$ is obtained by averaging over 500 single-shot readout.

The measurement outcome of the gate sequence is analyzed in the python package pyGSTi with CPTP model, which considers the gates, the state preparation and measurement as completely positive trace-preserving processes. The corresponding process matrices are estimated and multiple derived quantities can be computed. In the case of single-qubit GST, the estimated process of the single qubit gates can be projected and decomposed into rotation operators as listed in Table 5.2. For both single-qubit and two-qubit GST, we report gate errors metrics (Table 5.3, 5.4) and SPAM error (Table 5.5, 5.6). The tables include the averaged gate infidelity $1 - \frac{\text{tr}(G_{\text{exp}}^{-1}G_{\text{ideal}})+d}{d(d+1)}$, non-unitary averaged gate infidelity $\frac{d-1}{d}(1-\sqrt{u(G_{\text{exp}}^{-1}G_{\text{ideal}})}$, 1/2 trace distance $\frac{1}{2}\|J_a(G_{\text{ideal}}) - J_a(G_{\text{exp}})\|$, and 1/2 diamond-distance $\frac{1}{2}\max_\rho\|(G_{\text{ideal}} \otimes I)\rho - (G_{\text{exp}} \otimes I)\rho\|$. Here $d = 2^{N_{\text{qubits}}}$ is the dimension of the Hilbert space, G_{exp} is the process of the gate in the GST experiment in the form of Pauli transfer matrix (PTM), G_{ideal} is the PTM of the ideal gate, $u(M) = \text{tr}(J_a(M)^2)$ is the unitarity of the matrix M, $J_a(M)$ is the Jamiolkowski isomorphism map between the matrix M and the corresponding Choi Matrix, $\|.\|$ denotes the trace norm, and ρ is a density

Gate	Rotation axis $\hat{n} = (n_x, n_y, n_z)$	Rotation angle $\theta_{\text{rot}}(\pi)$
I_A	$(0.038, 0.027, 0.999)$	0.0038
X_A	$(1, 1\times10^{-3}, -1.7\times10^{-6})$	0.5018
Y_A	$(1\times10^{-3}, 1, 2\times10^{-7})$	0.5019
I_B	$(-0.0057, 0.014, 1)$	0.0051
X_B	$(1, -1\times10^{-4}, -2\times10^{-7})$	0.5015
Y_B	$(-1\times10^{-4}, 1, -4\times10^{-7})$	0.5016

Table 5.2: **Single qubit gate parameters determined from GST.**

matrix of dimension n^2 [34, 54].

Discrepancy between RB and GST in two-qubit gate benchmarking The different benchmarking results obtained by GST and interleaved RB may stem from the presence of low-frequency noise. In GST, the CZ gate is repeated to amplify and extract the single-gate dephasing error r_s. Similar to the Ramsey dephasing, repeating the CZ gate N-times results in an error $r(N) = r_s^{(N^\alpha)}$ where $\alpha = 1$ if the error is Markovian, or $\alpha \approx 2$ if the dephasing error is dominated by the energy level fluctuations with $1/f$ noise spectrum [55, 56]. In the latter case, the errors of the CZ gates in different position within a repeated CZ gate sequence (e.g. the first CZ gate and the second CZ gate) are correlated. This type of error with temporal correlation is non-Markovian. Analyzing the decay $r(N) = r_s^{(N^2)}$ using a Markovian error model can result in deviations of estimated single-gate errors from the actual error. The outcome of our GST experiments always shows model violations, which is in line with this hypothesis. On the other hand, in RB the CZ gates are placed between Cliffords that reduce the correlation of the CZ gate errors at different position of a sequence. According to the numerical study [56], under the $1/f$ noise the RB provides better than a factor-of-2 estimate of the gate error. We believe this worse-case deviation of the error estimate (a factor of 2) is smaller than the one from GST, in view of the $1/f$ noise and gate implementation in our system. Therefore, we consider the results of the interleaved RB to be more representative for the average gate fidelity, while GST is used to access the full tomographic reconstruction of the quantum processes.

Gate	Avg. gate infidelity (%)	Non-unitary avg. gate infidelity (%)	1/2 trace distance (%)	1/2 diamond-distance (%)	Eigenvalues 1/2 diamond-distance (%)
I_A	0.38 ± 0.02	0.38 ± 0.02	0.82±0.03	0.83±0.05	1.22±0.05
X_A	0.061 ± 0.008	0.061 ± 0.008	0.33±0.02	0.34±0.07	0.44±0.03
Y_A	0.058 ± 0.008	0.057 ± 0.008	0.35±0.02	0.35±0.05	0.45±0.02
I_B	0.71 ± 0.03	0.70 ± 0.03	1.32±0.06	1.33±0.09	1.97±0.09
X_B	0.019 ± 0.007	0.019 ± 0.007	0.24±0.02	0.25±0.03	0.36±0.03
Y_B	0.023 ± 0.007	0.022 ± 0.007	0.25±0.02	0.26±0.04	0.37±0.02

Table 5.3: **Single-qubit GST gate fidelity.** The single-qubit GST is performed under the same setting as single-qubit RB and two-qubit IRB and GST, where residual exchange coupling $J \approx 10-15$ kHz. The uncertainty represents the 95% confidence interval.

Gate	Avg. gate infidelity (%)	Non-unitary avg. gate infidelity (%)	1/2 trace distance (%)	1/2 diamond-distance (%)	Eigenvalues 1/2 diamond-distance (%)
$I_A \otimes I_B$	0.36 ± 0.27	0.36 ± 0.26	0.9±1.5	1.0±2.4	1.4±0.6
$X_A \otimes I_B$	0.46 ± 0.28	0.43 ± 0.28	2.0±0.9	2.7±2.4	3.6±1.6
$Y_A \otimes I_B$	0.82 ± 0.35	0.78 ± 0.35	2.7±1.2	3.5±4.5	4.4±2.4
$I_A \otimes X_B$	0.33 ± 0.27	0.32 ± 0.27	0.8±0.9	1.2±1.7	0.7±1.2
$I_A \otimes Y_B$	0.51 ± 0.39	0.49 ± 0.38	1.7±0.9	2.4±2.5	2.4±1.6
CZ	1.87 ± 0.52	1.78 ± 0.50	4.4±0.7	6.2±3.8	8.1±0.9

Table 5.4: **Two-qubit GST gate fidelity.** The parameter settings are identical to two-qubit IRB experiments, where magnetic field $B = 25$ mT and the CZ gate has maximum exchange coupling $J \approx 21$ MHz. The uncertainty represents the 95% confidence interval.

Qubit	Readout probability	Single-qubit GST experiment		Two-qubit GST experiment	
		Prepare $\|\downarrow\rangle$	Prepare $\|\uparrow\rangle$	Prepare $\|\downarrow\rangle$	Prepare $\|\uparrow\rangle$
Q_A	$P_\downarrow$ (%)	**96.9**	8.6	**97.3**	10.0
	$P_\uparrow$ (%)	3.1	**91.4**	2.7	**90.0**
Q_B	$P_\downarrow$ (%)	**95.0**	8.0	**95.1**	7.2
	$P_\uparrow$ (%)	5.0	**92.0**	4.9	**92.8**

Table 5.5: **Estimation of SPAM fidelity in single-qubit space based on single-qubit GST and two-qubit GST experiments.**

Readout probability	Prepare $\|\downarrow\downarrow\rangle$	Prepare $\|\downarrow\uparrow\rangle$	Prepare $\|\uparrow\downarrow\rangle$	Prepare $\|\uparrow\uparrow\rangle$
$P_{\downarrow\downarrow}$ (%)	**94.0**	6.2	8.6	1.5
$P_{\downarrow\uparrow}$ (%)	3.7	**90.7**	1.3	8.5
$P_{\uparrow\downarrow}$ (%)	2.1	0.7	**85.4**	6.0
$P_{\uparrow\uparrow}$ (%)	0.2	2.4	4.7	**84.0**

Table 5.6: **Estimation of SPAM fidelity based on two-qubit GST results.** We use the SPAM operations estimated by GST, including the initial state (a density matrix) and the positive operator-valued measure (POVM), to compute the expected readout probability when preparing specific computational states. The computational states are prepared using the imperfect initialization of $|\downarrow\downarrow\rangle$ and the perfect single-qubit gates.

EVALUATION OF THE SHUTTLING FIDELITY

In this section we show the connection between shuttling fidelity F_{shuttle} and the gate fidelity extracted from single-qubit randomized benchmarking. The $X_{\pi/2,A}$ gate is composed of four shuttling ramps of 2 ns and some idle periods. Because the spin state rotates during the 2 ns-ramp in a predictable way, we consider the 2 ns-ramp as a quantum gate. The average gate fidelity of this single-shuttle gate is taken as shuttling fidelity F_{shuttle}. In principle, the deterministic part of the gate can be compensated by applying a calibrated rotation after the ramp. The stochastic part of the gate (incoherent error) that cannot be compensated contributes to the shuttling infidelity.

In Table 5.9 we list the error sources and find that the wave function uncertainty due to pulse timing is the major error source. The non-integer waiting time between each shuttling step, as well as the differences in execution times of the Clifford gates, result in randomization of this error. We therefore consider the errors as uncorrelated, consistent with the assumptions of randomized benchmarking, and use the relation $r_{X_{\pi/2,A}} = 4r_{\text{shuttle}} + r_{\text{idle}}$, where $r_{X_{\pi/2,A}}$ is the infidelity of $X_{\pi/2,A}$, $r_{\text{shuttle}} = 1 - F_{\text{shuttle}}$ is the shuttling infidelity and r_{idle} is the infidelity that accounts for all the idling operations. This relation gives the lower bound of the shuttling fidelity, $F_{\text{shuttle}} = 1 - r_{\text{shuttle}} \geq 1 - \frac{1}{4} r_{X_{\pi/2,A}}$. Based on the single-qubit RB fidelity $F_{X_{\pi/2,A}} \geq 99.967(4)\%$, we calculate the shuttling fidelity $F_{\text{shuttle}} \geq 99.992(1)\%$. From the gate $X_{\pi/2,B}$ we estimate the shuttling fidelity $F_{\text{shuttle}} \geq 99.980(3)\%$. However, we remark that the quantization axis of qubit B is very close to 45°, which may result in decoupling, and therefore an underestimation of r_{idle} and possibly r_{shuttle}.

5.8. MEASUREMENT AND FIT OF DOUBLE QUANTUM DOT ENERGY SPECTRUM

SINGLE-QUBIT ENERGIES

Using the Ramsey sequence, we measure the free precession frequency as a function of detuning in the double quantum dot system D1-D4 as well as D2-D3, in order to characterize the tunnel couplings, the position of the anti-crossings, and the relative angle of the quantization axes under the voltage settings used for implementing the hopping-based quantum gates. The corresponding charge stability diagrams are shown in Figs. 5.7b, c. Following the modelling approach in the work [21], the system is described in the basis $\{|\mathrm{L},\uparrow_\mathrm{L}\rangle,|\mathrm{L},\downarrow_\mathrm{L}\rangle,|\mathrm{R},\uparrow_\mathrm{L}\rangle,|\mathrm{R},\downarrow_\mathrm{L}\rangle\}$, where 'L' or 'R' indicates the position of the hole in quantum dot $\mathrm{QD_L}$ or $\mathrm{QD_R}$ and $\uparrow_\mathrm{L}$ or $\downarrow_\mathrm{L}$ specifies its spin states in the frame of quantum dot L. Its Hamiltonian is written as:

$$H_{4\times4} = \begin{pmatrix} \epsilon & 0 & t_\mathrm{c} & 0 \\ 0 & \epsilon & 0 & t_\mathrm{c} \\ t_\mathrm{c} & 0 & -\epsilon & 0 \\ 0 & t_\mathrm{c} & 0 & -\epsilon \end{pmatrix} + \frac{1}{2}\mu_\mathrm{B} B \begin{pmatrix} g_\mathrm{L}(\epsilon) & 0 & 0 & 0 \\ 0 & -g_\mathrm{L}(\epsilon) & 0 & 0 \\ 0 & 0 & g_\mathrm{R}(\epsilon)\cos(\theta) & g_\mathrm{R}(\epsilon)\sin(\theta)\mathrm{e}^{-\mathrm{i}\phi} \\ 0 & 0 & g_\mathrm{R}(\epsilon)\sin(\theta)\mathrm{e}^{\mathrm{i}\phi} & -g_\mathrm{R}(\epsilon)\cos(\theta) \end{pmatrix}, \tag{5.1}$$

where ϵ is the detuning energy of the double quantum dot system (taken as zero at the charge transition), μ_B is the Bohr magneton and the g_i are the g-factors of the quantum dot i, θ (ϕ) is the polar (azimuthal) angle between the two quantization axes. An example of the energy levels is shown in Fig. 5.8. We note that this model is similar to that of a flopping-mode qubit [57]. Diagonalizing the Hamiltonian, we obtain the qubit resonance frequency f_res (at the limit of small Zeeman energy $\mu_\mathrm{B}B \ll t_\mathrm{c}$):

$$f_\mathrm{res} = \frac{\mu_\mathrm{B}B}{h} \frac{\sqrt{(2\epsilon^2 + t_\mathrm{c}^2)(g_\mathrm{L}(\epsilon)^2 + g_\mathrm{R}(\epsilon)^2) + 2\epsilon\sqrt{\epsilon^2 + t_\mathrm{c}^2}(g_\mathrm{R}(\epsilon)^2 - g_\mathrm{L}(\epsilon)^2) + 2g_\mathrm{L}(\epsilon)g_\mathrm{R}(\epsilon)t_\mathrm{c}^2\cos(\theta)}}{2\sqrt{\epsilon^2 + t_\mathrm{c}^2}}, \tag{5.2}$$

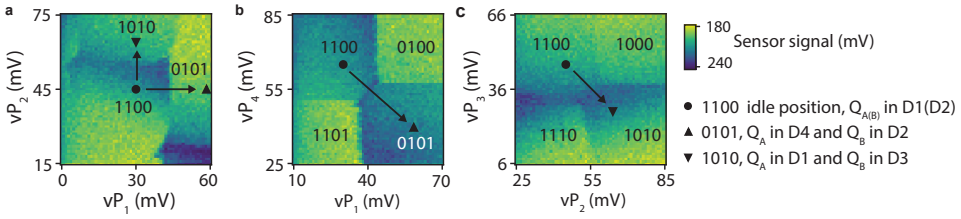

Figure 5.7: **Charge stability diagrams of the shuttling gates.** The diagrams in **a-c** show the voltages of the working points projected on the corresponding virtual plunger gates $\mathrm{vP_i}$. The hole occupancies are labelled as $\mathrm{n_1n_2n_3n_4}$. The idle position is marked as the circle, in which both qubits $\mathrm{Q_A}$ and $\mathrm{Q_B}$ are in quantum dots D1 and D2. The $\mathrm{X}_{\pi/2}$ on $\mathrm{Q_{A(B)}}$ is realized by shuttling between the idle position and the working point marked as the triangle in 0101 (1010) charge occupation.

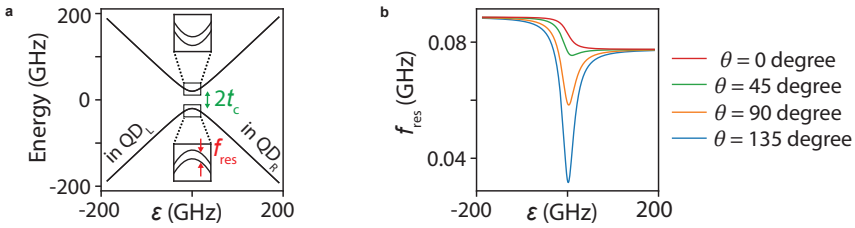

Figure 5.8: **Energy levels of a single spin. a,** An example of energy levels of the single spin in double quantum dot given by Eq. (5.1). **b,** The transition frequency between the lowest two states, f_{res}, as function of detuning energy ϵ for the quantization axes angle θ. Parameters used here: $\mu_B B g_{L(R)} = 0.078(0.089)$ GHz, $t_c = 20$ GHz.

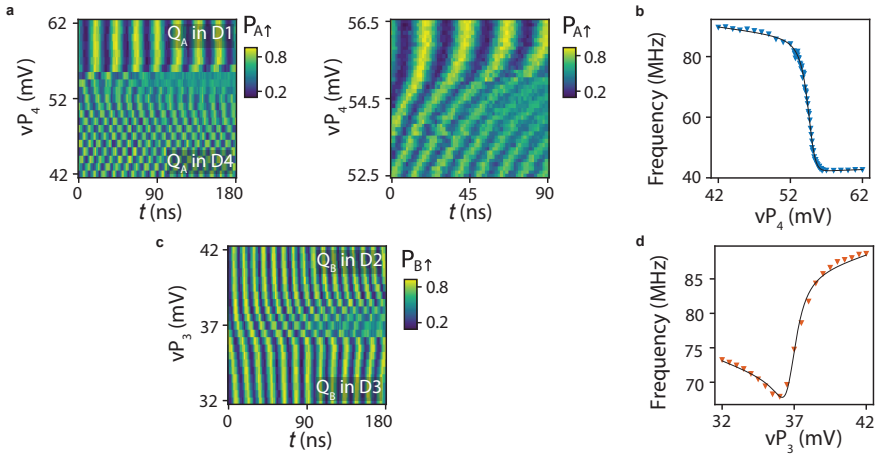

Figure 5.9: **Fitting of tunnel coupling at the shuttling gate settings via spin free precession measurement at the magnetic field of 25 mT. a,** The free evolution of Q_A at different detuning across D1-D4 anti-crossing. The panel on the right is the fine scan around the charge anti-crossing where the frequencies changes rapidly. The oscillation frequencies are extracted and plotted in **b**. **c,** The free evolution of Q_B at different detuning across D2-D3 charge anti-crossing. The oscillation frequencies are extracted and plotted in **d**. The black lines are the fits using Eq. (5.2), with the lever arm $\frac{\Delta\epsilon_{14(23)}}{\Delta vP_{4(3)}} = 0.086(0.082)$eV/V.

Assuming a linear dependence of g-factors $g_{L(R)}(\epsilon)$ on the detuning ϵ, we fit the above formula to the data and extract the tunnel coupling $t_{c,14} = 27 \pm 1$ GHz and the angle between quantization axes $\theta_{14} = 65 \pm 2°$ for the quantum dot pair D1-D4. In the quantum dot pair D2-D3 we extract the tunnel coupling $t_{c,23} = 20 \pm 1$ GHz and the angle $\theta_{23} = 51 \pm 2°$. The results are shown in Fig. 5.9. We notice that the extracted quantization axis angles are higher than the values extracted from the fitting in Fig. 5.1C and Fig. 6c of the supplementary material [31], where $\theta_{14} = 41.5°$ and $\theta_{23} = 44.7°$ (see Section 3 of the supplementary material [31]). This discrepancy might be attributed to the adiabaticity of the shuttling process, and the non-linear g-factor variation as a function of voltages around the charge anti-crossing.

TWO-QUBIT ENERGIES AND COHERENCE TIME

We measure the qubit energies and the coherence times of the two-qubit system as shown in Fig. 5.10. We observe several features, such as the non-monotonic dependence of qubit energies as function of barrier gate voltages. To explain this result, we model the two-qubit system using an extended minimal-size Fermi-Hubbard model with the six basis states $\{ S(2,0),\ S(0,2),\ T^{+}(1,1),\ S(1,1),\ T^{0}(1,1),\ T^{-}(1,1)\}$. The Hamiltonian is written as [58, 59, 60]

$$H_{2Q} = \begin{pmatrix} U+\epsilon_{2Q} & 0 & -t_y + i\,t_x & \sqrt{2}\,t_c & -i\sqrt{2}\,t_z & -t_y - i\,t_x \\ 0 & U-\epsilon_{2Q} & -t_y + i\,t_x & \sqrt{2}\,t_c & -i\sqrt{2}\,t_z & -t_y - i\,t_x \\ -t_y - i\,t_x & -t_y - i\,t_x & hf_{+} & 0 & 0 & 0 \\ \sqrt{2}\,t_c & \sqrt{2}\,t_c & 0 & 0 & hf_{-} & 0 \\ i\sqrt{2}\,t_z & i\sqrt{2}\,t_z & 0 & hf_{-} & 0 & 0 \\ -t_y + i\,t_x & -t_y + i\,t_x & 0 & 0 & 0 & -hf_{+} \end{pmatrix}. \tag{5.3}$$

The charging energy takes the value $U = 2.56$ meV [61]. The detuning energy of the two-spin system is ϵ_{2Q} (which is different than the single-spin system discussed in Section 3 of the supplementary material [31]). The Zeeman interactions are included in $hf_{\pm} = \frac{1}{2}(g_A \pm g_B)\mu_B B$. The hopping between the quantum dots is modelled through a spin-probability conserving tunnel coupling $t_c + i\,t_z$ and a spin-probability non-conserving tunnel coupling $t_x + i\,t_y$. The impact of a magnetic field is described by the Zeeman interaction Hamiltonian, where we use a local spin basis such that the two spins are aligned. Consequently, this redefines the spin-conserving and spin-non-conserving tunnel couplings.

In the experiments, we change the voltage vB_{12} at constant detuning to tune the tunnel couplings (t_c, t_x, t_y, t_z) and the resulting exchange coupling. We assume that all the tunnel couplings change exponentially as a function of the barrier gate [59] $\exp\{(-\frac{1}{2}\kappa \mathrm{vB}_{12})\}$ with identical $\kappa = 0.059$ mV^{-1} and estimate the prefactors by fitting the parameters to our measurements. This assumption also implies that the ratios $t_{x,y,z}/t_c$ remain constant. Since the eigenenergies of Hamiltonian (5.3) only depend on the absolute value of $t_c + i\,t_z$ and $t_x + i\,t_y$ and not on their complex argument (can be easily verified by computing the characteristic polynomial), the phases cannot be estimated by analyzing the eigenenergies. For the Zeeman interactions, we assume the g-factors depend linearly on the gate voltage, $g_{A(B)}(vB_{12}) = g^{(0)}_{A(B)} + g^{(1)}_{A(B)}\,vB_{12}$. Finally, we set the detuning ϵ_{2Q} to a fixed value of zero, because we operate at fixed plunger gate voltages (vP1, vP2) close to the symmetry point for all the two-qubit experiments.

We fit the qubit frequencies in Fig. 5.10c to the eigenenergies of Eq. (5.3). Our fit shows a good agreement between the model and the experiments. We find the relative strength between spin-dependent tunnel couplings to be $\frac{t_x^2+t_y^2}{t_c^2+t_z^2} = 0.11$. The corresponding energy levels are plotted in the inset of Fig. 5.10c, where we identify the anti-crossing between $|\uparrow\downarrow\rangle$ and $|\downarrow\downarrow\rangle$ as the cause of the bending of exchange coupling around $vB_{12} = -85$ mV.

Based on this model, we estimate the dephasing of the two-spin system by considering qubit frequency fluctuations due to three noise sources: the effective electric noise on vB_{12} and fluctuations of the g-factors $g^{(0)}_{A(B)}$ [12]. Assuming $1/f$ noise domi-

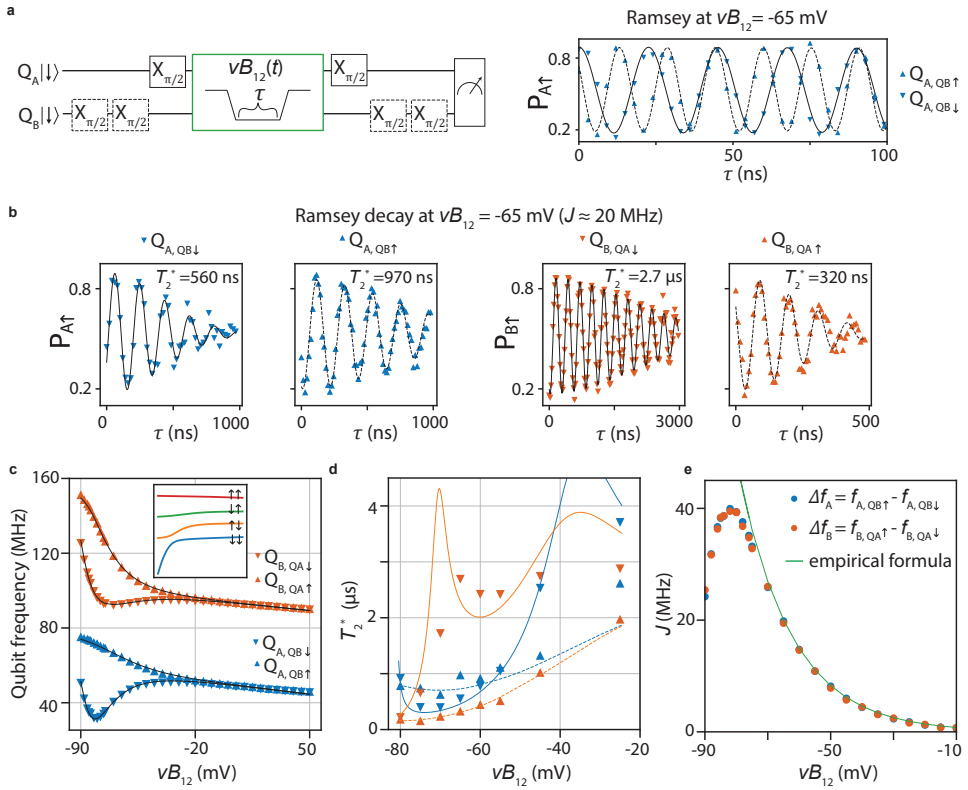

Figure 5.10: **Qubit frequencies and coherence time as a function of virtual barrier voltage at magnetic field of 25 mT. a,** The Ramsey experiments for measuring qubit frequencies as well as the free evolution decay time $T_2^\star$ at various virtual barrier gate voltage vB_{12}. The circuits here is an example of qubit A frequency measurement conditioned on qubit B state. The pulse on vB_{12} is trapezoidal with linear ramp times of 80 ns to avoid diabatic state transitions. **b,** Free induction decay of individual qubit conditioned on the other qubit at $vB_{12} = -65$ mV. The data are fitted to $P(\tau) = A\exp\left(-(\tau/T_2^\star)^2\right) + B$ to extract $T_2^\star$. **c,** The state-dependent qubit frequencies. The fitting results are plotted in black lines, with the energy diagram in the inset. **d,** The $T_2^\star$ measurement and the fitting curves. The sampling time and numbers of sample points are chosen to adapt for the qubit frequencies and decay rates that depends on vB_{12}, resulting in the $T_2^\star$ experiment time of 18-58 seconds for Q_A and 38-133 seconds for Q_B. **e,** The exchange couplings $J = \Delta f_{A(B)}$. The exchange couplings predicted by empirical formula $J = J_0 \exp(-\kappa\ (vB_{12} - \Delta vB_{12}))$ is plotted, where $J_0 = 0.24$ MHz and $\kappa = 0.059$ mV^{-1}, and $\Delta vB_{12} = 10$ mV. One set of the data Δf_A is also plotted in Fig. 5.4C. We note that the data displayed in this figure and in Fig. 5.4C are taken after a charge jump that shifts vB_{12} by about $\Delta vB_{12} = 10$ mV. As an example, the measurement taken at $vB_{12} = -65$ mV in this figure should be considered as the measurement taken at $vB_{12} \approx -75$ mV in other parts of the paper.

nates qubit dephasing, the coherence time reads $T_2^\star = \sqrt{2/(S_{1/f} \ln \frac{0.401}{t_e/t_m})}$ [55, 62], where we define the evolution time t_e as the high-frequency cutoff and the total measurement time t_m as the low-frequency cutoff, $S_{1/f}$ is the strength of the single-sided spectral density of the qubit angular frequency. The strength is related to the noise spectrum of a particular noise source $x \in \{vB_{12}, g_A, g_B\}$ by $S_{1/f} = (\frac{\partial\omega}{\partial x})^2 S^x_{1/f}$, where $\frac{\partial\omega}{\partial x}$ is the sensitivity of the qubit angular frequency and the strength of the $1/f$ noise $S^x_{1/f}$ is defined by

$S^x(\omega) = \int_0^\infty S^x(t)e^{i\omega t}dt = 2\pi S^x_{1/f}/\omega$ with the autocorrelation function $S^x(t) = \langle x(t)x(0)\rangle$. Here we choose $t_e = T_2^\star$ which is the evolution time relevant for a $T_2^\star$ measurement. We assume that the three noise sources are independent and their fluctuations uncorrelated, giving rise to a total dephasing time $T^\star_{2,\text{total}} = 1/\sqrt{{T^\star_{2,\nu B_{12}}}^{-2} + {T^\star_{2,g_A^{(0)}}}^{-2} + {T^\star_{2,g_B^{(0)}}}^{-2}}$. For the transition between two energy levels i and j, we use the derivatives of the transition angular frequency ω_{ij} with respect to the voltage fluctuations to compute theoretical predictions of the coherence time. We pay close attention to the different bandwidths (t_m, t_e) in the respective measurements. For example, the gate voltage noise $S^{\nu B_{12}}_{1/f}$ yields ${T^\star_{2,\nu B_{12}}}^{-2} = \frac{1}{2}\ln\frac{0.401}{t_e/t_m}(\frac{\partial\omega_{ij}}{\partial\nu B_{12}})^2 S^{\nu B_{12}}_{1/f}$. We now use the the fitting parameters obtained in Fig. 5.10c to fit the noise strength $S^{\nu B_{12},g_A,g_B}_{1/f}$ to the coherence time for all the transitions. We estimate the noise strengths by minimizing the square sum of the dephasing rate differences $\Delta\frac{1}{T_2^\star}$ between theoretical and measurement values. Fig. 5.10d shows the fitting results, having qualitative agreement between the model and the experiment. The model reproduce the trend and several features of $T_2^\star(\nu B_{12})$, and also predicts the relative dephasing time of different qubit transitions. We find the noise strength $S^{\nu B_{12}}_{1/f} = 0.031\text{mV}^2$, which is equivalent to $\sigma_{\nu B_{12}} = 0.78$ mV if integrating from 1μ s to 1000 seconds, a typical time scale for Ramsey measurement, and on the same order as the results reported in Ref. [12]. The noise strength of $S^{g_A(g_B)}_{1/f}$ at this magnetic field is equivalent to the qubit frequency noise $S^{f_{QA}(f_{QB})}_{1/f} = (\mu_B B)^2 S^{g_A(g_B)}_{1/f} = 130(200)\text{kHz}^2$, which translates to $\sigma_{f_{QA(QB)}} = 50(63)$ kHz and $T_2^\star = 4.5(3.5)\mu$s if integrating the noise from 1μs to 1000 seconds.

5.9. SIMULATIONS OF THE HOPPING-BASED SINGLE-QUBIT GATES

In the lab frame, we have three different models to describe the spin dynamics with decreasing complexity. The first model considers the full 4×4 Hamiltonian $H_{4\times4}$ as shown in Eq. (5.1). The second model is a 2×2 Hamiltonian $H_{2\times2}$ where the effective magnetic field experienced by the spin depends on the orbital wave function hybridization in the double quantum dot. It can be obtained by projecting the first model onto the orbital ground state, and can be written as

$$H_{2\times2} = \frac{hf_L}{4}(1-\frac{\epsilon}{\sqrt{t_c^2+\epsilon^2}})\begin{pmatrix}1&0\\0&-1\end{pmatrix} + \frac{hf_R}{4}(1+\frac{\epsilon}{\sqrt{t_c^2+\epsilon^2}})\begin{pmatrix}\cos\theta & \sin\theta e^{-i\phi}\\ \sin\theta e^{i\phi} & -\cos\theta\end{pmatrix}. \quad (5.4)$$

The third model is derived by the second model, Eq. (5.4), by taking the limit $t_c \to 0$

$$H_{\text{dis}} = \frac{hf_L}{2}\begin{pmatrix}1&0\\0&-1\end{pmatrix}\Theta(-\epsilon) + \frac{hf_R}{2}\begin{pmatrix}\cos\theta & \sin\theta e^{-i\phi}\\ \sin\theta e^{i\phi} & -\cos\theta\end{pmatrix}\Theta(\epsilon), \quad (5.5)$$

where we have replace the smooth step $\frac{1}{2}(1\mp\frac{\epsilon}{\sqrt{t_c^2+\epsilon^2}})$ by the Heaviside step function $\Theta(\mp\epsilon)$. Essentially, we discretize the dynamics and consider that the spin precession frequency as well as quantization axis angle only takes two discrete values, $\epsilon<0$ and $\epsilon>0$, instead of a continuous transition through the anti-crossing.

Model comparison We use QuTiP to compute the final state and the time evolution under the time dependent detuning $\epsilon_{14}(t)$ as depicted in Fig. 5.11a. The detuning is varied linearly from -337 GHz to 226 GHz, corresponding to the virtual plunger gate voltages shown in Fig. 5.7b, within the ramp time $t_{\text{ramp}} = 2$ ns. Other parameters used in the simulations are: the tunnel coupling $t_{c,14} = 27$ GHz, the angle between quantization axes $\theta_{14} = 65°$, frequency $f_L = 33.8$ MHz, frequency $f_R = 71.5$ MHz.

In Fig. 5.11c,f the small difference between the 2 by 2 model and the full (4 by 4) model shows that the tunnel coupling is large enough such that the charge degree of freedom is adiabatic. This agrees with the estimation of the vanishing Landau Zener probability of the excited orbital state induced by the detuning ramp, $P_{LZ} = \exp\left(-2\pi^2 t_{c,14}^2/(h\frac{d\epsilon_{14}}{dt})\right) = 9.9\times10^{-23}$. In Fig. 5.11d the difference between the discrete model and the full model is less than 0.11%. This good agreement is attributed to the short ramp time, low Larmor frequencies, and the large ratio of the detuning difference over tunnel coupling $\Delta\epsilon_{14}/t_{c,14}$. These conditions make the description of abrupt change of the spin Hamiltonian a good approximation. We use the discrete model in the manuscript and the rest of the supplementary material to describe the spin dynamics that involves multiple shuttling steps.

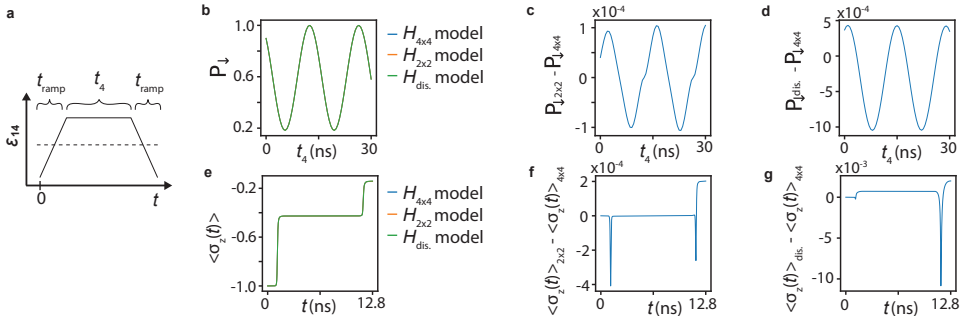

Figure 5.11: **Simulation and comparison of different spin shuttling models. a,** The pulse of detuning $\epsilon_{14}(t)$. **b,** The spin down probability of the final state $P_\downarrow$ as a function of the idle time t_4 in quantum dot D4, with the initial state of spin down. The simulation results given by three different models are plotted in blue, orange and green curves. These curves are overlapping because of the small difference between the curves. **c,** Comparing the 2×2 model and the 4×4 model by plotting the difference of final state spin down probability. **d,** Comparing the discrete model and the 4×4 model. **e,** The simulated state evolution under a detuning pulse, given by three different models. The results are presented in the form of spin polarization $\langle\sigma_Z(t)\rangle$ in the instantaneous eigenbasis at time t. **f,** Comparing the 2×2 model and the 4×4 model by plotting the difference of instantaneous spin polarization. **g,** Comparing the discrete model and the 4×4 model. In **e-g** the detuning pulse with $t_4 = 8.8$ ns is used in the simulation to show the maximal discrepancy between the models, based on the observation in (d) that the maximal deviation occurs around $t_4 = 8.8$ ns.

Impact of the azimuthal shuttling angle ϕ A two-shuttle process, shuttling to quantum dot 2 and back is described in the following by the time evolution

$$U(\theta,\phi,t) = \exp\left\{\left[-i\pi f_B t\begin{pmatrix}\cos\theta & \sin\theta e^{-i\phi}\\ \sin\theta e^{i\phi} & -\cos\theta\end{pmatrix}\right]\right\}. \tag{5.6}$$

While the polar shuttling angle θ is essential for the gate implementation, the azimuthal angle only adds a spin-dependent phase to the double-quantum dot system. This can be easily verified by the transformation

$$U(\theta,\phi,t) \rightarrow e^{i\beta\sigma_z/2}U(\theta,\phi,t)e^{-i\beta\sigma_z/2} \tag{5.7}$$

$$= U(\theta,\phi+\beta,t). \tag{5.8}$$

Since all remaining gates, the single-qubit z-gate implemented via idling and also the two-qubit CZ gate, commute with the phase gate, we can choose $\beta = -\phi$ allowing us to drop the azimuthal angle.

Gate simulations We use the discrete model in the lab frame to simulate an eight-shuttle process as a function of wait time in two double quantum dots, as shown in Fig. 5.12. The process consists of two identical four-shuttle pulses and a wait time in between, $\tau = 1/f_B$, which is assumed to be an identity operation. The time evolution of a four-shuttle pulse is a series of free precession for various duration $\{t_{2r},\ t_3+dt_3,\ t_2+dt_2,\ t_3+dt_3,\ t_{2r}\}$ around the corresponding quantization axes in {D2, D3, D2, D3, D2} with two distinct frequencies $\{f_{D2},\ f_{D3},\ f_{D2},\ f_{D3},\ f_{D2}\}$ as depicted in Fig. 5.12b. For simplicity we assume the Larmor frequencies of the dots to not change with detuning. Fitting to the experimental data gives $t_{2r} = 1.16$ ns, $dt_3 = 1.54$ ns, $dt_2 = 2.29$ ns, $f_{D2} = 70.9$ MHz, $f_{D3} = 62.0$ MHz, $\theta_{23} = 44.7°$ (different than $\theta_{23} = 51°$ obtained in Section 5.8). Applying the same fitting procedure for the quantum dot pair D1-D4 as shown in Fig. 5.1C, we obtain $t_{1r} = 0.98$ ns, $dt_4 = 1.94$ ns, $dt_1 = 1.94$ ns, $f_{D1} = 33.8$ MHz, $f_{D4} = 71.5$ MHz, $\theta_{14} = 41.5°$ (different than $\theta_{14} = 65°$ obtained in Section 5.8). For both double quantum dot pairs this effective model fits well to the experimental data. Based on the fitted parameters, we can find the wait times $t_2,\ t_3$ ($t_1,\ t_4$) in the individual quantum dot to construct a desired spin state rotation $R(\hat{n},\theta)$ on qubit Q_A (Q_B), as shown in the contour lines in Fig. 5.12c. Specifically, the $X_{\pi/2}$ gate is the rotation that satisfies the rotation angle $\theta = 90°$ as well as the rotation axis lying on the Bloch sphere equator, $\hat{n} \perp \hat{z}$. The rotation axis can be chosen to point along x-axis by redefining the azimuthal angle of the Bloch sphere, as shown in the previous paragraph.

When the waiting times lead to an exact $X_{\pi/2}$ gate, the spin-up probability shows a local maximum. This property is used for the initial tune-up in the experiment. The subsequent fine-tuning consists of calibrating the rotation axis direction via AllXY sequence [32], as shown in Fig. 5.13d. The calibration of the rotation angle is done by applying numbers of $X_{\pi/2}$ gate to amplify over-rotation error. The tuned-up $X_{\pi/2}$ gates are shown in Fig. 5.13d,e. The simulation of the state evolution is plotted in Fig. 5.13b,c.

Alternative pulse scheme We further consider the pulse with unequal wait times for the gate on qubit Q_A. We design the pulse such that the first rotation in D4 is π and the subsequent rotations in D1 and D4 are either close to π or 2π. The intuition is that, in this scheme the polarization $\langle\sigma_Z\rangle$ of the final state evolved from the initial spin-down state might have weaker dependence on the frequency fluctuations in D1 and D4, which may result in a gate rotation angle θ that is more robust against noise. We use the discrete model and the fitted parameters obtained above to compute the required waveform of the detuning pulse, as shown in Fig. 5.14a. It gives $t_{4a} = 3.65$ ns, $t_{1a} = 19.75$ ns,

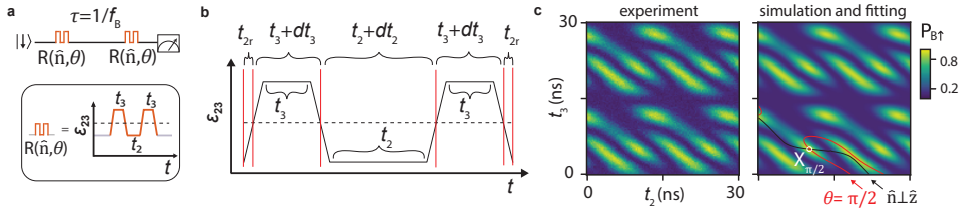

Figure 5.12: **Initial tune-up of the single qubit gate on qubit** Q_B**. a,** The pulse sequence for the experiment. **b,** The detuning pulse considered in the simulation. The horizontal dashed line marks the D2-D3 charge anti-crossing. The vertical red lines mark the start and end of individual evolution time $\{t_{2r},\ t_3+dt_3,\ t_2+dt_2,\ t_3+dt_3,\ t_{2r}\}$. **c,** The measured spin-up probability $P_{A\uparrow}(t_2,t_3)$ at magnetic field 20 mT is shown on the left. The simulation result is on the right. The black contour line indicates the wait times (t_2,t_3) in which the rotation axis $\hat{n}$ is on the equator of the Bloch sphere, while on the red lines indicate the rotation angle $\theta=\pi/2$. The intersection, marked in white, is the conditions for $X_{\pi/2}$ gates and corresponds to maximal spin-up probability. The black lines and red lines are periodic in t_2 and t_3, while for clear illustration we only plot a few of them.

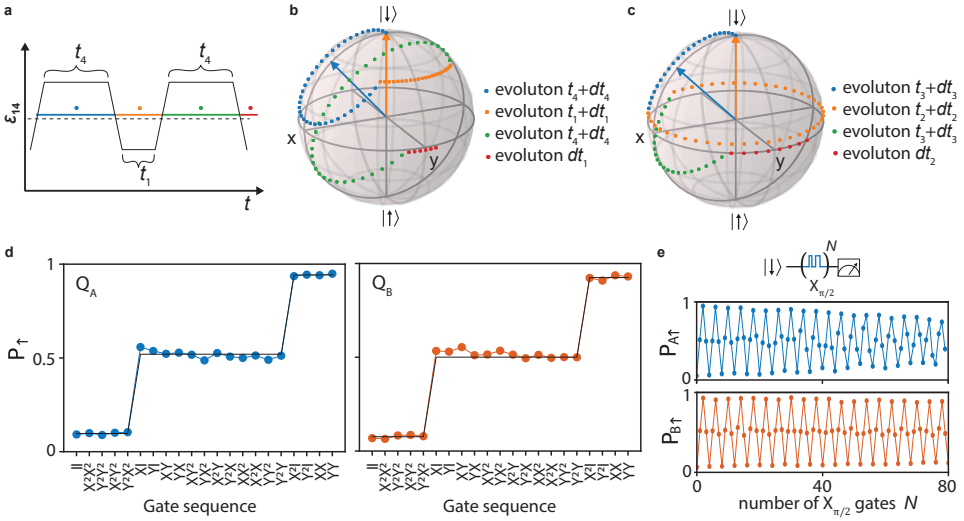

Figure 5.13: **Simulation and calibration of** $X_{\pi/2}$ **gates with equal wait times at 20 mT. a,** The detuning pulse $\epsilon_{14}(t)$ of the gate $X_{\pi/2,A}$ with equal wait times t_4 in D4. The horizontal dashed line marks the D1-D4 charge anti-crossing. In different parts of the pulse, marked by {blue,orange,green,red} lines, the spin rotates around quantization axes of {D4,D1,D4,D1} with frequencies $\{f_{D4}, f_{D1}, f_{D4}, f_{D1}\}$. The simulated state evolution, with the initial state $|\downarrow\rangle$, is plotted in **b**. The states at time t are plotted as points on the Bloch sphere with time step of 0.3 ns. The quantization axis of D1(D4) is represented by the orange (blue) arrow. **c,** The simulated state evolution of the gate $X_{\pi/2,B}$ with the initial state $|\downarrow\rangle$. **d,** The measured spin-up probability of Q_A and Q_B in AllXY experiments after the gates are calibrated. In each graph, three sections of the black horizontal lines mark the expected outcome of the ideal gates and take into account the state preparation and measurement (SPAM) error. If there is no SPAM error the black horizontal lines are at values of 0, 0.5, and 1. **e,** The spin-up probability after applying repeated $X_{\pi/2}$ gates on each qubit.

	four-shuttle X_A with unequal wait times		four-shuttle X_A with equal wait times	
	$\Delta\theta_{\text{rot}}(^\circ)$	$\Delta\theta_{\hat{\text{n}}}(^\circ)$	$\Delta\theta_{\text{rot}}(^\circ)$	$\Delta\theta_{\hat{\text{n}}}(^\circ)$
$\Delta f_{\text{D1}} = 100$ kHz	-0.22	1.44	-0.11	1.22
$\Delta f_{\text{D4}} = 100$ kHz	0.019	0.44	-0.53	0.34
$\Delta\theta_{14} = 0.1^\circ$	0.21	0.034	0.17	0.12
$\Delta\epsilon_{14,\text{AC}} = 10\mu eV$	-0.037	-0.49	0.67	-0.16

Table 5.7: **Estimation of X_A gate sensitivity to the fluctuations of the system parameters.** Here we assume both gates are operated at 25 mT. The values of uncertainty are not the measured values. They are chosen to make the calculation easier.

$t_{4b} = 10.51$ ns, $t_{1a} = 8.17$ ns. In the experiment we start with this set of wait times and further fine-tune the wait times using AllXY sequence and the repetition sequence $X^N_{\pi/2}$. The parameters after calibration experiments are $t_{4a} = 3.747$ ns, $t_{1a} = 19.33$ ns, $t_{4b} = 10.17$ ns, $t_{1a} = 9.4$ ns, which are close to the initial values predicted by the model. The AllXY and repetition sequences of a calibrated $X_{\pi/2,A}$ gate are shown in Fig. 5.14e,f. When comparing to Fig. 5.13e, the extended decay time in Fig. 5.14f might be explained by the pulse designed to be more robust in rotation angle. Further discussion and estimation are in Table 5.7 and the corresponding paragraph.

For the $X_{\pi/2}$ on qubit Q_B, we design a two-shuttle pulse because the quantization axis angle $\theta_{23} = 44.7^\circ$ is very close to 45°. In theory, the angle 45° can realize a gate with only two shuttles and at the same time have rotation angle insensitive to frequency fluctuations in both quantum dots. We therefore implement the two-shuttle gate in our experiment, even though in theory it will not make an exact $X_{\pi/2}$. Following similar procedure as described above, we start from the predicted values $t_3 = 4.91$ ns and $t_2 = 3.35$ ns (assume $\theta_{23} = 45^\circ$), perform calibration experiments and determine $t_3 = 4.86$ ns and $t_2 = 3.42$ ns, which only differ slightly from the initial predictions. The AllXY and repetition sequences of a calibrated $X_{\pi/2,B}$ gates are shown in Fig. 5.14e,f. These results show that the gate we created is very close to $X_{\pi/2}$. In particular from the repetition sequence in Fig. 5.14f we estimate a small rotation angle error $\sigma_{\theta,\text{rep}} = 0.2^\circ$. An alternative estimation using gate set tomography (GST) (Table 5.2) shows a small rotation angle error $\sigma_{\theta,\text{GST}} = 0.29^\circ$. Combining the rotation angle error $\sigma_{\theta,\text{GST(rep)}}$ and the values $\Delta\theta_{\text{rot}}, \Delta\theta_{23}$ in Table 5.8, we can estimate the lower bound $\theta_{23,\text{GST(rep)}} \geq 44.86(44.9)^\circ$.

The drift or fluctuation in the Larmor frequency, in the quantization axis angle, and in the timing of individual shuttling event can contribute to the gate rotation error. Using the model and parameters described above, we can estimate the corresponding variations of gate rotation angle θ_{rot} and the polar angle of the rotation direction $\theta_{\hat{\text{n}}} = \arccos(\hat{\text{n}} \cdot \hat{\text{z}})$. We denote such variations as $\Delta\theta_{\text{rot}}$ and $\Delta\theta_{\hat{\text{n}}}$. We consider the timing error of the shuttling events caused by the fluctuations in the position of the charge anti-crossing $\Delta\epsilon_{\text{ij,AC}}$. It is estimated to be $t_{\text{ramp}}\Delta\epsilon_{\text{ij,AC}}/\Delta\epsilon_{ij}$. The estimation is summarized in Table 5.7 and Table 5.8. From the estimation we observe the rotation angle θ_{rot} of the modified gates is more robust against fluctuations on most of the parameters. On the other hand, the rotation axis direction becomes more sensitive to certain parameters.

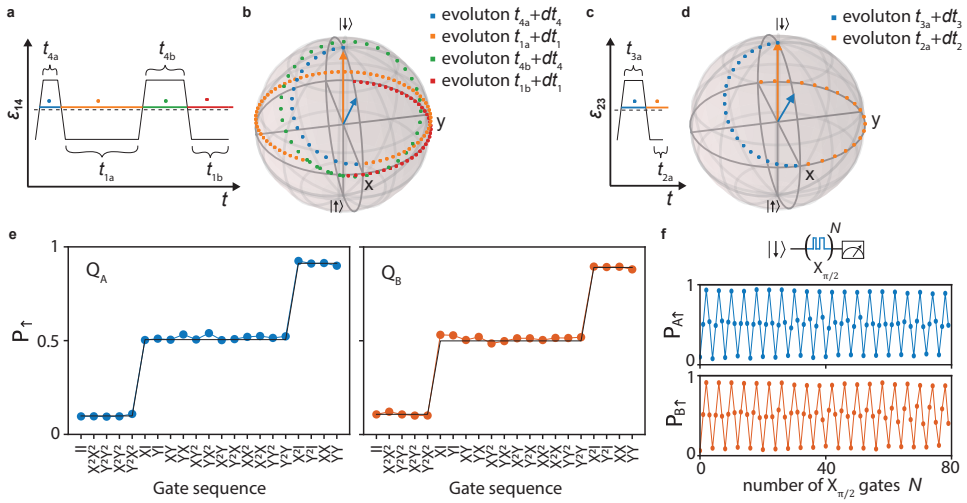

Figure 5.14: **Simulation and calibration of $X_{\pi/2}$ gates with unequal wait times at 25 mT. a,** The detuning pulse $\epsilon_{14}(t)$ of the gate $X_{\pi/2,A}$ with unequal wait times (t_{1a}, t_{1b}) in D1 and (t_{4a}, t_{4b}) in D4. The horizontal dashed line marks the D1-D4 charge anti-crossing. In different parts of the pulse, marked by {blue,orange,green,red} lines, the spin rotates around quantization axes of {D4,D1,D4,D1} with frequencies $\{f_{D4}, f_{D1}, f_{D4}, f_{D1}\}$. The simulated state evolution, with the initial state $|\downarrow\rangle$, is plotted in **b**. The states at time t are plotted as points on the Bloch sphere with time step of 0.3 ns. The quantization axis of D1(D4) is represented by the orange (blue) arrow. **c,** The detuning pulse $\epsilon_{23}(t)$ of the gate $X_{\pi/2,B}$ with two shuttles. **d,** The simulated state evolution of the gate $X_{\pi/2,B}$ with the initial state $|\downarrow\rangle$. **e,** The measured spin-up probability of Q_A and Q_B in AllXY experiments after the gates are calibrated. In each graph, three sections of the black horizontal lines mark the expected outcome of the ideal gates and take into account the state preparation and measurement (SPAM) error. If there is no SPAM error the black horizontal lines are at values of 0, 0.5, and 1. **f,** The spin-up probability after applying repeated $X_{\pi/2}$ gates on each qubit. Here we replot the data in Fig. 5.2C for easier comparison with Fig. 5.13e.

	two-shuttle X_B		four-shuttle X_B with equal wait times	
	$\Delta\theta_{rot}(^\circ)$	$\Delta\theta_{\hat{n}}(^\circ)$	$\Delta\theta_{rot}(^\circ)$	$\Delta\theta_{\hat{n}}(^\circ)$
$\Delta f_{D2} = 100$ kHz	0.0036	0.51	-0.46	0.58
$\Delta f_{D3} = 100$ kHz	0.0037	0.16	-0.29	0.24
$\Delta\theta_{23} = 0.1^\circ$	0.2	-0.0023	0.11	0.14
$\Delta\epsilon_{23,AC} = 10\mu eV$	-8.5×10^{-3}	-0.095	0.070	-0.27

Table 5.8: **Estimation of X_B gate sensitivity to the fluctuations of the system parameters.** Here we assume both gates are operated at 25 mT. The values of uncertainty are not the measured values. They are chosen to make the calculation easier.

5.10. ERROR MODELING

ERROR MODELING OF THE HOPPING-BASED SINGLE-QUBIT GATE

Noise estimation We model incoherent error originating from (1) fluctuations in Larmor frequencies of the individual quantum dot, (2) fluctuations in detuning energies, (3) waveform uncertainty, and (4) thermalization processes near the charge anti-crossing. First we estimate the noise strength of individual error sources. From the $T_2^\star = 7.0(4.5)\mu s$ of the static qubit A(B) at 25 mT, we estimate Larmor frequency fluctuation $\sigma_f = \frac{1}{\sqrt{2}\pi T_2^\star} =$ 32 kHz for Q_A and $\sigma_f = 50$ kHz for Q_B. For Larmor frequency fluctuations in D3 and D4, we assume that they are uncorrelated and have equal magnitude as Q_B. From the fitting of the coherence times in Fig. 5.15, we obtain the effective electric noise $\delta vP_4(\delta vP_3) =$ 0.19(0.14) mV, which is equivalent to the fluctuations in the position of the charge anti-crossing $\Delta\epsilon_{14(23),AC} = 17(12)\mu$eV and creates the timing fluctuation of 14(23) ps for shuttling operations of Q_A (Q_B). For the errors from waveform uncertainty (Fig. 5.21d), we compute the expected waveforms of the gates $X_{\pi/2,A(B)}$ for the time shifts t_{shift} ranging from 0 to 0.99 ns. Each waveform results in slightly different timing of shuttling, and therefore contributes to incoherent error.

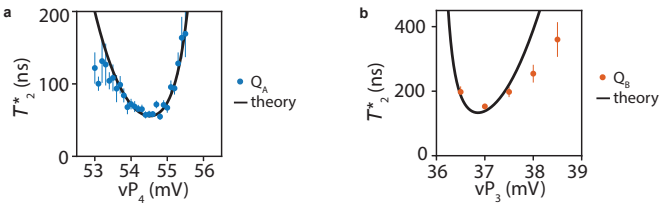

Figure 5.15: **Qubit coherence times near the charge anticrossings.** The coherence time for qubit A **(a)** and qubit B **(b)** extracted from Fig. 5.9 by fitting to the formula $P_1(\tau) = A\exp\left(-(\tau/T_2^\star)^2\right) + B$. The black curves are the expected coherence time assuming quasi-static electric noise on the gates vP4(vP3), $T_2^\star = \frac{1}{\sqrt{2}\pi\sigma_f}$ and the voltage-dependent qubit frequency fluctuation is $\sigma_f \approx \frac{\partial f}{\partial vP_i}\delta vP_i + \frac{1}{2}\frac{\partial^2 f}{\partial vP_i^2}\delta vP_i^2$ [63, 57]. We estimate the effective electric noise $\delta vP_4(\delta vP_3) = 0.19(0.14)$ mV, which minimize the square sum of dephasing rate difference $\Delta\frac{1}{T^\star}$ between the measured values and the theoretical values.

Error model We use the discrete model (Eq. (4) of the supplementary material [31]) to compute the unitary matrices of the target gates and noisy gates, and estimate the incoherent error. The method is described as follow. The unitary of a gate U is a series of free precession for various duration around the corresponding quantization axes of the quantum dots with different frequencies as depicted in Fig. 6b of the supplementary material [31]. A noise source can either change the duration or change the precession frequencies, resulting in a slightly different gate unitary. Averaging over the distribution of the noise parameter gives average gate infidelity, similar to the method used in Section 5.10. For the calculation of errors caused by waveform uncertainty, instead of using a single target unitary, we use a set of target unitaries generated by the waveforms with uniformly distributed time shift t_{shift}. This treatment results in a range of infidelity rather than a single value. We also estimated infidelity caused by T_1-like processes, where the qubits are thermalized to 50-50 population around the charge anti-

Error source	$X_{\pi/2,A}$ infidelity ($\times 10^{-5}$)	$X_{\pi/2,B}$ infidelity ($\times 10^{-5}$)
Larmor frequency fluctuations	3.1	0.8
detuning noise	7.2	0.13
waveform uncertainty	4.0 - 14.6	5.1 - 17.2
thermalization	0.04	0.05
total infidelity	14.3 - 25.0	6.0 - 18.1

Table 5.9: **Incoherent error estimation.** Here we present the error metric in terms of average gate infidelity in single-qubit space.

crossing with the time scale $1/\Gamma(\epsilon)$. This time scale depends on the detuning ϵ and has a minimum value around 300μs. The corresponding infidelity per gate is therefore estimated by integrating the transition rates over the ramp time and multiplying the number of shuttles, $\frac{N_{\text{shuttle}}}{3}\int_0^{t_{\text{ramp}}}\Gamma(\epsilon(t))dt$.

As summarized in Table 5.9, the results show that a large portion of errors arises from the waveform uncertainty. The relative impact of the detuning noise and Larmor frequency fluctuations depends on the details of the pulses and quantization axes angle. The thermalization process has little contribution, because of the extended thermalization time at low field and the short ramp time we use. The estimated infidelity of both qubits are on the same order as the measured infidelity, $r_{\text{X,A(B)}} \approx 0.03\ (0.04)\%$ given by randomized benchmarking (RB) and $r_{\text{X,A(B)}} \approx 0.06\ (0.02)\%$ given by gate set tomography (GST). The deviations can arise from unaccounted error sources as well as the robustness of the benchmarking protocols under realistic experimental conditions.

5

ERROR MODELING OF THE TWO-QUBIT GATE

In this section we estimate the average gate infidelity of the CZ gate due to the coherent error and incoherent error. In a d-dimensional Hilbert space, for a unitary operation implemented in the experiment, U_{exp}, the corresponding average fidelity is [64]

$$F = \frac{|\text{tr}(U_{\text{ideal}}^{-1}U_{\text{exp}})|^2 + d}{d(d+1)}. \tag{5.9}$$

Coherent error To evaluate coherent errors, we compute the time evolution of the two-qubit state under the influence of the gate voltage pulse $\nu B_{12}(t)$ with a pulse shape matching a Hamming window [37] as depicted in Fig. 5.4D by solving the time-dependent Schrödinger equation numerically [65]. If the system evolves adiabatically, the final state only acquires one conditional two-qubit phase and two single-qubit phases. These phases can be calibrated in the experiment by fine-tuning the time and amplitude of the pulse [37]. On the other hand, non-adiabatic state transitions, as shown in Fig. 5.26cd, result in errors that cannot be simply calibrated. In our simulation, we fine-tune the voltage pulses $\nu B_{12}(t)$ to achieve a conditional phase of π, compute the unitary time evolution operator of the quantum process without noise, and compensate for the single qubit Z rotations. We find the resulting unitary evolution has an average gate infidelity 0.089%. Additionally, we decompose the error in the Pauli basis and express the simulated unitary by the dominant terms, $U_{\text{exp}} = e^{-i(-0.010\text{YI}-0.021\text{XY}+0.021\text{YX})}U_{\text{ideal}}$. This

result is in good agreement with the fact that the implemented pulse shape is designed to suppress the transition $|\uparrow\downarrow\rangle \rightarrow |\downarrow\uparrow\rangle$ while the transitions induced by spin-non-conserving tunneling are not fully suppressed. We believe that a further reduction of non-adiabatic transitions can be achieved by incorporating Eq. (5.3) directly into the optimization process for finding the pulse.

Incoherent error Incoherent errors are dominantly caused by the 1/f-type low-frequency fluctuations in νB_{12} and g-factors $g_{\mathrm{A,B}}$, which result in the random deviations of the unitary operation U_{exp} from the ideal operation U_{ideal}. We can now write the unitary operation $U_{\mathrm{exp}}(x)$ that is dependent on a stochastic parameter x of the noise source. While this can be straightforward generalized to multiple sources, we consider for simplicity only fluctuations of the accumulated phases and neglect fluctuations of the transition matrix elements caused by the non-adiabatic time evolution discussed in the previous paragraph. This allows us to further approximate the 1/f spectral noise with quasistatic fluctuations by integrating over the corresponding frequencies $\sigma^2 = 2\int_{t_{\mathrm{m}}^{-1}}^{t_{\mathrm{e}}^{-1}} \frac{S_x}{f}\, df$. Assuming x to be a stochastic variable drawn from a Gaussian distribution with zero mean and standard deviation of σ, we can replace the quantity $|\mathrm{tr}(U_{\mathrm{ideal}}^{-1}U_{\mathrm{exp}})|$ in Eq. (5.9) with the expectation value [66, 67],

$$\langle|\mathrm{tr}(U_{\mathrm{ideal}}^{-1}U_{\mathrm{exp}})|^2\rangle = \int_{-\infty}^{\infty} |\mathrm{tr}(U_{\mathrm{ideal}}^{-1}U_{\mathrm{exp}}(x))|^2 \frac{1}{\sqrt{2\pi}\sigma} e^{-\frac{x^2}{2\sigma^2}}\, dx. \tag{5.10}$$

We estimate the accumulated phases by integrating the qubit frequencies $f_{\mathrm{Qi,Qj}}(t,x)$ over time under the influence of the voltage pulse $\nu B_{12}(t)$ and the noise amplitude x. The corresponding (stochastic) unitary matrix in the basis $|\downarrow\downarrow\rangle, |\uparrow\downarrow\rangle, |\downarrow\uparrow\rangle, |\uparrow\uparrow\rangle$ is then given by

$$U_{\mathrm{exp}}(x) = \begin{pmatrix} 1 & 0 & 0 & 0 \\ 0 & e^{-2\pi i \int f_{\mathrm{QB,QA}\downarrow}(t,x)dt} & 0 & 0 \\ 0 & 0 & e^{-2\pi i \int f_{\mathrm{QA,QB}\downarrow}(t,x)dt} & 0 \\ 0 & 0 & 0 & e^{-2\pi i \int f_{\mathrm{QA,QB}\downarrow}(t,x)+f_{\mathrm{QB,QA}\uparrow}(t,x)dt} \end{pmatrix}. \tag{5.11}$$

The standard deviation of the noise σ is estimated in a way similar to the $T_2^\star$ fitting in Fig. 5.10d and depends on the low(high)-frequency cutoff $t_{\mathrm{m}}^{-1}(t_{\mathrm{e}}^{-1})$ as $\sigma \propto \frac{1}{T_2^\star} \propto \sqrt{\ln \frac{0.401}{t_{\mathrm{e}}/t_{\mathrm{m}}}}$ [55, 62]. In the case of two-qubit IRB experiments, the total experimental time is $t_{\mathrm{m}} = 2680$ s and t_{e} is chosen as the total gate time of 108 ns (including padding time). Based on these experimental conditions and the results of the $T_2^\star$ fitting in Section 5.8, we estimate the effective standard deviations $\sigma_{\nu B_{12}} = 0.88$ mV, $\sigma_{f_{\mathrm{QA}}} = 57$ kHz and $\sigma_{f_{\mathrm{QB}}} = 72$ kHz during the IRB experiments. Taking the above considerations, we obtain an average gate infidelity 0.23%, where the main contribution from the noise is caused by fluctuations of νB_{12} accounting for an error of 0.19%.

In summary, we find that incoherent error caused by dephasing are dominant over coherent errors for the average gate fidelity. The total average gate infidelity from the models is equal to 0.32%, which is on the same scale as the estimated value of 0.67 ± 0.09% extracted from the IRB experiment, while it significantly differs from the estimated value of 1.87 ± 0.52% extracted from the GST experiment (Table 5.1 and Table 5.4). The

deviations can arise from unaccounted error sources as well as the robustness of the benchmarking protocols under realistic experimental conditions.

5.11. CHARGE TUNING AND VIRTUAL GATE CONTROL OF THE 10 QUANTUM DOT ARRAY

We prepare the 10 quantum dot system shown in Fig. 5.16 in the charge configuration with D1 and D4 in the single-hole regime, and the others in the empty charge regime. Figs. 5.17a-k display the charge stability diagrams acquired via charge sensing as a function of virtual plunger gates. At first, a virtual gate framework, with virtual matrix shown in Fig. 5.18, is defined in software to:

- compensate the cross-capacitance of each gate with fast (ac) control to the four charge sensors;
- achieve independent control of the quantum dots chemical potentials via virtual plunger gates vP1-vP10.

A second matrix, shown in Fig. 5.19, is used for the definition of virtual barriers J1-J12, as a linear combinations of vB1-vB12 and vP1-vP10. J1-J12 serve to independently control the interdot tunnel couplings, without changing the quantum dots chemical potentials.

5.12. HOPPING-INDUCED OSCILLATIONS IN OCCUPIED QUANTUM DOTS

Obtaining shuttling-induced oscillation in occupied quantum dots (as for the case of the filled quantum dots D1 and D4 of the main text) requires shuttling the spin back and forth between the corresponding quantum dot and an empty neighboring dot. In this section we motivate our procedure and explain why shuttling two times is required.
We assume to have two quantum dots D1 and D2 with a spin qubit Q1 in D1, and D2 empty. For simplicity, both sites have a g-factor of 0.05 and have a quantisation angle difference of 0.3π. If we want to obtain shuttling-induced oscillations of Q1 in D1, it is not sufficient to shuttle Q1 using the sequence D1 → D2 → D1, since the rotation in D1 needs to be projected onto another quantisation axis. Hence, we require shuttling the spin Q1 using this sequence: D1 → D2 → D1 → D2 → D1, as displayed in Fig. 5.20a. Here, we vary the second time in D1 and wait 10 ns between all shuttle events. This protocol enables to convert the free evolution in D1 around the z axis to a rotation around a different axis of the D1 Bloch sphere. The resulting oscillation is shown in Fig. 5.20b. The corresponding state evolution in the Bloch sphere for the points labelled as i-viii in Fig. 5.20b, are shown in Fig. 5.20c.

5.13. EXTENDED DATA

TIMING PRECISION OF SHUTTLING PULSES

High fidelity hopping-based gates require a precise timing of shuttling pulses. A qubit fidelity above 99.99% can be achieved when the rotation has an incoherent error of less than 1.3 degrees. In a simplified example where two quantum dots having quantization axes which are perpendicular, the timing error of ramps for an $X_{\pi/2}$ shuttling gate on a qubit with a Larmor frequency of 40 MHz should be less than 90 ps. This timing precision is far below the sample rate of 1 GSa/s of the used AWG. Ramps can be timed with

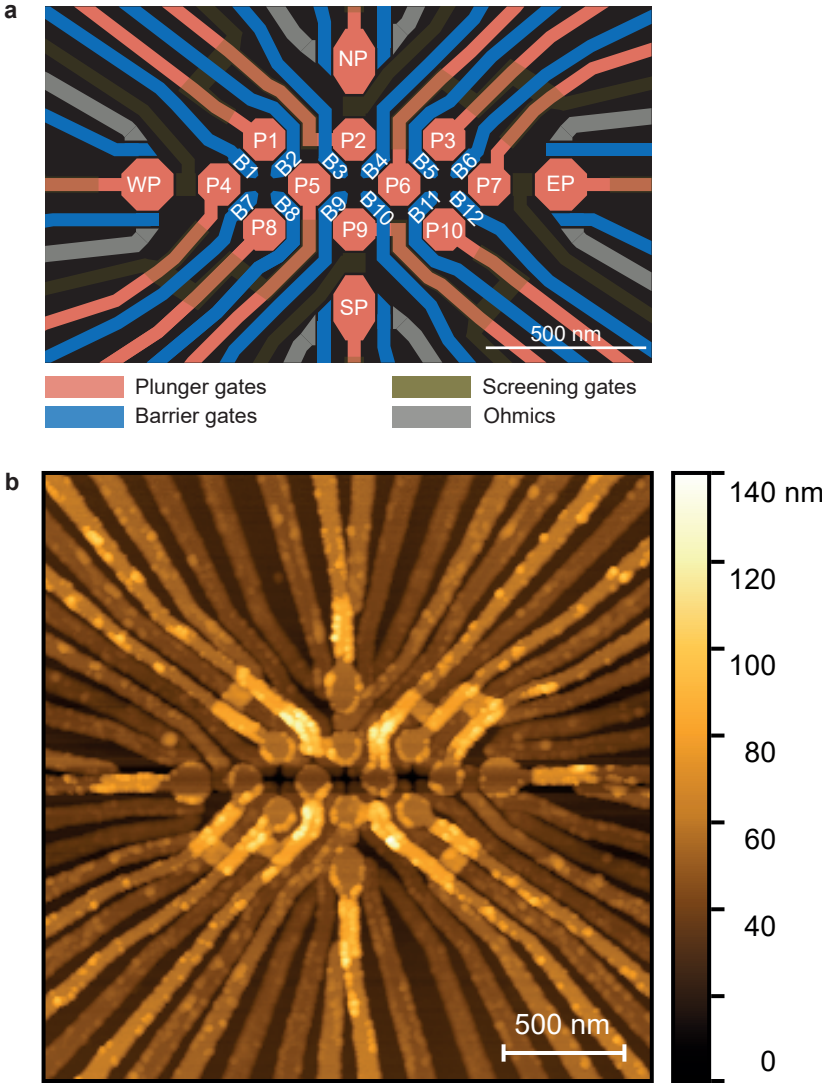

Figure 5.16: **The 10 quantum dot array device. a,** Layout of the device indicating the names of the relevant gates. Plungers and barriers are labelled with P and B, respectively. In analogy to the cardinal coordinates, the sensors plunger gates are labelled as NP (north), EP (east), SP (south), and WP (west). **b,** Atomic force microscopy image of the device.

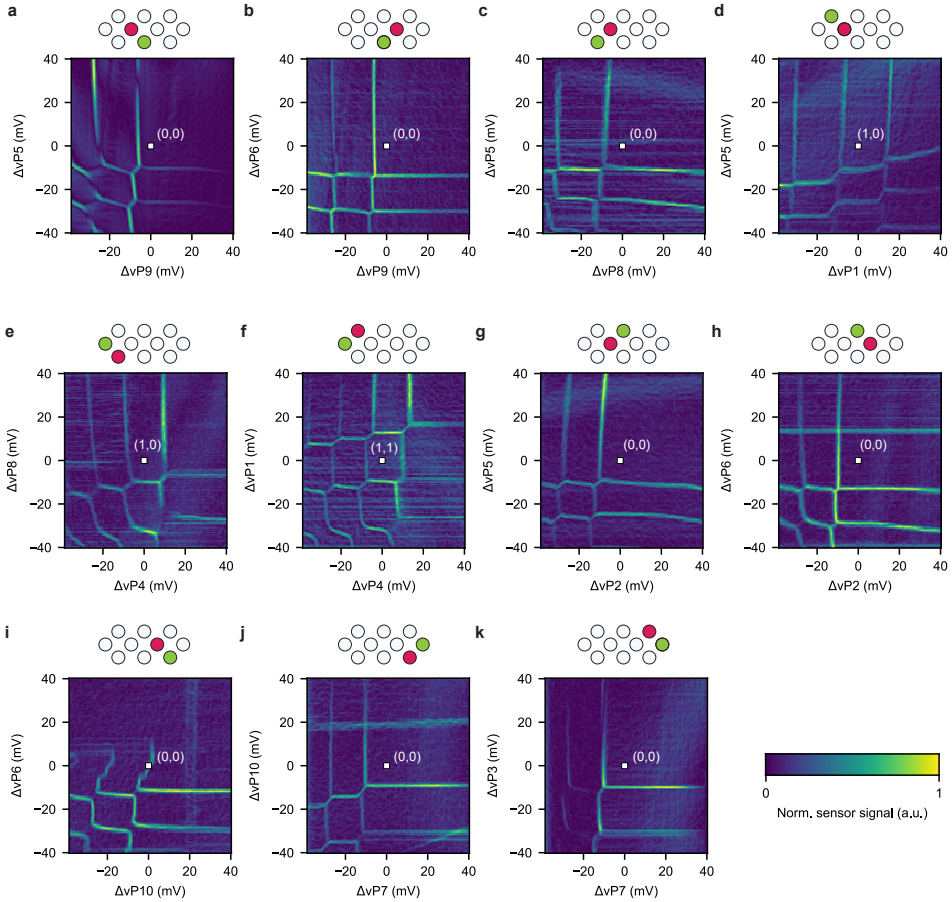

Figure 5.17: **Charge tune-up in the 10 quantum dot array. a-k,** Charge stability diagrams of the 10 quantum dot system showcasing the transition lines of each quantum dot. At the centre of each map (white square), quantum dots D1 and D4 are prepared in the single-hole regime, while all the other quantum dots are in an empty state. In the schematic above each map, the green quantum dot is tuned by the gate swept on the x axis, and the red dot by the gate swept on the y axis. The horizontal lines at ΔvP6 ~ 15 mV in panel **h** and at ΔvP10 ~ 20 mV are spurious quantum dots transition lines, while the deformation of the vertical transition lines in **i** is due to charge latching effects. Δv*Pi* indicates a relative voltage swing with respect to the dc voltage point.

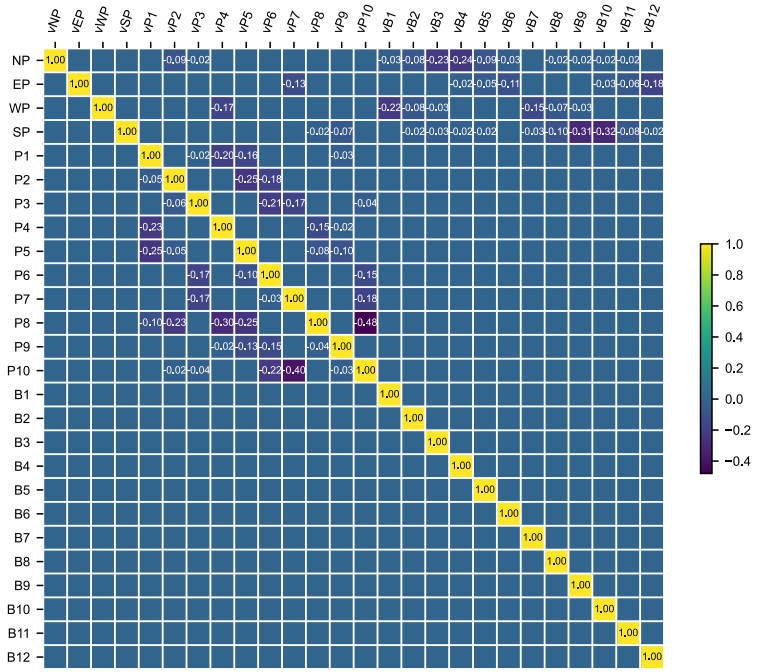

Figure 5.18: **Virtual gate matrix.** Virtual gates are defined to compensate the crosstalk to the charge sensors and to obtain independent control of the chemical potential of each quantum dot via virtual plungers (vP1-vP10).

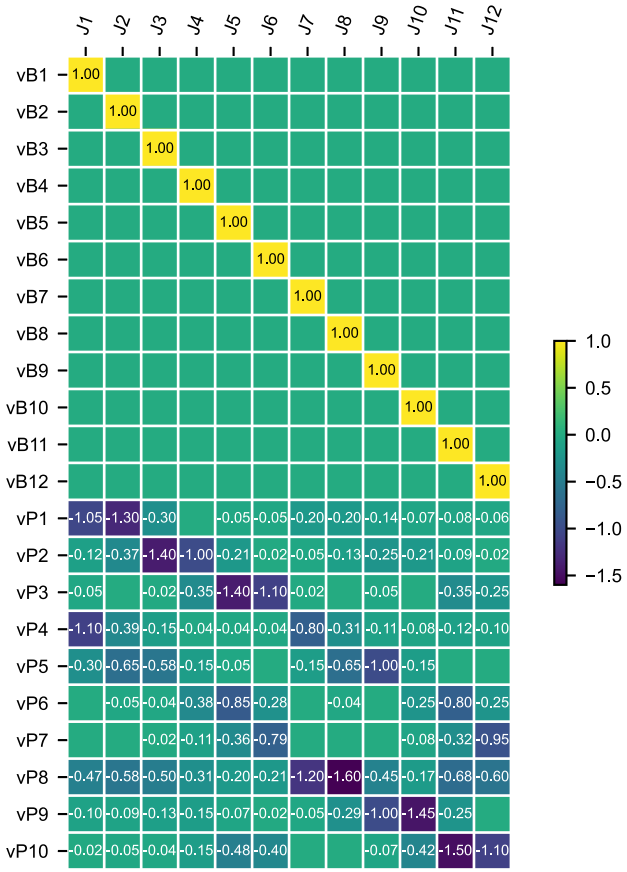

Figure 5.19: **Virtual barriers matrix.** J barriers are built as control parameters defined as linear combinations of the virtual barriers and virtual plungers. They are defined to obtain independent control over the interdot couplings, while leaving the quantum dots chemical potentials unaffected.

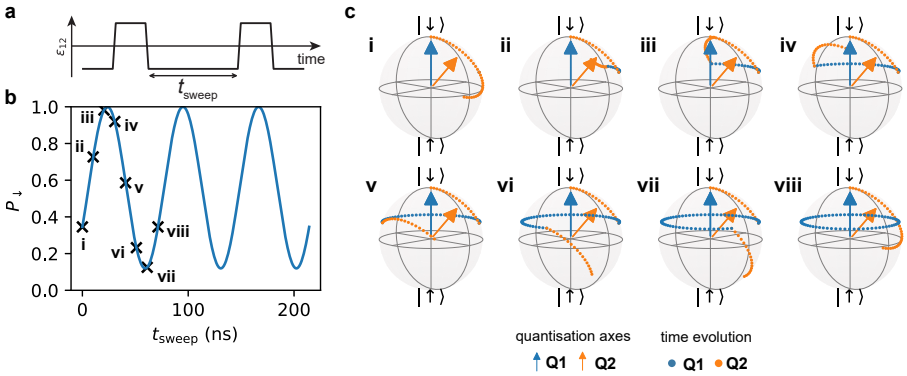

Figure 5.20: **Hopping-induced oscillations in occupied dots. a,** Shuttling sequence that moves Q1 from D1 to D2 and back to D1, twice. In the experiment, we vary the time in Q1, indicated as t_{sweep} **b,** Calculated spin down probability as a function of sweep time in D1. The visibility is dependent on the waiting times in D2 and the difference in quantization axis. **c,** State evolution during the shuttling sequence for different waiting times in D1, as indicated in **b**. The final time evolution around the z-axis is not displayed for clarity.

precision higher than the sample rate, because the voltage resolution of the AWG can be used to shift the ramp in time as shown in Fig. 5.21a. The time resolution Δt_{res} of a ramp with a duration long enough to be not affected by the transients at the start and end of the ramp can be approximated by $\Delta t_{\text{res}} = t_{\text{ramp}} \Delta V / A$, where t_{ramp} the duration of the ramp, ΔV the voltage resolution of the AWG and A the amplitude of the ramp. This approximation assumes that the low-pass filter has a cut-off frequency just below the Nyquist frequency. Surprisingly, the sample rate has no direct effect on the time resolution of the ramp. A higher sample rate combined with a higher cut-off frequency allows the generation of shorter ramps and shorter ramps have a higher time resolution. The voltage resolution and thus the time resolution effectively decrease when oversampling is used, i.e. when the cut-off frequency is significantly lower than the Nyquist frequency.

We have used AWGs with a voltage resolution of 0.37 mV and pulses with an amplitude on the order of 200 mV at the AWG outputs (this translates to 25.2 mV on the device due to the attenuation on the line) and a ramp time of 2 ns. This setting gives a time resolution of 3.7 ps, which meets the requirement for high-fidelity gates. However, the ramps for the shuttling pulses are short with respect to the transient response of the low-pass filter. The filter of the AWG adds small wiggles to the short ramps making the timing less precise. This effect is shown in Fig. 5.21d, where the time deviation for the ramps with different time shift t_{shift} are plotted. From these calculated ramps we have derived a maximum deviation of 30.4 ps from the average and a standard deviation of 19.4 ps, satisfying the basic requirements for 99.99% fidelity. We modeled our gate implementation in Section 3 of the supplementary material [31] and estimate the incoherent error due to such timing deviation, as summarized in Table 5.9.

COHERENCE TIMES OF THE INDIVIDUAL QUBITS

Because the g-tensor and hyperfine interaction for heavy hole qubits are expected to be highly anisotropic, a small magnetic field offset pointing towards an out-of-plane direc-

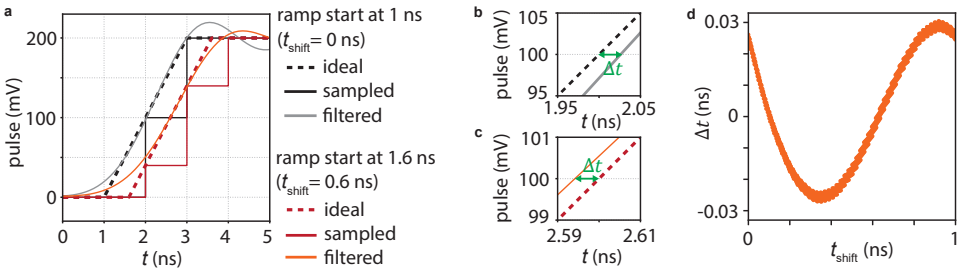

Figure 5.21: **Pulse timing. a,** Digital inputs and analogue outputs of the AWG for two pulses with time shifts $t_{\rm shift} = 0$ and 0.6 ns. The dotted lines are the ideal linear ramps with 0.6 ns time shift that we are aiming for. The solid lines are the digital inputs, represented by the discrete sampling with 1 ns resolution. To produce a time shift of 0.6 ns, a 60 mV decrement of the digital input is made on the rising ramp. The low-pass filtering of the AWG results in the smoothened output voltages represented by the solid curves, as well as the oscillations (ringing) after the ramp. **b, c,** Zoom-in of the pulses around the middle of the ideal ramps. The deviation in time between the ideal ramps and the analogue outputs at half of the voltage amplitude is denoted as Δt. **d,** The deviation Δt as a function of time shift $t_{\rm shift}$. The data set is generated with equally distributed time shifts from 0 to 0.999 ns. The mean of the distribution corresponds to $\Delta t = 0$. The analogue outputs in all the plots are calculated using the measured step response of the AWG.

5

tion can change the dephasing time significantly. For our device, we find that the measured qubit frequencies are not completely linear in magnetic field for field strength of 1 mT. Therefore, we can estimate the magnetic field offset for in-plane and out-of-plane direction by fitting the measured qubit frequency to $hf(B_{\rm ext}) = \sqrt{(g_\parallel \mu_B (B_{\rm ext} + B_0^\parallel))^2 + (g_\perp \mu_B B_0^\perp)^2}$ (Fig. 5.22b and inset). Our best fits show perpendicular magnetic field offsets $g_\perp \mu_B B_0^\perp =$ 1.4(1) MHz for Q_A, 1.8(2) MHz for Q_B and parallel offsets $B_0^\parallel = 0.08(3)$ mT for Q_A, 0.13(2) mT for Q_B. The perpendicular offsets are 10 and 13μT assuming an out-of-plane g-factor $g_\perp = 10$. The offsets might originate from magnetic materials on the sample board, trapped flux in superconducting magnet, polarized nuclear spins, Meisner effect of the metallic top gates, or the Earth magnetic field.

To estimate the magnetic field dependence of the dephasing time, we consider a simplified model assuming Gaussian quasi-static fluctuations of the qubit frequency originating from nuclear spin noise and quasi-static fluctuations of the g-factor caused by charge noise. The qubit frequency for an external applied magnetic field $B_{\rm ext}$ is given by

$$f(B_{\rm ext}, \delta g, \delta f_{\rm n}) = \frac{1}{h}\sqrt{((g_\parallel + \delta g)\mu_B (B_{\rm ext} + B_0^\parallel))^2 + (\delta f_{\rm n} + g_\perp \mu_B B_0^\perp)^2}. \tag{5.12}$$

In linear order, the in-plane g-factor fluctuation δg gives rise to qubit frequency fluctuation $\delta f_{\delta g} = f(B_{\rm ext}, \delta g, 0) - f(B_{\rm ext}, 0, 0)$ with standard deviation $\sigma_{f,\delta g}$ and the out-of-plane hyperfine field fluctuations $\delta f_{\rm n}$ give rise to qubit frequency fluctuation $\delta f_{\rm n} = f(B_{\rm ext}, 0, \delta f_{\rm n}) - f(B_{\rm ext}, 0, 0)$ with standard deviation $\sigma_{f,\delta f_{\rm n}}$. Assuming both noise sources to be independent and uncorrelated, the standard deviation of the total qubit frequency fluctuation at $B_{\rm ext}$ is $\sigma_f = \sqrt{\sigma_{f,\delta g}^2 + \sigma_{f,\delta f_{\rm n}}^2}$ giving rise to a coherence time $T_2^\star = \frac{1}{\sqrt{2}\pi\sigma_f}$. From our fit in Fig. 5.2B (replotted in Fig. 5.22c), we extract an effective hyperfine noise $\delta f_{\rm n} = 52(7)$ kHz for Q_A and 78(8) kHz for Q_B, corresponding to the coherent time $T_2^\star = 4.3(6)$ and 2.9(3)μ s. This result is larger than $\delta f_{\rm n} = 34.4$ kHz reported in Ref. [68] in D3 of the same de-

vice and significantly smaller than $\delta f_n = 250$ kHz reported in Ref. [24]. The difference could arise from microscopic details in the device, the simplicity of the model, as well as the complexity of the nuclear spin noise at low magnetic fields, where the ^{73}Ge nuclear spins have a quadrupolar splitting caused by strain which has a similar magnitude as the precession frequency.

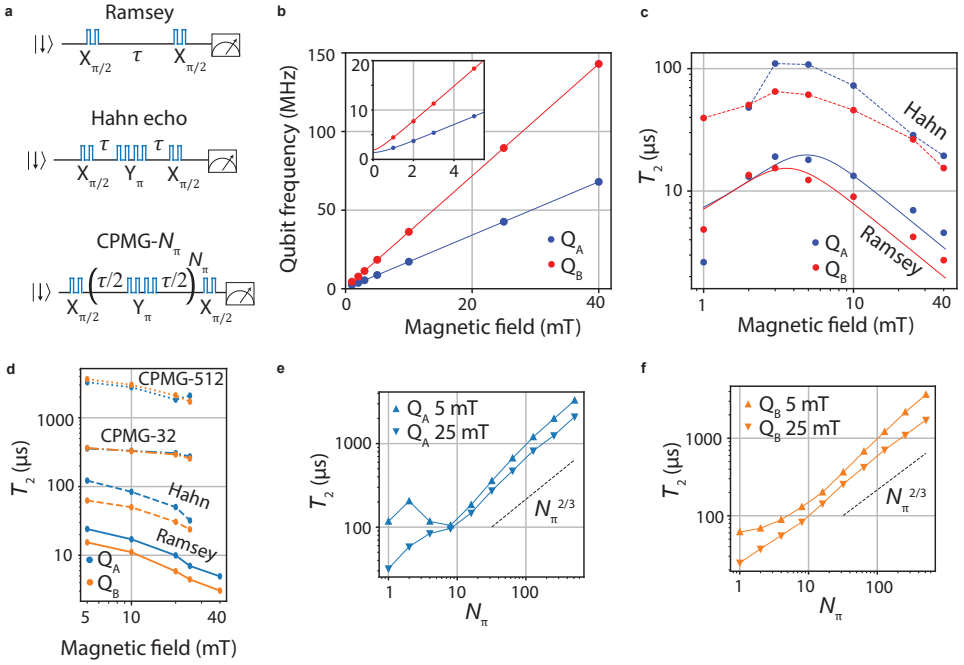

Figure 5.22: **Coherence time and dependence on magnetic field strength at the idle position of the qubits. a,** The pulse sequences consisting of hopping-based gates $X_{\pi/2}(Y_{\pi/2})$ for measuring qubit frequency and $T_2^\star$ (Ramsey), for T_2^H(Hahn echo), and T_2^{CPMG}(CPMG-N_π). **b,** The frequencies of qubits Q_A and Q_B as a function of external magnetic field. The inset is the zoom-in at low field regime, where a non-linear behavior is observed. The fitting method is described in the text. Here the superconducting magnet is in the driven mode. In this mode, the power supply is galvanically connected to its power supply. It introduces extra noise in the system compared to the normal operation mode. Note that field below 5 mT can only be reached with the magnet in driven mode. **c,** The $T_2^\star$ and T_2^H as a function of external magnetic field when the magnet is at the driven mode. The $T_2^\star$ is extracted from the Ramsey measurement with an average of 10 traces and the experimental time 12-19 minutes. Here we replot the data in Fig. 5.2B for easier comparison. **d,** The coherence time as a function of magnetic field above 5 mT when magnet is in the normal operation mode. The longest coherence time is obtained at 5 mT, with $T_2^\star = 24.1\mu$ s, $T_2^H = 122\mu$s and $T_2^{CPMG-512} > 3$ ms. The $T_2^\star$ is extracted from the Ramsey measurement with an average of 10 traces and the experimental time 12-19 minutes. When fitting $T_2^{CPMG-512}$ of Q_A, we disregard data points corresponding to total evolution time $\tau N_\pi > 4$ ms that are influenced by the reservoir-induced decay. Exemplary CPMG datasets are shown in Fig.5.23. **e,f,** The T_2^{CPMG} as function of number of π-pulses for both qubits at two different magnetic fields.

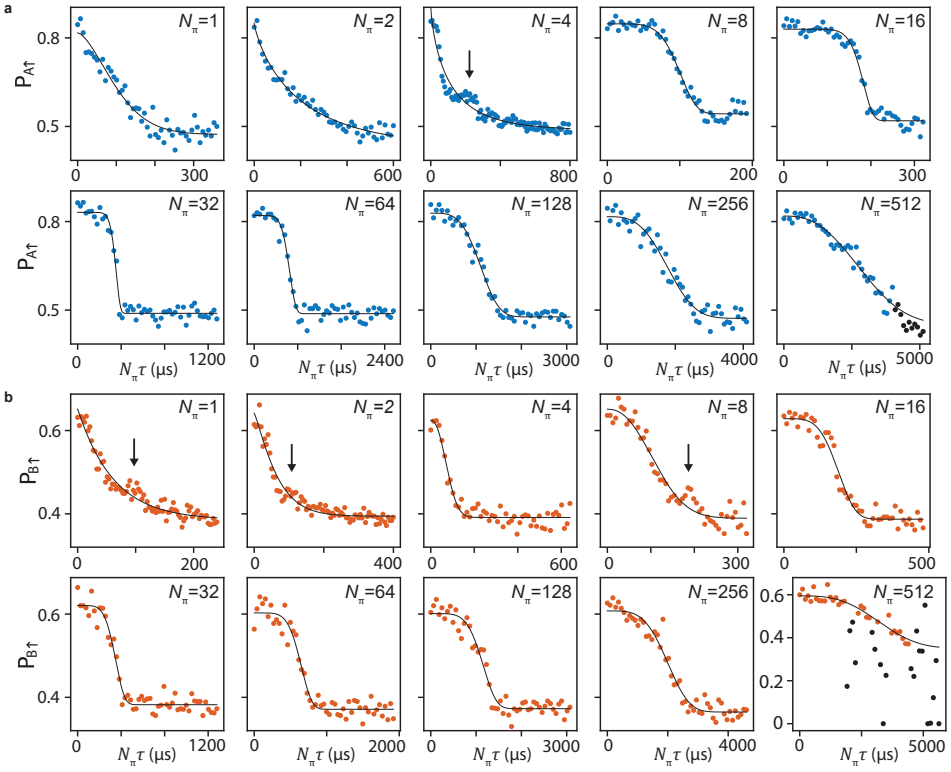

Figure 5.23: **Coherence time with dynamical decoupling pulses at magnetic field of 5 mT. a,** The coherence of qubit A and **b,** the coherence of qubit B as a function of total evolution time $N_\pi\tau$ with CPMG dynamical decoupling sequence (schematics depict in Fig. 5.22a). The collapse and revival of coherence (peaks marked by black arrows in the plots $N_\pi \leq 8$) should be attributed to hyperfine noise of ^{73}Ge nuclear spin. We notice that at such low magnetic field the expected linewidth of hyperfine noise becomes comparable to the nuclear spin precession frequency, which might explain the observed smoother features compared to the work [24]. Despite the collapse-and-revival features, we still fit the data to the formula $P(t) = A\exp\{(-(t/T_2)^\alpha)\} + B$ to extract coherence time T_2. We also notice the coherence at $N_\pi\tau = 0$ almost stay the same for the plots from $N_\pi = 1$ to $N_\pi = 512$, which implies the spin states do not have noticeable decay with numbers of shuttles up to 4096(2048) times for qubit $Q_{A(B)}$. We remark that the black data points in the plots $N_\pi = 512$ are removed from the coherence time fitting, due to the decay induced by tunnel coupling to the reservoir in (a), and due to the charge jumps of the sensor in (b). In both cases, the fitted T_2 should still be valid because the fitting curves agree with the data, and the fitted T_2 fall on the trend of T_2-N_π data in Fig. 5.22e,f.

MEASUREMENT PROTOCOL FOR RESIDUAL EXCHANGE COUPLINGS

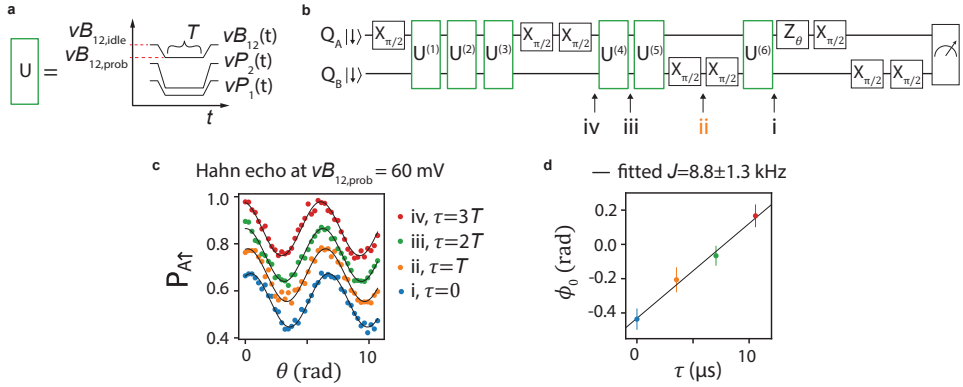

Figure 5.24: **Measurement of exchange coupling using a Hahn echo sequence at magnetic field of 25 mT. a,** Illustration of a pulse used to probe the exchange coupling at $vB_{12,\mathrm{probe}}$ starting from the idle point $vB_{12,\mathrm{idle}}$ where the single-qubit gates are performed. The virtual gate voltages $vP_{1,2}$ are ramped to the values used for the Ramsey experiments (Fig. 5.10) as well as the GST and RB experiments. **b,** The circuits for Hahn echo measurement, probing the difference of accumulated phases on qubit A induced by the flipped state of qubit B. Echo fringes of qubit A are measured in **c** by inserting $X^2_{\pi/2,\mathrm{B}}$ at various positions of the circuits {i,ii,iii,iv}, which lets Q_A interact with flipped Q_B for various amount of time $\tau = nT$, $n = \{0,1,2,3\}$. (b) shows the gates $X^2_{\pi/2,\mathrm{B}}$ inserting at the position ii. **c,** The fringes of the Hahn echo measurement. The data sets are shifted vertically for clearer display. The fringes are fitted to $A\cos(\theta+\phi_0)+B$ as black lines and the extracted phase offsets ϕ_0 are plotted in **d**. The linear fit of the phase offsets ϕ_0 as a function of evolution time τ gives the Q_B-state-dependent frequency variation of Q_A. The phase accumulation during the ramp and the idle time before and after the pulses $X^2_{\pi/2,\mathrm{B}}$ are corrected by the residual exchange at the idle position, which is 15(1) kHz measured via the same method. We note that the measurement displayed in this figure are taken after a charge jump of vB_{12}, similar to the situation described in the caption of Fig. 5.10.

CALIBRATION OF THE PULSE-SHAPED CZ GATES

We implement exchange pulses with a Hamming window $J(t) = J_{\mathrm{on}}(0.54-0.46\cos(\pi t/\tau_{\mathrm{ramp}}))$, using an empirical relation between the exchange coupling and the gate voltage vB_{12} , $J(vB_{12}) = J_0\exp(-\kappa\ vB_{12})$ where $J_0 = 0.24$ MHz and $\kappa = 0.059$ mV^{-1}. The CZ gate calibration is performed in the following order:

1. Conditional phase calibration: for a given pulse amplitude $vB_{12,\mathrm{on}}$, we measure the accumulated state-dependent phases as function of the ramp time τ_{ramp}, as described in Fig. 5.25bc. We find the ramp time $\tau_{\mathrm{ramp}} = \tau^{\pi}_{\mathrm{ramp}}$ that allows the state-dependent phase difference of π (Fig. 5.25d). The pulse amplitudes and ramp times allowing conditional phase of π are measured and plotted in Fig. 5.25e.

2. Single-qubit phase correction: as described in Fig. 5.4D, after applying an exchange pulse with a given pulse amplitude and the ramp time, the target qubit Q_A picks up a phase that should be calibrated to zero if the control qubit $|Q_B\rangle = |\downarrow\rangle$, and to π if the control qubit $|Q_B\rangle = |\uparrow\rangle$. The same correction needs to apply to both qubits.

3. GST calibration: we fine-tune the ramp time τ_{ramp} and the single-qubit phase correction with the error reports from gate set tomography (GST) [12, 54].

We measure the non-adiabatic transitions of the implemented exchange pulses in Fig. 5.25. We observed the gate is sufficiently adiabatic when maximum exchange is below 20 MHz, motivating the choice of CZ gate parameter $vB_{12,\text{on}} = -76$mV for two-qubit RB and GST experiments.

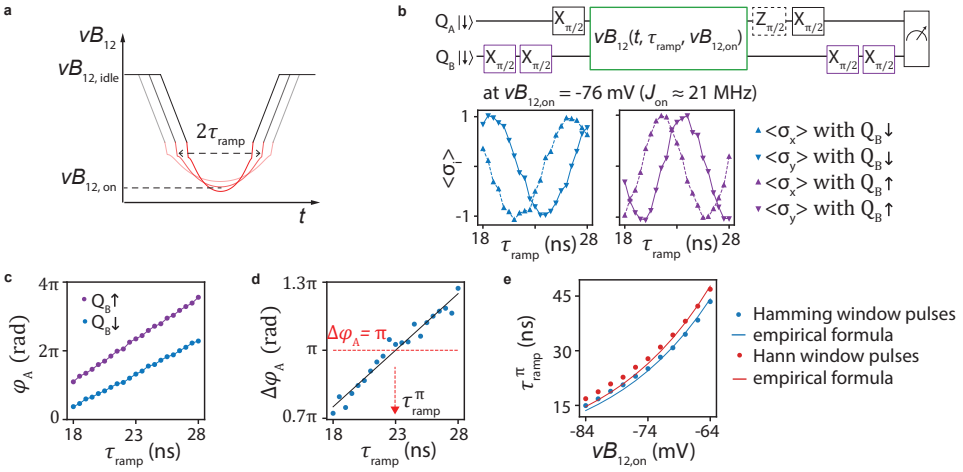

Figure 5.25: **Calibration of the conditional phase for the pulse-shaped CZ gates. a,** The illustration of virtual barrier gate voltage $vB_{12}(t)$ with two pulse parameters $vB_{12,\text{on}}$ and τ_{ramp} . The pulse $vB_{12}(t)$ generates Hamming window waveform $J(t) = J_{\text{on}}(0.54 - 0.46\cos(\pi t/\tau_{\text{ramp}}))$. The maximum exchange coupling J_{on} is predicted by empirical formula $J_{\text{on}} = J_0 \exp(-\kappa\, vB_{12,\text{on}})$, where $J_0 = 0.24$ MHz and $\kappa = 0.059$ mV^{-1}. **b,** The normalized $\langle\sigma_{\text{x(y)}}\rangle$ of qubit A depending on the state of qubit B, as a function of τ_{ramp} at a certain gate voltage $vB_{12,\text{on}}$. The values $\langle\sigma_{\text{x(y)}}\rangle$ are measured by the $X_{\pi/2}$ without (with) $Z_{\pi/2}$ before the readout, normalized with the Ramsey amplitudes of a reference experiments without the exchange pulse. Here is an example of $vB_{12,\text{on}} = -76$ mV. **c,** The state-dependent phases of the qubit A as a function of the ramp time τ_{ramp}. **d,** The ramp time for the state-dependent π phase shift, $\tau_{\text{ramp}} = \tau^{\pi}_{\text{ramp}}$, is determined by linear interpolation and finding the point where the state-dependent phase shift $\Delta\varphi_{\text{A}} = \varphi_{\text{A,B}\uparrow} - \varphi_{\text{A,B}\downarrow} = \pi$. **e,** The ramp time τ^{π}_{ramp} that results in CZ gate at various gate voltages $vB_{12,\text{on}}$. We also tune up the CZ gates with Hann window pulses using the same method. The predictions are based on the analytical formula $t_{\text{ramp}} = 0.25/(a_0 J_0 \exp(-\kappa\, vB_{12,\text{on}}))$, where $a_0 = 0.54(0.5)$ for Hamming (Hann) window.

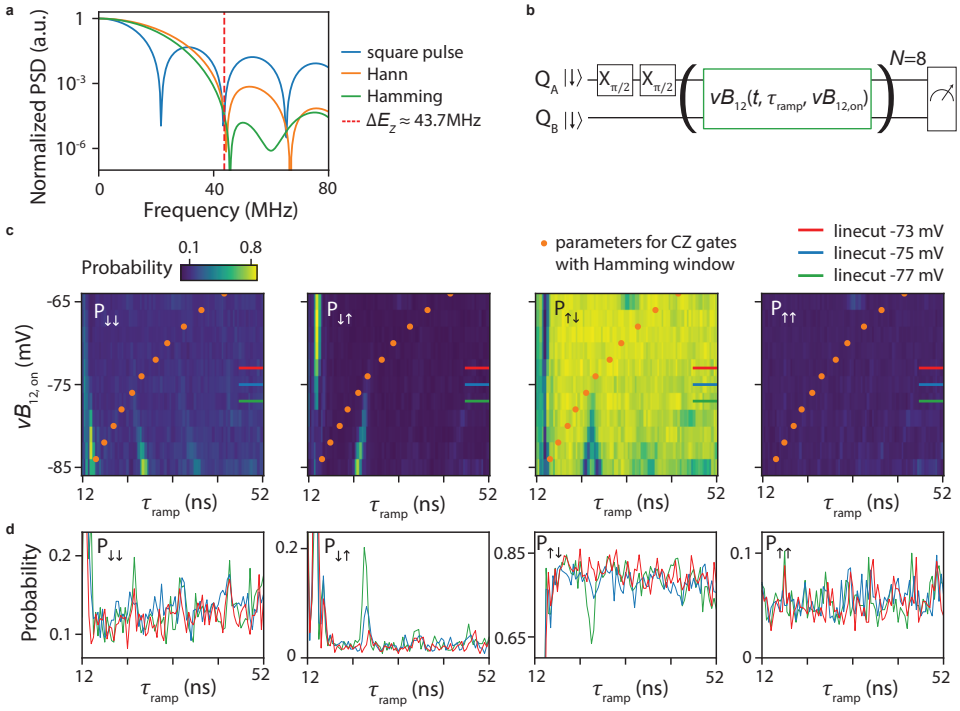

Figure 5.26: **Exchange pulse shapes and the resulting non-adiabatic state transitions.** **a,** The power spectrum density (PSD) of the exchange pulse shapes, indicating the energy emission that can drive non-adiabatic state transitions. Hamming (Hann) window functions are $J(t) = J_{\text{on}}(a_0 - (1-a_0)\cos(\pi t/\tau_{\text{ramp}}))$, where $a_0 = 0.54(0.5)$. All the shapes have the same pulse time of 46 ns, close to the value used in the RB and GST experiments. **b,** The circuit for measuring state transitions induced by the exchange pulses. We use eight exchange pulses to amplify the transition probability. The pulses with the Hamming window shape parameters $(\tau_{\text{ramp}}, vB_{12,\text{on}})$ are applied on the state $|\uparrow\downarrow\rangle$, and the full two-qubit state is readout at the end. **c,** The probability $P_{\sigma\sigma'}$ that indicates non-adiabatic state transitions are measured at 25 mT ($\Delta E_Z \approx 43.7$ MHz). The parameters $(\tau_{\text{ramp}}, vB_{12,\text{on}})$ for CZ gates, taken from Fig. 5.25e, are marked in orange circles. The linecuts at $vB_{12,\text{on}} = -73, -75, -77$ mV (corresponding $J_{\text{on}} \approx 18, 20, 23$ MHz) are displayed in **d**. An onset of SWAP transition, $|\uparrow\downarrow\rangle \rightarrow |\downarrow\uparrow\rangle$, is observed as the emerging dip (peak) around $\tau = 25$ ns in the plot of $P_{\uparrow\downarrow(\downarrow\uparrow)}$ when $vB_{12,\text{on}}$ becomes more negative. In the nearby parameter space we observe another transition dip (peak) $|\uparrow\downarrow\rangle \rightarrow |\downarrow\downarrow\rangle$. Combining with other measurement data (not showing here), we interpret this transition as Q_B-state-dependent Q_A transition.

SHUTTLING ACROSS MULTIPLE QUANTUM DOTS: DETUNING AND BARRIER VOLTAGE DEPENDENCE

We probe the oscillations induced by differences in quantization axes as a function of detuning and barrier voltages. In practice, to shuttle from D4 to D8, we follow this protocol:

1. initialize the D1, D4 double quantum dot system in the $|\uparrow\downarrow\rangle$;

2. ramp the gate voltages from the set point defined as (1,0) to the (0,1), passing through the (1,0)-(0,1) charge anticrossing (AC). Here, the first number defines the

filling of D4, and the second of D8. Ramp times in between these points are of ~ 10 ns;

3. wait in the (0,1) point for a varying free-precession time;
4. pulse back to the AC, and to the (1,0) setpoint;
5. readout the spin via Pauli spin blockade.

To probe the dependence of the D8 Larmor frequency, we sweep the detuning of the (0,1) set point. The results of this measurement are shown in Fig. 5.27a. Oscillations starts to arise when the gate voltage overcomes the charge anticrossing, that is found at $\epsilon_{4,8} = 10$ mV. For lower detuning voltages, the spin remains in D4, and therefore oscillations are not present. The Fast Fourier Transform of the data shows well the dependence of the Larmor frequency in the detuning voltage window. Similar measurements are shown for the case of a spin transfer from D8 to D5 (Fig. 5.27b), from D6 to D10 (Fig. 5.27c) and from D3 to D7 (Fig. 5.27d). We observe that, except for the region around the charge anticrossing, the qubit frequencies are not strongly affected by the detuning voltages. Rather, barrier gates do have a much stronger effect on the qubit frequencies, which mostly shift linearly, as illustrated in Fig. 5.28. Interestingly, the D7 Larmor frequency crosses zero as a function of J6, suggesting a change of sign in the g-factor of the qubit.

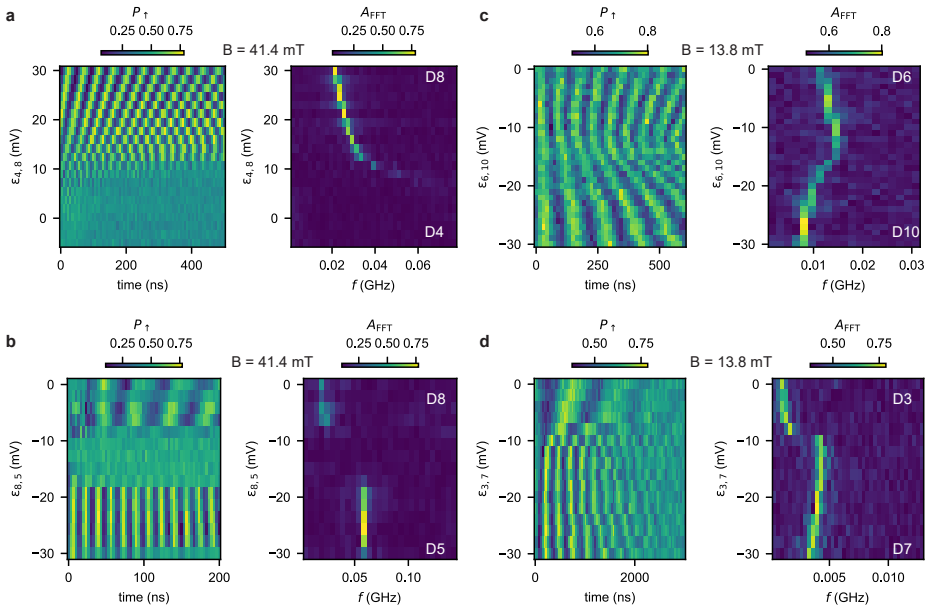

Figure 5.27: **Detuning dependence of the hopping-induced spin oscillations. a,** We vary the detuning gate voltage of the (0, 1) set point, corresponding to the shuttling sequence that moves the single spin from D4 to D8, i.e., from the (1,0) to the (0,1) charge state, across the charge interdot. Similarly to ref. [21], oscillations arise when the spin is transferred from one dot to the other. We observe that the onset of the oscillations corresponds to the charge interdot point. The panel on the right shown the FFT of the data. In **b, c, d,**, we illustrate similar measurements taken for spin shuttling from D8 to D5, from D6 to D10, from D3 to D7, respectively.

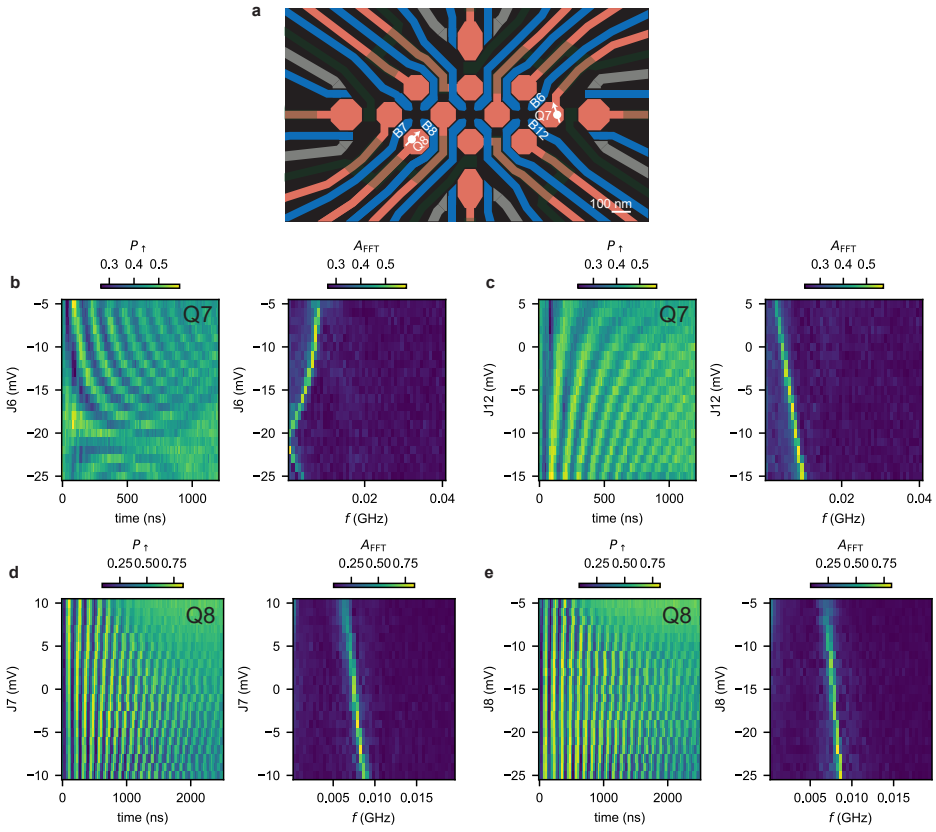

Figure 5.28: **Barrier gate dependence of the hopping-induced spin oscillations. a,** Device layout indicating the two quantum dots D8 and D7, together with the surrounding barrier gates. **b, c** D7 Larmor frequency evolution while sweeping the J6 and J12 voltages, respectively. **d, e** D8 Larmor frequency evolution as a function of J7 and J8. Small changes in the barrier voltages induce a linear shift of the D8 frequency.

DEPHASING TIMES AND LARMOR FREQUENCIES IN THE 10 QUANTUM DOT ARRAY

We study the dephasing times (T_2^*) of the 10 quantum dots by shuttling a spin diabatically from the double quantum dot system D1, D4 to each of the quantum dots, and let it evolve for a varying idle time. We measure the decay of the oscillations as a function of the time spent in each site by fitting the data shown in Fig. 5.29 and Fig. 5.5F using the equation: $A \cdot \sin\left(2\pi f t + \phi\right) \exp\left\{\left(-(t/T_2^*)^2\right)\right\} + C$. Here, $2 \cdot A$ is the visibility, f the Larmor frequency, t the free precession time, ϕ the starting phase, and C the oscillations offset. The Larmor frequency of an isolated Loss-diVincenzo spin qubit satisfies the relation: $f = \frac{g\mu_B B}{h}$, with g the g-factor, μ_B the Bohr magneton, B the applied magnetic field and h the Planck constant. From the measurements of the oscillations as a function of magnetic field, we extract the g-factor for all the 10 quantum dots (Fig. 5.30). We find that except for the tunnel coupled Q1, Q4 qubits, f shows a linear dependence to the magnetic field. The deviation from the linear trend can be explained from the coexistence of finite exchange coupling and non-parallel quantization axes.

In general, the lower-than-unity and varying visibilities of the hopping-induced oscillations (Figs. S21, S22, S24, S25) are caused by both SPAM errors and by the non-orthogonality of the quantization axes of adjacent quantum dots. As the estimated SPAM fidelities are typically in the range of 80-95% (details for qubits A, B in Tables 5.5 and 5.6), we speculate that the origin of oscillation amplitudes below ~ 0.8 and their variability are mainly due to unfavourable spin alignment. In the current approach, we adopted a simple and sequential tuning approach, which can result in reduced rotations in the Bloch sphere. However, we could envision more involved tuning protocols that would lead to a higher contrast if desired, such as further optimization of the time spent in each dot and possibly additional shuttling steps to ensure that a phase rotation in a dot leads to a full amplitude rotation.

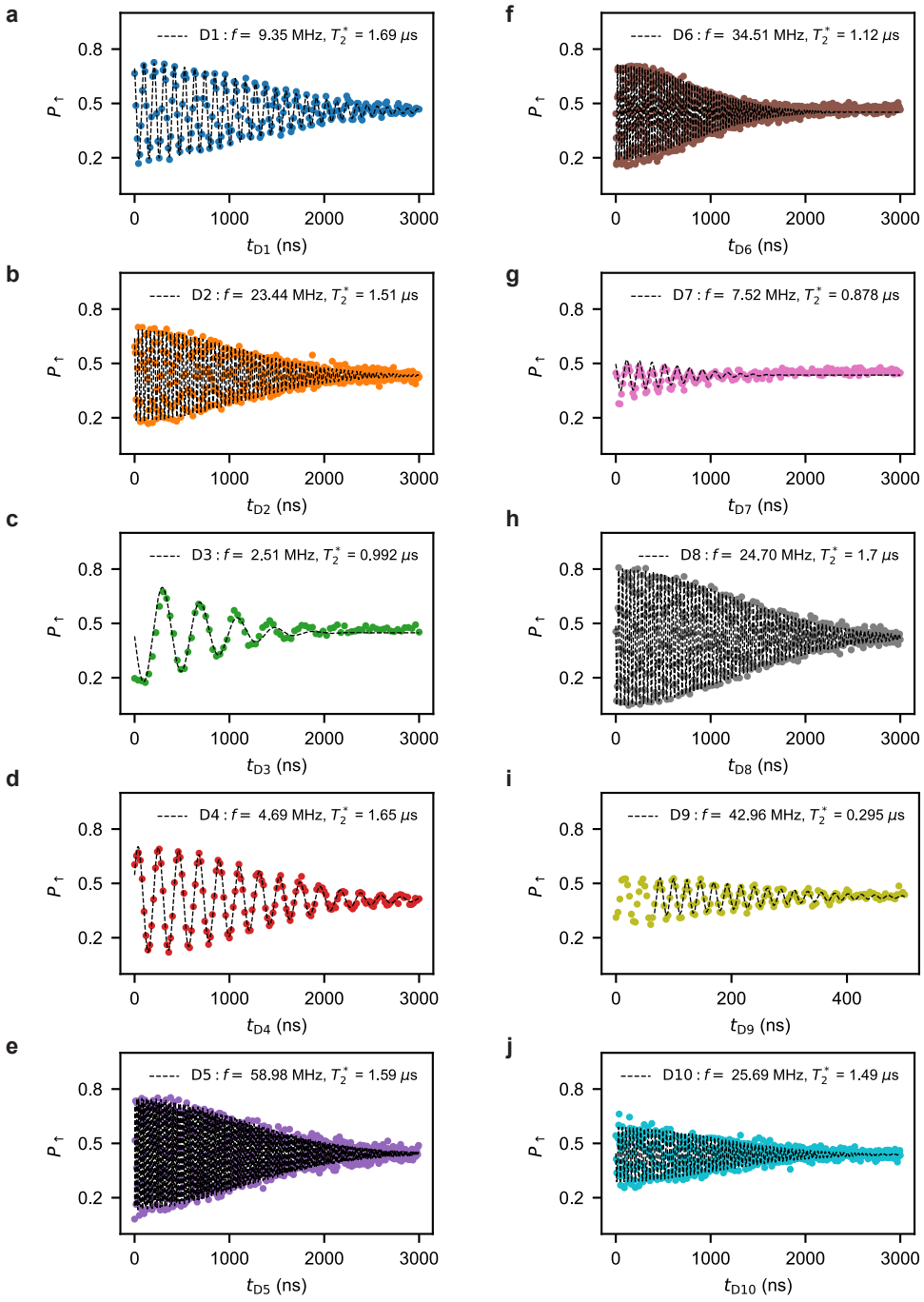

Figure 5.29: T_2^* **of the 10 quantum dot array at 41.4 mT. a-j,** Each panel is measured using the same method as presented in Fig. 5.5. We fit the dataset of D9 from 68 ns onward as we observe a frequency shift in the first ~ 100 ns possibly due to a delay in the electrical response.

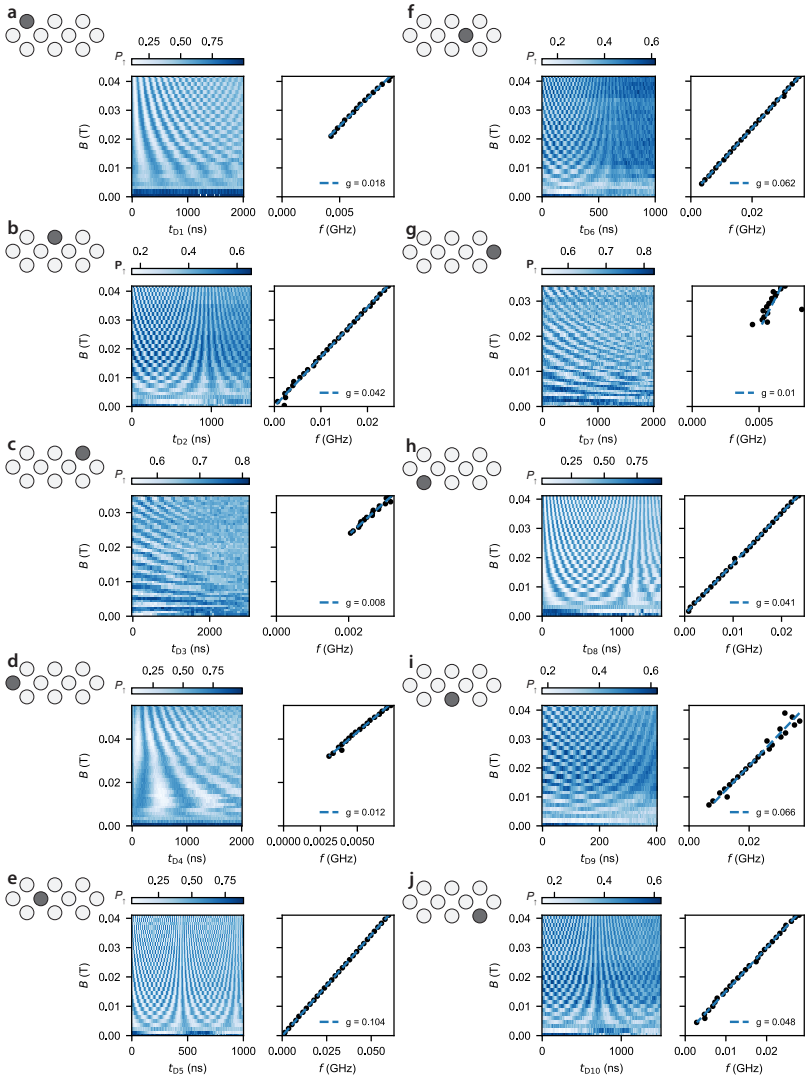

Figure 5.30: **Single-qubit rotations as a function of in-plane magnetic field for the 10 quantum dots. a-j,** We repeat the experiments shown in Fig. 5.5 and Fig. 5.29 as a function of magnetic field to obtain a more accurate estimate of the g-factors. We linearly fit the oscillation frequencies as a function of the magnetic field. We observe that all qubits but Q1 and Q4 display a Larmor frequency that intersects zero at zero magnetic field.

BIBLIOGRAPHY

[1] D. Loss and D. P. DiVincenzo. "Quantum computation with quantum dots". In: *Physical Review A* 57.1 (Jan. 1998), pp. 120–126. ISSN: 1050-2947.

[2] G. Burkard, T. D. Ladd, A. Pan, J. M. Nichol, and J. R. Petta. "Semiconductor spin qubits". In: *Reviews of Modern Physics* 95 (2 June 2023), p. 025003. ISSN: 0034-6861.

[3] F. H. L. Koppens, C. Buizert, K. J. Tielrooij, I. T. Vink, K. C. Nowack, T. Meunier, L. P. Kouwenhoven, and L. M. K. Vandersypen. "Driven coherent oscillations of a single electron spin in a quantum dot". In: *Nature* 442.7104 (Aug. 2006), pp. 766–771. ISSN: 1476-4687.

[4] M. Veldhorst, J. C. C. Hwang, C. H. Yang, A. W. Leenstra, B. de Ronde, J. P. Dehollain, J. T. Muhonen, F. E. Hudson, K. M. Itoh, A. Morello, and A. S. Dzurak. "An addressable quantum dot qubit with fault-tolerant control-fidelity". In: *Nature Nanotechnology* 9 (2014), pp. 941–985.

[5] M. Pioro-Ladrière, Y. Tokura, T. Obata, T. Kubo, and S. Tarucha. "Micromagnets for coherent control of spin-charge qubit in lateral quantum dots". In: *Applied Physics Letters* 90.2 (2007), p. 024105.

[6] J. Yoneda, K. Takeda, T. Otsuka, T. Nakajima, M. R. Delbecq, G. Allison, T. Honda, T. Kodera, S. Oda, Y. Hoshi, N. Usami, K. M. Itoh, and S. Tarucha. "A quantum-dot spin qubit with coherence limited by charge noise and fidelity higher than 99.9%". In: *Nature Nanotechnology* 13.2 (Feb. 2018), pp. 102–106. ISSN: 1748-3395.

[7] D. V. Bulaev and D. Loss. "Electric Dipole Spin Resonance for Heavy Holes in Quantum Dots". In: *Phys. Rev. Lett.* 98 (9 Feb. 2007), p. 097202.

[8] S. Nadj-Perge, S. M. Frolov, E. P. A. M. Bakkers, and L. P. Kouwenhoven. "Spin-orbit qubit in a semiconductor nanowire". In: *Nature* 468.7327 (2010), pp. 1084–1087. ISSN: 00280836.

[9] K. Wang, G. Xu, F. Gao, H. Liu, R.-L. Ma, X. Zhang, Z. Wang, G. Cao, T. Wang, J.-J. Zhang, D. Culcer, X. Hu, H.-W. Jiang, H.-O. Li, G.-C. Guo, and G.-P. Guo. "Ultrafast coherent control of a hole spin qubit in a germanium quantum dot". In: *Nature Communications* 13.1 (Jan. 2022), p. 206. ISSN: 2041-1723.

[10] N. W. Hendrickx, D. P. Franke, A. Sammak, G. Scappucci, and M. Veldhorst. "Fast two-qubit logic with holes in germanium". In: *Nature* 577.7791 (Jan. 2020), pp. 487–491. ISSN: 0028-0836.

[11] A. Noiri, K. Takeda, T. Nakajima, T. Kobayashi, A. Sammak, G. Scappucci, and S. Tarucha. "A shuttling-based two-qubit logic gate for linking distant silicon quantum processors". In: *Nature Communications* 13 (2022), p. 5740.

[12] X. Xue, M. Russ, N. Samkharadze, B. Undseth, A. Sammak, G. Scappucci, and L. M. K. Vandersypen. “Quantum logic with spin qubits crossing the surface code threshold”. In: *Nature* 601 (7893 Jan. 2022), pp. 343–347. ISSN: 0028-0836.

[13] S. G. J. Philips, M. T. Mądzik, S. V. Amitonov, S. L. de Snoo, M. Russ, N. Kalhor, C. Volk, W. I. L. Lawrie, D. Brousse, L. Tryputen, B. P. Wuetz, A. Sammak, M. Veldhorst, G. Scappucci, and L. M. K. Vandersypen. “Universal control of a six-qubit quantum processor in silicon”. In: *Nature* 609 (7929 Sept. 2022), pp. 919–924. ISSN: 0028-0836.

[14] K. Takeda, J. Yoneda, T. Otsuka, T. Nakajima, M. R. Delbecq, G. Allison, Y. Hoshi, N. Usami, K. M. Itoh, S. Oda, T. Kodera, and S. Tarucha. “Optimized electrical control of a Si/SiGe spin qubit in the presence of an induced frequency shift”. In: *npj Quantum Information* 4.1 (Oct. 2018), p. 54. ISSN: 2056-6387.

[15] B. Undseth, X. Xue, M. Mehmandoost, M. Rimbach-Russ, P. T. Eendebak, N. Samkharadze, A. Sammak, V. V. Dobrovitski, G. Scappucci, and L. M. Vandersypen. “Nonlinear Response and Crosstalk of Electrically Driven Silicon Spin Qubits”. In: *Phys. Rev. Appl.* 19 (4 Apr. 2023), p. 044078.

[16] B. Undseth, O. Pietx-Casas, E. Raymenants, M. Mehmandoost, M. T. Mądzik, S. G. J. Philips, S. L. de Snoo, D. J. Michalak, S. V. Amitonov, L. Tryputen, B. P. Wuetz, V. Fezzi, D. D. Esposti, A. Sammak, G. Scappucci, and L. M. K. Vandersypen. “Hotter is Easier: Unexpected Temperature Dependence of Spin Qubit Frequencies”. In: *Phys. Rev. X* 13 (4 Oct. 2023), p. 041015.

[17] M. Russ and G. Burkard. “Three-Electron Spin Qubits”. In: *J. Phys. Condens. Matter* 29.39 (2017), p. 393001.

[18] R. W. Andrews, C. Jones, M. D. Reed, A. M. Jones, S. D. Ha, M. P. Jura, J. Kerckhoff, M. Levendorf, S. Meenehan, S. T. Merkel, A. Smith, B. Sun, A. J. Weinstein, M. T. Rakher, T. D. Ladd, and M. G. Borselli. “Quantifying error and leakage in an encoded Si/SiGe triple-dot qubit”. In: *Nature Nanotechnology* 14.8 (Aug. 2019), pp. 747–750. ISSN: 1748-3395.

[19] A. J. Weinstein, M. D. Reed, A. M. Jones, R. W. Andrews, D. Barnes, J. Z. Blumoff, L. E. Euliss, K. Eng, B. H. Fong, S. D. Ha, D. R. Hulbert, C. A. C. Jackson, M. Jura, T. E. Keating, J. Kerckhoff, A. A. Kiselev, J. Matten, G. Sabbir, A. Smith, J. Wright, M. T. Rakher, T. D. Ladd, and M. G. Borselli. “Universal logic with encoded spin qubits in silicon”. In: *Nature* 615.7954 (Mar. 2023), pp. 817–822. ISSN: 1476-4687.

[20] G. Scappucci, P. J. Taylor, J. R. Williams, T. Ginley, and S. Law. “Crystalline materials for quantum computing: Semiconductor heterostructures and topological insulators exemplars”. In: *MRS Bulletin* 46.7 (2021), pp. 596–606.

[21] F. van Riggelen-Doelman, C.-A. Wang, S. L. de Snoo, W. I. L. Lawrie, N. W. Hendrickx, M. Rimbach-Russ, A. Sammak, G. Scappucci, C. Déprez, and M. Veldhorst. “Coherent spin qubit shuttling through germanium quantum dots”. In: *arXiv* (2023). eprint: 2308.02406.

[22] B. Jadot, P.-A. Mortemousque, E. Chanrion, T. Vivien, A. Ludwig, A. D. Wieck, M. Urdampilleta, C. Bäuerle, and T. Meunier. “Distant spin entanglement via fast and coherent electron shuttling”. In: *Nature Nanotechnology* 16 (2021), pp. 570–575.

[23] W. I. L. Lawrie, M. Rimbach-Russ, F. van Riggelen, N. W. Hendrickx, S. L. de Snoo, A. Sammak, G. Scappucci, J. Helsen, and M. Veldhorst. "Simultaneous single-qubit driving of semiconductor spin qubits at the fault-tolerant threshold". In: *Nature Communications* 14.3617 (2023).

[24] N. W. Hendrickx, L. Massai, M. Mergenthaler, F. J. Schupp, S. Paredes, S. W. Bedell, G. Salis, and A. Fuhrer. "Sweet-spot operation of a germanium hole spin qubit with highly anisotropic noise sensitivity". In: *Nature Materials* (May 2024). ISSN: 1476-4660.

[25] A. G. Fowler, M. Mariantoni, J. M. Martinis, and A. N. Cleland. "Surface codes: Towards practical large-scale quantum computation". In: *Physical Review A* 86 (3 Sept. 2012), p. 032324. ISSN: 1050-2947.

[26] D. Jirovec, P. M. Mutter, A. Hofmann, A. Crippa, M. Rychetsky, D. L. Craig, J. Kukucka, F. Martins, A. Ballabio, N. Ares, D. Chrastina, G. Isella, G. Burkard, and G. Katsaros. "Dynamics of hole Singlet-Triplet qubits with large g-factor differences". In: *Phys. Rev. Lett.* 128 (2022), p. 126803.

[27] C.-A. Wang, G. Scappucci, M. Veldhorst, and M. Russ. "Modelling of planar germanium hole qubits in electric and magnetic fields". In: *arXiv* (2022). eprint: 2208.04795.

[28] J. C. Abadillo-Uriel, E. A. Rodríguez-Mena, B. Martinez, and Y.-M. Niquet. "Hole-Spin Driving by Strain-Induced Spin-Orbit Interactions". In: *Phys. Rev. Lett.* 131 (9 Sept. 2023), p. 097002.

[29] C. Corley-Wiciak, C. Richter, M. H. Zoellner, I. Zaitsev, C. L. Manganelli, E. Zatterin, T. U. Schülli, A. A. Corley-Wiciak, J. Katzer, F. Reichmann, W. M. Klesse, N. W. Hendrickx, A. Sammak, M. Veldhorst, G. Scappucci, M. Virgilio, and G. Capellini. "Nanoscale Mapping of the 3D Strain Tensor in a Germanium Quantum Well Hosting a Functional Spin Qubit Device". In: *ACS Applied Materials & Interfaces* 15.2 (Jan. 2023), pp. 3119–3130. ISSN: 1944-8244.

[30] N. W. Hendrickx, W. I. Lawrie, M. Russ, F. van Riggelen, S. L. de Snoo, R. N. Schouten, A. Sammak, G. Scappucci, and M. Veldhorst. "A four-qubit germanium quantum processor". In: *Nature* 591.7851 (2021), pp. 580–585. ISSN: 14764687.

[31] C.-A. Wang, V. John, H. Tidjani, C. X. Yu, A. S. Ivlev, C. Déprez, F. van Riggelen-Doelman, B. D. Woods, N. W. Hendrickx, W. I. L. Lawrie, L. E. A. Stehouwer, S. D. Oosterhout, A. Sammak, M. Friesen, G. Scappucci, S. L. de Snoo, M. Rimbach-Russ, F. Borsoi, and M. Veldhorst. "Operating semiconductor quantum processors with hopping spins". In: *Science* 385 (6707 July 2024), pp. 447–452. ISSN: 0036-8075.

[32] M. Reed. "Entanglement and quantum error correction with superconducting qubits". In: *Dissertation (Yale University)* (2013).

[33] L. M. K. Vandersypen, H. Bluhm, J. S. Clarke, A. S. Dzurak, R. Ishihara, A. Morello, D. J. Reilly, L. R. Schreiber, and M. Veldhorst. "Interfacing spin qubits in quantum dots and donors — hot , dense , and coherent". In: *npj Quantum Information* December 2016 (2017), pp. 1–10. ISSN: 2056-6387.

[34] E. Nielsen, K. Rudinger, T. Proctor, A. Russo, K. Young, and R. Blume-Kohout. "Probing Quantum Processor Performance with pyGSTi". In: *Quantum Science and Technology* 5.4 (2020), p. 044002. ISSN: 2058-9565.

[35] R. Blume-Kohout, J. K. Gamble, E. Nielsen, K. Rudinger, J. Mizrahi, K. Fortier, and P. Maunz. "Demonstration of qubit operations below a rigorous fault tolerance threshold with gate set tomography". In: *Nature Communications* 8.1 (Feb. 2017), p. 14485. ISSN: 2041-1723.

[36] J. P. Dehollain, J. T. Muhonen, R. Blume-Kohout, K. M. Rudinger, J. K. Gamble, E. Nielsen, A. Laucht, S. Simmons, R. Kalra, A. S. Dzurak, and A. Morello. "Optimization of a solid-state electron spin qubit using gate set tomography". In: *New J. Phys.* 18.10 (Oct. 2016), p. 103018.

[37] M. Rimbach-Russ, S. G. J. Philips, X. Xue, and L. M. K. Vandersypen. "Simple Framework for Systematic High-Fidelity Gate Operations". In: *Quantum Science and Technology* 8.4 (2023), p. 045025. ISSN: 2058-9565.

[38] D. S. Wang, A. G. Fowler, and L. C. L. Hollenberg. "Surface code quantum computing with error rates over 1%". In: *Phys. Rev. A* 83 (2 Feb. 2011), p. 020302.

[39] B. Hetényi and J. R. Wootton. "Tailoring quantum error correction to spin qubits". In: *arXiv* (2023). eprint: 2306.17786.

[40] S. Bravyi, A. W. Cross, J. M. Gambetta, D. Maslov, P. Rall, and T. J. Yoder. "High-threshold and low-overhead fault-tolerant quantum memory". In: *Nature* 627 (2024), pp. 778–782.

[41] W. Ha, S. D. Ha, M. D. Choi, Y. Tang, A. E. Schmitz, M. P. Levendorf, K. Lee, J. M. Chappell, T. S. Adams, D. R. Hulbert, E. Acuna, R. S. Noah, J. W. Matten, M. P. Jura, J. A. Wright, M. T. Rakher, and M. G. Borselli. "A Flexible Design Platform for Si/SiGe Exchange-Only Qubits with Low Disorder". In: *Nano Letters* 22 (3 Feb. 2022), pp. 1443–1448. ISSN: 1530-6984.

[42] B. Martinez, J. C. Abadillo-Uriel, E. A. Rodríguez-Mena, and Y.-M. Niquet. "Hole spin manipulation in inhomogeneous and nonseparable electric fields". In: *Phys. Rev. B* 106 (23 Dec. 2022), p. 235426.

[43] S. Bosco, M. Benito, C. Adelsberger, and D. Loss. "Squeezed hole spin qubits in Ge quantum dots with ultrafast gates at low power". In: *Phys. Rev. B* 104 (11 2021), p. 115425.

[44] R. Li, L. Petit, D. P. Franke, J. P. Dehollain, J. Helsen, M. Steudtner, N. K. Thomas, Z. R. Yoscovits, K. J. Singh, S. Wehner, L. M. K. Vandersypen, J. S. Clarke, and M. Veldhorst. "A crossbar network for silicon quantum dot qubits". In: *Science Advances* 4 (7 July 2018). ISSN: 2375-2548.

[45] D. L. Campbell, Y.-P. Shim, B. Kannan, R. Winik, D. K. Kim, A. Melville, B. M. Niedzielski, J. L. Yoder, C. Tahan, S. Gustavsson, and W. D. Oliver. "Universal Nonadiabatic Control of Small-Gap Superconducting Qubits". In: *Phys. Rev. X* 10 (4 Dec. 2020), p. 041051.

[46] A. Sammak, D. Sabbagh, N. W. Hendrickx, M. Lodari, B. Paquelet Wuetz, A. Tosato, L. Yeoh, M. Bollani, M. Virgilio, M. A. Schubert, P. Zaumseil, G. Capellini, M. Veldhorst, and G. Scappucci. "Shallow and Undoped Germanium Quantum Wells: A Playground for Spin and Hybrid Quantum Technology". In: *Advanced Functional Materials* 29.14 (2019), p. 1807613. ISSN: 1616301X.

[47] M. Lodari, N. W. Hendrickx, W. I. L. Lawrie, T.-K. Hsiao, L. Vandersypen, A. Sammak, M. Veldhorst, and G. Scappucci. "Low percolation density and charge noise with holes in germanium". In: *Mater. Quantum. Technol.* 1 (2021), p. 011002.

[48] F. Borsoi, N. W. Hendrickx, V. John, M. Meyer, S. Motz, F. van Riggelen, A. Sammak, S. L. de Snoo, G. Scappucci, and M. Veldhorst. "Shared control of a 16 semiconductor quantum dot crossbar array". In: *Nature Nanotechnology* (Aug. 2023). ISSN: 1748-3395.

[49] D. M. Pozar. *Microwave engineering*. 4th ed. Wiley, 1998.

[50] A. C. Baynham, A. F. Gibson, and J. W. Granville. "On the Dielectric Constant of Germanium at Microwave Frequencies". In: *Proceedings of the Physical Society* 75.2 (Feb. 1960), p. 306.

[51] J. Krupka, P. Kamiński, R. Kozłowski, B. Surma, A. Dierlamm, and M. Kwestarz. "Dielectric properties of semi-insulating silicon at microwave frequencies". In: *Applied Physics Letters* 107.8 (Aug. 2015), p. 082105. ISSN: 0003-6951.

[52] L. S. Theis, F. Motzoi, S. Machnes, and F. K. Wilhelm. "Counteracting Systems of Diabaticities Using DRAG Controls: The Status after 10 Years (a)". In: *EPL (Europhysics Letters)* 123.6 (2018), p. 60001. ISSN: 0295-5075.

[53] F. D. Mbairi, W. P. Siebert, and H. Hesselbom. "High-Frequency Transmission Lines Crosstalk Reduction Using Spacing Rules". In: *IEEE Transactions on Components and Packaging Technologies* 31.3 (2008), pp. 601–610.

[54] R. Blume-Kohout, M. P. da Silva, E. Nielsen, T. Proctor, K. Rudinger, M. Sarovar, and K. Young. "A Taxonomy of Small Markovian Errors". In: *PRX Quantum* 3 (2 May 2022), p. 020335.

[55] J. M. Martinis, S. Nam, J. Aumentado, K. M. Lang, and C. Urbina. "Decoherence of a superconducting qubit due to bias noise". In: *Phys. Rev. B* 67 (9 Mar. 2003), p. 094510.

[56] J. M. Epstein, A. W. Cross, E. Magesan, and J. M. Gambetta. "Investigating the limits of randomized benchmarking protocols". In: *Phys. Rev. A* 89 (6 June 2014), p. 062321.

[57] M. Benito, X. Croot, C. Adelsberger, S. Putz, X. Mi, J. R. Petta, and G. Burkard. "Electric-field control and noise protection of the flopping-mode spin qubit". In: *Phys. Rev. B* 100 (2019), p. 125430.

[58] P. M. Mutter and G. Burkard. "All-electrical control of hole singlet-triplet spin qubits at low-leakage points". In: *Phys. Rev. B* 104 (19 2021), p. 195421.

[59] S. Geyer, B. Hetényi, S. Bosco, L. C. Camenzind, R. S. Eggli, A. Fuhrer, D. Loss, R. J. Warburton, D. M. Zumbühl, and A. V. Kuhlmann. "Two-Qubit Logic with Anisotropic Exchange in a Fin Field-Effect Transistor". In: *Nature Physics* (2022).

[60] X. Zhang, E. Morozova, M. Rimbach-Russ, D. Jirovec, T.-K. Hsiao, P. C. Fariña, C.-A. Wang, S. D. Oosterhout, A. Sammak, G. Scappucci, M. Veldhorst, and L. M. K. Vandersypen. “Universal Control of Four Singlet-Triplet Qubits”. In: *arXiv* (2023). eprint: 2312.16101.

[61] V. John, F. Borsoi, Z. György, C.-A. Wang, G. Széchenyi, F. van Riggelen-Doelman, W. I. L. Lawrie, N. W. Hendrickx, A. Sammak, G. Scappucci, A. Pályi, and M. Veldhorst. “Bichromatic Rabi Control of Semiconductor Qubits”. In: *Phys. Rev. Lett.* 132 (6 Feb. 2024), p. 067001.

[62] Ł. Cywi ński, R. M. Lutchyn, C. P. Nave, and S. Das Sarma. “How to enhance dephasing time in superconducting qubits”. In: *Phys. Rev. B* 77 (17 May 2008), p. 174509.

[63] M. Russ and G. Burkard. “Asymmetric Resonant Exchange Qubit under the Influence of Electrical Noise”. In: *Phys. Rev. B* 91.23 (2015), p. 235411.

[64] L. H. Pedersen, N. M. Møller, and K. Mølmer. “Fidelity of quantum operations”. In: *Physics Letters A* 367.1 (2007), pp. 47–51. ISSN: 0375-9601.

[65] J. R. Johansson, P. D. Nation, and F. Nori. “QuTiP 2: A Python Framework for the Dynamics of Open Quantum Systems”. In: *Computer Physics Communications* 184.4 (2013), pp. 1234–1240. ISSN: 0010-4655.

[66] T. D. Green and K. L. Knappenberger. “Relaxation dynamics of Au25L18 nanoclusters studied by femtosecond time-resolved near infrared transient absorption spectroscopy”. In: *Nanoscale* 4.14 (2012), p. 4111. ISSN: 2040-3364.

[67] J. van Dijk, E. Kawakami, R. Schouten, M. Veldhorst, L. Vandersypen, M. Babaie, E. Charbon, and F. Sebastiano. “Impact of Classical Control Electronics on Qubit Fidelity”. In: *Phys. Rev. Appl.* 12 (4 Oct. 2019), p. 044054.

[68] W. I. L. Lawrie. “Spin Qubits in Silicon and Germanium”. In: *PhD Thesis* (2022).

6

A VERTICAL DOUBLE QUANTUM DOT UNDER A SINGLE PLUNGER GATE

Gate-defined quantum dots in silicon-germanium heterostructures have become a compelling platform for quantum computation and simulation. Thus far, developments have been limited to quantum dots defined in a single plane. Here, we propose to advance beyond planar systems by exploiting heterostructures with multiple quantum wells. We demonstrate the operation of a gate-defined double quantum dot in a strained germanium double quantum well, where both quantum dots are tunnel coupled to both reservoirs and parallel transport occurs. We analyze the capacitive coupling to nearby gates and find both quantum dots to extract their position and size, from which we conclude that the double quantum dots are vertically stacked in the two quantum wells. We discuss challenges and opportunities of multilayer devices, and outline some potential applications in quantum computing and quantum simulation.

Parts of this chapter have been published in H. Tidjani , A. Tosato , A. Ivlev , C. Déprez , S. Oosterhout , L. Stehouwer , A. Sammak , G. Scappucci , and M. Veldhorst , Vertical gate-defined double quantum dot in a strained germanium double quantum well, *Phys. Rev. Appl.* 20, 054035 (2023).

6.1. INTRODUCTION

Efforts in scaling quantum dot based quantum computing platforms have been limited to dots defined in a single plane, in either one-or-two dimensional arrays[1, 2, 3]. Scaling quantum dots have led to the operation of a crossbar array comprising 16 quantum dots [4], and long-range quantum links may enable interconnecting modules of quantum dot arrays [5, 6, 7, 8]. However, the versatile nature of silicon-germanium heterostructures allows for further exploration. In particular, structures with multiple quantum wells can be grown, and double quantum wells of germanium [9] and silicon [10, 11] have been realized. An open question is thus whether multilayer heterostructures can become a relevant platform for quantum information. Here, we motivate potential applications and experimentally explore quantum dots in stacked quantum wells.

6.2. THE VERTICALLY COUPLED DOUBLE QUANTUM DOT

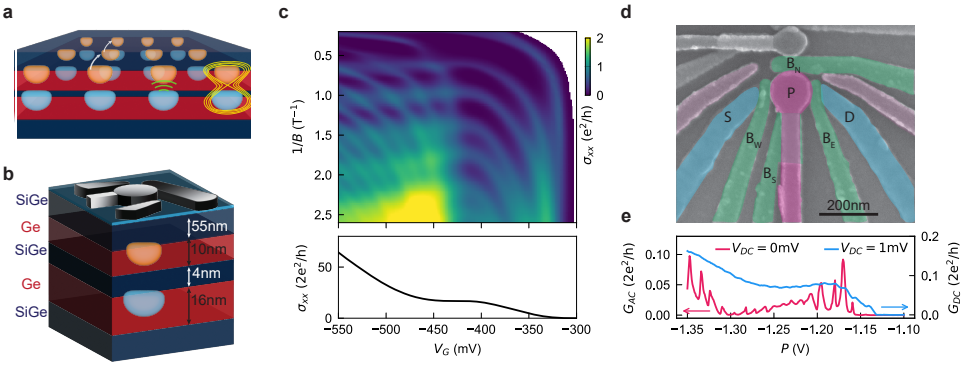

Figure 6.1: **Gate defined vertical double quantum dot in a bilayer heterostructure. a** Vision of a larger bilayer device, with different use-cases depicted, such as shuttling (white arrow), sensing (green) and vertical 2-qubit gates (yellow). **b** Schematic of the heterostructure and gate stack. The light blue layer in between the gates and SiGe layer indicates the aluminum oxide layer. **c** Hall bar shaped FinFET measurements on the heterostructure in **a**. Colour map of the conductivity σ_{xx} as a function of gate voltage V_G and the inverse magnetic field $1/B$. Dark regions correspond to filled Landau levels with vanishing σ_{xx} and correspondingly quantized σ_{xy}. Lower Panel: linecut at $B = 0$ T showing the zero field conductance trace. Density and mobility for the bilayer system are presented in appendix 6.5. **d** False coloured SEM image of a nearly identical device to the one used in this work. Quantum dots are defined under the plunger gate P (pink) and measured in transport using the ohmic contacts source (S) and drain (D) (blue). The coupling between the quantum dot and ohmics is tuned by B_E and B_W (green). The potential landscape is further shaped by the gates B_N and B_S (green). The experiments presented in this work are performed on a section of a larger device (see Appendix **??**). **e** Conductance trace as a function of the plunger gate voltage across S-D at V_{DC}=1 mV (blue line), and differential conductance trace (pink) at V_{DC}=0 mV and V_{AC} = 17 µV, $f_{\text{lock-in}}$ = 70 Hz.

Heterostructures with parallel quantum wells may support integration of important functionalities for spin qubit based quantum processors, as depicted in Fig.6.1a. Precise control over the growth of individual layers allows for the engineering of inter and intralayer properties. When charges residing in separate quantum wells are capacitively coupled, but have little to no tunnel coupling, charge sensors could be integrated into

separate layers from the qubits they sense. In an intermediate regime where tunnel coupling is in the order of one to a few tens of gigahertz, coherent spin shuttling between the wells could be realized [12]. Consequently, one layer may serve as a quantum link for qubits defined in the other layer, for example by offering shuttling lanes that connect remote qubits [13, 8]. In this regime, the second layer can also host dedicated ancilla qubits that aid in spin-to-charge conversion for initialization and readout. Tunnel-coupled quantum wells may also be used to develop novel qubit implementations such as vertical singlet-triplet qubits or flopping mode spin qubits [14]. Moreover, the thickness and atomic composition of each quantum well may be tuned to optimize g-tensors [15] and spin-orbit interactions [16], in order to provide dedicated functionality. In addition, double quantum wells engineered to provide different g-tensors could be used to execute quantum gates on spin qubits by shuttling the qubit between quantum dots defined in the two quantum wells [17, 12]. This would enable qubit control with baseband pulses, diminishing the need for high-power microwave electronics.

Quantum dots in multiple quantum wells may also present new opportunities for analog quantum simulation. While planar two-dimensional quantum dot arrays may be used to simulate correlated physics such as the resonating valence bond [18], quantum dots in a double quantum well may simulate even more exotic systems. For example, exciton condensation may be induced by the Coulomb interaction when the quantum dot occupation in one layer is almost filled and in the other almost empty, creating an effective electron and hole layer. Such a gate-defined quantum dot system may provide more control over individual parameters when studying excitons, when compared to quantum transport implementations [19, 20, 21, 22]. Quantum dots in multi-layer structures comprised of three or more quantum wells could also be envisioned. The confinement of quantum dots in three layers potentially supports artificial superconductivity. Attractive Coulomb interaction in quantum dot systems has been observed in planar systems [23, 24] and integration of such interactions into a trilayer system may provide a route toward tunable and controllable superconducting condensation.

These motivations warrant the study of quantum dots defined in multilayer heterostructures. However, there are also many challenges in the design and operation that need to be understood and overcome. We take a first step and demonstrate a gate-defined vertical double quantum dot in a strained germanium double quantum well heterostructure. Through quantum transport measurements, we obtain charge stability diagrams consistent with two quantum dots coupled in parallel. We characterise the capacitive interaction of the quantum dots to the surrounding gates and determine their location. The size of one of the quantum dots is estimated through bias-spectroscopy. Together, these findings point toward the formation of a double quantum dot vertically aligned under the same plunger gate.

6.3. RESULTS

An undoped and compressively-strained Ge/SiGe double quantum well heterostructure is epitaxially grown on a 100 mm Si(100) substrate. A 55 nm thick $Si_{0.2}Ge_{0.8}$ spacer separates the bilayer system from the gate stack. The top and bottom quantum wells in the bilayer are 10 nm and 16 nm thick respectively, and are separated by a 4 nm $Si_{0.2}Ge_{0.8}$ barrier (Fig. 6.1b). We perform magnetotransport characterization of a Hall-bar shaped

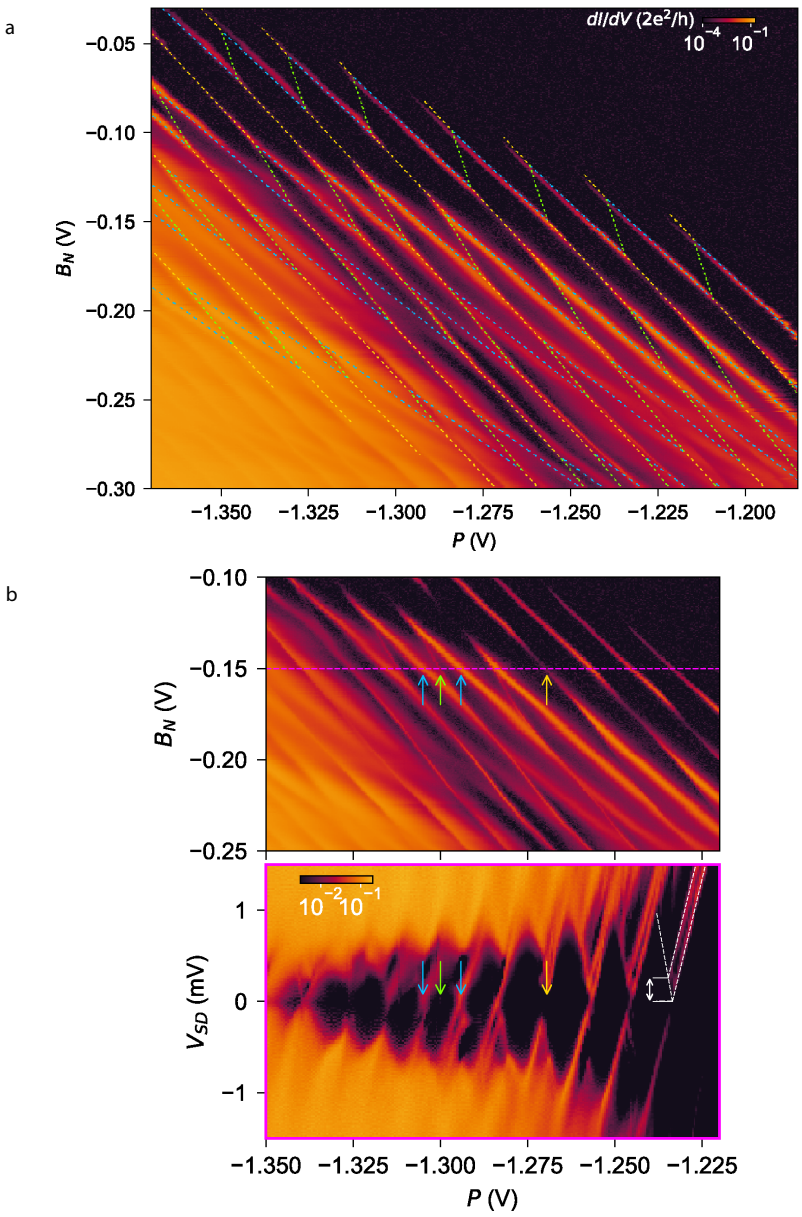

Figure 6.2: **Charge stability diagram of the vertical double quantum dot. a** By sweeping the gates P vs B_N, a honeycomb pattern emerges as the gates induce transport resonances. The dashed coloured lines overlain on the data correspond to the electrochemical simulation of the double-quantum dot system, detailed in Appendix 6.5.2. **b** Upper panel: A zoom-in of the data presented in panel a with coloured arrows corresponding to different transitions. Lower panel: Bias spectroscopy across a line-cut of panel b top (magenta) at $B_N = -0.15$V, the coloured arrows correspond to the transitions highlighted in the top panel. Measurement of the orbital energy for the first Coulomb diamond is indicated by the white lines and is extracted to be approximately 260 μeV. All measurements in this figure are acquired with a lock-in amplifier, with a typical frequency of 70 Hz, and amplitude of 17 μV.

heterostructure field effect transistor (FinFET) to infer the energy spectrum of the hole bilayer. The conductance map as a function of the external magnetic field in Fig. 6.1c reveals the emergence of two sets of Landau levels typical of such a bilayer system [9, 25]. At $V_G \approx -320\,\text{mV}$ the longitudinal conductivity σ_{xx} shows the first set of quantized Landau levels, corresponding to the subband localized in the bottom well. At $V_G \approx -400\,\text{mV}$ the conductance curve at zero-magnetic-field (Fig. 6.1c bottom panel) deviates from a linear increase and flattens out as the sub-band localized in the top well starts being populated. This originates from the electric field screening caused by the accumulation of charge carriers in the top well, while its density is still below the percolation threshold and transport is only available through the bottom well [9]. For more negative voltages, the carriers in the top well start contributing to transport and conductance increases. This confirms that this heterostructure is compatible with the accumulation of a bilayer 2D hole gas.

We then fabricate gates to electrostatically define quantum dots in this bilayer system (see Methods). A 3D schematic depicting the heterostructure and gate stack, and a scanning electron microscopy (SEM) image of a nominally identical device are respectively shown in Fig. 6.1b,d. The gate geometry is similar to quantum dot devices with a single quantum well [2]. The central plunger gate P is negatively biased to accumulate holes beneath it, while the barrier gates B_W and B_E are used primarily to tune the tunnel barrier to the ohmic contacts (S and D). The gates B_N and B_S further shape the potential landscape without significantly affecting the tunnel barrier to the ohmics. We measure the transport through the device with DC and low-frequency lock-in techniques (see Methods).

At high source-drain DC bias ($V_{DC} = 1\,\text{mV}$, Fig. 6.1e blue line) the conductance trace starts to increase as P is lowered and a transport channel opens. After a first increase, the conductance plateaus at $P = -1.2\,\text{V}$, before showing a second increase in conductance indicating the opening of a second transport channel. We study this same phenomenon at low bias $V_{DC} = 0\,\text{mV}$ and measure the differential conductance using a lock-in amplifier. The differential conductance trace I_{AC}/V_{AC} (pink line) reveals the emergence of Coulomb peaks, which begin at $-1.14\,\text{V}$. Interestingly, the Coulomb peaks show a decrease in amplitude between $-1.2\,\text{V}$ and $-1.3\,\text{V}$, after which the amplitude increases again. We speculate that this decrease in amplitude is caused by an increased tunnel coupling to a second parallel quantum dot which may not contribute to transport itself yet. If this second quantum dot has lower conductance, an increased wavefunction amplitude in this second quantum dot would reduce the Coulomb peak height [26]. This wavefunction delocalization across two tunnel-coupled quantum wells has also been predicted by Schrödinger-Poisson simulations [9]. At more negative voltages, the second quantum dot also starts contributing to transport, and Coulomb peaks re-emerge. While the intermediate voltage gives rise to a complex gate voltage dependence, the observation of a double turn-on suggests the presence of a second quantum dot.

To further investigate the quantum dots in this bilayer system, we map the charge stability diagram as a function of the gate voltages applied on B_N and P, shown in Fig. 6.2a,b. A distinct honeycomb pattern emerges, indicating the presence of a double quantum dot system [27]. This is confirmed by an overlayed electrochemical simulation of a double quantum dot coupled in parallel, which reproduces the location of the charge transitions

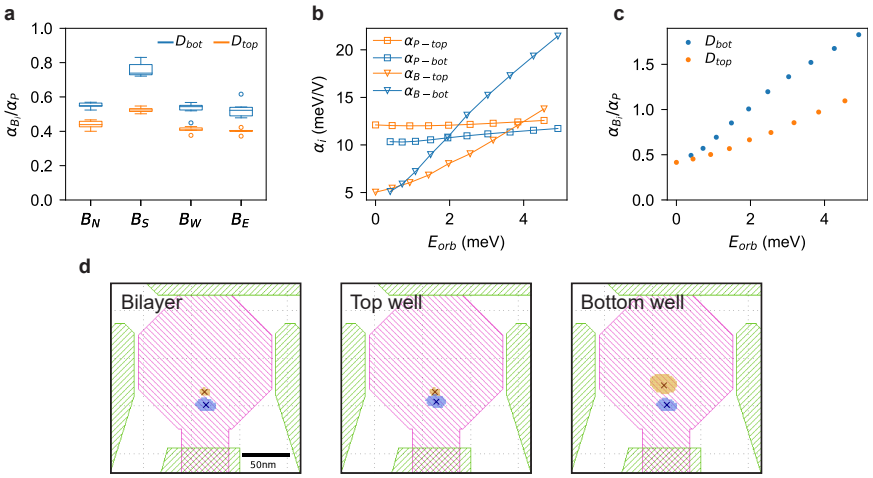

Figure 6.3: **Measured and simulated lever arm ratios of the surrounding gates to the quantum dots, and the triangulation of their centre points. a** Boxplot of the lever arm ratios ($\alpha_{B_i,D_i}/\alpha_{P,D_i}$) of each barrier gate B_i to the plunger gate P for the top and bottom quantum dot (D_i). These couplings are extracted from the slopes of different reservoir transitions in the charge stability diagrams as a function of B_i and P (see Appendix 6.5.2). The spread in $\alpha_{B_i,D_i}/\alpha_{P,D_i}$ for different occupations is small compared to the difference in $\alpha_{B_i,D_i}/\alpha_{P,D_i}$ between the two quantum dots, ensuring that the average value of $\alpha_{B_i,D_i}/\alpha_{P,D_i}$ for a quantum dot across a range of different occupations is a meaningful metric for assessing the positioning of the quantum dots with respect to the surrounding gates. **b** Simulated lever arms for the plunger gate P and barrier gate B to the top and bottom quantum dot calculated from the 2D Schrödinger-Poisson simulation described in Appendix 6.5.3. **c** Simulated lever arm ratios $\alpha_{B_i,D_i}/\alpha_{P,D_i}$ for the first 20 orbital states, plotted against the orbital energy (E_{orb}), with data extracted from the Schrödinger-Poisson simulation. **d** Triangulation of the position of the quantum dots by comparing the lever arm ratios in **a** with capacitive simulation (Appendix 6.5.4). The cross indicates the centre point of each quantum dot, and the coloured area represents the 1σ standard deviation of this value. In the 'Bilayer' panel the quantum dots are simulated one at a time in separate wells, with the orange quantum dot and blue quantum dot placed in the top and bottom well respectively. In the 'Top Well' and 'Bottom Well' panels, the quantum dots are simulated one at a time in the same layer.

(see Appendix 6.5.2 for details of the model). In the region between $P = -1.32\,\text{V}$ and $P = -1.25\,\text{V}$ we observe transport at every edge of this honeycomb, corresponding to the interdot charge transition and the two reservoir to quantum dot transitions.

To distinguish the inter-dot transitions from the reservoir transitions in the charge stability diagram of Fig. 6.2a,b, we measure the differential conductance as a function of V_{DC} and P. The bottom panel of Fig. 6.2b shows a set of Coulomb diamonds taken in the regime where $B_N = -0.15\,\text{V}$ (magenta line-cut shown in the top panel). The transition lines that fall on this line-cut corresponding to a signal at $V_{\text{DC}} = 0\,\text{mV}$ in the lower panel are indicated by the four coloured arrows. The transition lines indicated by the blue and orange arrows correspond to the edges of the Coulomb diamonds, and are attributed to quantum dot-reservoir transitions. In contrast, the transition line indicated by the green arrow lies in the middle of a Coulomb diamond, and a conductance peak is barely visible. This is the expected behaviour for an interdot transition, where transport is only possible through co-tunneling processes, such as elastic co-tunneling [28], resulting in a faint conductance signal, only when the two quantum dots are in resonance.

The unusual negative slope of the interdot transition is a result from both B_N and P predominantly coupling to the same quantum dot, corresponding to the orange transitions (see Appendix 6.5.1). With the four identified transition lines as a reference, we map each transition line in the charge stability diagram using the hexagonal pattern and slopes of the lines.

The presence of the two reservoir transition lines (blue and orange) indicates that both quantum dots are connected in parallel to the ohmic contacts. At the interdot transition line (green) series transport may occur. Since a simulated double quantum dot system fits our data well, we consider the formation of a triple quantum dot improbable. Such a triple quantum dot would produce pentagonal or heptagonal features [29] which we do not observe. We further exclude the possibility of a triple quantum dot as that would require at least two of the three quantum dots to be located in the same quantum well, and as a result have distinct lever arms to the surrounding gates, which we elaborate on further in the upcoming paragraphs. We observe just two distinct reservoir transitions, and we argue in the following paragraphs that these must correspond to vertically stacked quantum dots.

The behaviour of this bilayer quantum dot system outside of the explored parameter regimes may have different characteristics. Above $P = -1.2\,\mathrm{V}$, we expect there are two quantum dots, with one or both of them contributing to transport. Below $P = -1.35\,\mathrm{V}$, the system allows for multiple scenarios. The increased quantum dot size with occupancy may cause delocalization across the two quantum wells. High charge occupation may also result in a decreased charging energy and high coupling to the ohmics, which can give rise to a constant current, potentially observed in the bottom left region of Fig. 2a, if a dot opens to a channel. Additionally, a high top gate voltage may result in wavefunction localization in the top quantum well, resulting in only the top quantum dot contributing to transport.

Unlike a typical double-quantum dot charge stability diagram [27] where each quantum dot predominantly responds to its own dedicated plunger gate, transition lines in this diagram have very similar slopes, indicating that the gates have similar lever arm ratios α_{B_N}/α_P to both quantum dots. This observation is consistent with vertically stacked quantum dots of similar shape, as the lever arm ratio primarily depends on the in-plane position of the quantum dots. Crucially, we are still able to populate both quantum dots, which is not trivial for a vertically coupled double quantum dot due to possible screening by the top well (see Appendix 6.5.1). In this device, this is aided by a higher charging energy of the top dot resulting from increased confinement. On the other hand, the reduced confinement increases the size of the bottom quantum dot and hence its lever arm to surrounding gates.

Next, we extract the position of both quantum dots using the measured capacitive coupling to surrounding gates. We map the charge stability diagram as a function of B_i ($i = N, W, S, E$) and P (see Appendix Fig.6.8) and based on the slopes of the reservoir transitions we find that both quantum dots have comparable lever arms to all surrounding gates (Fig. 6.3a). A first observation is that both quantum dots are most strongly coupled to the plunger gate, giving a first indication that they are located underneath it. Importantly, we find that all barrier gates have a similar capacitive coupling to the quantum dots. The symmetry of this coupling suggests there are no spurious quantum dots, with

the observed quantum dots both being located underneath the plunger gate. Additionally, we find that one quantum dot has a higher lever arm ratio $\alpha_{B_i,D_i}/\alpha_{P,D_i}$ to all barrier gates. This is consistent with a stacked double quantum dot, where the top quantum dot is expected to be smaller, causing a reduction of the coupling o the barrier gates,

To further support the conclusion of having created a vertical double quantum dot, we estimate the position of both quantum dots using an electrostatic finite element method (FEM) simulation in Ansys Q3D [30], in which the heterostructure, gate layers and insulating layers are included (details can be found in Appendix 6.5.4). The quantum dots are simulated individually in both layers, to analyze all their possible locations (Fig.6.3d). Each quantum dot is modelled as a metallic disk as thick as the quantum well it is located in. The radius and position of this simulated metallic quantum dot are varied to analyze the effect on the capacitance. The geometric capacitance between each metallic quantum dot D and each gate G is determined and assumed to be directly proportional to the lever arm $\alpha_{G,D}$. By comparing the simulated capacitance with the measured lever arm ratio $\alpha_{B_i,D}/\alpha_{P,D}$, the position of a single quantum dot within either quantum well is triangulated. The predicted centre-centre distance between the quantum dots has an upper bound of 30 nm (Fig. 6.3d), regardless of which well the quantum dots are simulated in. This close proximity prohibits the coexistence of both quantum dots in the same layer without coalescing, suggesting that the quantum dots must be located in different quantum wells. We account for a 1σ error in the position, as indicated by the coloured area in Fig. 6.3d, which is based on the spread of the lever arm ratios that are extracted from each charge-stability diagram.

We estimate the size of one quantum dot from the orbital energy $E_{orb} = 260\,\mu$eV extracted from Fig.6.2b (lower panel, white lines). Assuming a harmonic in-plane potential $V_{xy} = \frac{1}{2}m^*\omega^2(x^2+y^2)$, where $\hbar\omega = E_{orb}$ and $m^* = 0.055m_e$, this gives a quantum dot diameter of about $d = \sqrt{\hbar/(\omega m^*)} = 137\,$nm, comparable to the plunger gate size of 150 nm. Based on the size approximation of this quantum dot and their mutual proximity, we conclude that the quantum dots cannot coexist in a single layer without coalescing. Overall, the measured lever arm ratios, together with the results from the FEM simulation and the estimates of the quantum dot size from the Coulomb diamonds, provide strong arguments for the quantum dots being vertically stacked under the plunger gate.

To identify in which quantum well each quantum dots resides, we perform a 2D Schrödinger-Poisson simulation (Fig. 6.3 b,c). We calculate the capacitive coupling between the plunger gate P and a barrier gate B for consecutive orbital fillings of the top and bottom quantum dot to deduce the lever arms (Fig. 6.3b). While the lever arm of the plunger gate to the top and bottom quantum dot (α_{P-top} and α_{P-bot}) remains approximately constant with increasing orbital number, the barrier gate lever arm to both quantum dots varies significantly with the orbital number. This originates from an increase in the wavefunction spread for consecutive orbitals, increasing the overlap and consequently the coupling to the barrier gate. Fig. 6.3c shows the corresponding lever arm ratio of the quantum dots formed in the top quantum dot (D_{top}) and bottom quantum dot (D_{bot}) for different orbitals. Panel c shows that for all simulated orbitals the bottom quantum dot has a relatively larger lever arm to the barrier gates. Comparing this to the measured lever arms ratios in Fig. 6.3a we conclude that D_{top} (orange transi-

tions in Fig. 6.2) corresponds to a quantum dot located in the upper quantum well and D_{bot} (blue transitions in Fig. 6.2a) to a quantum dot located in the bottom quantum well. This interpretation is confirmed by the position and slope of the interdot transitions in the charge stability diagrams. As the plunger gate voltage becomes more negative, attracting holes to the gate, a hole tunnels from D_{bot} to D_{top} across the interdot transition. We therefore conclude that D_{top} is localized in the top well.

6.4. DISCUSSION AND OUTLOOK

In this work we demonstrate a double quantum dot defined in a double quantum well heterostructure. A single gate can be used to simultaneously populate quantum dots in two wells, whilst the charge occupation can be tuned using one of the surrounding gates. From the double quantum dot charge stability diagrams obtained from mapping P vs B_i , we extract the lever arm ratios of the quantum dots to the surrounding gates and confirm that neither quantum dot couples strongly to a particular barrier gate, excluding the possibility of a spurious dot. By comparing the lever arm ratios to an electrostatic FEM simulation we triangulate the in-plane position of the quantum dots and find their centre point at approximately the same in-plane position. If the quantum dots were to be in the same quantum well, we would expect a much larger coupling than observed, and effectively a merged quantum dot. Furthermore, the estimated quantum dot diameter D_{bot} = 135 nm suggests that a double quantum dot can only exist by occupying both quantum wells. Based on these findings we conclude the realisation of a vertically coupled double quantum dot in a double quantum well.

Operating many quantum dots, and specifically many vertical double quantum dots, is certainly not an easy task. However, we can envision that a set of plunger gates, barrier gates, and gates at the corners in a 2D array could jointly provide a virtual gate space to control the charge occupation in the quantum dots, as well as the lateral tunnel coupling between the quantum dots. In doing so, vertically coupled quantum dots may provide new means for scaling, coupling, and addressing semiconductor quantum dot qubits.

6.5. METHODS

The device is fabricated on a Si_xGe_{1-x}/Ge/Si_xGe_{1-x}/Ge/Si_xGe_{1-x} heterostructure, where $x = 0.2$, grown by reduced pressure chemical vapour deposition. The virtual substrate on which the heterostructure is grown consists of a silicon substrate, upon which there is a 1.6 µm relaxed Ge layer; a 1 µm graded Si_xGe_{1-x} layer, with a final Ge composition of x = 0.2. On top of the SiGe virtual substrate, the bilayer system comprises a 16 nm thick bottom Ge quantum well, a 4 nm thick SiGe barrier, a 10 nm thick top Ge quantum well, and a final 55 nm thick SiGe spacer. At the top of the stack, a sacrificial Si cap is grown to provide a native SiOx layer. We define ohmic contacts using electron beam lithography and remove the Si cap in the exposed area using a buffered oxide etch. We then evaporate a 30 nm platinum layer and contact the quantum wells using a 10-minute rapid thermal anneal at 400°C, forming platinum germanosilicides. The ohmic layer is isolated using a 7 nm layer of Al_2O_3 grown by atomic layer deposition. Electrostatic gates used to define the quantum dots are patterned in two layers (3/17 nm and 3/37 nm of Ti/Pd.) and are separated by a 5 nm layer of Al_2O_3.

Devices are screened in 4 K liquid helium. Experiments reported in this paper are carried out in a Bluefors LD400 dilution refrigerator with a base temperature of 10 mK. The electrical properties of the quantum dots are investigated through two terminal AC and DC measurements. We apply a tunable DC bias V_{DC} across the source (S) and drain (D), and measure the resulting current with a Keysight digitizer and from this we calculate the conductance $G_{DC} = I_{DC}/V_{DC}$. To measure differential conductance we use a lock-in technique and apply a sinusoidal bias with frequency 70 Hz and amplitude V_{AC} =17 µV from which we can calculate the differential conductance $G_{AC} = dI/dV = I_{AC}/V_{AC}$. When we acquire with the digitizer, the amplitude of the lock-in input signal is reduced to $V_{AC} = 0.04\,\mu$V.

APPENDIX

MAGNETOTRANSPORT

Figure 6.4a shows the magnetotransport characterization of a Hall-bar shaped device. In the voltage range between −250 mV and −400 mV, only the bottom quantum well is occupied, and the density shows a linear dependence on gate voltage while the mobility and conductivity increase monotonically. The fan diagram in Fig. 6.4b shows the typical pattern of single channel transport. Below −400 mV population of the top well becomes energetically favourable, but its density remains below the percolation density until $V_G = -430$ mV, where it starts contributing to transport. Any further increase in the electric field in the bottom well is screened by the charge added to the top well, leaving the bottom well density unchanged. Within the voltage region where the density in the bottom well remains constant and the holes added to the top well are not mobile, the bilayer density measured from the Hall effect plateaus, as does the conductivity and mobility. Beyond this region for $V_G < -430$ mV, the top quantum well is above the percolation threshold, charges are mobile and contribute to transport, resulting in a second set of Landau levels. While the bilayer density and conductivity increase with increasing negative voltages, the mobility curve drops before reestablishing its increasing trend. We ascribe this temporary drop in mobility to interlayer scattering [9].

FULL DEVICE

Figure 6.5 shows a false-coloured SEM of the whole device, of which only the left most gates were used in this experiment.

6.5.1. DOUBLE QUANTUM DOT CHARGE STABILITY DIAGRAMS FOR DIFFERENT SYSTEM PARAMETERS

The features of a double quantum dot charge stability diagram strongly depend on the capacitive coupling between the gates and the quantum dots, as well as between the quantum dots themselves. These parameters are expected to be significantly different in a vertically coupled double quantum dot compared to more typical planar quantum dots. It is therefore instructive to qualitatively analyse the charge stability diagram of a double dot system that better describes a vertically coupled double quantum dot. This should aid the reader in interpreting the experimentally obtained charge stability diagrams in this paper.

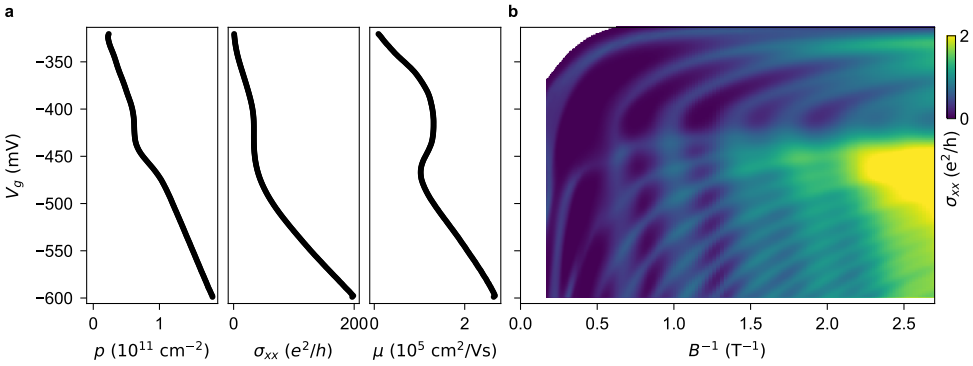

Figure 6.4: **Magnetotransport characterisation of the hole bilayer measured using a Hall-bar shaped field effect transistor. a** From left to right: gate voltage (V_g) dependence of the hole bilayer Hall density p, conductivity σ_{xx} at zero magnetic field, and mobility μ. **b** Colour map of the conductivity σ_{xx} as a function of V_g and the inverse magnetic field B^{-1}. Dark regions correspond to filled Landau levels with vanishing σ_{xx} and correspondingly quantized σ_{xy}.

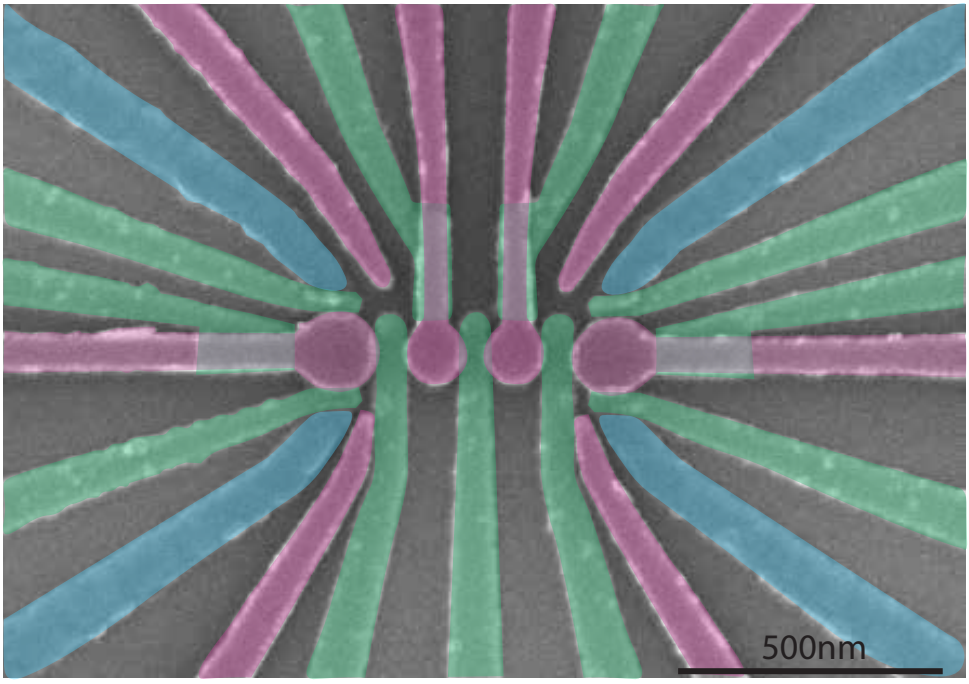

Figure 6.5: **A false-coloured SEM of a device similar to the one used in this experiment**. The experiments are conducted in quantum transport through the left quantum dot (purple) which is coupled to the ohmics (blue) and controlled via barrier gates (green).

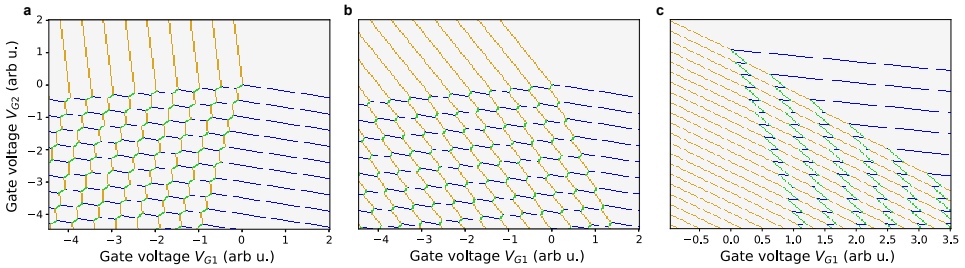

Figure 6.6: **Charge stability diagram dependence on different system parameters.** In each charge stability diagram G_1 satisfies (violates) inequality 6.1 (6.2). The charge carriers are assumed to be holes. **a** Regime where D_1 is not loaded via G_2 due to charge occupation in D_2, as inequality 1 is violated. **b** Regime where G_2 satisfies both inequalities. **c** Here G_2 violates inequality 6.2 while satisfying inequality 6.1.

In any double quantum dot system, a particular gate G can only subsequently load a quantum dot D_i if a voltage on G can offset the electrostatic energy arising from the loading of any other quantum dot. In particular, for G to load quantum dots D_1 or D_2 while the other one is occupied, the system has to respectively satisfy the following inequalities:

$$\frac{E_{C2}}{\alpha_{2,G}} > \frac{E_{Cm}}{\alpha_{1,G}} \tag{6.1}$$

$$\frac{E_{C1}}{\alpha_{1,G}} > \frac{E_{Cm}}{\alpha_{2,G}} \tag{6.2}$$

Here $\alpha_{1(2),G}$ is the lever arm between the gate G and $D_{1(2)}$, and $E_{C1(2)}$, the charging energy of $D_{1(2)}$, and E_{Cm} the electrostatic coupling energy [27]. If inequality 6.1 (6.2) is violated, then quantum dot D_1 (D_2) can not be occupied due screening from D_2 (D_1).

In planar double quantum dots, each quantum dot is predominantly coupled to a single plunger gate, which in return couples relatively weakly to the other quantum dot. That is, plunger gate G_1 couples predominantly to D_1 such that $\alpha_{1,G_1}/\alpha_{2,G_1} > 1$, and inequality 6.1 is satisfied, since $E_{Cm} < E_{C2}$. The same holds for D_2 and the corresponding plunger gate. Figures 6.6**a** and **b** display examples of typical planar double quantum dots hosting holes.

For a vertically coupled double quantum dot, the situation may be different. The lever arm between all gates and the bottom quantum dot can become smaller than to the top quantum dot, and the electrostatic coupling energy E_{Cm} is large due to the close proximity of the wavefunctions. Hence the loading of the top quantum dot might prevent the bottom quantum dot from being loaded, screening the bottom quantum dot. Denoting D_2 as the bottom quantum dot, it is no longer trivial that there is a gate G for which the second inequality is satisfied. Such a situation is depicted in figure 6.6**c**. Once D_1 becomes occupied an increasingly negative voltage on either gate will deplete D_2 instead of loading more holes onto it, making it more challenging to find the desired

charge occupation within the operating window of the device.

To ensure loading of the bottom quantum dot, it is therefore crucial to maximise $\alpha_{2,G}/\alpha_{1,G}$ for some gate G. In our experiment this is achieved by having more in-plane confinement of the top quantum dot, due to the close proximity to the top gates. Less in-plane confinement allows the bottom quantum dot to be more coupled to the surrounding barrier gates. Moreover, the stronger in-plane and out-of-plane confinement of the top quantum dot (D_1) increases the charging energy E_{C1} making condition 6.2 more easily satisfied. We note that in a realistic system, where the lever arms and charging energies are not constant, there could be a transition from one regime to another.

For vertically coupled quantum dots, the interdot transition also might have the opposite slope compared to that of a typical planar double quantum dot. In general for any double quantum dot system controlled by gates G_1 and G_2 an interdot transition occurs along a line in the voltage space (V_{G1}, V_{G2}) for which:

$$\alpha_{1,1}\Delta V_{G1} + \alpha_{1,2}\Delta V_{G2} = \alpha_{2,1}\Delta V_{G1} + \alpha_{2,2}\Delta V_{G2}$$

where $\alpha_{D,G}$ is the lever arm between dot D and gate G, and ΔV_G denotes a change in the voltage of gate G. The slope of this line is hence given by

$$\frac{\Delta V_{G2}}{\Delta V_{G1}} = \frac{\alpha_{21} - \alpha_{11}}{\alpha_{12} - \alpha_{22}}$$

For planar double quantum dots the plunger gates couple predominantly to different dots, such that $\alpha_{11} > \alpha_{21}$ and $\alpha_{22} > \alpha_{12}$. Planar double quantum dots will thus have a positive slope $\frac{\Delta V_{G2}}{\Delta V_{G1}} > 0$ for the interdot transition (Fig. 6.7a). However, for a vertical double quantum dot both gates generally couple predominantly to the same dot. This will lead to a negatively sloped interdot transition $\frac{\Delta V_{G2}}{\Delta V_{G1}} < 0$. In our measurements we observe the situation in Fig. 6.7c, suggesting that both gates in our charge-stability diagrams are dominantly coupled to the same quantum dot located in the upper quantum well. This also suggests that loading of the bottom dot is only possible due to the large charging energy of the top quantum dot, compared to the mutual electrostatic interaction.

6.5.2. COMPARISON BETWEEN MEASURED CHARGE STABILITY DIAGRAMS AND ELECTROCHEMICAL SIMULATION

In order extract the lever arm ratios of both quantum dots as described in the main text, charge stability diagrams (CSD) were measured by varying the plunger gate P voltage together with the voltage of surrounding barrier gates (Fig. 6.8). The inter-dot transitions in these measurements are less pronounced compared to figure 6.2 of the main text, which is attributed to a change in the tunnel coupling due to a different voltage regime. In this appendix, we compare these measurements with classical electrochemical simulations of a double quantum dot system [27].

The charge carriers in the simulation are holes, and gates couple to both quantum dots through the occupation-dependent lever arm matrix α. Hence the electrochemical po-

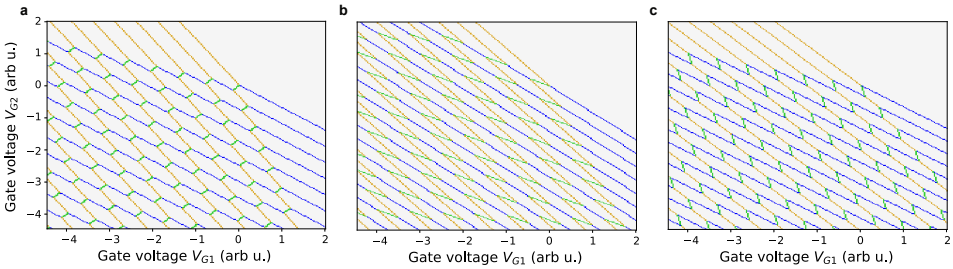

Figure 6.7: **Charge stability diagrams with different interdot slopes.** The interdot slope (depicted in green) depends on the ratio between the lever arms. We denote D_1 (D_2) as the quantum dots with the steep (shallow) reservoir transition line. A positive interdot slope as in **a** is observed whenever each gate couples predominantly to different quantum dots. If both gates couple stronger to D_2 than to D_1 the situation in **b** is observed. If both gates couple more to D_1 than to D_2 we observe the situation in **c**, as is the case in our experiments. We note that in a real system the different gate arrangements corresponding to **a**-**c** may also lead to a variation in charging voltage, which has not been highlighted in these simulations.

tential μ of the quantum dots is given by:

$$\begin{aligned}
\mu_1(N_1,N_2,\mathbf{V}) &= \Sigma_{n_1=1}^{N_1} E_{C1}(n_1) \\
&\quad + \Sigma_{n_2=1}^{N_2} E_{Cm}(N_1,n_2) \\
&\quad + \alpha_1(N_1,N_2,\mathbf{V})\mathbf{V} \\
\mu_2(N_1,N_2,\mathbf{V}) &= \Sigma_{n_2=1}^{N_2} E_{C2}(n_2) \\
&\quad + \Sigma_{n_1=1}^{N_1} E_{Cm}(n_1,N_2) \\
&\quad + \alpha_2(N_1,N_2,\mathbf{V})\mathbf{V}
\end{aligned} \tag{6.3}$$

$N_{1(2)}$ denotes the occupation of the top (bottom) quantum dot. $E_{C1(2)}(N_{1(2)})$ and $E_{Cm}(N_1,N_2)$ are the occupation-dependent charging energies of the top (bottom) quantum dot and the electrostatic inter-dot coupling energy respectively. $\mathbf{V}$ is the vector denoting the gate voltages. The coupling between the gates and the top (bottom) quantum dot is given by two row matrices $\alpha_{1(2)}$, with purely positive entries. These lever arms are generally taken to be occupation- and voltage-dependent. Since the charging energy is poorly defined for level-dependent lever-arms, these are defined at an (arbitrary) fixed reference voltage $\mathbf{V_{ref}}$:

$$\begin{aligned}
E_{C1(2)}(N_{1(2)}) \equiv\ & \mu_{1(2)}(N_{1(2)},N_{2(1)},\mathbf{V_{ref}}) \\
& - \mu_{1(2)}(N_{1(2)}-1,N_{2(1)},\mathbf{V_{ref}})
\end{aligned} \tag{6.4}$$

fixing $\mu(0,0,\mathbf{V_{ref}}) = 0$. The charging energies and the inter-dot capacitive energies are consistent across simulations in figure 6.8. To reduce the free parameters further the coupling matrix α is simplified. $\alpha_1(V_P)$ and $\alpha_2(N_2,V_P)$ are dependent on the plunger gate voltage V_P instead of on all the gate voltages, with the latter also depending on the occupation of the bottom quantum dot. With these assumptions, the data matches a charge stability diagram of a double quantum dot as seen in Figure 6.8 and Figure 6.2 of

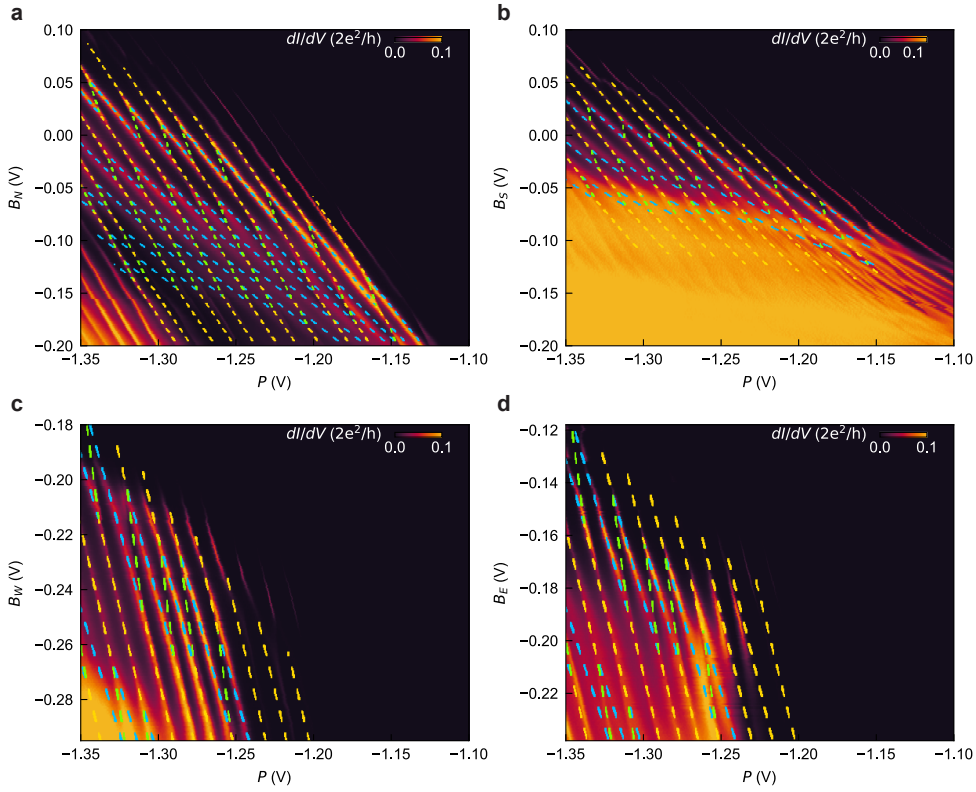

Figure 6.8: **Charge stability diagrams as a function of the Plunger gate P, and barrier gates $\mathbf{B_N}, \mathbf{B_S}, \mathbf{B_W}, \mathbf{B_E}$, with electrochemical simulation overlain.** Comparison between transport data and the double quantum dot simulation defined by equation 6.3. The data is measured with lock-in techniques
. Subfigures **a-d** give the differential conduction through the system as a function of the voltages on the plunger gate P against the voltage applied on respectively B_N, B_S, B_W and B_E. These plots share a common gate reference at $\mathbf{V_{ref}} = [P = -1.217\text{V}, B_N = 0\text{V}, B_S = 0\text{V}, B_W = -0.237\text{V}, B_E = -0.178\text{V}]$. The simulation has been limited to the double-quantum dot region. Data without the simulation is found in Fig. 6.9. The code used to produce the simulated transition lines can be found on Zenodo via the link provided in the main manuscript.

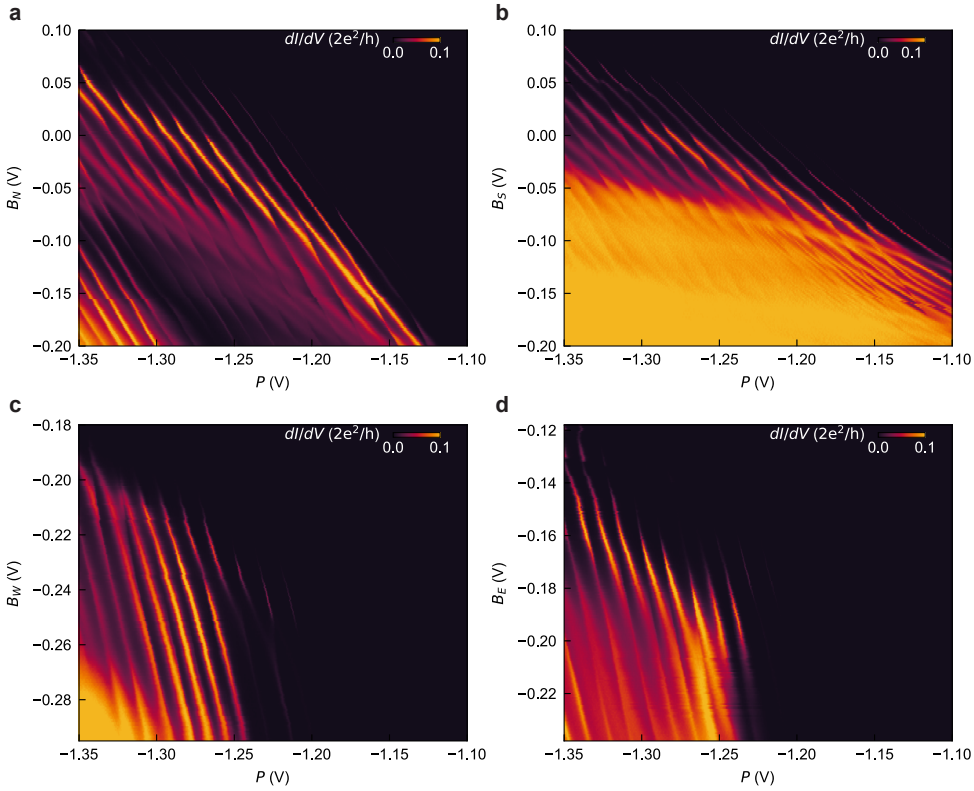

Figure 6.9: **Charge stability diagrams as a function of the Plunger gate P, and barrier gates B_N, B_S, B_W, B_E, without electrochemical simulation overlain.**

the main text. The used parameters can be found in full on Zenodo using the link provided in the main text. This match suggests that the system indeed consists of a double quantum dot, with no additional dot interacting with it in a meaningful way. The latter would namely result in additional (triangular, pentagonal or heptagonal) features that we do not observe.

To achieve the observed match, the lever arms between the gates and the bottom quantum dot need a significant dependency on the occupation of the bottom quantum dot. This is not as pronounced for the top quantum dot, which is expected from the stronger in-plane confinement. Any additional charges on the top quantum dot will have a larger impact on its size and thus on the coupling to the barrier gates.

We note that the plunger gate voltage has a significant effect on the lever arm of B_S, as seen by the curvature of the transition lines in Figure 6.9b. This suggests that the plunger gate significantly changes the capacitive coupling between B_S and the quantum dots, which would occur if the quantum dots are close to B_S. This is consistent with the estimated positions of the quantum dots that are presented in the main text.

Small discrepancies between the data and the electrochemical simulation are attributed to the limited parameters of the model, like the neglected dependence on the top quantum dot occupation and the exclusion of tunnel-coupling. Moreover for increasingly negative voltages on B_N and B_S the system is generally poorly described by a double quantum dot as seen in Figure 6.8a,b. For lower voltages on B_N (and P) the overall transport first decreases, which we attribute to the same phenomenon which leads to the decrease in the Coulomb peak amplitude in Figure 6.1c (lower panel). namely a larger tunnel-coupling between the top and bottom layer. This increased tunnel coupling could change the interaction between the quantum dots and the leads. At even lower voltages B_N and P a single-dot charge stability diagram emerges corresponding to loading of the top quantum dot, which corresponds to either the merging of the top and bottom quantum dot, or the screening of the bottom quantum dot by the top layer. For the latter case, the possibility of this transition is described in appendix 6.5.1. For lower voltages on B_S we observe a large background current (Fig. 6.8b). This background current seems to emerge as the resonances of one of the quantum dots become poorly defined and closely spaced. We propose that a conductive channel is formed under B_S through one of the layers of the quantum well. Despite these discrepancies, the good match between the data and this relatively simple model strongly supports that the system in question consists of a double quantum dot without any additional quantum dots.

The code and the parameters used to perform the simulation can be found in full on Zenodo using the link provided in the main text. Here the parameters to fit the charge stability diagram in Figure 6.2 of the main text are also found.

6.5.3. SCHRÖDINGER-POISSON SIMULATION

We perform 2D Schrödinger-Poisson simulation with Nextnano [31]. Figure 6.10a shows the heavy-hole (HH) band edge for the heterostructure ($z > 0$) where the top edges of the quantum wells are positioned at z=55 nm and z=69 nm. For $z < 0$ the gate stack is visible. This comprises of a plunger gate, two barrier gates and a layer of Al_2O_3. Fig. 6.10b shows the wavefunction amplitude for the first 20 2D orbitals for which we calculated the lever arm. The potential applied to the plunger and the barriers is -1.15 V and -0.25 V respec-

tively.
We estimate the tunnel coupling between the two quantum wells by solving the Schrödinger equation for this system and extracting the symmetric-antisymmetric gap between the first two energy states, from which we obtain $t_c^{QW} = 16\,\text{GHz}$. Assuming a harmonic confinement potential in the in-plane direction and the dot centre in the same axis, the single-hole dot-dot tunnel coupling can then be obtained from the radius of the two dots (r_{top} and r_{bottom}) $t_c^{QD} = t_c^{QW}(2r_1r_2)/(r_1^2 + r_2^2)$, with r the Bohr radius. From these assumptions, the upper bound on the estimated dot-dot tunnel coupling for the case of equally sized quantum dots is $t_c^{QD} = t_c^{QW} = 16\,\text{GHz}$.

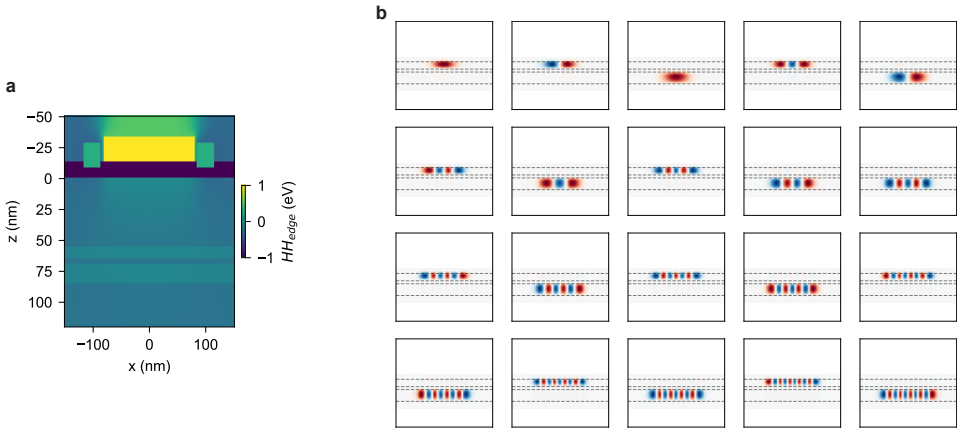

Figure 6.10: **Results of the 2D Schrödinger-Poisson simulations.** **a** Heavy hole band edge as a function of x and z coordinates for the bilayer heterostructure which also comprises the gate stack for $z < 0$, where z is the growth direction. **b** Colour map of the wavefunction amplitude for the first 20 energy levels ordered from left to right, top to bottom.

6.5.4. FINITE ELEMENTS SIMULATIONS OF CAPACITANCE

To get an indication of the position of the quantum dots based on the lever arms, a finite element simulation with Ansys Q3D [30] is performed, to extract the geometric capacitance between a gate and quantum dot. These simulated geometric capacitances are converted to lever arm ratios by dividing the absolute quantum dot-barrier gate capacitance by the quantum dot-plunger gate capacitance. The simulated lever arm ratios are then compared to those obtained from the charge-stability diagrams, and the position at which these best match each other is determined (see Fig. 6.11). This is simulated for the quantum dot being positioned in either the top or the bottom well. The heterostructure has been modelled up to 500 nm in-plane around the plunger gate, and up to a depth of 125 nm below the bottom quantum well. The reservoirs underneath the ohmic gates are excluded in this simulation. While these gates may affect the electrostatic coupling of the other gates to the quantum dot, their symmetric positioning will partly compensate for their impact on the quantum dot location. The dielectric material permittivities used in the simulation are found in table 6.1. The metallic gates have been simulated as uniform perfect conductors.

To emulate a quantum dot a circular, perfectly conducting, uniform disk is placed in either quantum well. This allows us to estimate the geometric capacitance between the quantum dot and the surrounding gates. Each quantum dot is simulated with different disk radii. We note that the wavefunction density of the quantum dot is not taken into account here, and non-circular shapes are not investigated.

Table 6.1: **Relative dielectric permittivity used in the Ansys simulation.** For the properties of $Si_{0.2}Ge_{0.8}$ a linear approximation based on the atomic concentration is used.

Material	ϵ_r
Al_2O_3 [32]	5.9
Ge [33]	15.8
$Si_{0.2}Ge_{0.8}$ [33]	15.0
SiO_2 [34]	3.9

To determine how well the simulations fit the experimental data, we determine the Euclidean distance $\Delta = \sqrt{\sum_{B_i}(\tilde{\alpha}_{B_i,\text{meas}} - \tilde{\alpha}_{B_i,\text{sim}})^2}$, where $\tilde{\alpha}_{B_i,\text{meas(sim)}}$ is the measured (simulated) lever arm ratio α_{B_i}/α_P and the sum is taken over the barrier gates B_N, B_S, B_E and B_W. This Δ is the cost-metric from which we estimate the position (and approximate radius) of the quantum dot.

For each analysed quantum dot and quantum well, there is a particular position and radius at which Δ is minimised (see Fig. 6.11). These are considered to be the most probable locations and radii of that particular quantum dot in the quantum well.

To achieve the minimal Δ, the quantum dots are both predicted to have a radius of about 30 nm and are positioned closer than that to each other (Fig. 6.12). The radius determined here is lower than expected from the plunger gate size, with the discrepancy arising from the approximation of the quantum dot as a uniform disk. From their proximity we conclude that the quantum dots are likely to be in two separate wells. Δ is minimised for D_{top} whenever it is located in the top well, and for D_{bot} when it is in the bottom well. This is consistent with the allocation made in the main text.

Future improvements on this method would consider the electrostatic potential arising from the gates, the strain of the system and the effects of the disorder. Moreover, the interplay between multiple quantum dots spread across the wells can be taken into account in the future, as we stress that currently just a single quantum dot is simulated at a time. A self-consistent 3D Schrödinger-Poisson approach could make this possible.

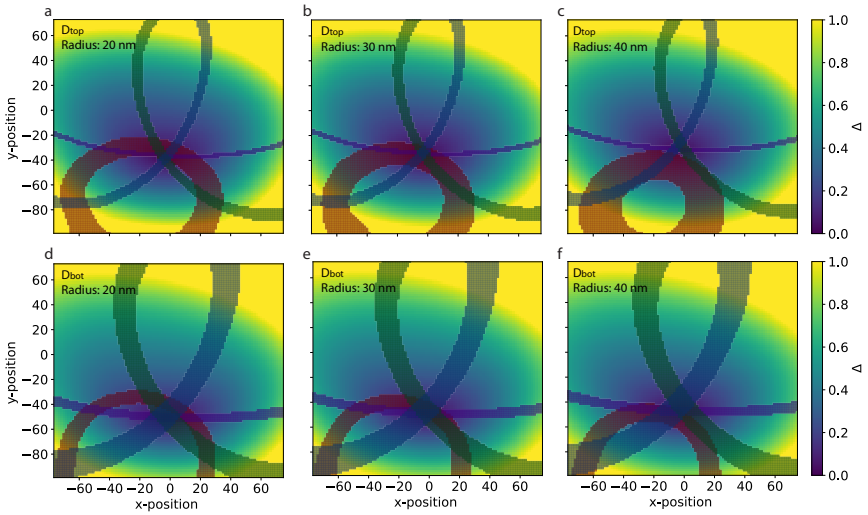

Figure 6.11: **Triangulation of the quantum dots.** Within the red, purple, green and blue contours, the simulated lever arm to the respective gate is within the standard deviation of the empirically extracted values. For D_{top} these are $\tilde{\alpha}_{B_N,\text{meas}} = 0.44 \pm 0.02$, $\tilde{\alpha}_{B_S,\text{meas}} = 0.53 \pm 0.02$, $\tilde{\alpha}_{B_W,\text{meas}} = 0.41 \pm 0.02$, $\tilde{\alpha}_{B_E,\text{meas}} = 0.40 \pm 0.02$ respectively. For D_{bot} these are $\tilde{\alpha}_{B_N,\text{meas}} = 0.55 \pm 0.01$, $\tilde{\alpha}_{B_S,\text{meas}} = 0.76 \pm 0.04$, $\tilde{\alpha}_{B_W,\text{meas}} = 0.53 \pm 0.04$, $\tilde{\alpha}_{B_E,\text{meas}} = 0.53 \pm 0.05$ respectively. The measurement and simulation agree best at the position for which Δ is minimal. The origin is defined at the centre of the plunger gate. Subfigures **a-c** show the results for D_{top}, simulated in the top quantum well for radii of a 20, 30 and 40 nm. Similarly subfigures **d-e** show the results for D_{bot}, as it is simulated in the bottom quantum well for radii of a 20, 30 and 40 nm. For both quantum dots other radii and simulation within the other quantum well result in a higher minimal Δ.

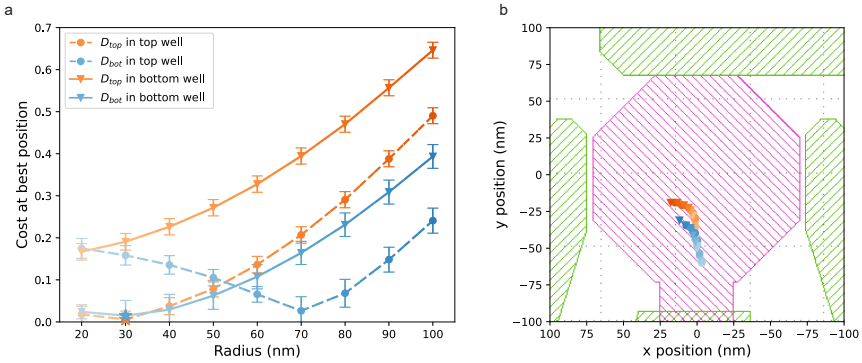

Figure 6.12: **Simulated quantum dot radius and position. a** The Δ corresponding to the most likely quantum dot position for a given quantum dot radius. The simulation and experiments have been compared for either quantum dot in both wells

. Quantum dot 1 (2) corresponds to the orange (blue) transitions in the Fig. 6.2 of the main text. For each quantum dot, the most likely radius is 30 nm. Error bars are based on the standard deviation in the slopes extracted from the raw data in 6.8. **b** The expected position for each radius of the two quantum dots in either the bottom or the top well. For all radii, the quantum dots are close to one another. The darker colours correspond to the larger radii as depicted in **a**.

BIBLIOGRAPHY

[1] S. G. J. Philips, M. T. Mądzik, S. V. Amitonov, S. L. de Snoo, M. Russ, N. Kalhor, C. Volk, W. I. L. Lawrie, D. Brousse, L. Tryputen, B. P. Wuetz, A. Sammak, M. Veldhorst, G. Scappucci, and L. M. K. Vandersypen. "Universal control of a six-qubit quantum processor in silicon". In: *Nature* 609 (7929 Sept. 2022), pp. 919–924. ISSN: 0028-0836.

[2] N. W. Hendrickx, W. I. L. Lawrie, M. Russ, F. van Riggelen, S. L. de Snoo, R. N. Schouten, A. Sammak, G. Scappucci, and M. Veldhorst. "A four-qubit germanium quantum processor". In: *Nature* 591 (7851 Mar. 2021), pp. 580–585. ISSN: 0028-0836.

[3] P. Stano and D. Loss. "Review of performance metrics of spin qubits in gated semiconducting nanostructures". In: *Nature Reviews Physics* 4 (2021), pp. 672–688.

[4] F. Borsoi, N. W. Hendrickx, V. John, M. Meyer, S. Motz, F. van Riggelen, A. Sammak, S. L. de Snoo, G. Scappucci, and M. Veldhorst. "Shared control of a 16 semiconductor quantum dot crossbar array". In: *Nature Nanotechnology* (Aug. 2023). ISSN: 1748-3387.

[5] L. M. K. Vandersypen, H. Bluhm, J. S. Clarke, A. S. Dzurak, R. Ishihara, A. Morello, D. J. Reilly, L. R. Schreiber, and M. Veldhorst. "Interfacing spin qubits in quantum dots and donors—hot, dense, and coherent". In: *npj Quantum Information* 3.1 (Sept. 2017), p. 34. ISSN: 2056-6387.

[6] Z. Wang, M. Feng, S. Serrano, W. Gilbert, R. C. C. Leon, T. Tanttu, P. Mai, D. Liang, J. Y. Huang, Y. Su, W. H. Lim, F. E. Hudson, C. C. Escott, A. Morello, C. H. Yang, A. S. Dzurak, A. Saraiva, and A. Laucht. "Jellybean Quantum Dots in Silicon for Qubit Coupling and On-Chip Quantum Chemistry". In: *Advanced Materials* n/a.n/a (2023), p. 2208557.

[7] F. Borjans, X. G. Croot, X. Mi, M. J. Gullans, and J. R. Petta. "Resonant microwave-mediated interactions between distant electron spins". In: *Nature* 577.7789 (Jan. 2020), pp. 195–198. ISSN: 1476-4687.

[8] J. Yoneda, W. Huang, M. Feng, C. H. Yang, K. W. Chan, T. Tanttu, W. Gilbert, R. C. C. Leon, F. E. Hudson, K. M. Itoh, A. Morello, S. D. Bartlett, A. Laucht, A. Saraiva, and A. S. Dzurak. "Coherent spin qubit transport in silicon". In: *Nature Communications* 12.1 (July 2021), p. 4114. ISSN: 2041-1723.

[9] A. Tosato, B. Ferrari, A. Sammak, A. R. Hamilton, M. Veldhorst, M. Virgilio, and G. Scappucci. "A High-Mobility Hole Bilayer in a Germanium Double Quantum Well". In: *Advanced Quantum Technologies* 5 (5 May 2022), p. 2100167. ISSN: 2511-9044.

[10] D. Laroche, S.-H. Huang, E. Nielsen, C. W. Liu, J.-Y. Li, and T. M. Lu. "Magnetotransport of an electron bilayer system in an undoped Si/SiGe double-quantum-well heterostructure". In: *Applied Physics Letters* 106.14 (Apr. 2015). 143503. ISSN: 0003-6951. eprint: https://pubs.aip.org/aip/apl/article-pdf/doi/10.1063/1.4917296/13050894/143503_1_online.pdf.

[11] M. G. Borselli, R. S. Ross, A. A. Kiselev, E. T. Croke, K. S. Holabird, P. W. Deelman, L. D. Warren, I. Alvarado-Rodriguez, I. Milosavljevic, F. C. Ku, W. S. Wong, A. E. Schmitz, M. Sokolich, M. F. Gyure, and A. T. Hunter. "Measurement of valley splitting in high-symmetry Si/SiGe quantum dots". In: *Applied Physics Letters* 98.12 (Mar. 2011), p. 123118. ISSN: 0003-6951. eprint: https://pubs.aip.org/aip/apl/article-pdf/doi/10.1063/1.3569717/14446901/123118_1_online.pdf.

[12] F. van Riggelen-Doelman, C.-A. Wang, S. L. de Snoo, W. I. L. Lawrie, N. W. Hendrickx, M. Rimbach-Russ, A. Sammak, G. Scappucci, C. Déprez, and M. Veldhorst. *Coherent spin qubit shuttling through germanium quantum dots*. 2023. arXiv: 2308.02406 [cond-mat.mes-hall].

[13] T. Fujita, T. A. Baart, C. Reichl, W. Wegscheider, and L. M. K. Vandersypen. "Coherent shuttle of electron-spin states". In: *npj Quantum Information* 3.1 (June 2017), p. 22. ISSN: 2056-6387.

[14] P. M. Mutter and G. Burkard. "Natural heavy-hole flopping mode qubit in germanium". In: *Physical Review Research* 3 (1 Feb. 2021), p. 13194. ISSN: 2643-1564.

[15] H. Malissa, D. Gruber, D. Pachinger, F. Schäffler, W. Jantsch, and Z. Wilamowski. "Design and fabrication of a SiGe double quantum well structure for g-factor tuning". In: *Superlattices and Microstructures* 39 (5 May 2006), pp. 414–420. ISSN: 07496036.

[16] G. Scappucci, C. Kloeffel, F. A. Zwanenburg, D. Loss, M. Myronov, J. J. Zhang, S. De Franceschi, G. Katsaros, and M. Veldhorst. "The germanium quantum information route". In: *Nature Reviews Materials* 6.10 (Dec. 2020), pp. 926–943. ISSN: 20588437.

[17] R. Vrijen, E. Yablonovitch, K. Wang, H. W. Jiang, A. Balandin, V. Roychowdhury, T. Mor, and D. DiVincenzo. "Electron-spin-resonance transistors for quantum computing in silicon-germanium heterostructures". In: *Physical Review A* 62 (1 June 2000), p. 012306. ISSN: 1050-2947.

[18] C.-A. Wang, C. Déprez, H. Tidjani, W. I. L. Lawrie, N. W. Hendrickx, A. Sammak, G. Scappucci, and M. Veldhorst. "Probing resonating valence bonds on a programmable germanium quantum simulator". In: *npj Quantum Information* 9 (1 June 2023), p. 58. ISSN: 2056-6387.

[19] S. Conti, S. Saberi-Pouya, A. Perali, M. Virgilio, F. M. Peeters, A. R. Hamilton, G. Scappucci, and D. Neilson. "Electron–hole superfluidity in strained Si/Ge type II heterojunctions". en. In: *npj Quantum Materials* 6.1 (2021), p. 41. ISSN: 2397-4648.

[20] D. Nandi, A. D. K. Finck, J. P. Eisenstein, L. N. Pfeiffer, and K. W. West. "Exciton condensation and perfect Coulomb drag". In: *Nature* 488 (7412 Aug. 2012), pp. 481–484. ISSN: 0028-0836.

[21] R. Wang, T. Sedrakyan, B. Wang, D. Lingjie, and D. Rui-Rui. “Excitonic topological order in imbalanced electron–hole bilayers”. In: *Nature* 619 (2023), pp. 57–62.

[22] D. Buterakos and S. D. Sarma. *Magnetic Phases of Bilayer Quantum-Dot Hubbard Model Plaquettes*. 2023. arXiv: 2308.04504 [cond-mat.mes-hall].

[23] A. Hamo, A. Benyamini, I. Shapir, I. Khivrich, J. Waissman, K. Kaasbjerg, Y. Oreg, F. von Oppen, and S. Ilani. “Electron attraction mediated by Coulomb repulsion”. In: *Nature* 535 (7612 July 2016), pp. 395–400. ISSN: 0028-0836.

[24] C. Hong, G. Yoo, J. Park, M.-K. Cho, Y. Chung, H.-S. Sim, D. Kim, H. Choi, V. Umansky, and D. Mahalu. “Attractive Coulomb interactions in a triple quantum dot”. In: *Phys. Rev. B* 97 (24 June 2018), p. 241115.

[25] A. R. Hamilton, E. H. Linfield, M. J. Kelly, D. A. Ritchie, G. A. Jones, and M. Pepper. “Transition from one- to two-subband occupancy in the 2DEG of back-gated modulation-doped GaAs-AlxGa1-xAs heterostructures”. In: *Physical Review B* 51.24 (1995), pp. 17600–17604. ISSN: 01631829.

[26] D. Y. Baines, T. Meunier, D. Mailly, A. D. Wieck, C. Bäuerle, L. Saminadayar, P. S. Cornaglia, G. Usaj, C. A. Balseiro, and D. Feinberg. “Transport through side-coupled double quantum dots: From weak to strong interdot coupling”. In: *Phys. Rev. B* 85 (19 May 2012), p. 195117.

[27] W. G. van der Wiel, S. De Franceschi, J. M. Elzerman, T. Fujisawa, S. Tarucha, and L. P. Kouwenhoven. “Electron transport through double quantum dots”. In: *Rev. Mod. Phys.* 75 (1 Dec. 2002), pp. 1–22.

[28] S. D. Franceschi, S. Sasaki, J. M. Elzerman, W. G. van der Wiel, S. Tarucha, and L. P. Kouwenhoven. “Electron Cotunneling in a Semiconductor Quantum Dot”. In: *Physical Review Letters* 86 (5 Jan. 2001), pp. 878–881. ISSN: 0031-9007.

[29] D. Schröer, A. D. Greentree, L. Gaudreau, K. Eberl, L. C. L. Hollenberg, J. P. Kotthaus, and S. Ludwig. “Electrostatically defined serial triple quantum dot charged with few electrons”. In: *Phys. Rev. B* 76 (7 Aug. 2007), p. 075306.

[30] *Ansys® Electronics Desktop, Release 22.2*. 2022.

[31] S. Birner, T. Zibold, T. Andlauer, T. Kubis, M. Sabathil, A. Trellakis, and P. Vogl. “nextnano: General Purpose 3-D Simulations”. In: *IEEE Transactions on Electron Devices* 54.9 (2007), pp. 2137–2142.

[32] M. Groner, J. Elam, F. Fabreguette, and S. George. “Electrical characterization of thin Al2O3 films grown by atomic layer deposition on silicon and various metal substrates”. In: *Thin Solid Films* 413.1 (2002), pp. 186–197. ISSN: 0040-6090.

[33] W. C. Dunlap and R. L. Watters. “Direct Measurement of the Dielectric Constants of Silicon and Germanium”. In: *Phys. Rev.* 92 (6 Dec. 1953), pp. 1396–1397.

[34] S. M. Sze. *Physics of Semiconductor Devices*. New York: Wiley, 1981.

7

COUPLED VERTICAL DOUBLE QUANTUM DOTS AT SINGLE-HOLE OCCUPANCY

Gate-defined quantum dots define an attractive platform for quantum computation and have been used to confine individual charges in a planar array. Here, we demonstrate control over vertical double quantum dots confined in a double quantum well, silicon-germanium heterostructure. We sense individual charge transitions with a single-hole transistor. The vertical separation between the quantum wells provides a sufficient difference in capacitive coupling to distinguish quantum dots located in the top and bottom quantum well. Tuning the vertical double quantum dot to the (1,1) charge state confines a single hole in each quantum well beneath a single plunger gate. By simultaneously accumulating holes under two neighbouring plunger gates, we are able to tune to the (1,1,1,1) charge state. These results motivate quantum dot systems that exploit the third dimension, opening new opportunities for quantum simulation and quantum computing.

Parts of this chapter have been published in A.S. Ivlev, H. Tidjani, S.D. Oosterhout, A. Sammak, G. Scappucci, M. Veldhorst, Coupled vertical double quantum dots at single-hole occupancy, *Applied Physics Letters* **125** (2)

7.1. INTRODUCTION

Attaining control over individual charges in silicon[1, 2] and germanium [3, 4] constituted a necessary prerequisite to enable quantum computation with gate-defined quantum dots[5]. Planar quantum dot systems have progressed significantly, supporting high-fidelity single and two-qubit logic, multi-qubit logic, rudimentary error correction, and control over a 16 quantum dot array[6, 7, 8, 9, 6, 10, 11, 12, 13, 14]. The development of a double germanium quantum well heterostructure [15] has enabled the realisation of a vertically coupled double quantum dot [16], by taking advantage of the third dimension. Gaining control over single charges confined in quantum dots in multilayer systems may become a key asset in obtaining high connectivity in large quantum dot arrays [16]. In the near term, single-charge control in bilayer quantum dot systems may enable the realization of small-scale quantum simulators of magnetic phases in correlated spin systems [17].

Here, we demonstrate a vertical double quantum dot formed under a single plunger gate and tuned to single-hole occupancy. The occupancy is detected by charge sensing with a single-hole transistor. Using a second plunger gate, the system is extended to a 2x2 quantum dot array in the x-z plane parallel to the (100) heterostructure growth direction, filled down to the (1, 1, 1, 1) hole occupation. In comparison, achieving such a charge configuration in planar systems is non-trivial and have been demonstrated only recently in planar germanium [18] and silicon [19].

7.2. RESULTS

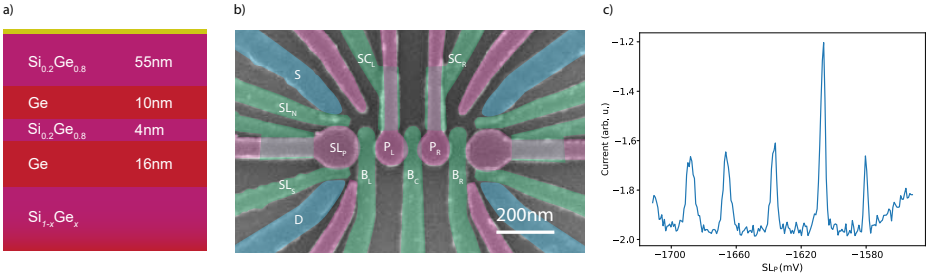

Figure 7.1: **Double quantum well heterostructure and top gate layout. a** Schematic of the double quantum well heterostructure. The yellow layer denotes the SiOx. **b** False coloured SEM of a device nominally identical to the one used in this experiment. The device is designed to have two charge sensors (outermost plunger gates) and two central plunger gates for confining individual holes. **c** Typical Coulomb oscillations of the single-hole transistor formed underneath the plunger gate SL_P, at a typical source-drain bias of 100 µV.

Fig. 7.1a depicts a schematic of the Ge/SiGe heterostructure, grown by reduced pressure chemical vapor deposition as detailed in Tosato et al.[15]. The heterostructure features two strained Ge quantum wells embedded in strain-relaxed Si0.2Ge0.8 with thicknesses of 16 nm and 10 nm. The separation between the quantum wells is 4 nm and the separation of the top quantum well from the semiconductor-dielectric interface is

55 nm, mirroring current heterostructures[20] hosting spin qubit devices. Ti/Pd metallic gates (Fig. 7.1b) are fabricated in two layers and separated by Al_2O_3, to electrostatically confine holes in the quantum wells (for further details on fabrication see [16]). Four plunger gates are patterned with the outer two plunger gates designed to operate as charge sensors. The left sensor is defined under plunger gate SL_P, and the right sensor acts only as a reservoir in this experiment. The barrier gates $SL_{N\,(S)}$ control the tunnelling between the charge sensor and the ohmic contacts. We define quantum dots localised in the two quantum wells using plunger gates P_L and P_R, and barrier gates B_L, B_C and B_R. Additionally, screening gates SC_L and SC_R provide further fine-tuning and prevent the formation of unwanted quantum dots. Barrier gates B_L and B_R also control the loading of charge carriers from the reservoirs to the quantum dots.

To facilitate charge sensing, a 100 µV bias is applied across the ohmic contacts S and D. The current signal through the sensor is determined by two-terminal DC measurements using low impedance lines and resulting in an integration time in the order of 100 µs. We calibrate the gate voltages to observe well-defined Coulomb peaks corresponding to the transport of holes through the single hole transistor (SL_P), as seen in Fig. 7.1c. At the edge of a Coulomb peak, the source-drain current is highly sensitive to the electrostatic environment and in particular to the charge occupation of any quantum dots under plunger gates P_L and P_R, similar to charge sensors in single quantum well systems. During all following measurements the voltage on SL_P is tuned such that it maintains a high sensitivity to the studied charge states. Previous works have observed that the transport signal through a single-hole transistor may be diminished in a double quantum dot regime [16], therefore we carefully tune the sensor to obtain regular and well-defined Coulomb peaks. We speculate that in this regime only one quantum well is contributing SL_P to transport through the charge sensor.

The charge sensor SL_P effectively detects the charge state beneath the plunger P_L. We begin by accumulating under P_L, while keeping P_R depleted, in order to avoid a lateral double quantum dot signature. Using P_L and B_C, we tune to a double dot regime under P_L, and control the occupation of the two quantum dots QD_{L1} and QD_{L2}. Given their strong coupling to P_L,it is likely the dots are positioned underneath P_L. To achieve orthogonal control of the charge occupation in the quantum dots we construct a virtual gate matrix which couples QD_{L1} to vP_L, and QD_{L2} to vB_C. This is enabled by a difference in the lever arm ratio $\alpha_{L1,BC}/\alpha_{L1,PL} < \alpha_{L2,BC}/\alpha_{L2,PL}$, where $\alpha_{D,G}$ is the lever arm between gates G and quantum dot D. As a result, we can construct virtual gates vP_L and vB_C (Fig. 7.2) to obtain independent control of the loading onto each quantum dot, down to the single hole regime. The linearly defined virtual gate space is effective in a small voltage regime but is insufficient to virtualise subsequent transitions of the double quantum dot under P_L (Fig. 7.2a). In particular, the transitions of QD_{L2} have a strongly varying lever arm across consecutive occupations. This difference between the quantum dots can be explained by a weaker in-plane confinement of QD_{L2}, which is consistent with it being located in the bottom quantum well.

To establish that each quantum dot is indeed located in a distinct quantum well, we qualitatively estimate the location of both quantum dots. This is done by extracting the lever arm ratios of the surrounding gates to each quantum dot from the charge

stability diagrams, similar to the method used by Tidjani et al. [16]. We find that the two quantum dots have approximately equal coupling to the two surrounding barrier gates B_L and B_C. In particular we determine $\alpha_{L1,BC}/\alpha_{L1,PL} \approx \alpha_{L1,BL}/\alpha_{L1,PL} \approx 1.0$ and $\alpha_{L2,BC}/\alpha_{L2,PL} \approx \alpha_{L2,BL}/\alpha_{L2,PL} \approx 1.6$ (see Supplementary II) for the corresponding charge stability diagrams). These lever arms indicate that both quantum dots are equidistant in position between B_L and B_C. We note that B_L and B_C have similar shape and are fabricated in the same layer and we therefore ignore geometric effects. On the other hand $\alpha_{L1,SC_L}/\alpha_{L1,PL} \approx \alpha_{L2,SC_L}/\alpha_{L2,PL} \approx 0.4$, indicates that neither quantum dot is significantly closer to SC_L.

Together these findings suggest that the quantum dots are vertically stacked beneath plunger gate P_L. Since the quantum dots are well-defined with a distinct interdot transition and charge signal to the sensor, we conclude that they are separated in the z-direction, with each quantum well confining one quantum dot. We assign QD_{L2} to the bottom quantum well as its relative coupling to the barrier gates is larger than that of QD_{L1}, which has a stronger in-plane confinement [16]. Moreover, an interdot transition $(N_{L1}, N_{L2}+1) \rightarrow (N_{L1}+1, N_{L2})$ is induced by applying an increasingly negative P_L voltage, indicating that QD_{L1} is located closer to P_L. The vertically coupled double quantum dot is visualised in Fig. 7.2b.

Our conclusions are further supported by our finding of comparable results for the two quantum dots QD_{R1} and QD_{R2} under P_R, which we also tune to the (1,1) regime and where we similarly argue that each quantum dot is located in a different quantum well underneath P_R (Supplementary III). This reproducibility bodes well for future efforts in operating larger arrays.

The observation of a distinct $(1,0)-(0,1)$ interdot transition line in the right panel of Fig. 7.2a indicates a distinct capacitative coupling between each quantum dot and SL_P. This distinct capacitive coupling is encouraging, since the current heterostructure has a modest inter-layer separation, suggesting potential for further enhancement. The current ability to distinguish in which quantum well a charge is located is holds promise for vertical Pauli spin-blockade (PSB) readout. This gives perspective for the integration of a readout ancilla that can be used for PSB directly underneath or above a data qubit. This distinguishability furthermore allows to better study the inter-layer tunnel coupling itself. The control over the coupling between the quantum wells may be limited and largely predefined by their separation. Nonetheless, controlling the quantum dot occupation may serve as means to discretely change the tunnel coupling due to the varying wavefunction densities of different orbitals. The appreciable difference in the lever arms of the gates to the quantum dots furthermore suggests gate-based tunability of the inter-layer tunnel coupling and exchange interaction. An applied gate voltage could shift the quantum dots relative to one another, allowing to decrease their overlap and reducing the tunnel coupling. Alternatively, the gate voltage could influence the penetration of the wavefunction into the SiGe barrier. However, a more systematic study is needed to understand to which extent the charge occupation and tunnel couplings can be tuned independently *in situ*.

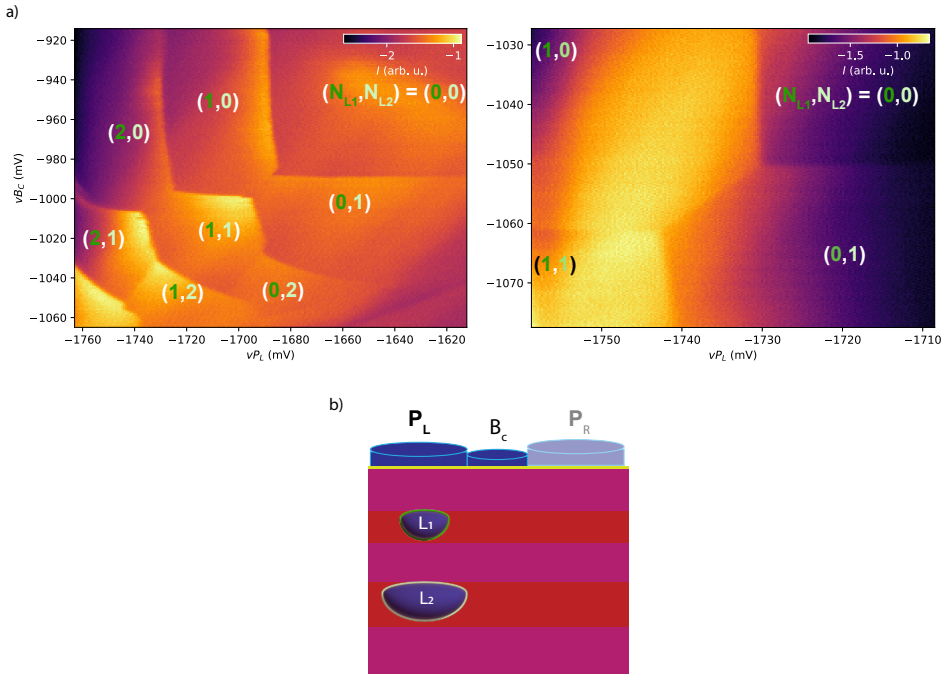

Figure 7.2: **Single-hole occupancy in a vertical double quantum dot. a.** The left panel shows the charge-stability diagram of a double quantum dot formed underneath plunger gate P_L measured by charge sensing. The occupation (N_{L1},N_{L2}) for quantum dots QD_{L1} and QD_{L2} is noted in each region and is controlled by the gate voltages on P_L and B_C, which are applied as virtual gates vP_L=P_L-0.55B_C-0.2SL_P and vB_C=-0.9P_L+B_C-0.18SL_P to maintain visibility of the charge sensor. In the right panel we focus on the (1,0)-(0,1) transition. The charge sensor is optimized to distinguish the interdot transition. Here the virtual gate definition is set to vP_L=P_L-0.58B_C-0.18SL_P and vB_C=-0.95P_L+B_C-0.14SL_P. The gate voltages at the center of **b** are P_L=−1381 mV and B_C=−183 mV. **b.** Schematic depicting the double occupation under P_L while P_R is kept below the accumulation voltage.

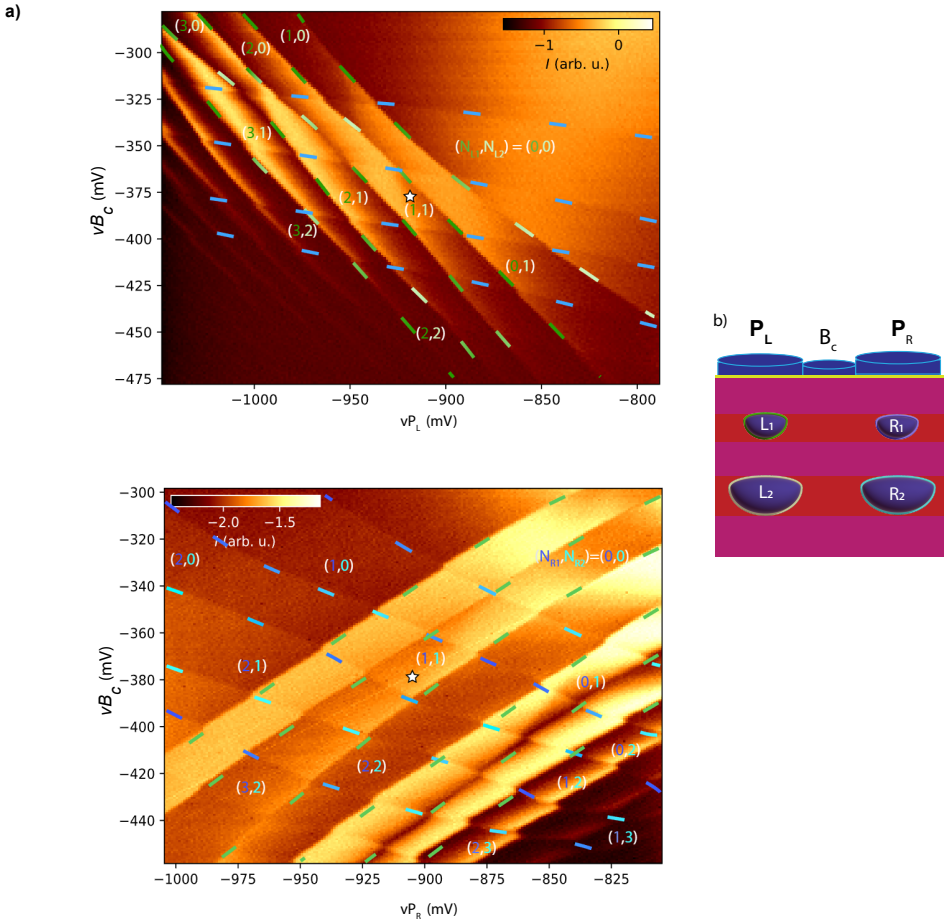

Figure 7.3: **Single-hole occupancy in two coupled vertical double quantum dots. a.** The top panel shows the charge-stability diagram with individual transitions of the double quantum dot underneath P_L, where dark (light) dashed green lines correspond to reservoir transitions of $QD_{L1(2)}$, serving as a guide to the eye. In addition, blue transitions correspond to the double quantum dot under P_R. We note that the individual quantum dots are poorly distinguishable due to the small lever arms between P_L and the quantum dots underneath P_R. The lower panel similarly shows the charge-stability diagram with individual transitions of the double quantum dot underneath P_R, with the transition to $QD_{R1(2)}$ indicated with dark (light) blue. The transitions corresponding to the double quantum dot under P_L are indicated in green. In both subfigures the virtual gate voltages are $vP_L = P_L\text{-}0.2P_R\text{-}0.17SL$ and $vB_C = B_C\text{-}0.22SL$ and $vP_R = P_R\text{-}0.4P_L\text{-}0.5B_C\text{-}0.075SL$. To capture multiple transitions of the sensor in the right panel of **a**, the signal is averaged over multiple data sets at different sensor voltages SL_P. The stars correspond to the same voltage values. **b.** Schematic depicting the 2x2 array.

Having established individual control over the double quantum dots underneath each plunger gate, we now focus on simultaneous control over the hole occupation under both plungers to demonstrate a 2x2 array in the x-z plane. Starting in the few hole regime under P_R, we maintain the (1,1) P_R occupation and tune the system towards the voltage regime in which both quantum dots under P_L become occupied with a single hole. The left (right) panel of Fig. 7.3a demonstrates the charge-stability diagram of $vP_{L(R)}$ vs vB_C. In each diagram one can distinguish the double quantum dot under its corresponding plunger gate, as well as additional transitions corresponding to the double quantum dot under the other plunger gate. In the middle of the measurement range, the vertical 2x2 array is in the (1,1,1,1) charge occupation, depicted in Fig. 7.3b. In this regime, it becomes more challenging to distinguish individual transitions from each quantum dot due to the noticeably increased inter-layer tunnel coupling. This increased coupling likely stems from the central barrier voltage being increased to B_C=13mV, compared to B_C=−182 mV in Fig. 7.2, which increases the in-plane confinement. Increasing B_C was necessary to achieve the desired (1,1,1,1) charge state. The high B_C voltage reduces the intralayer capacitive and tunnel coupling, consistent with the observed small interdot transitions between the P_L and P_R quantum dots.

7.3. DISCUSSION

In conclusion, we have established single-hole charge control over quantum dots in a double quantum well. A significant challenge remains in obtaining control over the interdot coupling and in particular when the coupling is interlayer, since the gates controlling the occupation also control the coupling. Despite this, we have shown that even in a strongly coupled system, charge sensing and orthogonal control of quantum dots in each quantum well is possible, through the construction of virtual gate matrices. Furthermore, we have demonstrated a 2x2 quantum dot array oriented perpendicular to the quantum well plane, and tuned to the (1,1,1,1) charge state. Small extensions in the system size, such as a 2x2x2 quantum dot array, may allow the study of intriguing physics arising in bilayer Hubbard models [17]. Moreover, the ability to control single charges in multilayer systems may facilitate high-connectivity semiconductor quantum processors.

7.4. LEVER ARM ANALYSIS

LEVER ARM ANALYSIS FOR THE DOUBLE QUANTUM DOT UNDER P_L

We triangulate the position of the double quantum dots most strongly coupled to P_L, whose charge stability diagram is in figure 2 of the main text. This is obtained from the lever arms ratios $\alpha_{d,G_1}/\alpha_{d,G_2}$ where $\alpha_{d,G}$ is the lever arm between gates G and dot d. These lever arm ratios are extracted from the slopes of the transition lines in the charge stability diagrams (Fig. 7.4). While subsequent reservoir transitions have different lever arms, in our analysis we only consider the reservoir transitions corresponding to the loading into the (1,1) state. To determine the lever arm ratio $\alpha_{d,P_L}/\alpha_{d,SC_L}$ for any quantum dot d we combine the lever arms $\alpha_{d,B_C}/\alpha_{d,SC_L}$ and $\alpha_{d,P_L}/\alpha_{d,B_C}$. We justify this approach based on the very similar slopes for the reservoir transitions in the charge stabil-

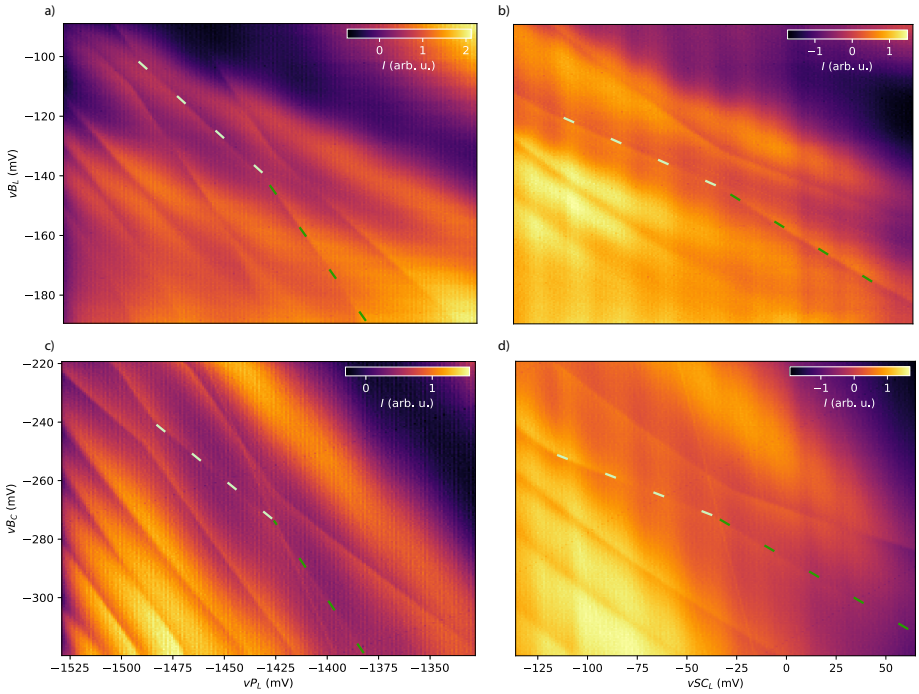

Figure 7.4: **Charge stability diagrams of the double quantum dot under P_L.** We extract the slopes corresponding to the loading of quantum dot $L_{1(2)}$ indicated in the dark (light) green to retrieve the lever arm ratios of the gates to the quantum dots. These are the reservoir transitions corresponding to the loading onto the (1,1). During these measurements the virtual gates are defined to maintain high charge sensor visibility: vP_L=P_L-0.06SL_P, vSC_L=SC_L-0.1SL_P,vB_L=B_L-0.4SL_P and vB_C = B_C-0.04SL_P. The gate voltage values at the centre of these datasets are P_L = −1331 mV, B_C = −203 mV, SC_L = −36 mV and B_L = −139 mV.

ity diagram of P_L and SC_L, which doesn't allow us to directly identify a slope $\alpha_{d,P_L}/\alpha_{d,SC_L}$ with a particular quantum dot d.

The extracted lever arm ratios are summarized in table 7.1. From the observation that each quantum dot couples similarly to the barrier gates on either side, and neither quantum dot couples dominantly to the screening gate SC_L, we conclude that the quantum dots are centred around the same point in the x-y plane. Given that the quantum dots are sufficiently distinct and don't effectively merge into a single quantum dot, they are understood to be in distinct quantum wells, with quantum dot $L_{1(2)}$ being in the top (bottom) well for the reasons outlined in the main text.

We note that in this analysis the compensation on the charge sensor SL_P is neglected, which we warrant through its minor effect on the quantum dot compared to the plunger and barrier gates.

Table 7.1: **Lever arm ratios for the quantum dots under P_L.** The lever arm ratios for quantum dot $L_{1(2)}$ are extracted from the slope of the dark (light) green line in the corresponding charge stability diagrams in figure 7.4. The compensation on the charge sensor SL_P has been neglected in this analysis. $\alpha_{SC_L}/\alpha_{P_L}$ is calculated by combining the other ratios, since the transitions of the individual quantum dots could not be distinguished from this data set. An error of 3mV is assumed when determining the slope.

QD	$\alpha_{B_L}/\alpha_{P_L}$	$\alpha_{B_C}/\alpha_{P_L}$	$\alpha_{B_L}/\alpha_{SC_L}$	$\alpha_{B_C}/\alpha_{SC_L}$	$\alpha_{SC_L}/\alpha_{P_L}$
L1	0.97 ± 0.08	1.04 ± 0.09	2.45 ± 0.19	2.45 ± 0.20	0.41 ± 0.04
L2	1.57 ± 0.15	1.59 ± 0.17	3.48 ± 0.38	3.74 ± 0.55	0.44 ± 0.05

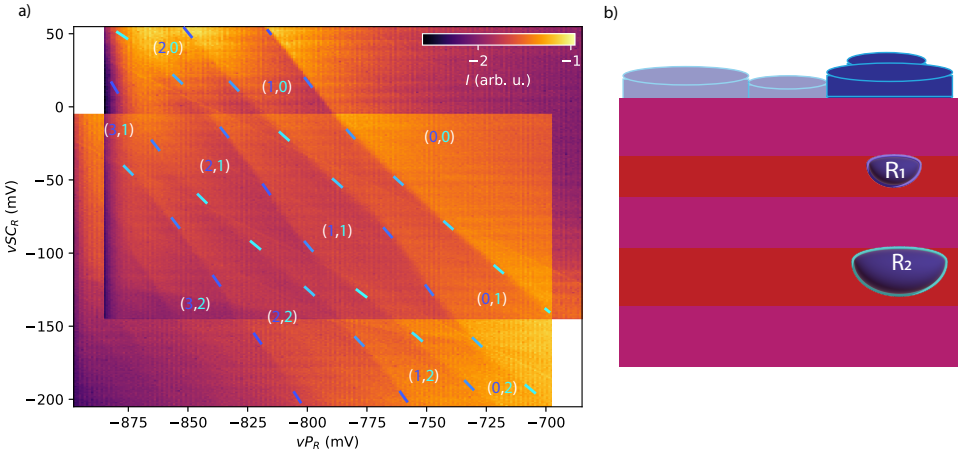

Figure 7.5: **A double quantum dot under P_R in the few hole regime**. Two overlapping data sets demonstrate multiple transitions of distinct quantum dots that are coupled to plunger gate P_2. The occupation (N_{R1},N_{R2}) is denoted in the different charge regions. Here $vP_R = P_R - 0.055SL_P$ and $vSC_R = SC_R - 0.075SL_P$. We attribute the charge transition crossing the y-axis at about −120 mV to a spurious dot near SC_R. The gate voltage values at the centre of these data sets are given by $P_R = -791$ mV and $SC_R = -75$ mV. The two data-sets that are used are averaged at the points of overlap. The dashed lines are added to guide the eye.

7

LEVER ARM ANALYSIS FOR THE DOUBLE QUANTUM DOT UNDER P_R

We demonstrate the formation of the double quantum dots under P_R and triangulate their position as we have done in supplementary 7.4. For these measurements, the charge sensor on the left side of the device is used. The increased distance between the P_R and the sensor results in the weaker signal in figure 7.5 compared to figure 2 of the main text. Still, we distinguish two distinct transitions lines, each attributed to a different dot. The lack of further transitions in the (0,0) region shows that indeed the single-hole regime is reached. Plunger gate P_L is depleted such that no dots underneath it are occupied.

We further triangulate the exact positions of the double dots by determining the lever arm ratios of the surrounding gates to these quantum dots (Fig. 7.6) and summarize the values in Table 7.2). The reservoir transitions used for extracting the lever arms have been denoted with blue and cyan dashed lines in Fig.7.6, as these transitions can be consistently identified across the different charge stability diagrams. We see that the lever

arm ratios are not as homogeneous as was found for the quantum dots under P_L, as in particular quantum dot QD_{R2} seem to be coupled more with B_R than B_C. Still neither quantum dot couples particularly weakly or strongly to any surrounding gate, and therefore they are unlikely to be spurious dots underneath any particular gate, as that would result in strong coupling to that gate and low coupling to a further-positioned gate. Based on the studied reservoir transitions alone we can not decisively argue that the two quantum dots must be located in different quantum wells. In particular, based on the given lever arm ratios (Table 7.6), an alternative interpretation would be that both quantum dots are located in the same quantum well, both between barrier gates B_C and B_R, but with QD_{R2} closer towards SC_R than QD_{R1}. However, this interpretation suggests that an increasingly negative voltage on SC_R would be able to transfer a hole from QD_{R1} into QD_{R2}. Yet the (0,1)-(1,0) interdot transition (white dashed line in Fig. 7.6) suggests that an increasingly negative voltage on SC_R (B_C, B_R or P_R) would localise the single hole into QD_{R1}. This would suggest that $\alpha_{R1,G} > \alpha_{R2,G}$ with G being SC_R,B_C,B_R or P_R which, together with the lever arm ratio in table 7.2, conflicts with any configuration of in-plane double quantum dots. Hence we conclude that the two quantum dots are located in different quantum wells. More precisely, by a similar reasoning as for the double quantum dots under P_L we suggest that $QD_{R1(2)}$ is located in the top (bottom) quantum well (see Fig. 7.5b for a schematic).

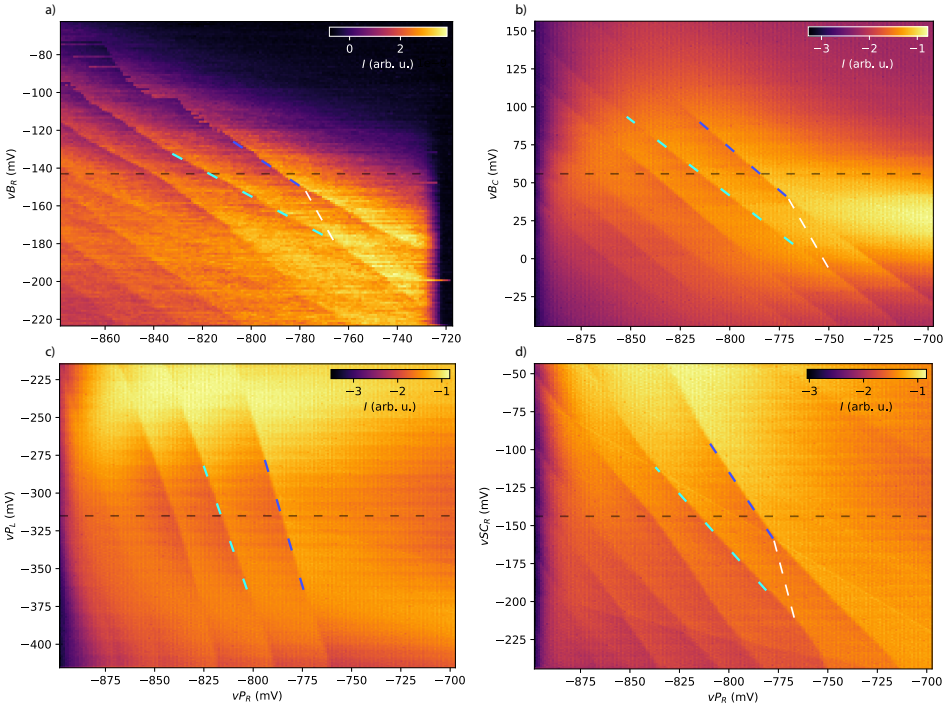

Figure 7.6: **Charge Stability Diagrams of the double dot under P_R.** We extract the slopes corresponding to the loading of quantum dot $QD_{R1(2)}$ indicated in the dark (light) blue to retrieve the lever arm ratios between the gates and the quantum dots. The black dashed lines indicate points of equal voltage across the different CSDs. The white line connects the two triple points at the (0,1)-(1,0) interdot transition, whenever these are distinguishable. The CSD with B_R was taken using a slower scan due to the limited bandwidth of the DC-line connected to B_R. In that CSD the latching effect becomes pronounced as B_R is more positive, as the quantum dots are loaded from the right reservoir. Across this data, the virtual gates are defined such that the sensor-voltage is compensated as such: $vP_R = P_R\text{-}0.055SL_P$, $vSC_R=SC_R\text{-}0.075SL_P$, $vB_C=B_C\text{-}0.2SL_P$, $vP_L=P_L\text{-}0.1SL_P$ and $vB_R=B_R\text{-}0.045SL_P$. The exception to this is CSD figure **a** which has $vP_R=P_R\text{-}0.05SL_P$. The gate voltage values at the centre of these datasets are given by $P_R = -798$ mV,$P_L = -315$ mV, $B_C = 56$ mV, $SC_R = -144$ mV and $B_R = -143$ mV.

Table 7.2: **Lever arm ratios for the quantum dots under P_R.** Similar to table 7.1 the lever arm ratios for quantum dot $QD_{R1(2)}$ are extracted from the slope of the dark (light) blue line in the corresponding charge stability diagrams in figure 7.6. The compensation on the charge sensor SL has been neglected in this analysis. An error of 3 mV is assumed when determining the slope.

QD	α_{B2}/α_{P2}	α_{B12}/α_{P2}	α_{P1}/α_{P2}	α_{S2}/α_{P2}
R1	1.07 ± 0.16	0.89 ± 0.07	0.23 ± 0.03	0.51 ± 0.05
R2	1.44 ± 0.13	1.02 ± 0.06	0.27 ± 0.04	0.69 ± 0.05

BIBLIOGRAPHY

[1] S. J. Angus, A. J. Ferguson, A. S. Dzurak, and R. G. Clark. “Gate-Defined Quantum Dots in Intrinsic Silicon”. In: *Nano Letters* 7.7 (2007), pp. 2051–2055.

[2] C. B. Simmons, M. Thalakulam, N. Shaji, L. J. Klein, H. Qin, R. H. Blick, D. E. Savage, M. G. Lagally, S. N. Coppersmith, and M. A. Eriksson. “Single-electron quantum dot in Si/SiGe with integrated charge sensing”. In: *Applied Physics Letters* 91.21 (Nov. 2007), p. 213103. ISSN: 0003-6951.

[3] N. W. Hendrickx, D. P. Franke, A. Sammak, M. Kouwenhoven, D. Sabbagh, L. Yeoh, R. Li, M. L. V. Tagliaferri, M. Virgilio, G. Capellini, G. Scappucci, and M. Veldhorst. “Gate-controlled quantum dots and superconductivity in planar germanium”. In: *Nature Communications* 9.1 (July 2018), p. 2835. ISSN: 2041-1723.

[4] W. I. L. Lawrie, H. G. J. Eenink, N. W. Hendrickx, J. M. Boter, L. Petit, S. V. Amitonov, M. Lodari, B. Paquelet Wuetz, C. Volk, S. G. J. Philips, G. Droulers, N. Kalhor, F. van Riggelen, D. Brousse, A. Sammak, L. M. K. Vandersypen, G. Scappucci, and M. Veldhorst. “Quantum dot arrays in silicon and germanium”. In: *Applied Physics Letters* 116.8 (Feb. 2020), p. 080501. ISSN: 0003-6951.

[5] D. Loss and D. P. DiVincenzo. “Quantum computation with quantum dots”. In: *Phys. Rev. A* 57 (1 Jan. 1998), pp. 120–126.

[6] J. Yoneda, K. Takeda, T. Otsuka, T. Nakajima, M. R. Delbecq, G. Allison, T. Honda, T. Kodera, S. Oda, Y. Hoshi, N. Usami, K. M. Itoh, and S. Tarucha. “A quantum-dot spin qubit with coherence limited by charge noise and fidelity higher than 99.9%”. In: *Nature Nanotechnology* 13.2 (Feb. 2018), pp. 102–106. ISSN: 1748-3395.

[7] W. I. L. Lawrie, M. Rimbach-Russ, F. v. Riggelen, N. W. Hendrickx, S. L. d. Snoo, A. Sammak, G. Scappucci, J. Helsen, and M. Veldhorst. “Simultaneous single-qubit driving of semiconductor spin qubits at the fault-tolerant threshold”. In: *Nature Communications* 14.1 (June 2023), p. 3617. ISSN: 2041-1723.

[8] N. W. Hendrickx, W. I. L. Lawrie, M. Russ, F. van Riggelen, S. L. de Snoo, R. N. Schouten, A. Sammak, G. Scappucci, and M. Veldhorst. “A four-qubit germanium quantum processor”. In: *Nature* 591 (7851 Mar. 2021), pp. 580–585. ISSN: 0028-0836.

[9] S. G. J. Philips, M. T. Mądzik, S. V. Amitonov, S. L. de Snoo, M. Russ, N. Kalhor, C. Volk, W. I. L. Lawrie, D. Brousse, L. Tryputen, B. P. Wuetz, A. Sammak, M. Veldhorst, G. Scappucci, and L. M. K. Vandersypen. “Universal control of a six-qubit quantum processor in silicon”. In: *Nature* 609.7929 (Sept. 2022), pp. 919–924. ISSN: 1476-4687.

[10] X. Xue, M. Russ, N. Samkharadze, B. Undseth, A. Sammak, G. Scappucci, and L. M. K. Vandersypen. “Quantum logic with spin qubits crossing the surface code threshold”. In: *Nature* 601.7893 (Jan. 2022), pp. 343–347. ISSN: 1476-4687.

[11] A. Noiri, K. Takeda, T. Nakajima, T. Kobayashi, A. Sammak, G. Scappucci, and S. Tarucha. “Fast universal quantum gate above the fault-tolerance threshold in silicon”. In: *Nature* 601.7893 (Jan. 2022), pp. 338–342. ISSN: 1476-4687.

[12] K. Takeda, A. Noiri, T. Nakajima, T. Kobayashi, and S. Tarucha. “Quantum error correction with silicon spin qubits”. In: *Nature* 608.7924 (Aug. 2022), pp. 682–686. ISSN: 1476-4687.

[13] F. van Riggelen, W. I. L. Lawrie, M. Russ, N. W. Hendrickx, A. Sammak, M. Rispler, B. M. Terhal, G. Scappucci, and M. Veldhorst. “Phase flip code with semiconductor spin qubits”. In: *npj Quantum Information* 8.1 (Oct. 2022), p. 124. ISSN: 2056-6387.

[14] F. Borsoi, N. W. Hendrickx, V. John, M. Meyer, S. Motz, F. van Riggelen, A. Sammak, S. L. de Snoo, G. Scappucci, and M. Veldhorst. “Shared control of a 16 semiconductor quantum dot crossbar array”. In: *Nature Nanotechnology* (Aug. 2023). ISSN: 1748-3395.

[15] A. Tosato, B. Ferrari, A. Sammak, A. R. Hamilton, M. Veldhorst, M. Virgilio, and G. Scappucci. “A High-Mobility Hole Bilayer in a Germanium Double Quantum Well”. In: *Advanced Quantum Technologies* 5.5 (2022), p. 2100167.

[16] H. Tidjani, A. Tosato, A. Ivlev, C. Déprez, S. Oosterhout, L. Stehouwer, A. Sammak, G. Scappucci, and M. Veldhorst. “Vertical gate-defined double quantum dot in a strained germanium double quantum well”. In: *Phys. Rev. Appl.* 20 (5 Nov. 2023), p. 054035.

[17] D. Buterakos and S. D. Sarma. “Magnetic phases of bilayer quantum-dot Hubbard model plaquettes”. In: *Physical Review B* 108 (23 Dec. 2023), p. 235301. ISSN: 2469-9950.

[18] F. van Riggelen, N. W. Hendrickx, W. I. L. Lawrie, M. Russ, A. Sammak, G. Scappucci, and M. Veldhorst. “A two-dimensional array of single-hole quantum dots”. In: *Applied Physics Letters* 118.4 (Jan. 2021), p. 044002. ISSN: 0003-6951.

[19] F. K. Unseld, M. Meyer, M. T. Mądzik, F. Borsoi, S. L. de Snoo, S. V. Amitonov, A. Sammak, G. Scappucci, M. Veldhorst, and L. M. K. Vandersypen. “A 2D quantum dot array in planar 28Si/SiGe”. In: *Applied Physics Letters* 123.8 (Aug. 2023), p. 084002. ISSN: 0003-6951.

[20] M. Lodari, N. W. Hendrickx, W. I. L. Lawrie, T.-K. Hsiao, L. M. K. Vandersypen, A. Sammak, M. Veldhorst, and G. Scappucci. “Low percolation density and charge noise with holes in germanium”. In: *Materials for Quantum Technology* 1.1 (Jan. 2021), p. 011002.

8

A THREE-DIMENSIONAL ARRAY OF QUANTUM DOTS

I almost wish I hadn't gone down that rabbit-hole—and yet—and yet—it's rather curious, you know, this sort of life!

Alice in Wonderland, Lewis Carroll

Quantum dots can confine single electrons or holes to define spin qubits that can be operated with high fidelity. Experimental work has progressed from linear to two-dimensional arrays of quantum dots, enabling qubit interactions that are essential for quantum simulation and computation. Here, we explore architectures beyond planar geometries by constructing quantum dot arrays in three dimensions. We realize an eight-quantum dot system in a silicon-germanium heterostructure comprising two stacked germanium quantum wells, where quantum dots are positioned at the vertices of a cuboid. Using electrostatic gate control, we load a single hole into any of the eight quantum dots. To demonstrate the potential of multilayer quantum dot systems, we show coherent spin control and hopping-induced spin rotations by shuttling between the quantum wells. The ability to extend quantum dot arrays in three dimensions provides opportunities for novel quantum hardware and high-connectivity quantum circuits.

Parts of this chapter have been published in H. Tidjani , D. Denora , M. Chan, J.H. Ungurer, B. van Straaten, S. D. Oosterhout , L. Stehouwer, G. Scappucci , and M. Veldhorst, A Three-Dimensional Array of Quantum Dots, *ArXiv Preprint:* arXiv:2512.01634 (2025).

8.1. INTRODUCTION

Interacting quantum systems can give rise to a wide range of phenomena. Predicting their behavior remains a formidable challenge and is considered one of the first practical applications of quantum computers [1]. Quantum simulation may be particularly powerful when there exists a direct mapping. For example, a two-dimensional quantum simulator with nearest-neighbor interactions may be used to explore nontrivial phase transitions in the Fermi-Hubbard model [2]. However, real systems extend in three dimensions, and thus even higher connectivity may be needed for simulations of nature [3].

Quantum connectivity is also highly relevant for quantum computation and has a large impact on the performance and efficiency of quantum error correction schemes. Two-dimensional arrays with nearest-neighbor interactions may support surface codes with error thresholds as high as 1% [4, 5]. Even higher connectivity may drastically lower the physical qubit overhead to construct logical qubits [6].

Atomic qubits such as trapped ions and neutral atoms can have high connectivity, due to the use of collective vibrational modes, by shuttling, or by arranging qubits in three dimensions [7, 8, 9]. In the solid state, achieving high connectivity is more challenging. For example, spin qubits in semiconductor quantum dots have only recently been scaled into small systems with two-dimensional connectivity [10, 11, 12, 13].

A first route to further increase the connectivity between spin qubits could be to exploit quantum links based on shuttling [14] or superconducting resonators [15]. A complementary route would be the construction of quantum dot arrays with a higher connectivity. Advances in heterostructure growth have led to high-quality double quantum well systems [16] and first realizations of stacked quantum dots [17, 18], providing prospects for the construction of quantum dot arrays with intrinsic connectivity beyond planar systems.

Here, we explore the construction of quantum dots in three dimensions using multi-quantum well structures. Our device is based on a strained-germanium double quantum well embedded in a silicon-germanium heterostructure. We first tune a vertical double quantum dot, to then define quantum dot arrays on the facets of a cuboid. Understanding this system allows us to define eight quantum dots positioned at the corners of a cuboid. Finally, we demonstrate that the system supports quantum operation and enables the coherent displacement of single spins between quantum dots that reside in different quantum wells.

8.2. DEVICE

Our experiments are performed on a silicon germanium (SiGe) heterostructure with two strained germanium quantum wells, depicted in Fig. 8.1a. The heterostructure is undoped and deposited on a $Si_{0.2}Ge_{0.8}$ strained relaxed buffer obtained by reverse grading on a Si(001) wafer [16, 19]. A SiGe spacer with a thickness of 55 nm separates the bilayer system from the gate stack. The top and bottom strained quantum wells have a thickness of 10 nm and 16 nm, and are separated by a 10 nm $Si_{0.2}Ge_{0.8}$ barrier. The quantum well separation is larger compared to earlier work that demonstrated vertical double quantum dots [17, 18], aiming to reduce the tunnel coupling between the wells.

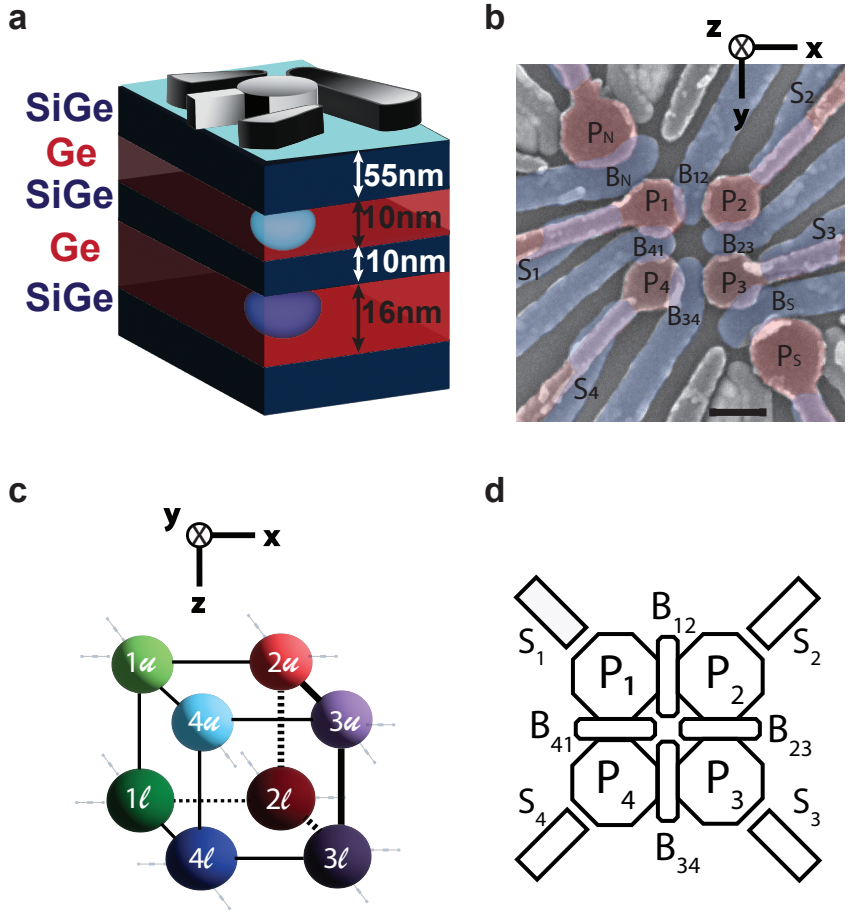

Figure 8.1: **Heterostucture and device layout for the three-dimensional quantum dot array a,** Schematic of the Ge/SiGe double quantum well heterostructure, with 10 nm of $Si_{0.2}Ge_{0.8}$ separating two Ge quantum wells with a thickness of 10 nm and 16 nm. **b,** False-colored SEM image of a nominally identical device. A planar 2×2 array of plunger gates P_i (red) is used to accumulate charges in the underlying germanium quantum wells. The barrier gates B_{ij} (blue) and screening gates S_i (blue) provide further control. For charge readout, two RF-single hole transistors (SHT) are defined using the gates labeled $P_{N,S}$ and $B_{N,S}$. The scale bar denotes 100 nm. **c,** Schematic representation of cuboid quantum dot configuration, with $iu(\ell)$ denoting a quantum dot in the upper (lower) quantum well, under plunger gate P_i. **d,** Simplified gate layout showing the gates involved in triangulating the position of the quantum dots.

Control over the quantum dots is provided by a gate stack deposited on top of the heterostructure, as shown by a false-colored SEM-image of a nominally identical device in Fig. 8.1b. The device design is similar to a 2×2 planar germanium qubit array including ohmics to define charge sensors at the corners [10], but here the plunger gates are used to confine vertical double quantum dots, while barrier gates provide further control of the potential landscape. The device can therefore host up to eight quantum dots, with four quantum dots in each well, as schematically shown in Fig. 8.1c. Here, the spheres represent the upper (u) or lower (ℓ) quantum dots, under the plunger gates P_i with $i = 1-4$. Experimentally, we probe the position of the quantum dots in the array using triangulation, by sweeping the plunger gates against all surrounding gates and fitting the charge stability diagrams. In Fig. 8.1d, we show a simplified version of the gate layout only with the gates involved in the triangulation procedure.

8.3. RESULTS

Figure 8.2 shows experimental and simulated charge stability diagrams of vertical double quantum dots. The simulations are performed using the Python package Qarray [20], based on the constant-interaction model [21]. Vertical quantum dot arrangements give rise to distinct features as shown in Fig. 8.2a. In particular, we observe two reservoir transition lines strongly coupled to the same plunger gate and a long interdot transition line due to strong capacitative coupling between the vertically stacked quantum dots.

To arrive in the regime of vertically stacked quantum dots in the few-hole regime, we tune the dc electrostatic potential of the dots independently. We do so by exploiting their difference in lever arms from the surrounding gates. In our simulations, we tune the capacitances to find reasonable agreement with the experimental data, see Figs. 8.2a and 8.2b. The main difference is caused by latching which is present in the experiments and not considered in simulations. To provide further evidence of quantum dots residing in both wells, we perform triangulation based on the relative lever arms, see Fig. 8.2c and Appendix 8.8. For the pair P_i - P_j, we extract slopes by scanning P_i and P_j independently against all surrounding gates and extract the relative lever arm of the gates with respect to the plunger gate, at the same DC point. The charge stability diagrams are manually fitted to extract the slope of the charge transition lines in response to the surrounding gates, as shown in Appendix 8.8.

Identifying the charge states in stability diagrams with more than two quantum dots can be challenging, but we do find that bilayer systems can be of high-quality and stability. In Fig. 8.2e, the simulation shows two vertical double quantum dots. For low-hole fillings, we see a good correspondence between the experimental and simulated data of two vertical double quantum dots shown in Figs. 8.2d and 8.2e.

8.3.1. FOUR 2 X 2 ARRAYS

Having established that we can tune between the planar and bilayer regime using the surrounding gates, we continue to form four 2×2 arrays aligned in the xz or yz planes, across the different faces of the cuboid. In Fig. 8.3a-d we tune to have a 2×2 array under the plunger gates P_1-P_4, P_1-P_2, P_3-P_2, and P_3-P_4, while keeping the other two plunger gates well above the accumulation voltage, in order to simplify quantum dot character-

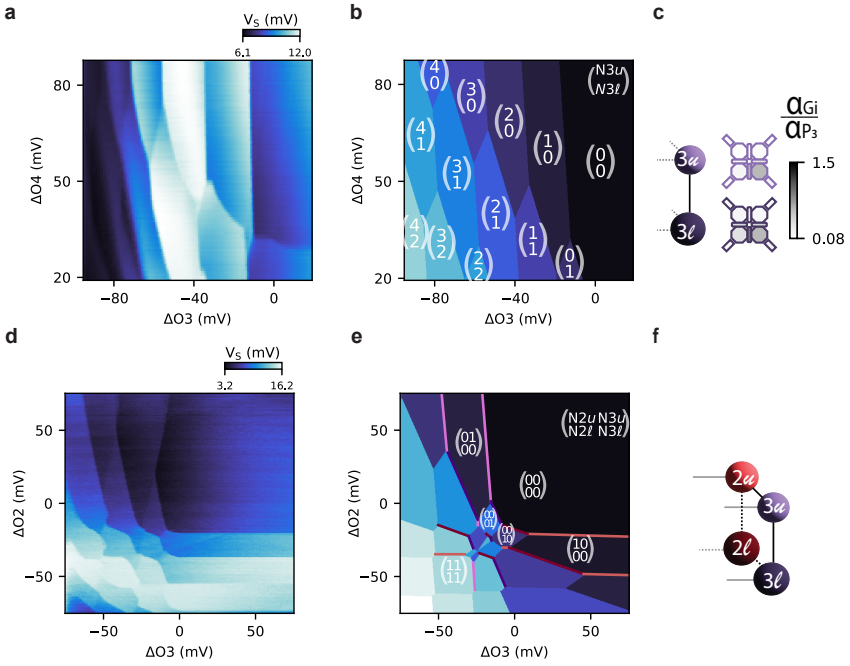

Figure 8.2: **Simulated and measured vertical double quantum dot charge stability diagrams in 10nm separated quantum wells. a,** Reflected signal of the rf-SHT underneath P_S showing a charge-stability diagram that corresponds to a vertical double quantum dot located beneath P_3, while P_4 is not yet accumulated. **b,** The simulated charge-stability diagram based on a constant-capacitance model [20] of a vertical double quantum dot localised under the plunger gate P_3. **c,** Schematic of the respective vertical double dot and triangulation heatmap. The triangulation results stem form the fitted charge transition lines, providing the relative lever arm of each gate to the respective quantum dots. **d,** Reflected signal of the rf-SHT underneath P_N showing a charge-stability diagram that corresponds to a 2×2 array underneath P_2 and P_3 in the yz-plane. Two quantum dots are located underneath each plunger gate. The gates O2 and O3 represent the orthogonalized virtualized plunger gates, with respect to the quantum dots in the upper layer, QD2u and QD3u. **e,** Simulated charge stability diagram of a 2×2 array aligned in the xz plane. The capacitances are chosen to find qualitative agreement with the experimental results. **f,** Schematic denoting the respective facet of the quantum dot cuboid.

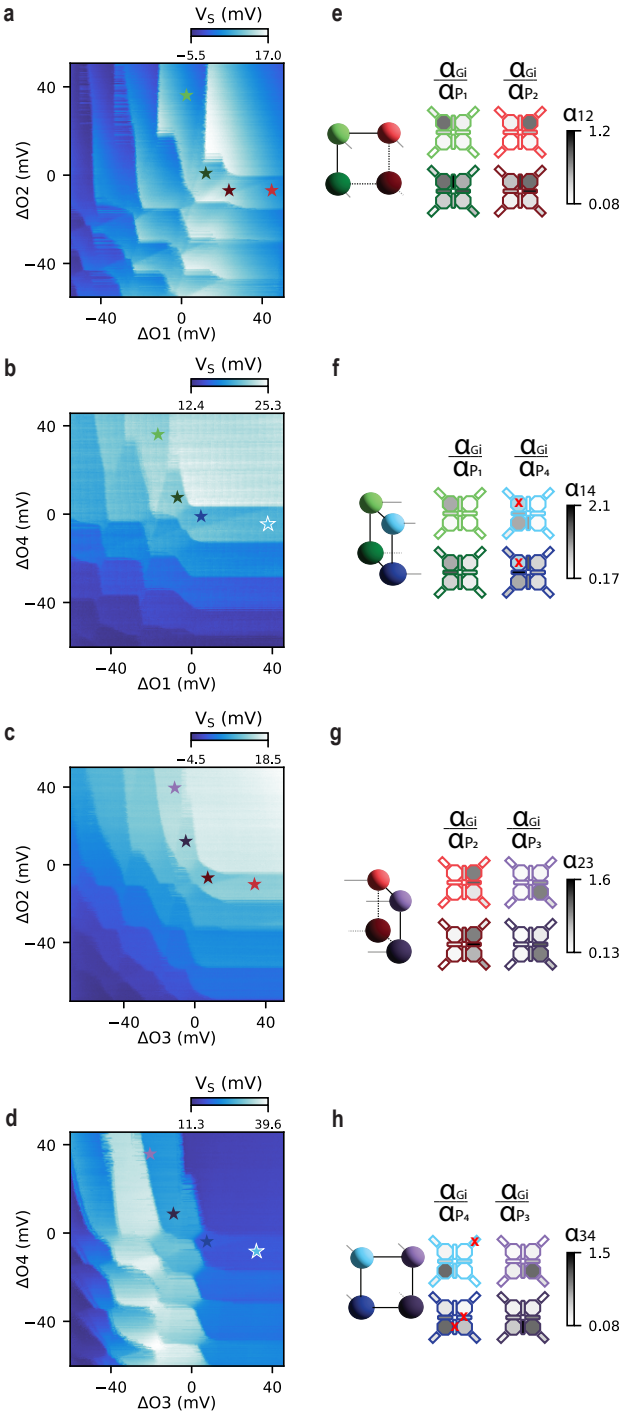

Figure 8.3: **Vertically aligned 2 × 2 quantum dot arrays a-d,** Reflectometry signal V_S exhibiting stability diagrams of different facets of the cuboid. Here, the plunger gates that are not swept on the x or y axes are kept far from the accumulation voltage, so there are only four quantum dots in the system. **e-h,** Schematics and triangulation heatmaps of the quantum dots denoting the relative lever arms $\alpha_{G_i}/\alpha_{P_i}$ of the relevant gates. e-h correspond to a-d in alphabetic order and the color code indicates the considered charging transition. See Fig. 8.1c for a labeled gate schematic. The relative lever arms are extracted from auxiliary gate-sweeps.

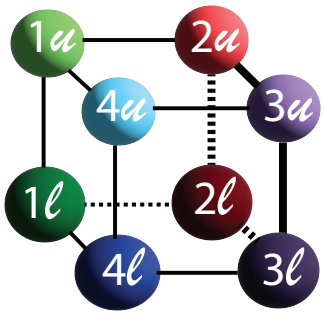

Figure 8.4: Schematic of a cuboid quantum dot configuration.

ization. The 2 × 2 array formed on the face of the device is indicated by the cartoon in Fig.8.3e-h, corresponding to the charge stability diagram above the cartoon. Across all faces, the charge stability diagrams are rather similar, showing four distinct transition lines in each stability diagram, confirming the presence of four quantum dots. Importantly, we also observe four distinct transitions corresponding to the loading of a single hole, consistent with operating four quantum dots.

To determine the location of the quantum dots, we repeat the triangulation procedure outlined previously. The colourmaps in Figs. 8.3e-h indicate the relative coupling of the gates to the respective plunger gates that are being swept. For the quantum dots in the top layer, the plunger gate always provides the strongest coupling to the quantum dot. The quantum dots associated with loading into the bottom layer exhibit a stronger overall coupling to the surrounding gates, consistent with being less electrostatically confined, in agreement with previous studies [17, 18]. We note that we observe nonlinear capacitance, in particular for the barrier gates, such that the constant-interaction model can only be applied in limited regions. Additionally, we observe extended interdot lines [22], in particular for the quantum dots under the gates $P_{2,4}$, as they load holes via the quantum dots under $P_{1,3}$.

Across all the triangulation diagrams, the relative lever arms indicate two quantum dots located predominantly under the same plunger gate. In some cases a barrier gate next to the relevant plunger gate has a lever arm larger than the plunger gate. We note that in our fabrication we pattern the barrier gates before the plunger gates, which increases the lever arms of the barrier gates.

8.3.2. QUANTUM DOT QUBOID

We now extend our investigation to the simultaneous tuning of all 8 quantum dots, shown in Fig. 8.5a-d. We first tune a 2 × 2 array under the plunger gates P_1 and P_2, after which we gradually accumulate under P_3 and P_4. We find that the reduced confinement in this operational regime results in a larger overall tunnel coupling between the quan-

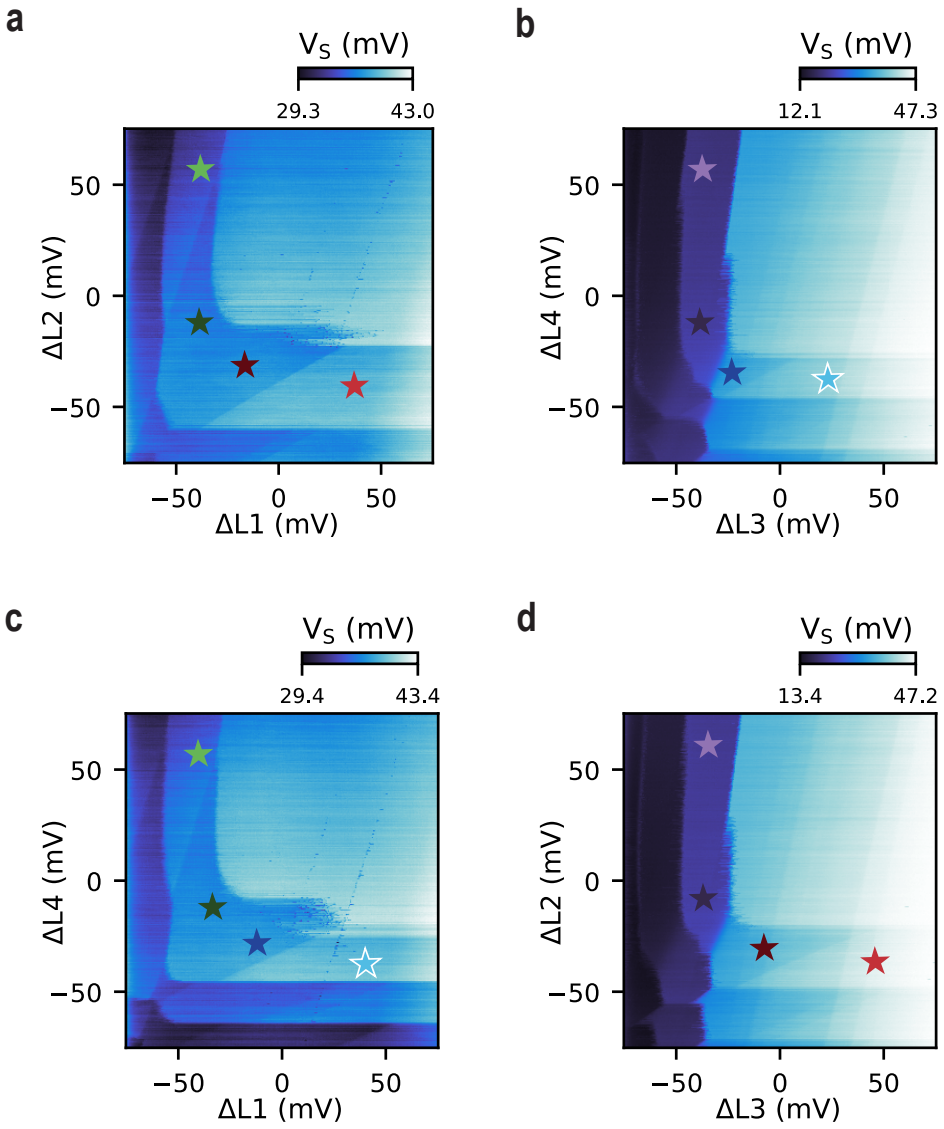

Figure 8.5: **A 2 × 2 × 2 with a single hole filling quantum dot array.a-d,**Stability diagrams corresponding to the eight quantum dot system. Here, the DC voltages (center of the 2D maps) lay ~ 10 mV above single-hole accumulation. The color of the star in the single hole regime corresponds to the quantum dot in the schematic in Fig.8.4. By sweeping pairs of virtualized plunger gate voltages ΔL_i, we identify eight distinct charging transitions that correspond to quantum dots on all corners of a cuboid underneath the plunger gates. The virtual gate voltages ΔLi correspond to orthogonal control of the lower quantum dots. The virtualization matrices are reported in Appendix 8.7.

tum dots. In particular, the stability diagrams indicate strong lateral coupling between the lower quantum dots. We see this most prominently in Fig. 8.5a,c. Nonetheless, we can still observe the latched loading lines of the lower quantum dots under P_2 and P_4. Importantly, we find loading into four distinct charge states for the single-hole regime, indicating four quantum dots in each diagram. In these experiments, we keep the DC voltage point 15 mV above accumulation to avoid crossing loading lines from opposite quantum dots due to uncompensated crosstalk. The combination of these four charge stability diagrams therefore demonstrates the loading of a single hole into eight quantum dots arranged in three dimensions.

8.3.3. COHERENT SPIN OPERATION IN A BILAYER SYSTEM

A key question for the prospects of multilayer quantum wells for quantum information is whether spin coherence is compromised in multi-well systems. As a first step to address this question, we use the pair QD1u and QD4u and tune to the few-hole regime, see Fig. 8.6a. We initialise a triplet $|\downarrow,\downarrow\rangle$ state by adiabatically ramping from the (2,0) to the (1,1) charge state. We then perform a spin rotation through resonant microwave control and readout the resulting spin states using Pauli spin blockade. Fig. 8.6b shows Ramsey experiments using this method and charge readout using the sensor dot. We measure $T_2{}^* = 2.31\,\mu s$ at $B_x = 30$ mT. This value is appreciable given the typical timescales required to execute quantum gates with germanium qubits and falls within the range of measured coherence times for hole spins in single strained germanium quantum wells [12], suggesting that the presence of multiple quantum wells does not significantly affect the quantum coherence and may allow for high-fidelity operation.

Another intriguing question is whether hole spins can be shuttled between the quantum wells through the silicon-germanium barrier. To study this, we choose to operate in an isolated mode (see Appendix 8.6 for details and stability diagrams in isolated mode) [23]. This is achieved by reducing the tunnel coupling of the quantum dots to the reservoir during operation, see Fig. 8.6d. To test whether we can coherently shuttle between the two quantum wells, we utilize the large sensitivity of the spin quantization axis of hole spins in germanium to the electric and magnetic fields and implement a shuttling protocol [24, 11]. Figs. 8.6e and 8.6f show the protocol and experimental results. In particular we find that once we shuttle from the top to the bottom quantum well, the larmor precession is evolving around a tilted axis, resulting in qubit rotations. We note that the finite visibility observed is expected to be limited by the difference between quantization axes. Further research is needed to investigate the quality of vertical hopping and to which extent the difference in the g-tensor can be engineered, for example by differences in the strain between the quantum wells.

8.4. DISCUSSION AND OUTLOOK

Silicon-germanium heterostructures define a versatile and high-quality platform. We have investigated quantum dot operation in multilayer quantum wells and demonstrated that quantum dots can be interconnected in three spatial dimensions. We find that three-dimensional quantum dot structures yield stable and clean charge-stability diagrams and allow for coherent spin control.

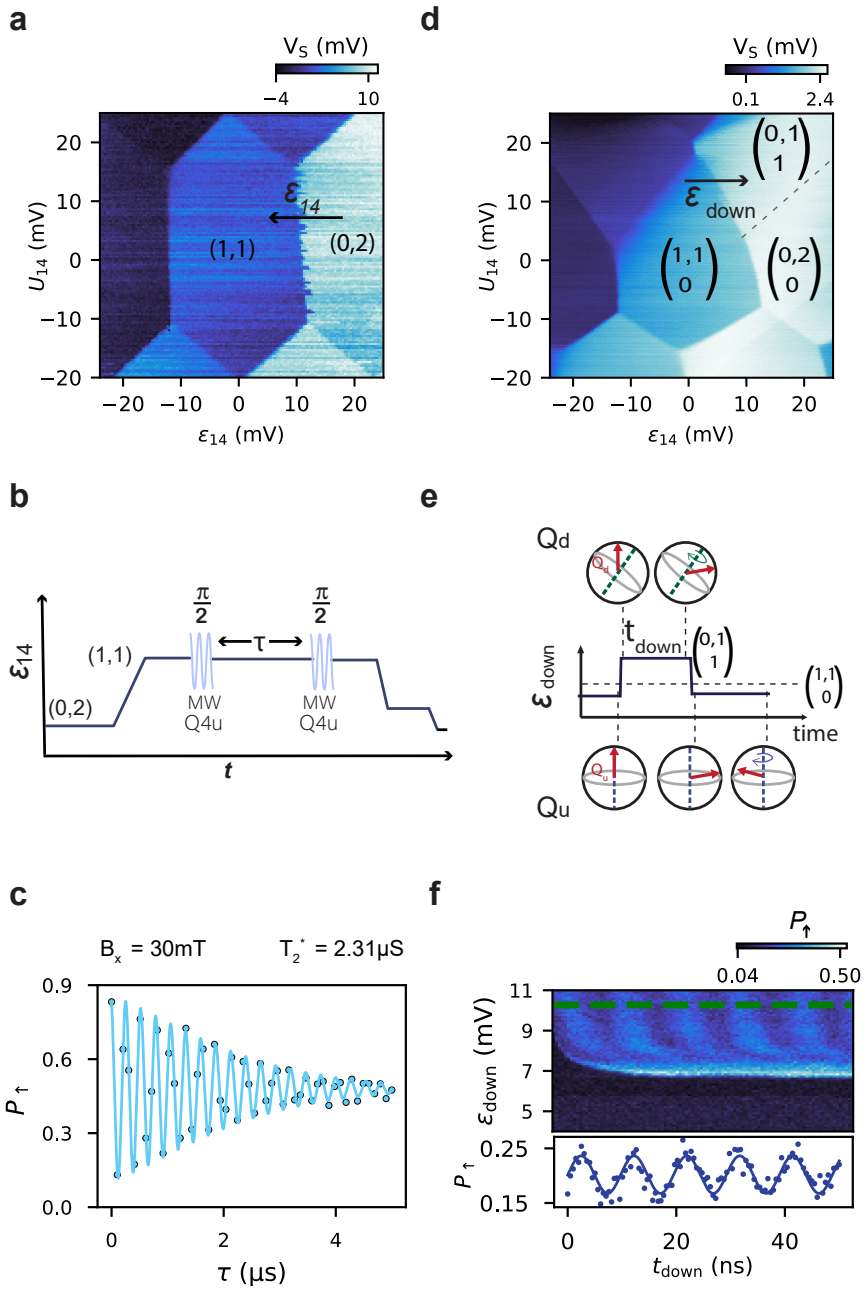

Figure 8.6: **Coherent operation in a bilayer heterostructure. a,** Isolated mode charge stability diagram of QD1u and QD4u when only the upper quantum well is accumulated with a total of 3 holes trapped in the system. **b,** Ramsey sequence depiction on QD4u, in the regime of **a**. **c,** Experimental data of the ramsey sequence on QD4u, from which we deduce a T_2^* of 2.31μs at a magnetic field B_x= 30 mT. **d,** Charge stability diagram with two upper and one lower quantum dot in isolated mode, with the charge state notation $\begin{pmatrix} QD1u & QD4u \\ QD\ell & \end{pmatrix}$. **e** Depiction of the shuttling sequence between QD1u and the lower quantum dot. A triplet is adiabatically initialised in QD4u and QD1u. The hole in QD1u is then diabatically shuttled across ϵ_{down} and allowed to precess for time t_{down}, before shuttling back to the original quantum dot and read out by Pauli spin blockade between two quantum dots in the upper layer.. **f,** Shuttling induced oscillations by diabatically pulsing across ϵ_{down} into the lower quantum dot and back to the original quantum dot, as detailed in **e**. The lower panel shows a linecut of the oscillations on the dotted line in the upper panel at ϵ_{down} = 10.27 mV.

Operating three-dimensional quantum dot arrays may offer new opportunities for quantum simulation and computation [25]. In our work, we have also identified several challenges in building such systems. Compared to planar systems, multilayer systems have smaller operational windows due to a low number of control parameters compared to the system size. Future designs may address this by the inclusion of additional gates, where the small effective mass of germanium can be beneficial [26, 27], as it allows increasing the quantum dot size. Furthermore, the simultaneous confinement of holes in the two quantum wells and operation in the few-hole regime depend strongly on heterostructure design choices, as well as on aspects such as quantum dot size and applied gate voltage. This highlights the need for a co-design approach involving material growth, device fabrication, and system operation. Importantly, the observed quality of the double quantum well system offers promising prospects for model-based design and further advancement.

In our experiments, we qualitatively find that quantum dots in multilayer systems can be strongly coupled. This would be beneficial for quantum simulations where large couplings are desired. Future experiments may also investigate strained quantum wells with larger separation to reduce the coupling between the layers to optimize high-connectivity quantum dot arrays for quantum computing.

APPENDIX

8.5. SENSOR TUNING

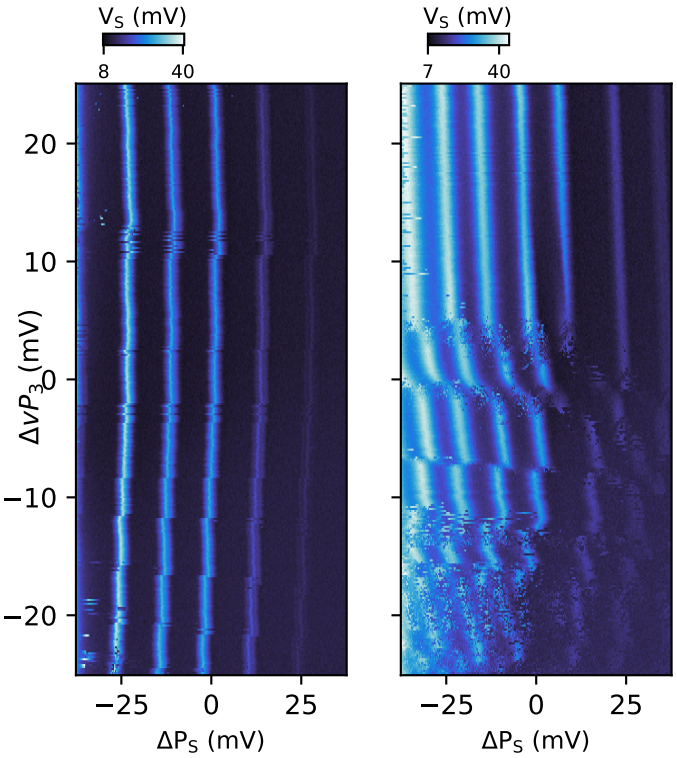

Figure 8.7: **Sensor operation.** In the left panel, the sensor is a single quantum dot. The experiments show measurement of a quantum dot under P_3. In the right panel, the sensor contains a vertical double quantum dot.

As the sensing dots can also be composed of a vertical double quantum dot, this can interfere with the charge signal when detecting charge transitions of the quantum dots in the plunger array. To avoid this, we strongly confine the sensing dot in order to have a single quantum dot. This can come at the expense of reduced contrast in the charge transitions of the quantum dots in the array. A vertical double quantum dot in the sensing dot may compromise the quality of the rf-signal, due to the crosstalk within the sensing dot, interfering with the charge signal from the device.

8.6. MULTI-DOT ISOLATED MODE

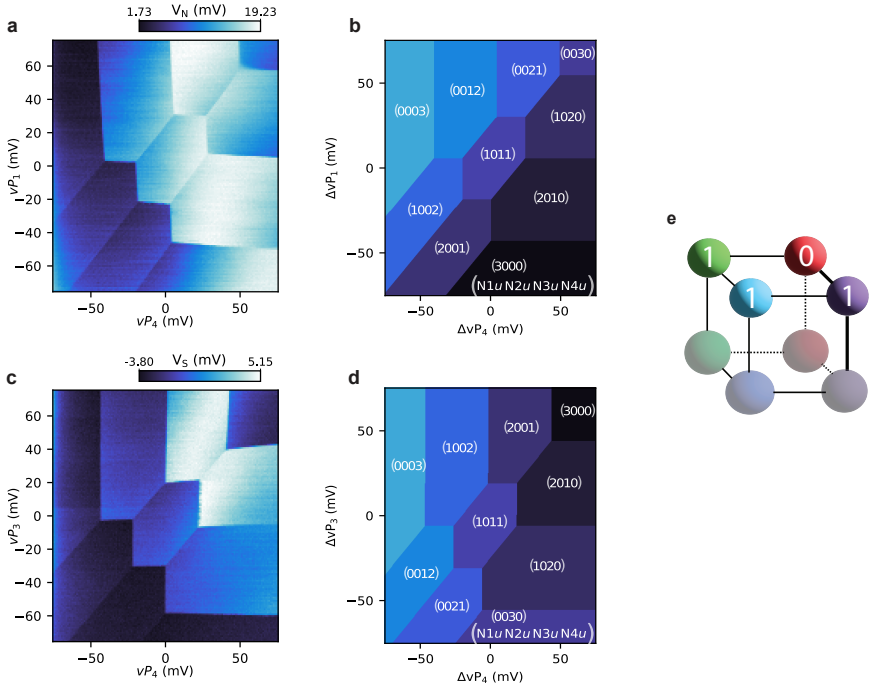

Figure 8.8: **Triple dot charge stability diagrams in isolated mode while only the upper layer is accessible**. Charge stability diagrams for the QD1u-QD4u pair **(a)** and QD3u-QD4u **(c)** pair considering a total of 3 holes and 4 QDs. **b,d** Simulated charge stability diagrams for a triple dot system hosting three holes, corresponding to **a,c** respectively. **a,c** are acquired at the same DC point and pulsing ±100 mV on the virtualized plungers. **e** Schematic representation of cuboid quantum dot configuration. The number in each sphere represent the charge occupation in the corresponding dot in isolated mode at the DC point at the center of the charge stability diagram.

Demonstrating the capability to control the charge degree of freedom of quantum dots formed in a bilayer Ge/SiGe heterostructure is a key requirement for spin operation. Generally, precise control over tunnel coupling between quantum dots is required to achieve high-quality initialization, operation, and readout for both ST and LD qubits. The barrier between the sensor and the first dot (B_S and B_N) in the array affects the charge loading of the upper or lower quantum dots from the sensor reservoir differently, leading to asymmetric charge decay rates for the upper- or lower-layer quantum dots. Moreover, when the lower dot is accumulated, the (1,1) and (2,0)/(0,2) charge states are no longer connected. This prevents the initialization of spins in the upper layer and the subsequent shuttling of single spins down without implementing pulsing schemes for initialization and readout. For this reason, the system is operated in the closed regime, also known as the isolated regime, where a fixed number of holes is trapped[23]. This is

achieved by pinching off the barriers that separate the sensors from the central dot array, namely B_S and B_N.

An example of a triple dot charge stability diagram for the upper layer in isolated mode is shown in Fig. 8.8. The holes are first loaded via P_S, then by increasing the barrier voltage (B_S) below the accumulation threshold tunneling to the ohmic reservoir is suppressed. All the lines in the charge stability diagram represent interdot transitions which preserve the total number of charges. Three holes are trapped in the system between QD1u, QD3u and QD4u. Each QD hosts 1 hole at the DC voltage point. Fig. 8.8a shows the P_1-P_4 gate pair and 8.8c shows P_3-P_4. The resulting charge stability maps are consistent with the simulation in isolated mode performed using Qarray as shown in Fig.8.8b, 8.8d. The labeling of the charge state is independently assigned using the simulation.

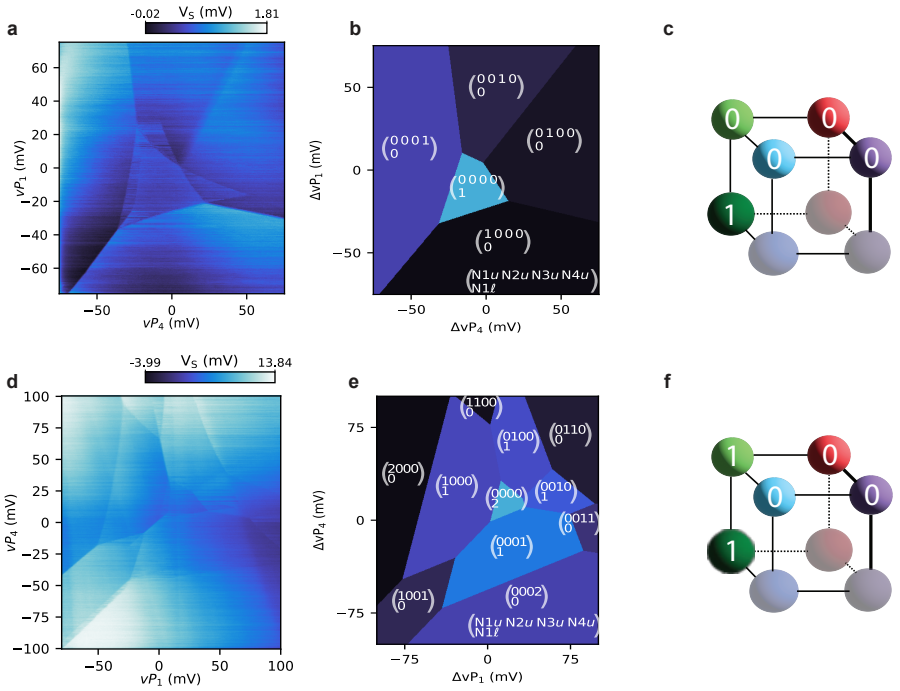

Figure 8.9: **Multi-dot charge stability diagrams isolated mode with the lower layer occupied**. **a, c** Charge stability diagram, scanning P_1 and P_4, of a 5 quantum dot array in isolated mode hosting 1 and 2 holes respectively. The isolated hole(s) has access to 1 lower layer quantum dot (QD1ℓ) and all the four upper layers dots.**b,d** Simulated charge stability diagrams corresponding respectively to **a, c**. Both simulations are made with the same capacitance matrices, chosen to qualitatively fit the experiment best. **c,f** Schematic representation of cuboid quantum dot configuration. The number in each sphere represents the charge occupation of the corresponding dot in isolated mode at the DC point at the center of the charge stability diagram.

By modeling the system in isolated mode, we can also study how the presence of the lower quantum dots will affect the shape of the isolated charge stability diagram.

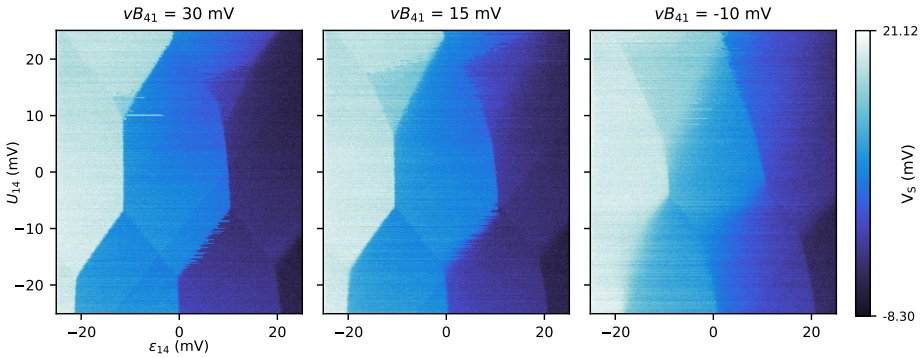

Figure 8.10: **Series of CSD in isolated mode which shows the lower layer tunability using the barrier vB_{41}.**

We note in Fig. 8.9 that the presence of an extra dot in the lower layer appears as an additional set of transition lines orthogonal to the interdot line between the pair of upper quantum dots from which the plungers are swept.

Indeed, by decreasing the barriers and screening of the 2x2 quantum dot array it is possible to bring one the lower dots close to accumulation. An example of this is shown in Fig.8.10, where the barrier between the P_1 and P_4 dots (vB_{41}) is pulsed in steps of 20 mV. An additional charge state appears above the (2,0,1)-(1,1,1) interdot transition as well as (0,2,1)-(1,1,1) transition. A comparison between simulation and experiment for a total charge occupation of 1 and 2 holes with an additional lower layer quantum dot in isolated mode is shown in Fig.8.9. The tilt of the up-to-low interdot line is related to how strong the plunger-to-lower layer lever arm is. Interesting to note in Fig.8.10 is that also the latching of the up-to-down transition depends on the barrier value which points towards a tunable up-to-down interdot coupling. The ability to operate both layers without any changes in hole occupation throughout initialization, control and readout is a main prerequisite for scaling it up to large three-dimensional arrays.

8.7. VIRTUALISATION

We use an embedded form of virtual gate matrices. This gives us the flexibility easily to define the same gate in multiple different ways. We begin by virtualising the gates to the sensing dots, then gate-gate. Here we show the inverted virtual gate matrix M^{-1}, which is defined as $M^{-1} *$ Virtual Gates = Real Gates. The virtualisation may change between different tuning regimes, and the exact forms can be found in the metadata.

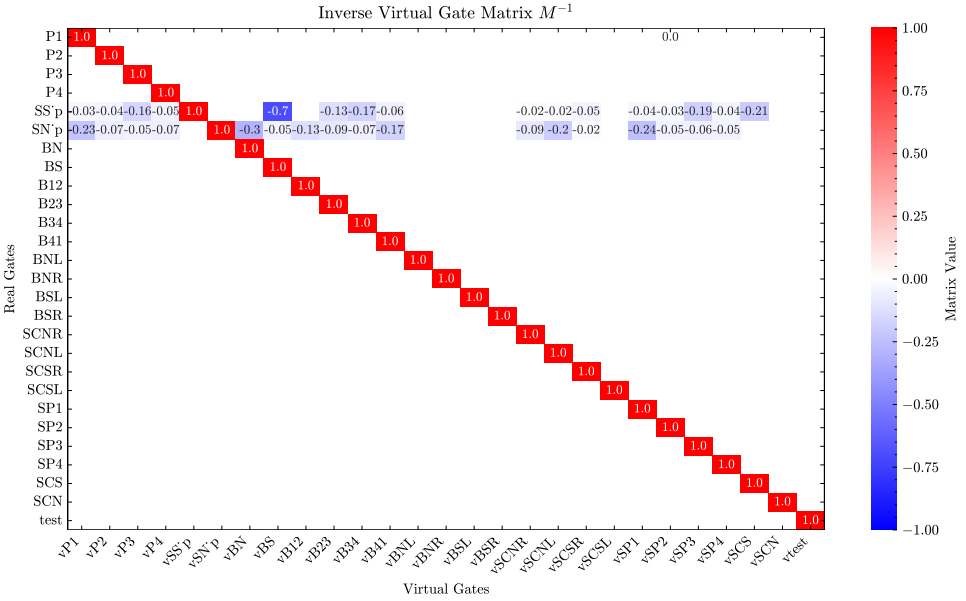

Figure 8.11: Virtual gate matrix for compensating the sensor signal.

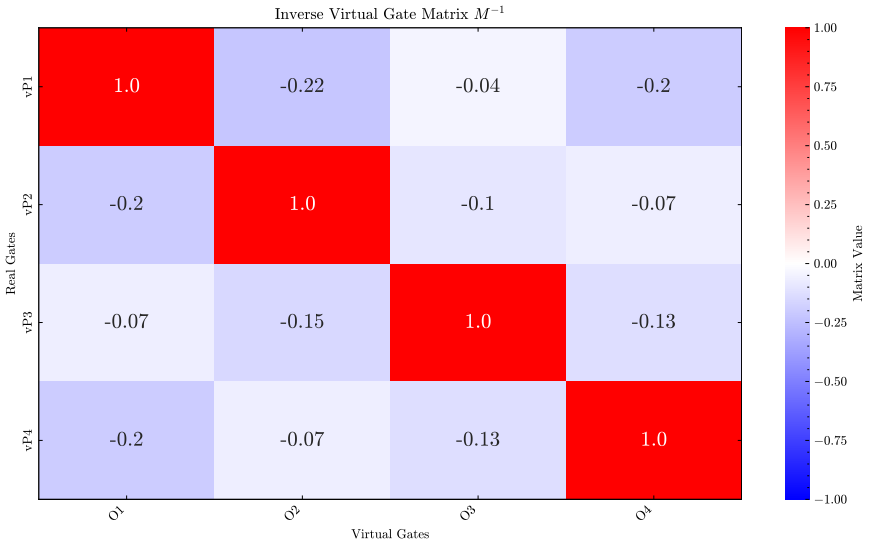

Figure 8.12: Plunger to Plunger gate virtualisation for the upper quantum dots.

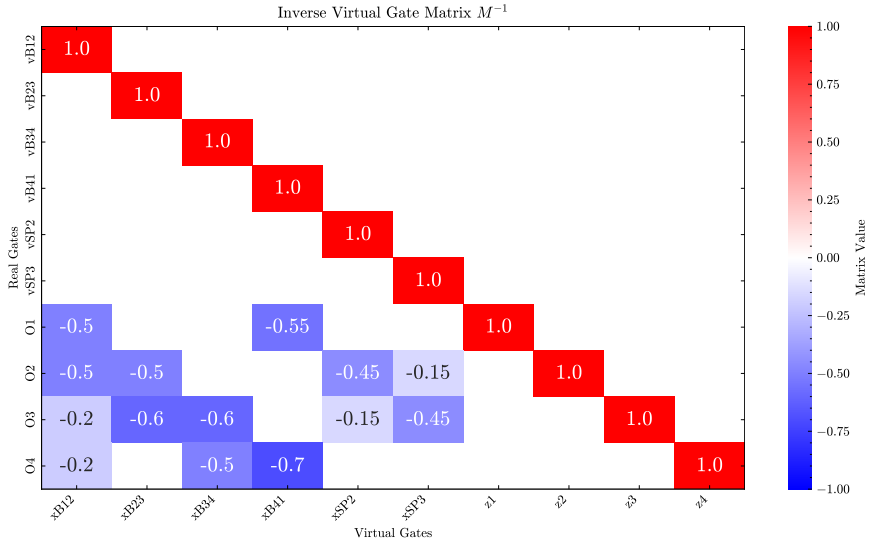

Figure 8.13: Barrier to Plunger gate virtualisation.

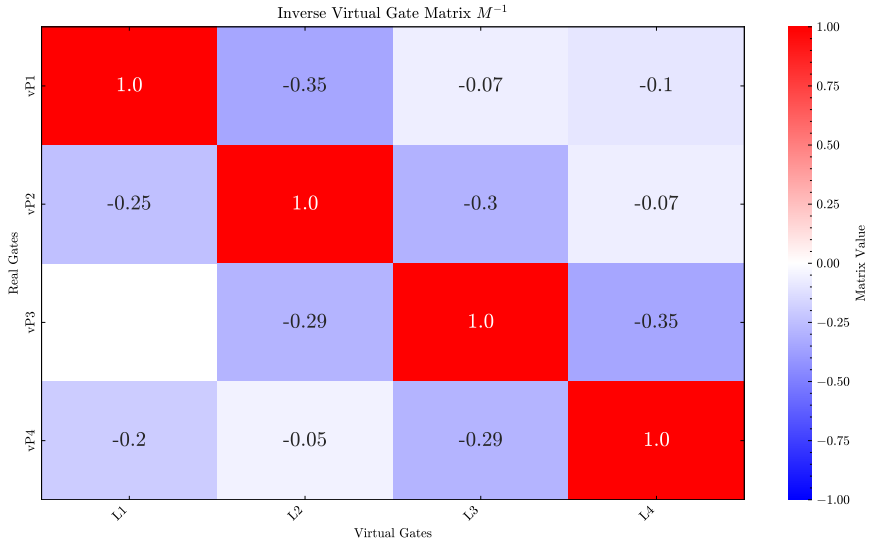

Figure 8.14: Plunger gate to Lower quantum dot virtualisation matrix.

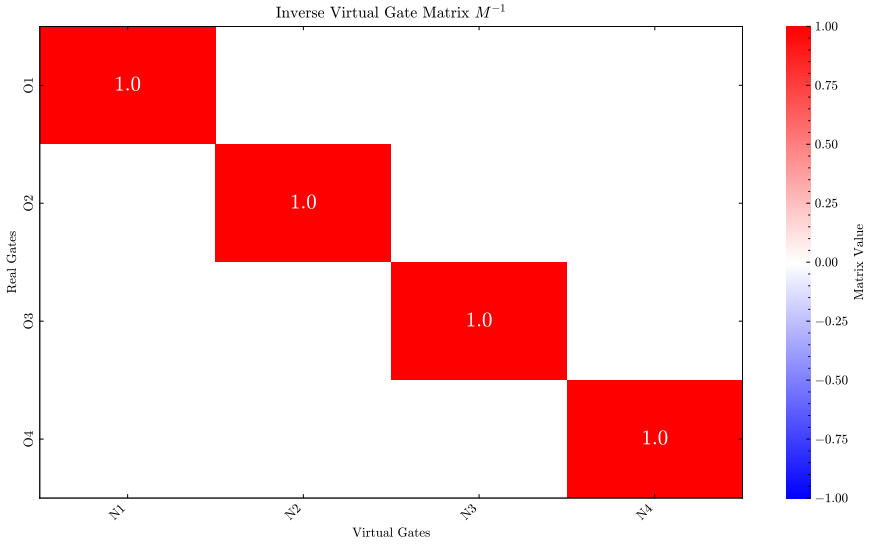

Figure 8.16: One to one orthogonal gates to normalised gates mapping.

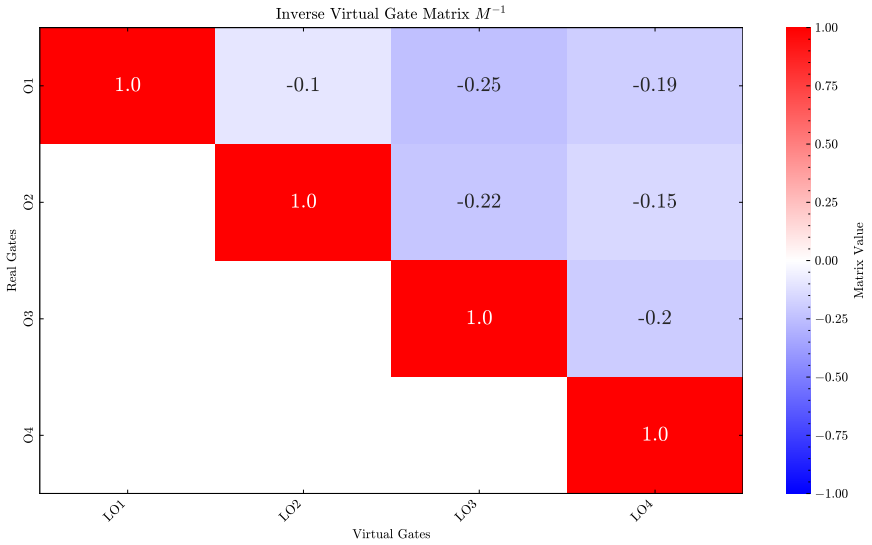

Figure 8.15: Orthogonalised plunger gate virtualisation to lower orthogonal gates.

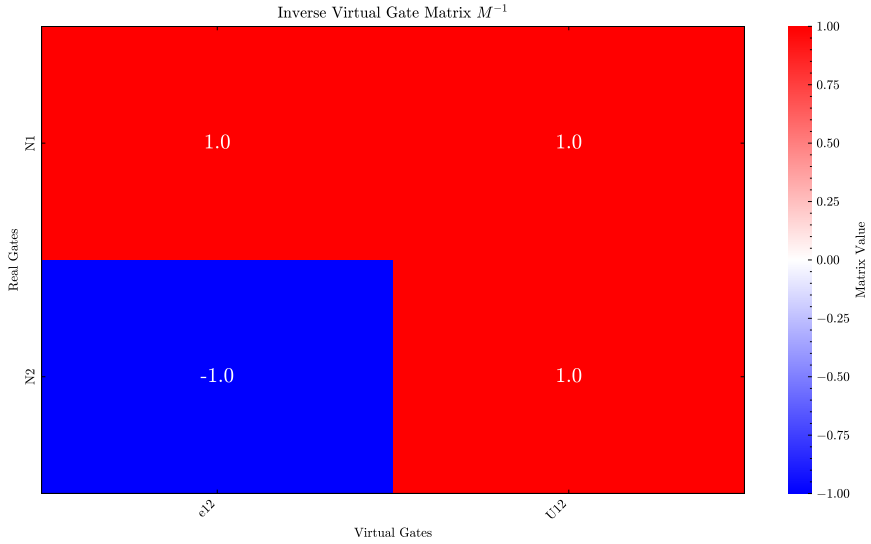

Figure 8.17: Detuning ϵ_{12} and Potential energy U_{12} virtual gate matrix.

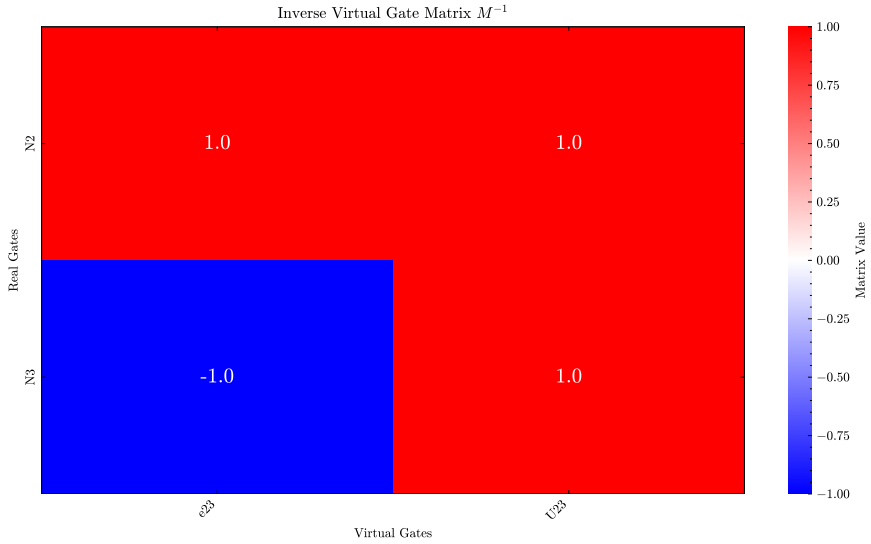

Figure 8.18: Detuning ϵ_{23} and Potential energy U_{23} virtual gate matrix.

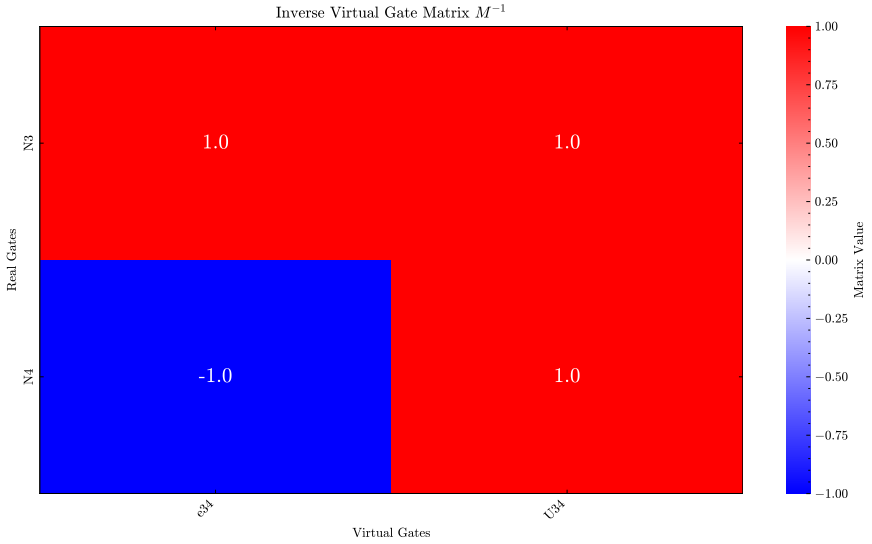

Figure 8.19: Detuning ϵ_{34} and Potential energy U_{34} virtual gate matrix.

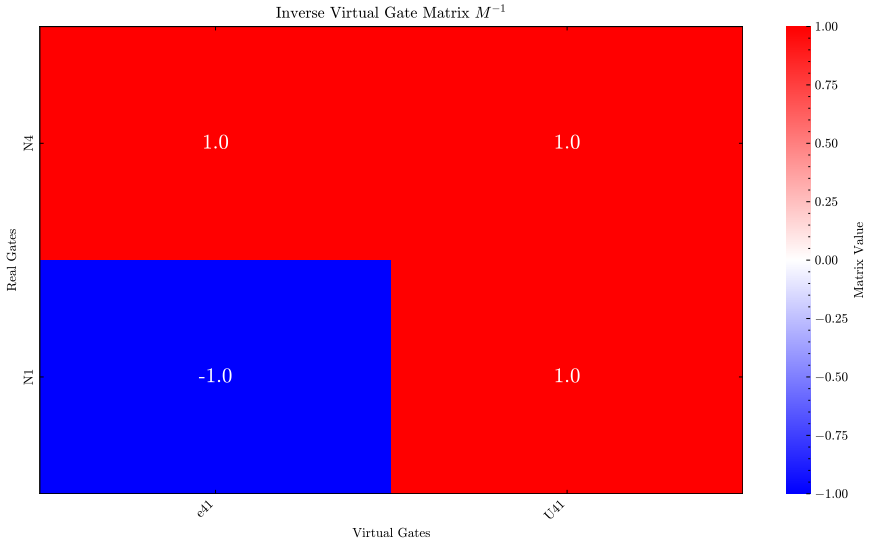

Figure 8.20: Detuning ϵ_{41} and Potential energy U_{41} virtual gate matrix.

8.8. MANUAL FITTING OF CHARGE STABILITY DIAGRAMS FOR TRIANGULATION

TRIANGULATION

In order to find the relative lever arms of the gates to the quantum dots, we collect charge stability diagrams of the plunger gate P_i vs all surrounding gates G_j. The full set of diagrams, fitted and unfitted are shown below. The diagrams are centered around a particular reservoir transition line for the gate being swept. The plots are then manually fitted, ensuring that all of the transitions correspond to the same intersection along the y=0 axis.

We collect data of all of the gates vs the virtual gate L_I, where i= 1,2,3,4. The L gates are virtualised such that all the surrounding gates are virtualised to the lower quantum dot charge transition. We then manually fit the charge transition lines on all the charge stability diagrams, by categorizing the slopes into 'steep' (red), 'less steep' (blue), and 'interdot transition' lines (purple). When the gate is on the $y = 0$, we correlate the charge transitions across the different fits and ensure they are self-consistent. We then separately find the averages of the slopes $\bar{\alpha_G}$. As we do not measure the absolute lever arm, we must find the lever arm relative to a common gate. We choose L_i, which is swept on the x-axis, as this common gate and find the relative lever arm to be

$$\alpha = \frac{\bar{\alpha_G}}{\bar{\alpha_{L_i}}} \tag{8.1}$$

We normalize to the plunger gate which is swept on the x-axis, and show the spread in the slopes.

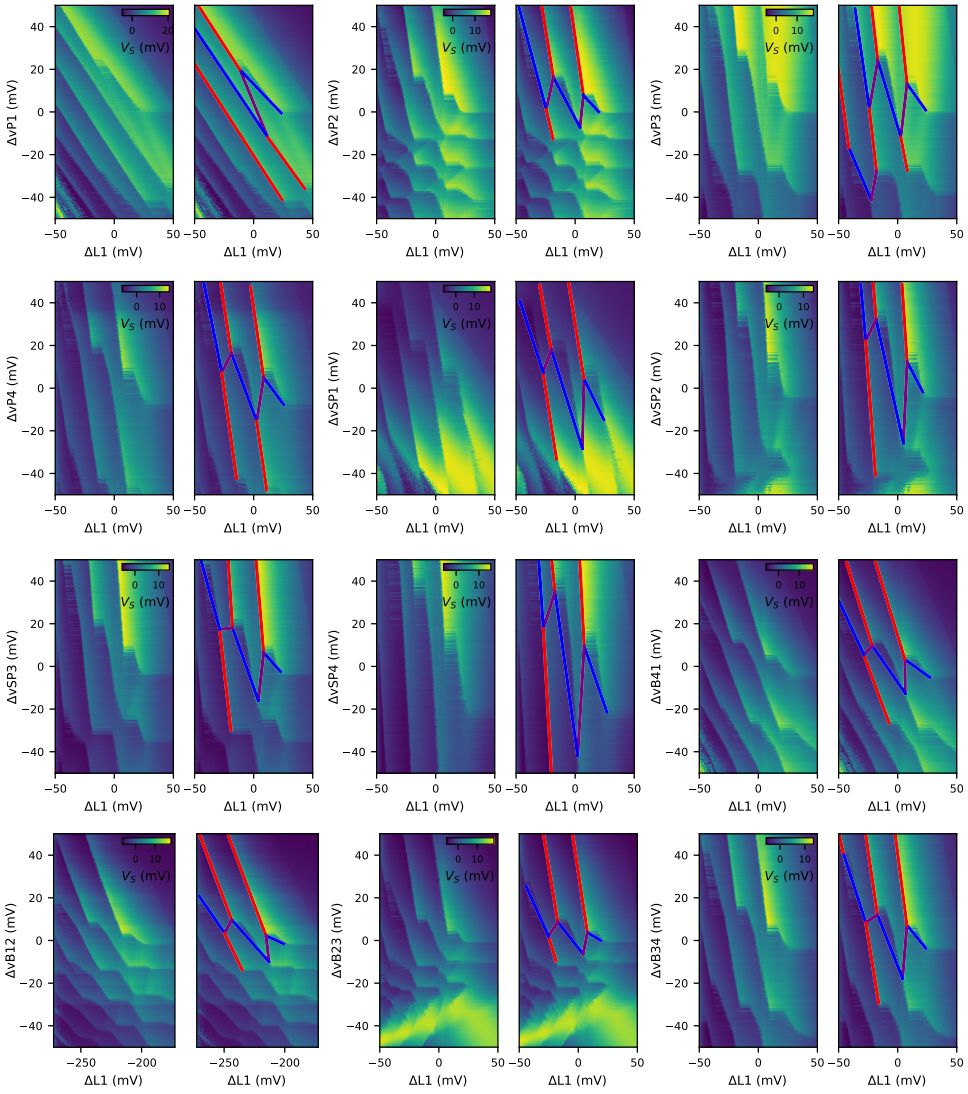

Figure 8.21: Triangulation data and the fitted triangulation data for the double dot pair under plunger gates P_1 and P_2.

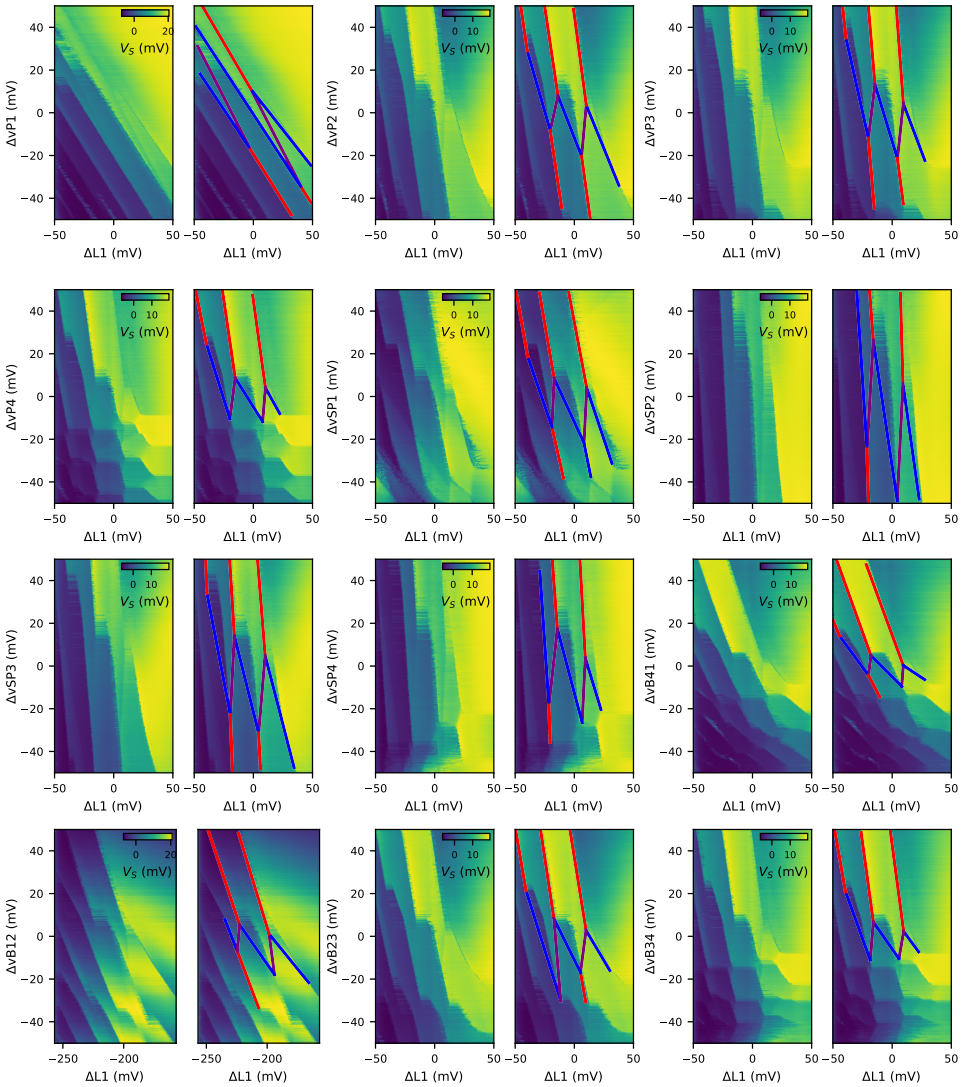

Figure 8.22: Triangulation data and the fitted triangulation data for the double dot pair under plunger gates P_1 and P_4.

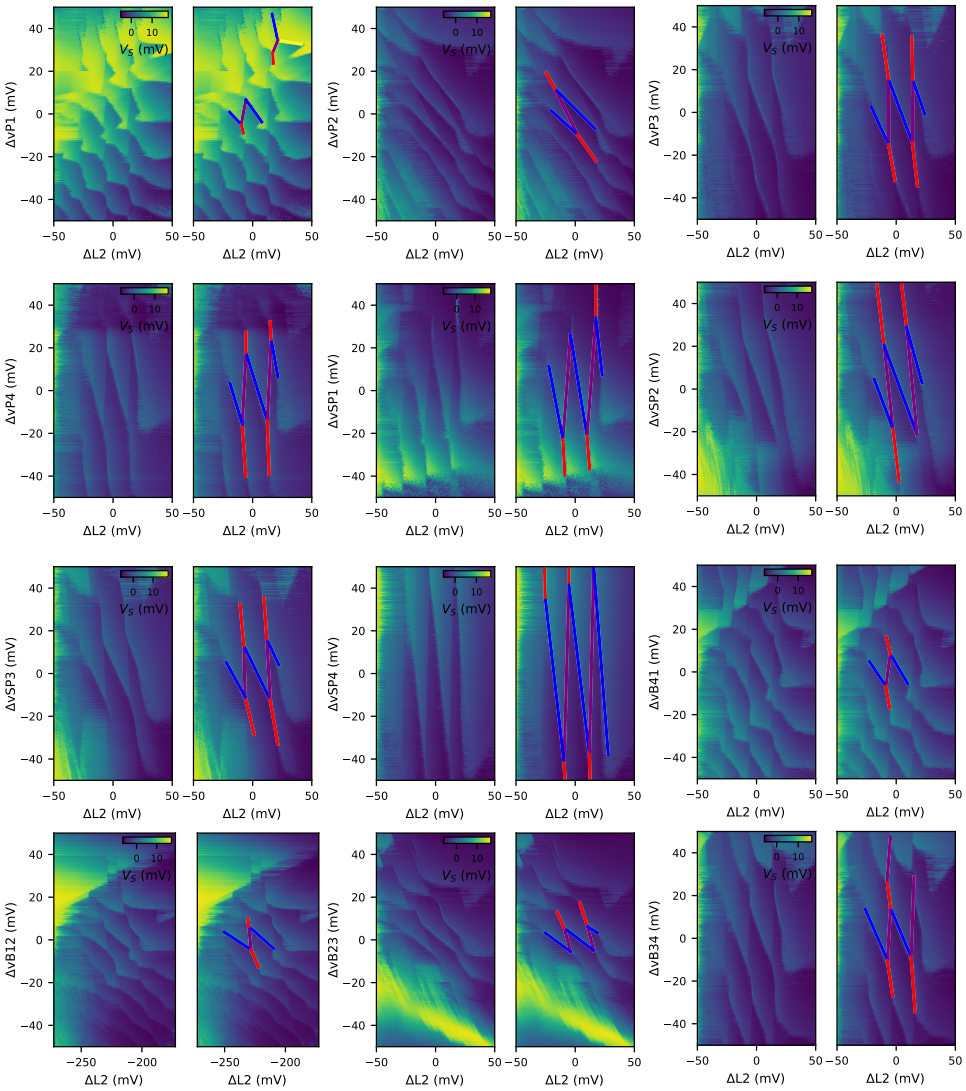

Figure 8.23: Triangulation data and the fitted triangulation data for the double dot pair under plunger gates P_2 and P_1.

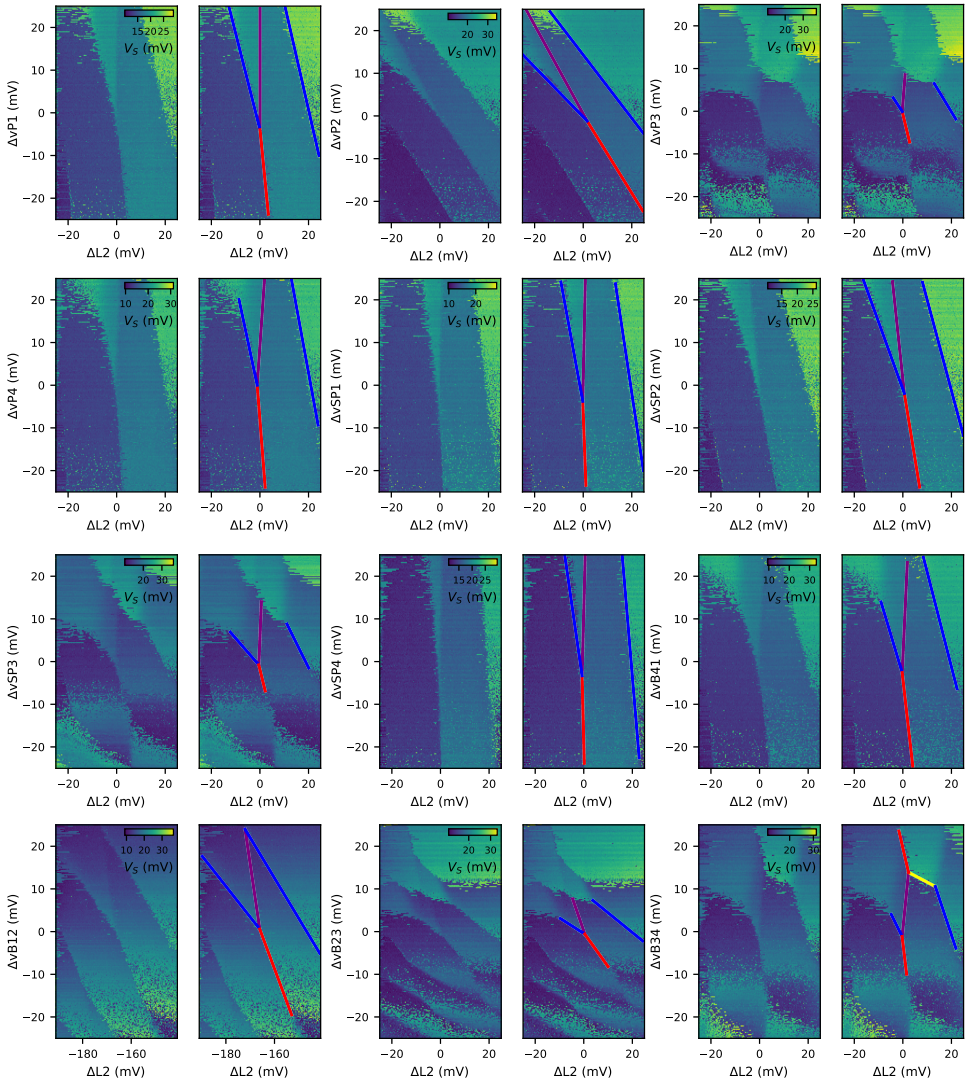

Figure 8.24: Triangulation data and the fitted triangulation data for the double dot pair under plunger gates P_2 and P_3.

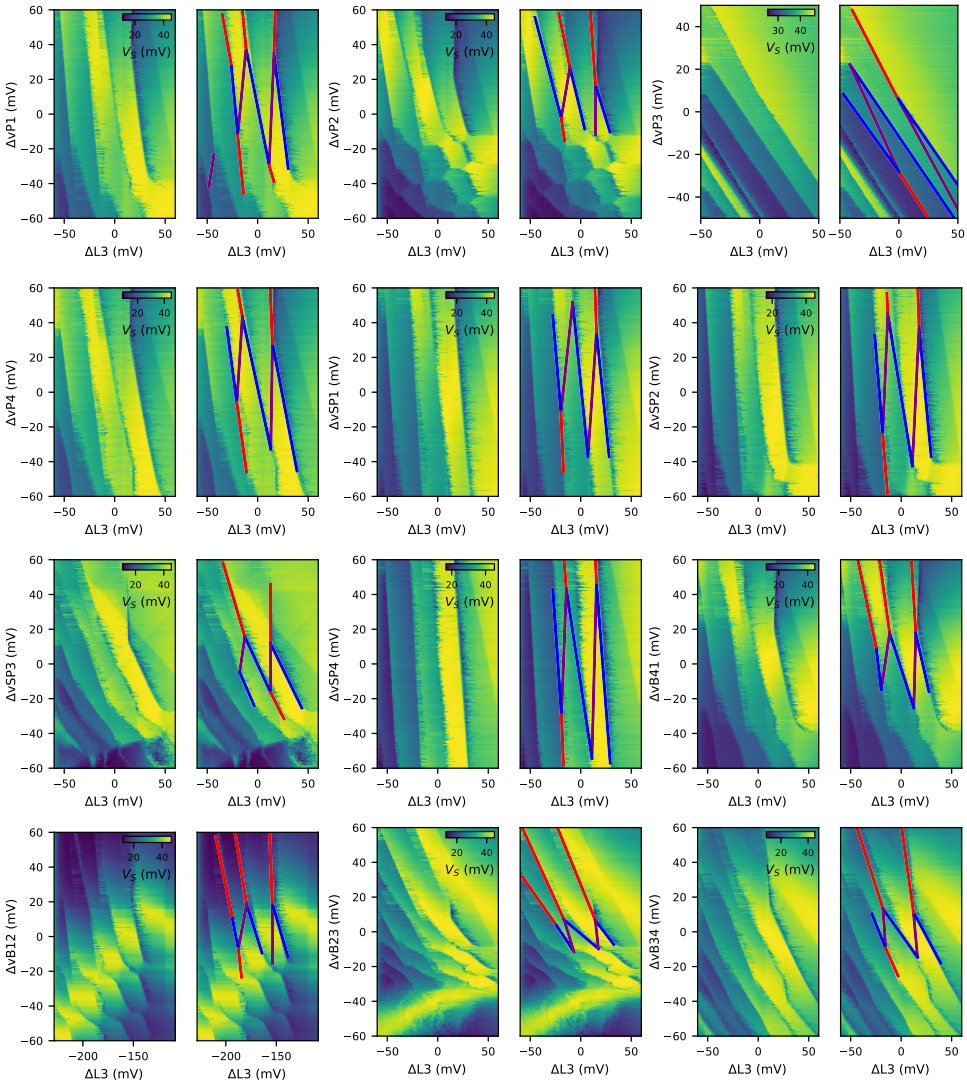

Figure 8.25: Triangulation data and the fitted triangulation data for the double dot pair under plunger gates P_3 and P_2

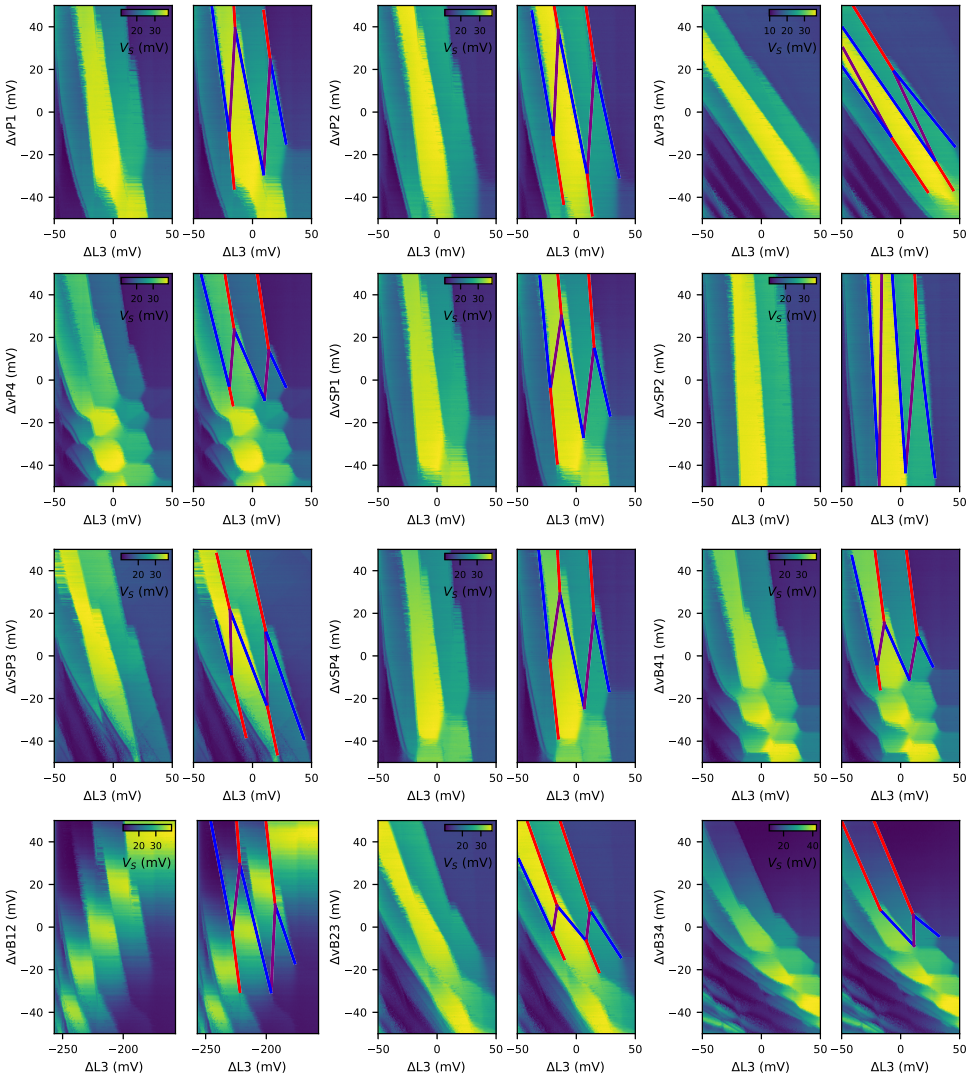

Figure 8.26: Triangulation data and the fitted triangulation data for the double dot pair under plunger gates P_3 and P_4

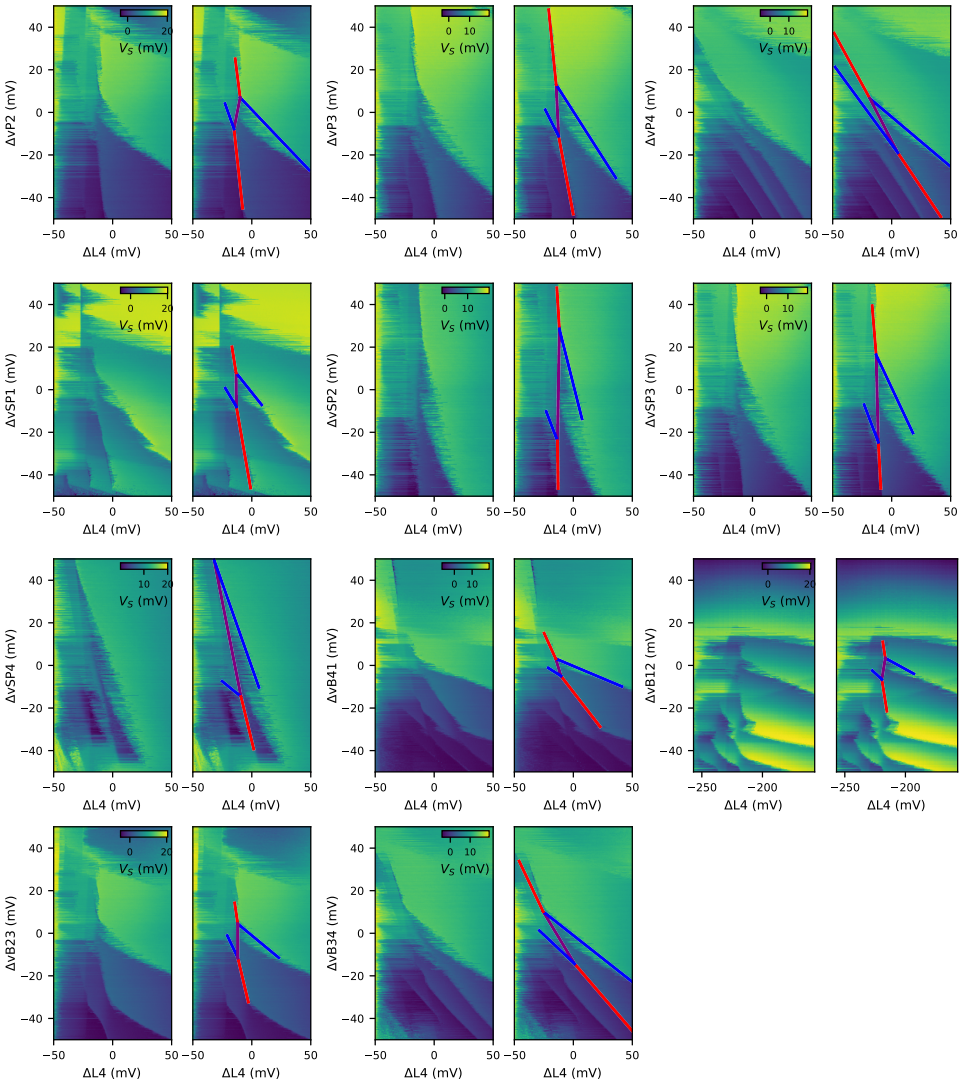

Figure 8.27: Triangulation data and the fitted triangulation data for the double dot pair under plunger gates P_4 and P_1

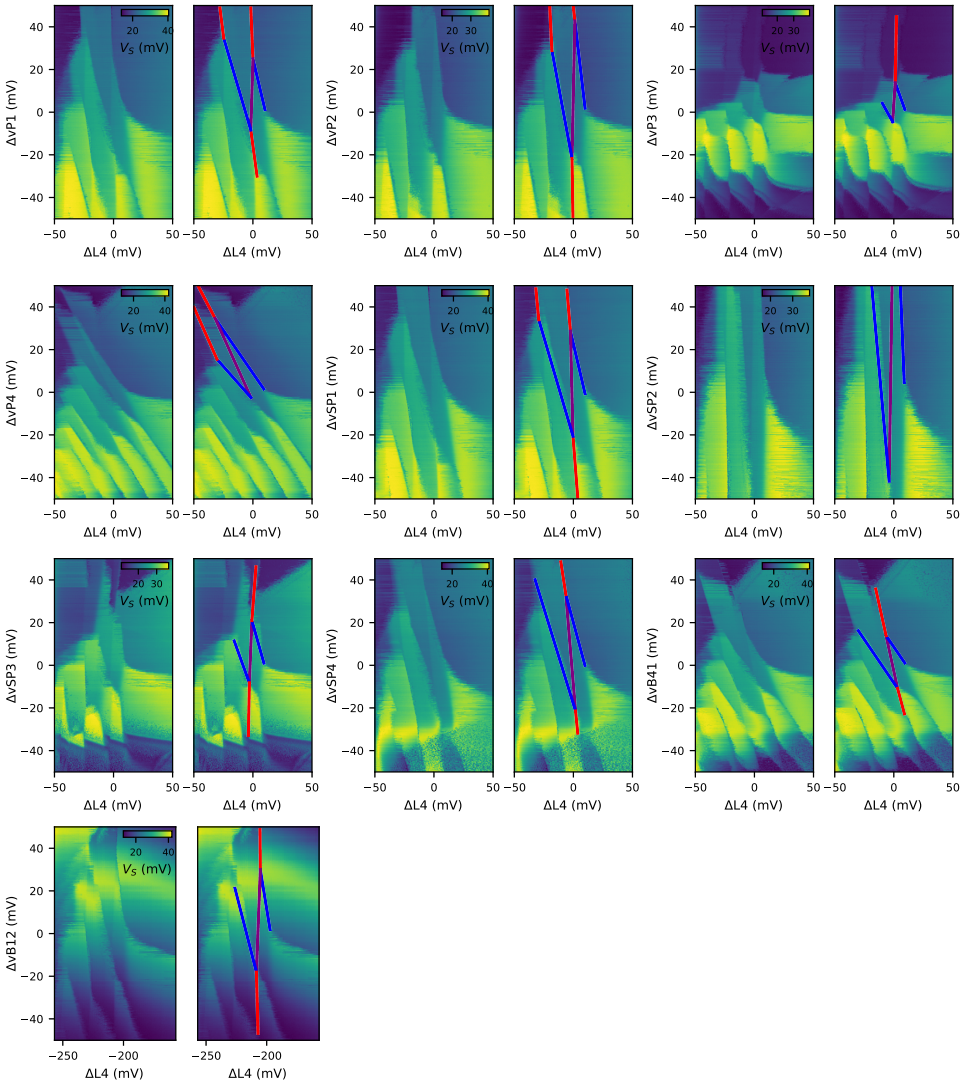

Figure 8.28: Triangulation data and the fitted triangulation data for the double dot pair under plunger gates P_4 and P_3

In Fig.8.29 we show the intersection points for each charge stability diagram along the linecut of $y = 0$. We do this to ensure that the line categorisation is consistent across charge stability diagrams.

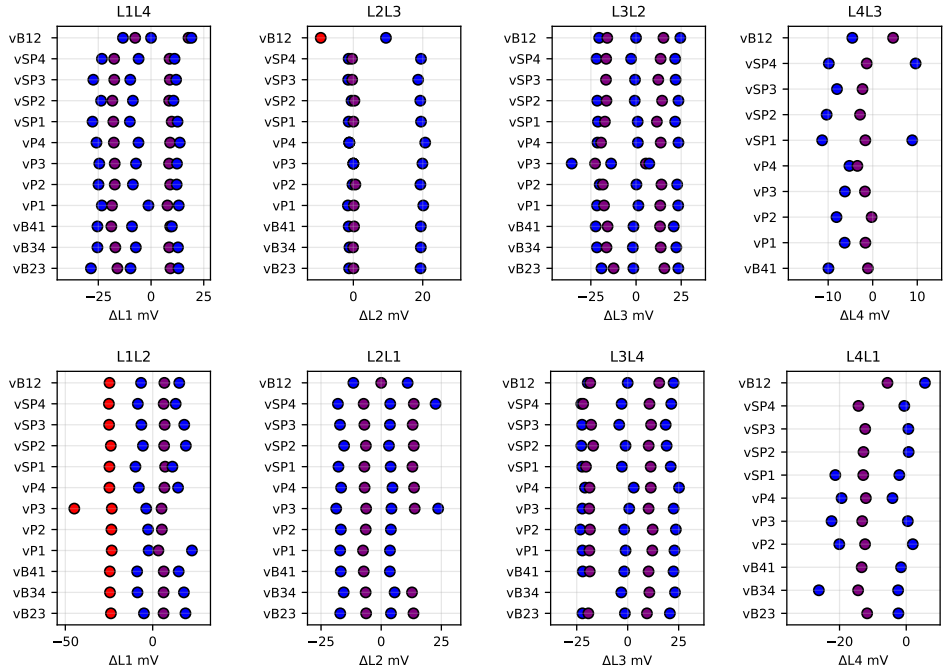

Figure 8.29: The intersection points along y=0 for all the fitted data sets.

8

In the figures below, we plot the standard deviation of the relative lever arms of the gates. In some, we see that nearby barrier gates have a larger coupling to the bottom quantum dot than the plunger gate. This is consistent with schroedinger-poisson simulation results reported in [17], where the large spread in the wavefunction of the lower quantum dot due to decreased confinement, and some screening from the charges in the upper quantum dot, reduces the coupling of the plunger gate to the lower quantum dot. Additionally, the barrier gates have a non-linear effect on the lower quantum dot in particular, moving it as their voltages change. This means there can be large differences in the slopes between transitions.

Additionally, there is further complication for the gates which do not have direct reservoir transitions being P2 and P4. As they load via the dots closest to the sensor (P1 and P3), when swept on the fast axis they have strong latching features. Therefore, we centre the diagram on a known transition, then flip the axis. In this way, we know which transition we are at on our DC point, and then can categorise the other slopes based on their steepness. This also decreases the number of transitions we can reliably fit.

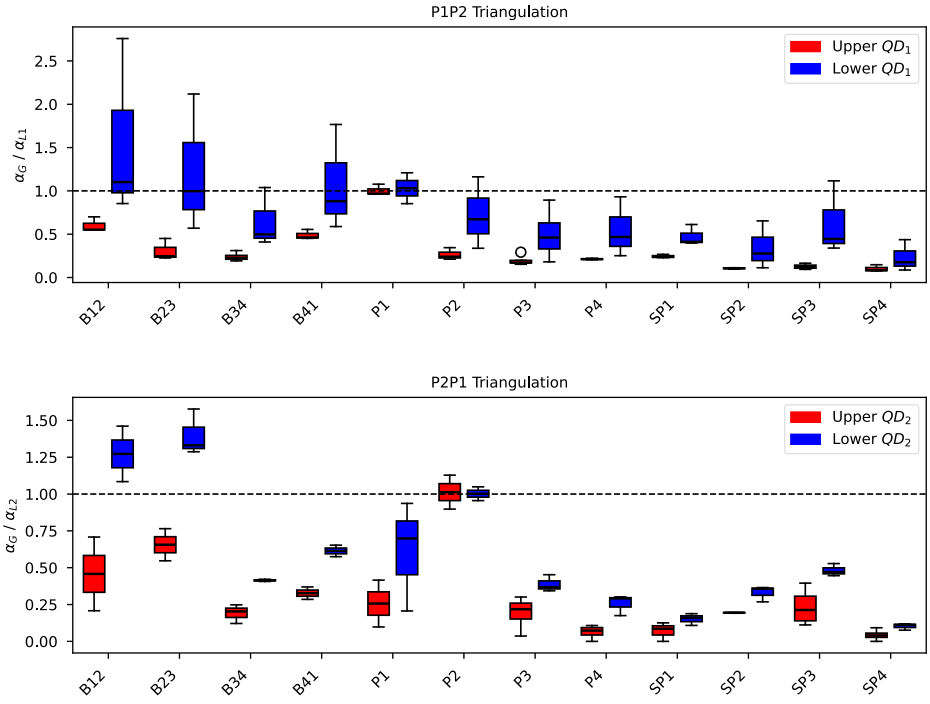

Figure 8.30: Boxplots indicating the spread in the relative lever arm across the various transitions.

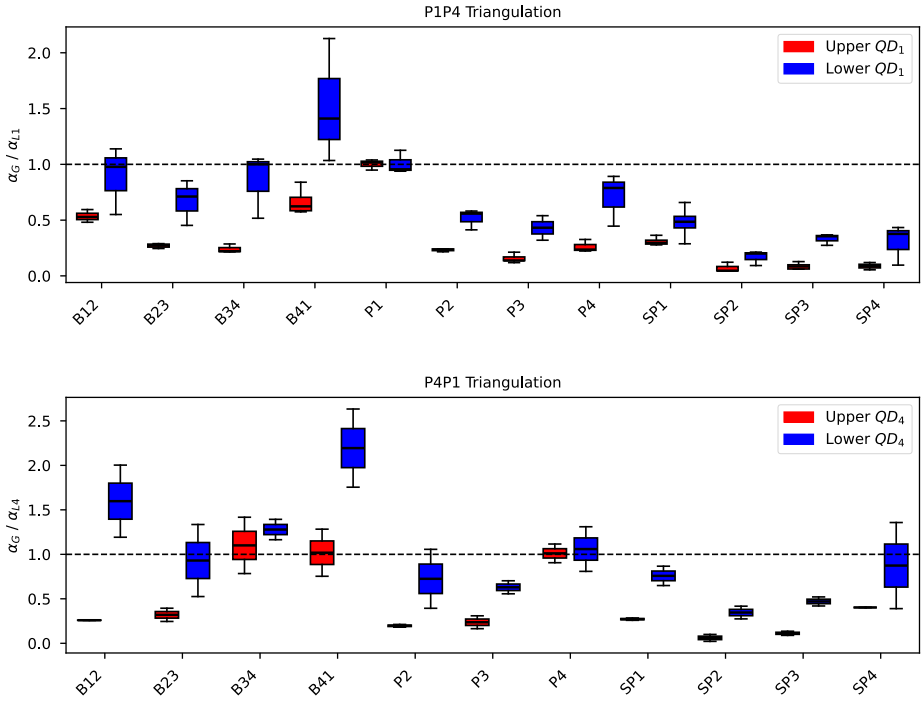

Figure 8.31: Boxplots indicating the spread in the relative lever arm across the various transitions.

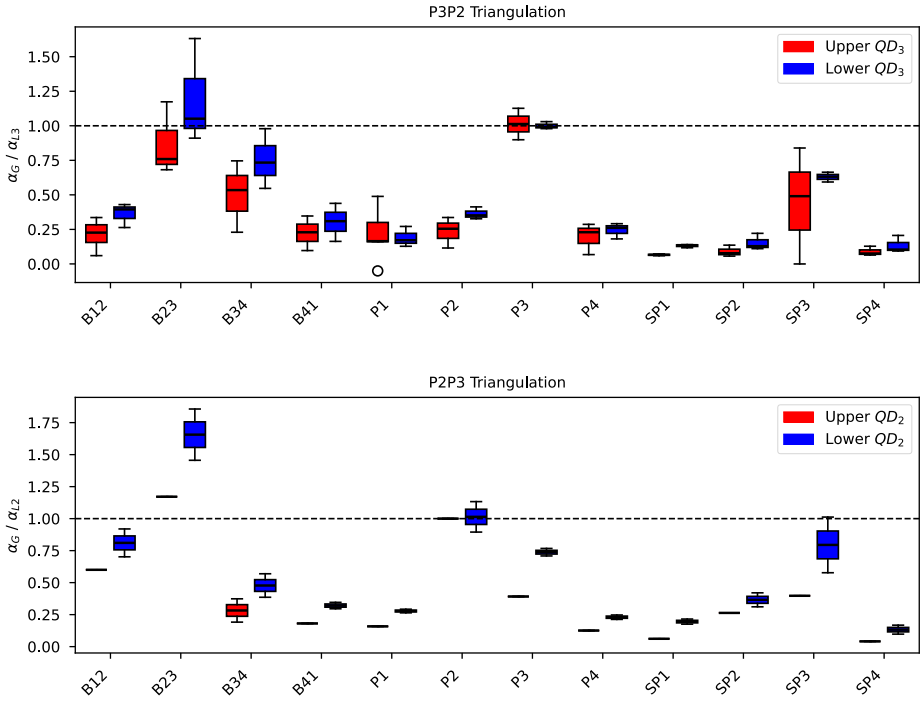

Figure 8.32: Boxplots indicating the spread in the relative lever arm across the various transitions.

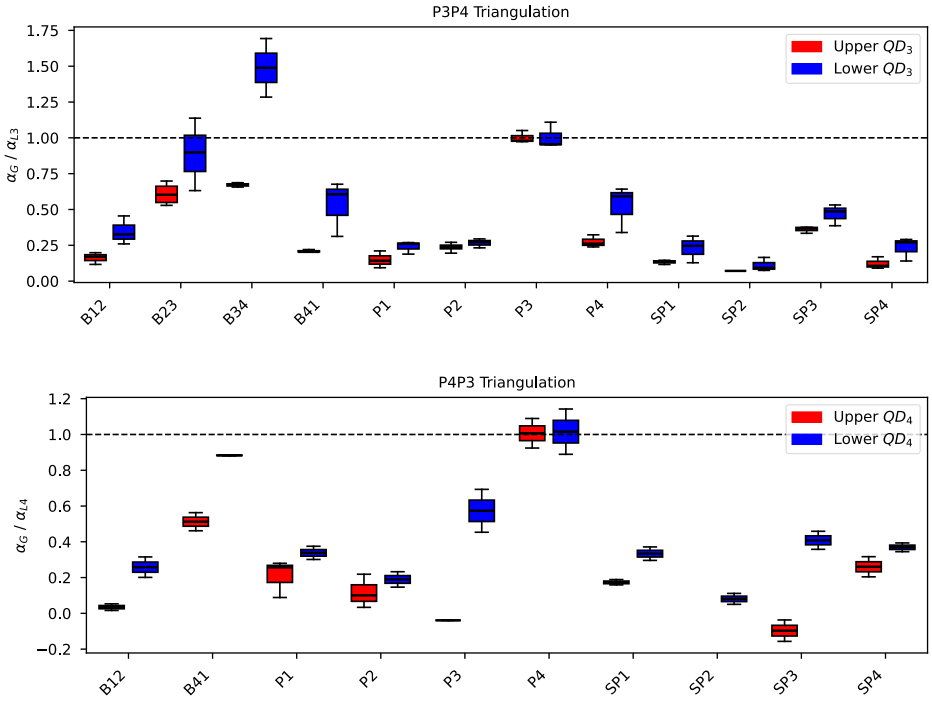

Figure 8.33: Boxplots indicating the spread in the relative lever arm across the various transitions.

8.9. CAPACITANCE MODELLING

The charge stability diagrams observed in experiments and presented can be reproduced using a capacitance simulation. We employ Qarray, an open source package[20], to simulate charge stability diagrams through the constant capacitance model. Normally, for a simple simulation such as of a double quantum dot, we require two plunger gates under which the two quantum dots are formed. The number of plunger gates is equal to the number of quantum dots. However, in a device with a bilayer heterostructure, we can now have that two quantum dots couple primarily to the same plunger, i.e. a vertical double quantum dot, while no quantum dot(s) are formed underneath the other plunger gate(s). Nevertheless, for the simulations we will still consider all four plunger gates. Firstly, because of the virtualization used in experiments, which we include in the simulation as well. Second, because we also use the unaccumulated plunger gates in simulation as levers, as alluded to in the main manuscript, to detune the chemical potential of the lower layer with respect to the upper. That is, to move the loading lines of the lower dots relative to the loading lines of the upper dots in the simulated charge stability diagram.

The Qarray simulations require capacitance matrices C_{dd} and C_{gd} as input, which we determine by manually fitting the charge stability diagram. Here, we show these capacitance matrices for the fit in Fig.8.2, in which two quantum dots are formed in the

upper and lower quantum well, underneath plunger gate 2 and 3 each. The capacitive couplings between the four dots are contained within the capacitance matrix C_{dd}:

$$C_{dd} = \begin{bmatrix} 0 & 0.00267 & 0.016 & 0.00133 \\ 0.00267 & 0 & 0.00133 & 0.016 \\ 0.016 & 0.00133 & 0 & 0.008 \\ 0.00133 & 0.016 & 0.008 & 0 \end{bmatrix} \begin{matrix} 2u \\ 3u \\ 2\ell \\ 3\ell \end{matrix} \tag{8.2}$$

The inputs to this matrix mainly determine the length of the interdot transitions between different quantum dots.

C_{gd} is used to represent the capacitive couplings of the four plungers to the four quantum dots underneath P_2 and P_3:

$$C_{gd} = \begin{matrix} \\ \\ \\ \\ \end{matrix} \begin{matrix} P_1 \\ \\ \\ \\ \end{matrix} \begin{matrix} P_2 \\ \\ \\ \\ \end{matrix} \begin{matrix} P_3 \\ \\ \\ \\ \end{matrix} \begin{matrix} P_4 \\ \\ \\ \\ \end{matrix} \begin{bmatrix} 0.00267 & 0.03466 & 0.00267 & 0.0 \\ 0.0 & 0.00267 & 0.03466 & 0.00267 \\ 0.00533 & 0.01067 & 0.00533 & 0.0 \\ 0.0 & 0.00533 & 0.01067 & 0.00533 \end{bmatrix} \begin{matrix} 2u \\ 3u \\ 2\ell \\ 3\ell \end{matrix} \tag{8.3}$$

It primarily determines the slope and spacing between transition lines in the charge stability diagram.

The simulations using the manually fitted capacitance matrices are qualitatively in agreement with the experimentally measured charge stability diagrams. Although these capacitance matrices differ for each simulation, we observe some trends between them. One is that the largest scale in C_{dd} seems to be capacitive coupling between quantum dots on top of each other followed by coupling between quantum dots in the lower layer. First, this indicates that quantum dots in different quantum wells are formed at a similar positions, below the plunger gates. Moreover, it also means that quantum dots in the lower quantum well feel each other more strongly than if they were in the upper quantum well. This conforms to our expectation, as we have seen from previous work that the wavefunctions of holes in the lower quantum dots are less localised[17]. Furthermore, we note from the fitted C_{gd} that the coupling of the plunger to the upper quantum dot is larger than the lower one, which is again in agreement with previous work [17]. The argument for this observation is that in the perspective of the lower quantum dot, the upper quantum dot partially screens the electric field generated by the plunger gate. This leads to a reduced lever arm of the lower quantum dot. This implies again that the wavefunction is more spread out in contrast to the upper quantum dots which are more localized under their respective plunger gate. Nevertheless, the coupling of the lower dot seems to be largest under its respective plunger gate indicating that this lower dot is formed underneath the plunger and not in between plungers gates. We note that because of the blurring/broadening of transition lines and latching, there is a (small) error margin in the fitted capacitance matrices. However, the error in the capacitances does not significantly change its value, or rather, more importantly, does not change the order between the different capacitances.

Differences between measured and simulated charge stability diagrams can also be attributed to the inherent limitations of the constant capacitance model. This includes the assumption that the capacitances do not vary as a function of gate voltage, while we

do see in e.g. Fig.8.2 that the charging energy decreases at higher occupation. In addition, it does not capture quantum mechanical effects such as tunneling which is known to bend transition lines [28]. This can also lead to differences between the experimentally measured and simulated charge stability diagram, especially if the lower quantum dots are strongly tunnel coupled to each other.

BIBLIOGRAPHY

[1] R. P. Feynman. “Simulating physics with computers”. In: *International Journal of Theoretical Physics* 21 (6-7 June 1982), pp. 467–488. ISSN: 0020-7748.

[2] B. Fauseweh. “Quantum many-body simulations on digital quantum computers: State-of-the-art and future challenges”. In: *Nature Communications* 15.1 (2024), p. 2123.

[3] H.-J. Shao, Y.-X. Wang, D.-Z. Zhu, Y.-S. Zhu, H.-N. Sun, S.-Y. Chen, C. Zhang, Z.-J. Fan, Y. Deng, X.-C. Yao, et al. “Antiferromagnetic phase transition in a 3D fermionic Hubbard model”. In: *Nature* 632.8024 (2024), pp. 267–272.

[4] R. Raussendorf and J. Harrington. “Fault-tolerant quantum computation with high threshold in two dimensions”. In: *Physical review letters* 98.19 (2007), p. 190504.

[5] A. G. Fowler, M. Mariantoni, J. M. Martinis, and A. N. Cleland. “Surface codes: Towards practical large-scale quantum computation”. In: *Physical Review A—Atomic, Molecular, and Optical Physics* 86.3 (2012), p. 032324.

[6] B. M. Terhal. *Quantum error correction for quantum memories*. 2015.

[7] J. I. Cirac and P. Zoller. “Quantum computations with cold trapped ions”. In: *Physical review letters* 74.20 (1995), p. 4091.

[8] A. Ashkin. “Optical trapping and manipulation of neutral particles using lasers”. In: *Proceedings of the National Academy of Sciences* 94 (10 May 1997), pp. 4853–4860. ISSN: 0027-8424.

[9] D. Barredo, V. Lienhard, S. de Léséleuc, T. Lahaye, and A. Browaeys. “Synthetic three-dimensional atomic structures assembled atom by atom”. In: *Nature* 561 (7721 Sept. 2018), pp. 79–82. ISSN: 0028-0836.

[10] N. W. Hendrickx, W. I. L. Lawrie, M. Russ, F. van Riggelen, S. L. de Snoo, R. N. Schouten, A. Sammak, G. Scappucci, and M. Veldhorst. “A four-qubit germanium quantum processor”. In: *Nature* 591 (7851 Mar. 2021), pp. 580–585. ISSN: 0028-0836.

[11] C.-A. Wang, V. John, H. Tidjani, C. X. Yu, A. S. Ivlev, C. Déprez, F. van Riggelen-Doelman, B. D. Woods, N. W. Hendrickx, W. I. L. Lawrie, L. E. A. Stehouwer, S. D. Oosterhout, A. Sammak, M. Friesen, G. Scappucci, S. L. de Snoo, M. Rimbach-Russ, F. Borsoi, and M. Veldhorst. “Operating semiconductor quantum processors with hopping spins”. In: *Science* 385 (6707 July 2024), pp. 447–452. ISSN: 0036-8075.

[12] V. John, C. X. Yu, B. van Straaten, E. A. Rodríguez-Mena, M. Rodríguez, S. Oosterhout, L. E. A. Stehouwer, G. Scappucci, S. Bosco, M. Rimbach-Russ, Y.-M. Niquet, F. Borsoi, and M. Veldhorst. “A two-dimensional 10-qubit array in germanium with robust and localised qubit control”. In: *arXiv preprint, arXiv:2412.16044* (Dec. 2024).

[13] F. K. Unseld, B. Undseth, E. Raymenants, Y. Matsumoto, S. Karwal, O. Pietx-Casas, A. S. Ivlev, M. Meyer, A. Sammak, M. Veldhorst, et al. “Baseband control of single-electron silicon spin qubits in two dimensions”. In: *arXiv preprint arXiv:2412.05171* (2024).

[14] J. Taylor, H.-A. Engel, W. Dür, A. Yacoby, C. Marcus, P. Zoller, and M. Lukin. “Fault-tolerant architecture for quantum computation using electrically controlled semiconductor spins”. In: *Nature Physics* 1.3 (2005), pp. 177–183.

[15] M. Trif, V. N. Golovach, and D. Loss. “Spin dynamics in InAs nanowire quantum dots coupled to a transmission line”. In: *Physical Review B—Condensed Matter and Materials Physics* 77.4 (2008), p. 045434.

[16] A. Tosato, B. Ferrari, A. Sammak, A. R. Hamilton, M. Veldhorst, M. Virgilio, and G. Scappucci. “A High-Mobility Hole Bilayer in a Germanium Double Quantum Well”. In: *Advanced Quantum Technologies* 5 (5 May 2022), p. 2100167. ISSN: 2511-9044.

[17] H. Tidjani, A. Tosato, A. Ivlev, S. O. Corentin Déprez, L. Stehouwer, A. S. G. Scappucci, and M. Veldhorst. “Vertical gate-defined double quantum dot in a strained germanium double quantum well”. In: *Physical Review Applied* (Nov. 2023). ISSN: 054035.

[18] A. Ivlev, H. Tidjani, S. D. Oosterhout, L. Stehouwer, A. Sammak, G. Scappucci, and M. Veldhorst. “Coupled vertical double quantum dots at single-hole occupancy”. In: *Applied Physical Letters* (July 2024).

[19] A. Sammak, D. Sabbagh, N. W. Hendrickx, M. Lodari, B. P. Wuetz, A. Tosato, L. Yeoh, M. Bollani, M. Virgilio, M. A. Schubert, P. Zaumseil, G. Capellini, M. Veldhorst, and G. Scappucci. “Shallow and Undoped Germanium Quantum Wells: A Playground for Spin and Hybrid Quantum Technology”. In: *Advanced Functional Materials* 29 (14 Apr. 2019), p. 1807613. ISSN: 1616-301X.

[20] B. van Straaten, J. Hickie, L. Schorling, J. Schuff, F. Fedele, and N. Ares. “QArray: A GPU-accelerated constant capacitance model simulator for large quantum dot arrays”. In: *SciPost Physics Codebases* (Oct. 2024), p. 35. ISSN: 2949-804X.

[21] W. G. van der Wiel, S. De Franceschi, J. M. Elzerman, T. Fujisawa, S. Tarucha, and L. P. Kouwenhoven. “Electron transport through double quantum dots”. In: *Rev. Mod. Phys.* 75 (1 Dec. 2002), pp. 1–22.

[22] C. H. Yang, A. Rossi, N. S. Lai, R. Leon, W. H. Lim, and A. S. Dzurak. “Charge state hysteresis in semiconductor quantum dots”. In: *Applied Physics Letters* 105 (18 Nov. 2014). ISSN: 0003-6951.

[23] W. H. Lim, T. Tanttu, T. Youn, J. Y. Huang, S. Serrano, A. Dickie, S. Yianni, F. E. Hudson, C. C. Escott, C. H. Yang, et al. “A 2x2 quantum dot array in silicon with fully tuneable pairwise interdot coupling”. In: *arXiv preprint arXiv:2411.13882* (2024).

[24] F. van Riggelen-Doelman, C.-A. Wang, S. L. de Snoo, W. I. L. Lawrie, N. W. Hendrickx, M. Rimbach-Russ, A. Sammak, G. Scappucci, C. Déprez, and M. Veldhorst. *Coherent spin qubit shuttling through germanium quantum dots*. 2023. arXiv: 2308.02406 [cond-mat.mes-hall].

[25] P. C. Fariña, D. Jirovec, X. Zhang, E. Morozova, S. D. Oosterhout, S. Reale, T.-K. Hsiao, G. Scappucci, M. Veldhorst, and L. M. Vandersypen. "Site-resolved magnon and triplon dynamics on a programmable quantum dot spin ladder". In: *arXiv preprint arXiv:2506.08663* (2025).

[26] M. Lodari, A. Tosato, D. Sabbagh, M. A. Schubert, G. Capellini, A. Sammak, M. Veldhorst, and G. Scappucci. "Light effective hole mass in undoped Ge/SiGe quantum wells". In: *Physical Review B* 100 (4 July 2019). ISSN: 24699969.

[27] G. Scappucci, C. Kloeffel, F. A. Zwanenburg, D. Loss, M. Myronov, J. J. Zhang, S. De Franceschi, G. Katsaros, and M. Veldhorst. "The germanium quantum information route". In: *Nature Reviews Materials* 6.10 (Dec. 2020), pp. 926–943. ISSN: 20588437.

[28] R. Hanson, L. P. Kouwenhoven, J. R. Petta, S. Tarucha, and L. M. K. Vandersypen. "Spins in few-electron quantum dots". In: *Rev. Mod. Phys.* 79.December (2007), pp. 1217–1265.

9

Conclusions and Outlook

It always seems impossible until it's done

Nelson Mandela

CONCLUSIONS AND OUTLOOK

Through the work in this thesis I have gained experience in many elements of quantum computing engineering from the context of spin qubits in Ge/SiGe and Si/SiGe. Alongside SiMOS, these are considered the three frontrunners currently being pushed by academia and industry as our best contenders for spin qubit quantum computers. I give my thoughts on the prospects and challenges the field needs to overcome in order to realise a gate defined spin qubit quantum computer. For the field to keep up with other platforms, it is important to ask why spin qubits, and what do we need to overcome in order to scale them.

Spin qubits remain highly tunable but each qubit has its own personality: qubit to qubit variability, device-to-device variability, voltage bounds for dot charge states remain large and nonlinear virtual-gate responses create overheads before operation even begins. For Si/SiGe electrons, consistently large valley splittings and control over valley phases are essential. Holes avoid valley physics and benefit from a small effective mass, but need to decrease SPAM errors from the spin orbit interaction. Across modalities, fast and reliable initialization/readout and operation inside dense arrays are central bottlenecks.

The three main topics covered in this thesis give insight in:

Quantum simulation: In Chapter 4, we tune the exchange couplings in a 2×2 array in order to achieve a coherent four spin state, simulating the resonating valence bond. The calibrations are very technically involved and take a long time to set up. Testing whether this bond is a mechanism for high temperature superconductivity as predicted by Anderson[1] would require a similar experiment in a much larger array.

Baseband control: In Chapter 5 we show that spin qubits can be operated with high fidelity, at low magnetic field, and with very fast gate times, fully controlled by baseband pulses. Baseband pulses relax hardware requirements and increase the feasibility of scaling spin qubits. Engineering the g-tensor misalignment would provide a path to having deterministic gate times.

Bilayer devices: Chapters 6, 7 and 8 demonstrate that spin qubits can be scaled beyond the xy plane. They can host coherent spin physics, and provide a platform for efficiently wired hopping based qubits. To fully exploit bilayers there needs to be progress in gate designs which can enable fully orthogonal control of the quantum dots. Through just the addition of another quantum well, there are many possibilities for rich physical experiments to be conducted in bilayers. The platform is in its infancy, and there are many routes for development and potential gains.

9.1. FUTURE DIRECTIONS FOR BILAYER DEVICES

ENHANCING CONTROL

Whilst virtual gates can be utilised to control all quantum dots in a bilayer, it would be ideal to have one plunger gate per qubit. Such a proposal for an improved gate design to enable fully orthogonal control of bilayers would be in introducing plunger gate design

with an additional, plunger gate ring around it, such as in Figure9.1, in combination with virtualisation techniques demonstrated in this thesis to decouple the upper and lower quantum dots.

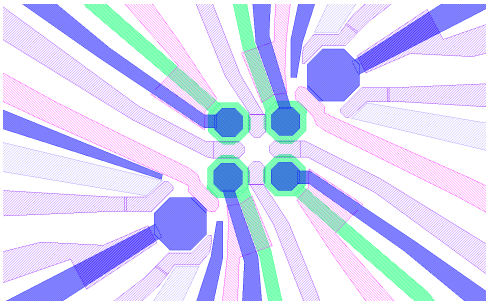

Figure 9.1: **A double plunger gate design, where the green ring controls the lower quantum dot, and the upper quantum dot is controlled by the blue plunger gate.** This design exploits the difference in wavefunction size of the upper and lower quantum dots, whilst maintaining the number of surrounding gates in a single well device.

ENGINEERING THE STRAIN

The strain of the heterostructure is defined by the lattice mismatch between the quantum well material and the surrounding materials. By tuning the concentration of Si in the quantum well, the strain of the quantum wells can be independently tuned[2]. This provides a route to consistently engineering the strain in the quantum well. As the uniformity of the upper gate layouts through the adoption of industrial fabrication, quantum well strain could become the dominant factor when comparing the g-tensor anisotropy between quantum dots[3, 4]. This paves the way towards predictable gate timings for hopping qubits when applied to vertical double quantum dots.

Another important consideration is the material development in germanium heterostructures. As silicon is much more abundant than germanium, most heterostructures are grown on silicon wafers, with reverse graded germanium grown by CVD on top. This process creates a lot of dislocations within the heterostructure forming a cross hatch pattern. This cross hatch pattern appears to significantly effect the strain properties. It appears to be the natural progression to move towards germanium wafers as they have higher mobility and less disorder, however they will also result in different g-tensor properties[5, 6].

ENGINEERING THE TUNNEL COUPLING

The confinement and separation of the quantum wells determines how tunnel coupled they are. Quantum wells that are too close will result in highly tunnel-coupled to possibly even merging quantum dots. However, a too large separation will lower the tunnel coupling to strengths that prevent coherent experiments.

After a first calibration by tuning the growth, fine-tuning of the coupling between vertical quantum dots may be established through electrostatic gate control. For example, by tuning the relative in-plane displacement of one quantum dot compared to the

other, the tunnel coupling between the two quantum dots may be effectively controlled.

APPLICATIONS FOR BILAYERS

Given that the mechanism for virtually controlling the upper and lower quantum dots is quite well understood and can be harnessed to virtualise a $2 \times n \times m$ array of quantum dots, the future possibilities for bilayers can be explored, beyond the context of higher connectivity and lower overheads on error correction.

One could also consider using the separate layers for separate applications, For instance, one quantum well could be used for transferring information, while the other one could be used for gate operations. Furthermore, one could imagine using one layer for sensing and the other layer for qubits. Additionally, the lower layer could be used to induce two qubit interactions when brought in close proximity, which may be a useful tool in sparse arrays where quantum dots may not have their own individual barrier gates.

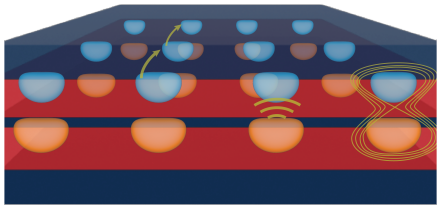

Figure 9.2: Future visions for extended bilayer systems from[7].

OUTLOOK FOR THE FIELD

Despite the field maturing, there are still new qubit encodings being proposed, from microwave driven single spins, exchange only qubits, to hopping qubits, with debate on whether holes or electrons are better vehicles for qubits. In the near term, developments are underway to fully automate the tuning process of spin qubits, from a grounded device to a qubit without human intervention[8]. The overhead to get to this stage is rather high. Automation could be eased by high quality materials, with predictable voltage uniformity across the devices[9]. Materials and devices are being advanced from industry in both the fabrication and material development, and this should accelarate progress. Controlling large scale gate defined quantum dot systems which are stored within dilution fridges will require cryo-CMOS integration, which is underway[10, 11, 12]. There may be no perfect qubit platform; ultimately, it is an engineering challenge.

BIBLIOGRAPHY

[1] P. W. Anderson. "The Resonating Valence Bond State in La_2CuO_4 and Superconductivity". In: *Science* 235 (1987), pp. 1196–1198.

[2] J. P. Dismukes, L. Ekstrom, and R. J. Paff. "Lattice Parameter and Density in Germanium-Silicon Alloys". In: *The Journal of Physical Chemistry* 68 (10 Oct. 1964), pp. 3021–3027. ISSN: 0022-3654.

[3] A. Sarkar, P. Chowdhury, X. Hu, A. Saraiva, A. S. Dzurak, A. R. Hamilton, R. Rahman, and D. Culcer. "Effect of disorder and strain on the operation of planar Ge hole spin qubits". In: (Apr. 2025).

[4] A. Sarkar, Z. Wang, M. Rendell, N. W. Hendrickx, M. Veldhorst, G. Scappucci, M. Khalifa, J. Salfi, A. Saraiva, A. S. Dzurak, A. R. Hamilton, and D. Culcer. "Electrical operation of planar Ge hole spin qubits in an in-plane magnetic field". In: *Physical Review B* 108 (24 Dec. 2023), p. 245301. ISSN: 2469-9950.

[5] L. E. A. Stehouwer, A. Tosato, D. Degli Esposti, D. Costa, M. Veldhorst, A. Sammak, and G. Scappucci. "Germanium wafers for strained quantum wells with low disorder". In: *Applied Physics Letters* 123.9 (2023), p. 092101.

[6] L. E. A. Stehouwer, C. X. Yu, B. van Straaten, A. Tosato, V. John, D. D. Esposti, A. Elsayed, D. Costa, S. D. Oosterhout, N. W. Hendrickx, M. Veldhorst, F. Borsoi, and G. Scappucci. "Exploiting strained epitaxial germanium for scaling low-noise spin qubits at the micrometre scale". In: *Nature Materials* (July 2025). ISSN: 1476-1122.

[7] H. Tidjani, A. Tosato, A. Ivlev, C. Déprez, S. Oosterhout, L. Stehouwer, A. Sammak, G. Scappucci, and M. Veldhorst. "Vertical gate-defined double quantum dot in a strained germanium double quantum well". In: *Phys. Rev. Appl.* 20 (5 Nov. 2023), p. 054035.

[8] C. Carlsson, J. Saez-Mollejo, F. Fedele, S. Calcaterra, D. Chrastina, G. Isella, G. Katsaros, and N. Ares. "Automated All-RF Tuning for Spin Qubit Readout and Control". In: (June 2025). arXiv: ¯arXiv:2506.10834 [cond-mat].

[9] S. Neyens, O. K. Zietz, T. F. Watson, F. Luthi, A. Nethwewala, H. C. George, E. Henry, M. Islam, A. J. Wagner, F. Borjans, E. J. Connors, J. Corrigan, M. J. Curry, D. Keith, R. Kotlyar, L. F. Lampert, M. T. Mądzik, K. Millard, F. A. Mohiyaddin, S. Pellerano, R. Pillarisetty, M. Ramsey, R. Savytskyy, S. Schaal, G. Zheng, J. Ziegler, N. C. Bishop, S. Bojarski, J. Roberts, and J. S. Clarke. "Probing single electrons across 300-mm spin qubit wafers". In: *Nature* 629 (8010 May 2024), pp. 80–85. ISSN: 0028-0836.

[10] S. Subramanian, T. M. Mladenov, S. Schaal, B. Patra, L. Lampert, N. K. Robinson, J. Roberts, and S. Pellerano. "A Scalable mK Cryo-CMOS Demultiplexer Chip for Voltage Biasing and High-Speed Control of Silicon Qubit Gates". In: *2024 IEEE Symposium on VLSI Technology and Circuits (VLSI Technology and Circuits)*. IEEE, June 2024, pp. 1–2. ISBN: 979-8-3503-6146-9.

[11] X. Xue, B. Patra, J. P. G. van Dijk, N. Samkharadze, S. Subramanian, A. Corna, B. P. Wuetz, C. Jeon, F. Sheikh, E. Juarez-Hernandez, B. P. Esparza, H. Rampurawala, B. Carlton, S. Ravikumar, C. Nieva, S. Kim, H.-J. Lee, A. Sammak, G. Scappucci, M. Veldhorst, F. Sebastiano, M. Babaie, S. Pellerano, E. Charbon, and L. M. K. Vandersypen. "CMOS-based cryogenic control of silicon quantum circuits". In: *Nature* 593 (7858 May 2021), pp. 205–210. ISSN: 0028-0836.

[12] S. K. Bartee, W. Gilbert, K. Zuo, K. Das, T. Tanttu, C. H. Yang, N. D. Stuyck, S. J. Pauka, R. Y. Su, W. H. Lim, S. Serrano, C. C. Escott, F. E. Hudson, K. M. Itoh, A. Laucht, A. S. Dzurak, and D. J. Reilly. "Spin-qubit control with a milli-kelvin CMOS chip". In: *Nature* 643 (8071 July 2025), pp. 382–387. ISSN: 0028-0836.

SUMMARY

Gate defined germanium spin qubits appear to demonstrate many attractive properties for building block of a future quantum computer. In this thesis we explore beyond the necessities, demonstrating three key results. In chapter4, a resonating valence bond is realised on a 2×2 qubit array, utilising precise control over the exchange interaction. The rich intrinsic physics provided by the spin orbit coupling gives many possibilities for controlling Ge spin qubits. While it can enable all electrical control using microwaves, we demonstrate that fast, high fidelity, and long coherence all electrical control can even be achieved with baseband pulses. Through the development of hopping based spin qubits, we exploit the g-tensor misalignment between quantum dots in order to produce quantum gates by diabatically and coherently shuttling spins between quantum dots. In chapter5 we show that the g-tensor anisotropy can be exploited for low power, baseband qubit control, with fast gate times and high fidelity. We obtain high single qubit gate fidelities, and measure two-qubit gate fidelities of $F_{CZ} = 99.3\%$ using IRB, and $F_{CZ} = 98.1\%$ using GST. It is certainly a step in the right direction; we don't require strong magnetic fields, or microwave pulses, however this approach does depend on precise timing control, and more work is needed to determine how gates in a scaled computer would be timed.

In chapters 6, 7, 8, the toolbox of spin qubits is expanded once more and we show that spin qubits need not be confined to planar architectures, but can be scaled in the out of plane direction. Further to this, they support coherent spin physics. We establish methods to tune multi-well systems and realise a three-dimensional dot array. Bilayers promise higher connectivity and future research may indicate whether they can enable hopping-based qubits where the quantization axis can be consistently controlled by engineering the strain of the quantum wells. The extra tuning complexity introduced by additional layers may offset these gains; whether it would stand to benefit the community to adopt multilayer heterostructures remains an open question. When considering wiring bottlenecks this may reveal an efficient approach to circumventing the problem, and to achieve connectivities which can efficiently simulate natural systems it may be necessary to have three-dimensional quantum dot arrays.

SAMENVATTING

Poort-gedefinieerde germanium-spinqubits vertonen vele aantrekkelijke eigenschappen als bouwstenen voor een toekomstige kwantumcomputer. In dit proefschrift gaan we verder dan de noodzakelijke vereisten en presenteren we drie kernresultaten. In hoofdstuk 4 wordt een resonating resonerende valentieband gerealiseerd op een 2×2 kwantumbit raster, gebruikmakend van nauwkeurige controle over de uitwisselingsinteractie. De rijke intrinsieke fysica die voortkomt uit spin-baankoppeling biedt vele mogelijkheden voor de aansturing van germanium-spin kwantumbits. Hoewel dit volledige-elektrische controle met microgolven mogelijk maakt, laten wij zien dat snelle, hoog-fideliteit en lange-coherentie alle-elektrische controle zelfs met baseband-pulsen kan worden bereikt. Door de ontwikkeling van op hoppende gebaseerde spinqubits benutten we de g-tensor-misuitlijning tussen quantum dots om kwantumpoorten te realiseren via diabatisch en coherent verplaatsen van spins tussen kwantum stippen. In hoofdstuk 5 tonen we aan dat de g-tensor-anisotropie kan worden benut voor laag-vermogen baseband qubitcontrole, met snelle poorttijden en hoge fideliteit. We behalen hoge enkel-qubit-poortfideliteiten en meten twee-qubit-poortfideliteiten van $F_{CZ} = 99{,}3\%$ met IRB en $F_{CZ} = 98{,}1\%$ met GST. Dit is duidelijk een stap in de veelbelovende richting: sterke magnetische velden of microgolfpulsen zijn niet nodig; deze aanpak is echter wel afhankelijk van zeer nauwkeurige timing, en er is meer werk nodig om te bepalen hoe poorten in een opgeschaalde computer getimed zouden worden. In de hoofdstukken 6, 7 en 8 wordt de gereedschapskist van spinqubits verder uitgebreid en laten we zien dat spinqubits niet beperkt hoeven te blijven tot planaire architecturen, maar ook buiten het vlak kunnen worden opgeschaald. Bovendien ondersteunen zij coherente spinfysica. We ontwikkelen methoden om multi-put-systemen af te stemmen en realiseren een driedimensionale stip raster. Bilagen beloven een hogere connectiviteit, en toekomstig onderzoek kan uitwijzen of zij hop-gebaseerde qubits mogelijk maken waarbij de kwantisatie-as consistent kan worden gecontroleerd door het spanningsprofiel van de kwantum putten te ontwerpen. De extra afstemmingscomplexiteit die door aanvullende lagen wordt geïntroduceerd kan deze voordelen echter tenietdoen; of het voor de gemeenschap gunstig is om multilaag-heterostructuren te adopteren blijft daarmee nog een open vraag. Met het oog op bedradingsknelpunten kan dit een efficiënte aanpak blijken om het probleem te omzeilen, en om connectiviteiten te bereiken die natuurlijke systemen efficiënt kunnen simuleren kunnen driedimensionale quantum-dotarrays noodzakelijk zijn.

ACKNOWLEDGMENTS

Condensing the experiences over five years of PhD and life is no easy task and there are so many people who I am grateful for in making my time here in Delft as fruitful as it has been. First of all, thanks to my supervisor **Menno**, you have been a thoughtful and inspiring supervisor. I have learned a lot under your supervision and grown as a person. Thanks for taking a chance on me, and always bringing a new perspective in our scientific discussions. **Giordano**, my (co)promotor you have always been around for a chat about physics and about life, your vibrant presence is appreciated. Your enthusiasm on the bilayers project always gave me encouragement to keep on going. The materials your group provides are the backbone of all we do. **Lieven**, you help make a friendly and collaborative environment within the spin qubit groups.

To my paranymphs (bodyguards) and friends, **Pablo** and **Irene**. **Pablo** (*pabby*) we started in the same week, and we end it in the same week. We have so many wonderful memories to look back on, music, biking, accidents and hospitals. We figured our way through the PhD and a good portion of life together. This journey would have been a completely different one without your friendship. **Irene**, my sister, my muse. When you joined you were a breath of fresh air and a role model for me. We have had so many adventures together, (*KYOTOO, "sit down, stay home"*), and most importantly been enriching to each others spirits. I'll always be dancing in the front row. Thank you for your continued support, encouragement and belief in the things I pursue.

The PhD became so much more than research and the corridors of building 22 became a place of familiarity and joy, thanks to the wonderful friends I made here and colleagues I worked with. I am indebted to you for helping me keep my sanity. **Daniel**, you have a heart of gold and a mind of steel. We will keep ski week alive- my promise is on this paper. You made work not so much like work. Thanks for always being there for a chat when I had a singlet-triplet emergency, or a life one. **Uri**, the first time I met you was when you were pulled off the streets by Pablo and brought to one of the first of my parties in my $33m^2$ DUWO apartment. Am I glad he did! You risked getting covid for me when I needed someone to talk to. Good luck on being a dog dad, Atlas is one lucky pupper <3. **Davide**, you are a pillar of stability in an ever changing world, and always watching out for people. Your efforts are appreciated. Help me move one last time?

Karina, you elevate every room you walk into and bring colour to an otherwise beige world, especially to mine. Keep on adding a sprinkle of fairy dust wherever you go. **Maia**, you were my bachelors student when I was still new. We both know it wasn't optimal, but we learned a lot from each other and have had a beautiful friendship since. I'm proud of how far you have come in the time I have known you, and you came even further before that. Good luck with your PhD, you deserve all the success in the world. When are you giving me a bachelors student grandchild? **Ralf**, lets keep on dancing our way through lifes troubles, thanks for all the brunches and joy.

Corny, you are a great friend, and brought a lot of joy in the mid PhD stage. Thanks

for always listening to my rants and being down to make some delicious food. It was fun exploring Australia with you. I hope you get all the success you are working for. **Kenji,** you brighten up any room you walk into, and I will always be down for a game of chess. **Barnaby** always good to have another brit around. Your simulator helped make sense of the bilayer CSDs, so thanks for preventing my impending madness (at least for a while). **Brennan**, thank you for enchanting us with piano at the end of a party, i'm glad we had each other to use obscure vocabulary with. All the ravers who took joy in celebrating life, **Vicky**, **Irene**, **Corny**, **Kenji**, **Tobi**, **Anton**, **Hjalmar**, **Riccardo**, **James** and those who joined along the way. You were a proper solid gang. **Leonhard**, always good to have a tea with you, hopefully next time in your hand crafted pots. **Matteo**, thanks for the food, dancing, music, and general shenanigans. **Django,** the last few months of a PhD get exponentially more difficult, thank you for supporting me.

When I joined QuTech there were two women in the spin qubit groups. I'm glad that isn't the case anymore, and i'm proud we were able to form the coven. Thanks **Karina, Irene, Michelé, Zarije, Liza, Tess, Maia, Alice, Sugeiva, Eline and Vicky** for the magic that feminine energy brings, and the warmth of the space we built together. **Eline,** I will always cherish the feeling of everyone seeing that we have returned from a lunch-time run. It was fun having you here, best of luck with your family and career. **Bea**, thanks for sharing your love of sailing with me, it is now a love of mine. **Nick**, when we were two new people in Delft, we had each other to chill by the canal with in the evenings. Glad we have made it through to the other end. **Bertie**, thanks for all the friendship and fun, you are a window into a different world. We will always be co-athors for life. **Stephan**, thanks for teaching me the fundamentals of spin qubits and about stoofvlees, it is still a favourite. Good luck to both of you with your start-up. **Lukas**, thanks for entrusting pimpim to me and Alberto, she's in good hands and adventures in Kralingse Bos now. **Florian**, thanks for showing me the ropes of the dipstick setup back when it looked like a steampunk monster. **Asser**, your presence has a way of lightening any situation, keep on bringing joy and banter. **Dario**, very few know the complexity of understanding a bilayer system, so well done for joining the project and getting great results since. Good luck for the rest of your PhD. **Michael**, thanks for your contributions to the experiments. Good luck wrapping up your PhD. **Sergey, Stefan** and **Chien-an** thanks for teaching me how to fab. **Chien-an**, you took the PMMA incident like a champ. It was a pleasure to work with you over the years. You have a quiet wisdom and perseverance, and I'm glad your hard work was recognized. **Jann**, I wish you could have stayed longer in Delft, you were a pleasure to work with, bringing positivity and Friday music. Thanks for bringing your enthusiasm to the project.

Thanks to the previous group members who I didn't overlap much with, but built strong foundations upon which so much research was carried out, **Nico, Will, Gertjan, Luca**. **Luca**, thanks for the warm welcome to the group. **Corentin, Cécile** and **Francesco**, I really appreciated your presence in the group, you really helped to bring us together. **Valentin**, your cooking is outstanding, thanks for sharing it. Combined with the high standard and everyone's contributions there was definitely a golden age of Mennoknight group dinners. **Sasha**, you are a brilliant scientist and also a wonderful colleague. Working with you is always a pleasure and I wish you all the success in your career. The château sauna mission in France still makes me smile. **Floor**, you

could always be counted on to speak up- ensuring our Uitjes were not forgotten. For all the young Mennoknights, you are already doing great, and good luck with the rest of your PhDs/Post-docs, **Zarije**, **Pietro**, **Damien**, **Michael**, **Harold**, **Naoual**, **Alice**, **Sasha**, **Michael**, **Marion**, **Setareh** and **Barnaby**.

It is great to see the spin qubit groups have grown so strong and recruited so many people, however it comes with the regret that I cannot acknowledge everyone by name. Thanks to everyone in the **Vandersypen, Bosco, Scappucci, Rimbach-russ and Chaterjee** groups who make the environment collaborative, fun and ambitious.

Thanks to all the people who called F214 their office, **Desa, Anne-marije, Floor, Brian, Maia, Zarije, Barnaby and Lucas.** We made it a great place to work in. Thanks to the T2*s, (formally Q2) who liven up most QuTech events. It was fun playing with you, **Luc, Sander, Bart, Laurens, Julia, Pablo, Maia, Desa, Timo** and especially **Gustavo** for unofficially leading. Although we will never know the charm of Egmond, it was great organising the first Uitje after covid with you **Julia, Alvaro, Luc, Nick, Christian, Pablo** and throwing a great party here in Delft.

Thanks to the engineers, secretaries and board who keep QuTech moving so smoothly. **Jason** your patience with the bonder is appreciated. **Olaf**, thanks for doing dialysis on the fridge in a moment of crisis! **Sander** the software and assistance you provide makes the spin qubit group a unique place to do research in and are a key reason we are able to do advanced experiments.

Thanks to everyone at Intel who made my internship there educational and fun, especially **Elliot** for your mentorship. It was nice to bat for the other team for a while. Trappers, you made the time there extra special.

I am very grateful to my committee for taking the time to read my thesis and seeing me through this final stage, **Andrea**, **Lieven**, **Menno**, **Floris**, **Giordano** and **Stefano**.

Within the safe confines of Delft I have explored and expanded thanks to all the wonderful people who I have met along the way. So although you are not sentient, I would like to thank the little city of Delft. Finally, I am deeply grateful to all of the teachers, family, and friends whose guidance, support, and encouragement have shaped the path that led me to obtaining my PhD.

CURRICULUM VITÆ

Hanifa TIDJANI

July 30th 1996, Luton, England.

EDUCATION

2007-2012 **High School**
Challney High School for Girls, Luton, England

2012-2014 **Luton Sixth From College**
Luton, England

2015-2019 **Integrated masters in Physics with Theoretical Physics**, First class
King's College London, London, England

2020 **PhD. Applied Physics**
Delft University of Technology
Thesis: Extending quantum dot arrays into three dimensions
Promotor: Prof. dr. ir. M. Veldhorst

2025 **Industry Internship**, Quantum Computing Group
Intel Corporation, Hillsboro, USA
Manager: Jeanette Roberts
Title: Operating exchange only qubits in 3x3 arrays

LIST OF PUBLICATIONS

5. **H. Tidjani**, D. Denora, M. Chan, J.H. Ungerer, B. van Straaten, S.D. Oosterhout, L.E.A. Stehouwer, G. Scappucci, M. Veldhorst, *A Three-Dimensional Array of Quantum Dots*, arXiv preprint arXiv:2512.01634 (2025).

4. C.A. Wang, V. John, **H. Tidjani**, C.X. Yu, A.S. Ivlev, C. Déprez, N.W. Hendrickx, A. Sammak, G. Scappucci, M. Veldhorst, *Operating semiconductor quantum processors with hopping spins*, Science **385**(6707), 447–452 (2024).

3. C.A. Wang, C. Déprez, **H. Tidjani**, W.I.L. Lawrie, N.W. Hendrickx, A. Sammak, G. Scappucci, M. Veldhorst, *Probing resonating valence bonds on a programmable germanium quantum simulator*, npj Quantum Information **9**, 58 (2023).

2. A.S. Ivlev, **H. Tidjani**, S.D. Oosterhout, A. Sammak, G. Scappucci, M. Veldhorst, *Coupled vertical double quantum dots at single-hole occupancy*, Applied Physics Letters **125**, 022101 (2024).

1. **H. Tidjani**, A. Tosato, A.S. Ivlev, C. Déprez, S.D. Oosterhout, L.E.A. Stehouwer, N.W. Hendrickx, A. Sammak, G. Scappucci, M. Veldhorst, *Vertical gate-defined double quantum dot in a strained germanium double quantum well*, Physical Review Applied **20**, 054035 (2023).

ISBN: 978-94-6384-921-0